HIGH TEMPERATURE AQUEOUS ALTERATION AND DIAGENESIS: UNEXPECTED INSIGHTS WITH IMAGING SPECTROSCOPY FROM MICRONS TO METERS

BY
REBECCA N. GREENBERGER
A.B., EARTH AND PLANETARY SCIENCES, WASHINGTON UNIVERSITY IN ST. LOUIS, 2010
Sc.M., GEOLOGICAL SCIENCES, BROWN UNIVERSITY, 2012

A DISSERTATION SUBMITTED IN PARTIAL FULFILLMENT OF THE REQUIREMENTS FOR THE DEGREE OF DOCTOR OF PHILOSOPHY IN THE DEPARTMENT OF EARTH, ENVIRONMENTAL, AND PLANETARY SCIENCES AT BROWN UNIVERSITY

PROVIDENCE, RHODE ISLAND
MAY 2015

This dissertation by Rebecca N. Greenberger is accepted in its present form by the Department of Earth, Environmental, and Planetary Sciences as satisfying the dissertation requirement of the degree of Doctor of Philosophy.

Date_____ _____
John F. Mustard, Advisor

Recommended to the Graduate Council

Date_____ _____
Reid F. Cooper, Reader

Date_____ _____
Ralph E. Milliken, Reader

Date_____ _____
Peter H. Schultz, Reader

Date_____ _____
Joel A. Hurowitz, Reader

Approved by the Graduate Council

Date_____ _____
Peter M. Weber, Dean of the Graduate School

CURRICULUM VITAE

Rebecca N. Greenberger

(314) 458-9745; rebecca_greenberger@brown.edu
Date of birth: October 8, 1987 (Columbus, Ohio)

Education

Brown University, Department of Earth, Environmental, and Planetary Sciences, Advisor: John Mustard

- Ph.D. Earth, Environmental and Planetary Sciences, May 2015. Thesis title: High Temperature Aqueous Alteration and Diagenesis: Unexpected Insights with Imaging Spectroscopy from Microns to Meters
- M. Sc. Geological Sciences, May 2012. Thesis title: Low temperature aqueous alteration of basalt: mineral assemblages of Deccan basalts and implications for Mars

Washington University in St. Louis, A.B. Earth and Planetary Sciences, August 2010, Arts & Sciences College Honors

Manuscripts submitted or in preparation

Greenberger, R. N., J. F. Mustard, E. A. Cloutis, P. Mann, J. H. Wilson, R. L. Flemming, K. Robertson, M. R. Salvatore, and C. S. Edwards, Hydrothermal alteration and diagenesis of terrestrial lacustrine pillow basalts: coordination of hyperspectral imaging with laboratory measurements, *Geochim. Cosmochim. Acta*, in revision.

Greenberger, R.N., J. F. Mustard, E. A. Cloutis, P. Mann, and J. H. Wilson, Characterization of aqueous alteration resulting from volcano-lacustrine interactions in the Hartford Basin: implications for Mars, *Chem. Geol*, in review.

Greenberger, R. N., J. F. Mustard, G. R. Osinski, L. L. Tornabene, A. Pontefract, C. L. Marion, R. L. Flemming, J. H. Wilson, and E. A. Cloutis, Hyperspectral mapping of alteration assemblages at a hydrothermal calcite-marcasite vug at the Haughton impact structure, *Meteorit. Planet. Sci,* in review.

Greenberger, R. N., J. F. Mustard, B. L. Ehlmann, D. L. Blaney, E. A. Cloutis, J. H. Wilson, and R. O. Green, Imaging spectroscopy of geological samples and outcrops: unexpected insights from microns to meters, in preparation for submission to *GSA Today*.

Publications

Greenberger, R. N., J. F. Mustard, E. A. Cloutis, L. M. Pratt, P. E. Sauer, P. Mann, K. Turner, M. D. Dyar, and D. L. Bish (2015), Serpentinization, iron oxidation, and aqueous conditions in an ophiolite: Implications for hydrogen production and habitability on Mars, *Earth Planet. Sci. Lett.*, *416*, 21–34, doi:10.1016/j.epsl.2015.02.002.

Greenberger, R. N., J. F. Mustard, P. S. Kumar, M. D. Dyar, E. A. Breves, and E. C. Sklute (2012), Low temperature aqueous alteration of basalt: Mineral assemblages of Deccan basalts and implications for Mars, *J. Geophys. Res.*, 117, E00J12,

doi:10.1029/2012JE004127.

Arvidson, R. E., J. F. Bell III, P. Bellutta, N. A. Cabrol, J. G. Catalano, J. Cohen, L. S. Crumpler, D. J. Des Marais, T. A. Estlin, W. H. Farrand, R. Gellert, J. A. Grant, **R. N. Greenberger**, E. A. Guinness, K. E. Herkenhoff, J. A. Herman, K. D. Iagnemma, J. R. Johnson, G. Klingelhöfer, R. Li, K. A. Lichtenberg, S. A. Maxwell, D. W. Ming, R. V. Morris, M. S. Rice, S. W. Ruff, A. Shaw, K. L. Siebach, P. A. de Souza, A. W. Stroupe, S. W. Squyres, R. J. Sullivan, K. P. Talley, J. A. Townsend, A. Wang, J. R. Wright, and A. S. Yen (2010), Spirit Mars Rover Mission: Overview and selected results from the northern Home Plate Winter Haven to the side of Scamander crater, J. Geophys. Res., 115, E00F03, doi:10.1029/2010JE003633.

Arvidson, R, R. Bonitz, M. Robinson, J. Carsten, R. Volpe, A. Trebi-Ollenu, M. Mellon, P. Chu, K. R. Davis, J. Wilson, A. Shaw, **R. Greenberger**, K. Siebach, T. Stein, S. Cull, W. Goetz, R. Morris, D. Ming, H. Keller, M. Lemmon, H. Sizemore, and M. Mehta, (2009). Results from the Mars Phoenix Lander Robotic Arm Experiment., *J. Geophys. Res.*, 114, E00E02, doi:10.1029/2009JE003408..

Arvidson, R.E., S. W. Ruff, R. V. Morris, D. W. Ming, L. S. Crumpler, A. S. Yen, S. W. Squyres, R. J. Sullivan, J. F. Bell, N. A. Cabrol, B. C. Clark, W. H. Farrand, R. Gellert, **R. Greenberger**, J. A. Grant, E. A. Guinness, K. E. Herkenhoff, J. A. Hurowitz, J. R. Johnson, G. Klingelhöfer, K. W. Lewis, R. Li, T. J. McCoy, J. Moersh, H. Y. McSween, S. L. Murchie, M. Schmidt, C. Schröder, A. Wang, S. Wiseman, M. B. Madsen, W. Goetz, and S. M. McLennan (2008), Spirit Mars Rover Mission to the Columbia Hills, Gusev Crater: Mission overview and selected results from the Cumberland Ridge to Home Plate, *J. Geophys. Res.*, 113, E12S33, doi:10.1029/2008JE003183.

Li, R., B. Wu, K. Di, A. Angelova, R. E. Arvidson, I. C. Lee, M. Maimone, L. H. Matthies, L. Richer, R. Sullivan, M. H. Sims, **R. Greenberger**, and S. W. Squyres (2008), Characterization of traverse slippage experienced by Spirit rover on Husband Hill at Gusev Crater, *J. Geophys. Res.*, 113, E12S35, doi:10.1029/2008JE003097.

Wang, A., J. F. Bell, R. Li, J. R. Johnson, W. H. Farrand, E. A. Cloutis, R. E. Arvidson, L. Crumpler, S. W. Squyres, S. M. McLennan, K. E. Herkenhoff, S. W. Ruff, A. T. Knudson, W. Chen, and **R. Greenberger** (2008), Light-toned salty soils and coexisting Si-rich species discovered by the Mars Exploration Rover Spirit in Columbia Hills, *J. Geophys. Res.*, 113, E12S40, doi:10.1029/2008JE003126.

Conference abstracts

Greenberger, R. N., J. F. Mustard, G. R. Osinski, L. L. Tornabene, A. Pontefract,C. L. Marion, R. L. Flemming, J. H. Wilson, and E. A. Cloutis (2014), Hydrothermal Formation and Oxidation of a Calcite-Marcasite Vug at the Haughton Impact Structure: Mapping of Alteration Assemblages with Hyperspectral Imaging, *46th LPSC*, Abstract #2267.

Greenberger, R. N., J. F. Mustard, E. A. Cloutis, L. M. Pratt, P. E. Sauer, P. Mann, K. Turner, and M. D. Dyar (2014), Aqueous Conditions and Habitability Associated with Formation of a Serpentinite: Using Analyses of Ferric Iron and Stable Carbon Isotopes to Reconstruct Hydrogen Production, *AGU Fall Meeting*,

Abstract #2211.

Lawson, M. J., E. S. Amador, B. L. Carrier, A. Albuja, J. Bapst, K. R. S, Cahill, F. Ebersohn, S. Gainey, G. Gartrelle, **R. N. Greenberger**, J. M. Hale, S. Johnston, J. Olivares, C. E. Parcheta, J. P. Sheehan, A. K. Thorpe and S. K. Zareh (2014), Enceladus Environmental Explorer (EVE): A Mission Concept, *AGU Fall Meeting*, Abstract #11621.

Greenberger, R. N., J. F. Mustard, E. A. Cloutis, L. M. Pratt, P. E. Sauer, P. Mann, K. Turner, and M. D. Dyar (2014), Understanding the Nature of Water-rock Interactions in a Serpentinizing System: Implications for Planetary Exploration and Subsurface Habitability, *GSA Annual Meeting*, Abstract #246202.

Greenberger, R. N., J. F. Mustard, E. A. Cloutis, P. Mann, and J. H. Wilson (2014), Characterization of Alteration of Lacustrine Pillow Basalts: Insights from Hyperspectral Imaging and Implications for Water-rock Interactions on Mars, *GSA Annual Meeting*, Abstract #246143.

Greenberger, R. N., J. F. Mustard, E. A. Cloutis, P. Mann, and J. H. Wilson (2014), Aqueous Alteration Rinds in Basalt: Mineralogic Characterization from Hand Sample to Outcrop with Hyperspectral Imaging and Implications for Mars 2020, *8th International Mars Conference*, Abstract #1028.

Cannon, K. M., J. F. Mustard, C. B. Agee, J. H. Wilson, and **R. N. Greenberger** (2014), Black Beauty's Rainbow: Hyperspectral Imaging of NWA 7034, *8th International Mars Conference*.

Wilson J. H. and **R. N. Greenberger** (2014), Utility of hyperspectral imagers in the mining industry: Italy's gypsum reserves, *Proc. SPIE* 9104, Spectral Imaging Sensor Technologies: Innovation Driving Advanced Application Capabilities, 91040E; doi:10.1117/12.2054981.

Greenberger, R. N., J. F. Mustard, G. R. Osinski, L. L. Tornabene, C. L. Marion, A. Pontefract, and E. A. Cloutis (2014), Spectral Mapping of Alteration Phases within a Hydrothermal Vug at the Haughton Impact Structure, *45th LPSC*, Abstract #1923.

Greenberger, R. N., J. F. Mustard, E. A. Cloutis, P. Mann, J. H. Wilson, and K. M. Cannon, (2014), Remote Sensing of Volcano-Lacustrine Interactions: Implications for Mars, *45th LPSC*, Abstract #1543.

Mann, P., E. A. Cloutis, **R. N. Greenberger**, R. E. Milliken, T. Hiroi, J. F. Mustard, R. L. Klima, C. A. Hibbitts, J. B. Plescia, J. F. Bell III, T. L. Roush, J.L. Bishop, and B. L. Ehlmann (2014), An Interlaboratory UV/VIS/NIR Wavelength Calibration Study, *45th LPSC*, Abstract #2392.

Tornabene L. L., G. R. Osinski, **R. N. Greenberger**, J. L. Bishop, E. A. Cloutis, C. L. Marion, J. F. Mustard, A. Pontefract, and M. S. Ramsey (2014), The Pre-, Syn- and Post-Impact Origin of Hydrated Phases: A Case Study Based on the Remote Sensing and Ground-Truth at the Haughton Impact Structure, Nunavut, Canada, *45th LPSC*, Abstract #2710.

Greenberger, R. N., J. F. Mustard, E. A. Cloutis, P. Mann, K. M. Cannon, and J. H. Wilson (2014), Mineral Assemblages and Spectral Signatures of Altered Lacustrine Pillow Basalts: A Northeastern U.S. Analog for Lava-Water Interactions on Mars, *49th annual GSA Northeastern Section meeting*, Abstract# 236217.

Greenberger, R. N., J. F. Mustard, E. A. Cloutis, P. Mann, and K. M. Cannon (2013), Outcrop-Scale Remote Sensing of Lava-Water Interactions: Implications for Assessing Water-Rock Interactions on Mars, *AGU Fall Meeting,* Abstract V53C-2807.

Greenberger, R. N., J. F. Mustard, E. A. Cloutis, P. Mann, and K. Turner (2013), Iron Oxidation State in Serpentines from Visible Imaging Spectroscopy: Implications for Planetary Exploration and Assessment of Astrobiological Potential, *44th LPSC,* Abstract# 1296.

Cloutis, E., L. Whyte, A. Qadi, L. Anderson-Trocme, J.F. Bell III, G. Berard, A. Boivin, A. Ellery, **R. Greenberger**, E. Haddad, W. Jamroz, R. Kruzelecky, P. Mann, J. Mustard, K. Olsen, M. Perrot, D. Popa, M. Ralchenko, T. Rhind, C. Samson, R. Sharma, J. Stromberg, K. Strong, A. Tremblay, and B. Wing (2013), The Mars Methane Analogue Mission (M3): Results of the 2012 Field Deployment, *44th LPSC,* Abstract# 1579.

Greenberger, R. N., J. F. Mustard, E. A. Cloutis, P. Mann, and K. Turner (2012), Field hyperspectral visible imaging spectroscopy of serpentine deposits in Quebec: implications for the value of visible spectroscopy in planetary exploration, *GSA Annual Meeting,* Abstract# 210978.

Greenberger, R. N. and Mustard, J. F. (2012), Mineral Assemblages of Al-Phyllosilicate Deposits on Mars: Implications for Leaching Processes, Water Chemistry, and Atmosphere-Water Interactions, *Third Conference on Early Mars: Geologic, Hydrologic, and Climatic Evolution and the Implications for Life,* Abstract# 7063.

Greenberger, R. N., J. F. Mustard, P. S. Kumar, M. D. Dyar, E. A. Breves, and E. C. Sklute (2012), Mineral Assemblages of Deccan Basalts and Al-Phyllosilicate Deposits on Mars: Implications for Leaching Processes on Mars, *43rd LPSC,* Abstract# 1907.

Greenberger, R. N., J. F. Mustard, P. S. Kumar, M. D. Dyar, E. A. Breves, and E. C. Sklute (2011), A Vertical Section of Deccan Basalts as a Spectroscopic and Mineral Assemblage Analog to Phyllosilicate Stratigraphies on Mars, *GSA Annual Meeting.*

Mustard, J. F., **R. N. Greenberger**, M. R. Salvatore, and B. L. Ehlmann. (2011), Traversing the Aqueous History of Mars Through Analogs, Geological Society of America Annual Meeting.

Greenberger, R. N., J. F. Mustard, P. S. Kumar, M. D. Dyar, E. A. Breves, and E. C. Sklute (2011), Weathering Products of Deccan Basalts and Implications for Mars, *42nd LPSC,* Abstract# 2548.

Work Experience

Research or Teaching Assistant, Brown University (2010-present). Advisor: John Mustard

Teaching assistant for GEOL 0010: Face of the Earth, Spring 2013 (Professor: Peter Gromet)

Undergraduate Research, Earth and Planetary Sciences Remote Sensing Lab (2007-2010). Advisor: Ray Arvidson.

Teaching Assistant for part of Planetary Spectroscopy and Remote Sensing short course taught by Washington University at Shandong University, Weihai, China (July

2009)

Documentarian and Geology Science Theme Group Member. Mars Phoenix Lander surface operations (May-October 2008)

Intern. The Ohio State University Mapping and GIS Lab (Summer 2006). Supervisor: Ron Li.

Awards, Honors, and Travel Grants

Brown University dissertation fellowship (Fall 2014)

Geological Society of America Planetary Geology Division travel grant for GSA Annual Meeting (2014)

Geological Society of America Northeastern Section travel grant for GSA Annual Meeting (2012, 2014)

NASA Mars student travel grant to attend Eighth International Mars Conference (2014)

Lunar and Planetary Institute Career Development Award (2014)

Geological Society of America Northeastern Section travel grant for Northeastern Section Meeting (2014)

AGU student travel grant (2013)

Brown University first year fellowship (2010)

Arthur Holly Compton Fellowship, Washington University (2006-2010)

J. Steven Fossett Fellowship, Washington University (2006-2010)

Professional Organizations

Sigma Xi (2010)

Geological Society of America, member (2011-present)

American Geophysical Union, member (2012-present)

Professional Development Activities

NASA Planetary Science Summer School (2014)

Josep Comas i Solà International Summer School in Astrobiology: "Biosignatures: The Fingerprints of Life" (2013)

NASA Planetary Volcanology Field Workshop (2013)

University of Missouri, Columbia, Geology Field Camp (2010)

Service and outreach activities

Co-proposed accepted session for Geological Society of America Annual Meeting (2015)

Reviewed manuscripts for *Journal of Geophysical Research: Planets* and *Journal of Selected Topics in Applied Earth Observations and Remote Sensing* (2014)

Vartan Gregorian Elementary School volunteer (2010-present): teach science to second grade students through Brown University Geology Department program

Rhode Island Science Olympiad (2013): co-organized and ran remote sensing test

Geoclub treasurer (2011-2012)

Languages

Conversational in Mandarin Chinese

ACKNOWLEDGMENTS

First, my interest in geology began with Ray Arvidson, who, through his classes, trips to the Mojave Desert and Hawaii, and promises of working on Mars missions, showed me the incredible field of geology. Before I knew it, I couldn't see myself doing anything else. I never thought I would have these opportunities in my life, especially not as an undergraduate. Thank you, Ray. You always seem to know what I want to do before I do.

When I came to Brown, I had only done remote sensing and had little field or lab experience, but I knew that I loved being outside and getting my hands dirty. For my first project, Jack Mustard handed me fourteen samples from in India. After months of grinding and sieving, then analyzing those samples, I realized how much I liked working in the lab. Then, I started applying those results to Mars and quickly discovered that I just don't like working with CRISM data. Despite the fact that Jack's planetary students (and nearly all planetary grad students at Brown) work with CRISM or some other planetary remote sensing dataset, Jack found a way for me to go a different direction and work on something that really interested me. As he put it, I wanted fieldwork, and he wanted science. Though he doubted for months that there would be science, somehow I think we found the science. Jack, thank you for sending me to a Target parking lot in Connecticut, an asbestos mine in Quebec, Winnipeg in January, and, most especially, an impact structure in the High Arctic. I have had some incredible experiences at Brown. And thank you for letting me drain your research account year after year to do this research. To my committee, thank you for supporting and challenging me. In addition, thank you to the administrative staff (Karen Leap-Canis, Jessica Muirhead, and Melissa Shein) and

technical staff (Joe Boesenberg, Bill Collins, Dave Murray, and Joe Orchardo) for all of their help over the years.

To my collaborators from outside of Brown, thank you for working with me and for all of your contributions to my thesis. None of this work would have been possible without you all. Ed Cloutis, you trusted me to take your hyperspectral cameras to three different field sites because "it's better than them collecting dust in the lab," and you have been so helpful, responsive, and supportive of my research. Paul Mann, thank you for helping me time after time to make sure that I get the data that I needed for my thesis. I am sorry if some of your equipment may have come back from the field a little muddy (blame Oz!). Gordon "Oz" Osinski, I have had so much fun doing fieldwork and working with you and your group. Thank you for letting me join you all in the Arctic and collaborate with you. Livio Tornabene, you have been so supportive of my research and development as a scientist. Thank you for all of that and for making sure I ate lunch in the field when I was scrambling to image outcrops before the generator died, for letting me stay with you to make my visit to Western cheaper, etc. Cass Marion and Alex Pontefract, I am so glad I got to spend two weeks in the field with you. Thanks for everything! To all of you, thank you for everything above, and thank you for showing me that planetary science really is more than remote sensing and that it is okay to want to do fieldwork. You have done more for me than you know. And finally, Lisa Pratt, you suggested a new direction for my research and taught me how to work with isotopes. Then, when I couldn't do multiple sets of measurements at Brown, you got them done for me at your university. Thank you for all of that and for the hours that you spent on the phone with me trying to understand isotopes the week before a conference.

Two former grad students are not only friends but have become collaborators. Janette Wilson, you welcomed me to Brown and helped me through my first two years. I've missed you since you left, but I'm glad to see you so much happier now. You have been an amazing friend. When it seemed like I'd never get the high quality data that I desperately needed for my thesis, you convinced your bosses to let me image my samples at Headwall Photonics. Then, when the data were better than I could have imagined and I wanted more, you made that happen. I have a thesis because of you. Mark Salvatore, you were the older student at Brown who also did primarily field and lab work. You helped me begin to do lab work and figure out where everything was, and you always have and continue to answer my many, many questions. You helped me through some of the most difficult times in grad school when no one else could. Thank you so much for all of the time you spent time helping me.

The group of graduate students at Brown is amazingly friendly and supportive. Thank you all for being there for me throughout my time here. Mary Peterson, you've been a fantastic roommate, and we have a cat! Angela Stickle, you've told me too many times to count that I can do this and that things will get better. Leah Cheek and Jenny Whitten, I miss you guys in the mission room. Diane Wetzel and Tess Caswell, you two enabled my bubble tea addiction. Steph Quintana, you're an awesome climbing buddy and friend. Steph Spera, and it's been great having another Pathfinder in the lab group. Thank you for supporting me, telling me "you're fine" every other day, and indulging my last minute Paintnite requests when I need to get away. To everyone else who started with me and is still here (Tim Goudge, Dan Moriarty, Tabb Prissel, Kat Scanlon, Kei Shimizu, and Io Wicaksono), thank you for all of the support along the way. We're almost done!

To everyone I forgot in this last week of thesis writing, thank you for everything!

To my family, thank you for always supporting me and encouraging me to pursue my dreams, no matter where they may take me (summer in China or fieldwork on an uninhabited island in the Arctic?). I love you all so much. Sarah, it's been so much fun to run off to various warm destinations with you. Jonathan, it's been great having you so close! And to my cousins in Rhode Island, thank you for taking care of me here. It's been so nice to be near family.

I must of course thank the cats. Andie, you always make the world seem a little better when you curl up on my lap. You force me to take breaks from thesis writing mid-sentence, jumping up next to me with that determined look that I know means "I am climbing onto your lap whether your laptop is there or not" and the implied threats of rotating my screen, disabling the touchpad, and closing various files. I may call you the Anti-Thesis Cat, but those breaks have kept me sane. And Iggy, though in two short months you managed to destroy everything that we left within your reach, stole our pens, and left shredded cardboard everywhere, you could always make me smile chasing the laser pointer with such intensity that you'd skid into walls. Thank you to their owners, Sandra and Charlie Wiseman and Bronwen Konecky, for letting them stay with us.

Trader Joe's, thank you for selling the cheapest and best dark chocolate covered espresso beans. They have given the energy to finish more of my thesis than I should admit. Similarly, the various bubble tea places on Thayer Street have kept me going. Thank you, SnoTea Caffe and Sushi and Bubble Tea Company, for selling me way too many caffeinated, sugary drinks.

Finally, I would like to thank Bethany Ehlmann for giving me a chance, offering

me a postdoc, and giving me a lot to look forward to. I can't wait to move to Pasadena and work with you!

PREFACE

There is widespread evidence for water billions of years ago on Mars, from ancient valley networks (e.g., Baker et al., 1992; Howard et al., 2005; Fassett and Head III, 2008a), and lakes (e.g., Cabrol and Grin, 1999; Fassett and Head III, 2008b; Goudge et al., 2012a, 2012b) to identifications of secondary minerals formed through interaction with water (e.g., Bibring et al., 2005, 2006; Bishop et al., 2008; Mustard et al., 2008). All of these detections suggest the intriguing possibility that there may once have been habitable conditions under which life evolved on Mars. Yet questions remain as to what environments might have been present. Some argue that Mars was once warmer and wetter (Craddock and Howard, 2002; Carter et al., 2015), while others suggest that low-grade water-rock interactions or deuteric alteration in the subsurface produced much of the spectral signatures of alteration (Ehlmann et al., 2011; Meunier et al., 2012) or that early Mars was cold and icy (e.g., Head et al., 2014).

The mineralogic evidence for widespread aqueous activity on Mars comes from orbital spectroscopic observations by the Compact Reconnaissance Imaging Spectrometer for Mars (CRISM; e.g., Murchie et al., 2007, 2009; Mustard et al., 2008), the Observatoire pour la Minéralogie, l'Eau, les Glaces et l'Activité (OMEGA; e.g., Bibring et al., 2005, 2006), and the Thermal Emission Spectrometer (TES; e.g., Christensen et al., 2000, 2001; Wyatt and McSween, 2002; Bandfield et al., 2003). A few landed missions greatly expanded the understanding of local or regional aqueous processes, especially when combined with orbital datasets (e.g., Squyres et al., 2004, 2012; Morris et al., 2010; Arvidson et al., 2014; Grotzinger et al., 2014; Vaniman et al., 2014). However, these missions only ground truth a small fraction of the global detections of hydrated minerals.

Studies of terrestrial analogs therefore are necessary to connect aqueous processes and the resulting secondary mineral assemblages with their remotely-sensed signatures. These types of studies have been done in a variety of environments. For example, oxidative weathering rinds that form through anhydrous processes have been characterized in Antarctica (Salvatore et al., 2013). The mineralogies and spectral signatures of relatively fresh basalts altered in low temperature and hydrothermal environments have been studied in Iceland (Ehlmann et al., 2012). Highly leached basalts in India and serpentinized peridotite in Australia have been characterized as analogs for Al-phyllosilicate over Fe/Mg-smectite stratigraphies on Mars (Gaudin et al., 2011; Greenberger et al., 2012). The spectral signatures of hydrothermal alteration have been measured in a variety of locations (e.g., Bishop et al., 2002, 2004; Warner and Farmer, 2010; Cousins et al., 2013). All of these studies utilize point measurements of spectroscopy, often measured in the laboratory and with powdered samples. Chemistry and mineralogy measurements generally analyze powders or thin sections. A few studies have made a concerted effort to coordinate measurements of chemistry, mineralogy, and spectroscopy (Bishop et al., 2014, 2013), but these studies coordinate analyses of powders and lose the original petrologic contexts. A fundamental gap therefore exists between these measurements and the 18+ m/pixel orbital imaging spectroscopy measurements of the natural whole-rock or outcrop exposures on Mars.

This thesis attempts to bridge this divide between processes on Earth and orbital remote sensing observations of Mars by using imaging spectroscopy of thick sections and hand samples in the laboratory and outcrops in the field to investigate and characterize geological processes using measurements more analogous to Mars. Imaging spectroscopy

at this scale identifies and maps mineralogies at extremely high spatial resolution (up to ten's to hundred's of μm/pixel depending on observing distance) and is a powerful mineralogic and petrologic tool. The framing questions of this thesis are (1) what mineral assemblages form through high temperature aqueous alteration in diverse environments? (2) how do these assemblages later alter through diagenesis and/or low temperature weathering, and how are they preserved in the geologic record? and (3) what are the spectral signatures of this alteration at sub-millimeter to tens of meters scales, and how does mineralogy vary spatially with changes in water/rock ratios, temperatures, chemistries, and redox states? This thesis characterizes high temperature aqueous alteration and later diagenesis or weathering in three settings: metamorphic (Chapter 1), volcanic (Chapters 2-3), and impact (Chapter 4). In addition to providing additional insight into the spectral signatures of known alteration processes for comparison with data from Mars, this thesis also provides unexpected insights into the alteration processes on Earth by identifying phases and mapping mineralogies and iron oxidation states and coordination environments throughout samples and outcrops.

Chapter 1 characterizes the aqueous conditions and formation of biologically-important byproducts (molecular hydrogen and methane) during serpentinization at an outcrop of Early Ordovician serpentinites in Norbestos, Quebec. This work was done with two main types of analyses, imaging spectroscopy of samples and outcrops and stable isotope analyses of carbon and oxygen in blebs of carbonate, along with supporting analyses of chemistry, mineralogy, and oxidation state. The imaging spectroscopy results suggest that advanced serpentinization occurred at that site with liberal production of hydrogen under reducing conditions. The stable isotope analyses retain a signature of

methane production during serpentinization at low water/rock ratios in a carbon-limited system closed to carbon addition but open to methane escape. The preservation of this ancient signature is promising for the detection of any potential biosignatures in serpentine-bearing terrains on Mars.

Chapters 2 and 3 characterize hydrothermal alteration and diagenesis of Early Jurassic lacustrine pillow lavas exposed at an outcrop in Meriden, Connecticut. This field site is an analog for any potential volcano-lacustrine interactions on Mars. Chapter 2 uses coordinated analyses of one pillow lava characteristic of greener alteration rinds present at a portion of the outcrop to understand the detailed alteration history of the sample. The coordinated analyses were done on a thick section prepared across the alteration rind, and these results are scaled to the hand-sample and outcrop. In Chapter 3, the broader types and distributions of alteration at the outcrop are discussed, including baking of sediments, formation of red coatings on sediments and some pillow lavas, red- and purple-hued alteration of pillow lavas, formation of alteration rinds, mineralization of vesicles and veins, and alteration of hyaloclastite breccias. There is pervasive low-grade alteration at the outcrop with localized, more intense alteration, and specific types of alteration vary throughout the outcrop. These results have implications for understanding any similar deposits on Mars.

Chapter 4 uses imaging spectroscopy to map a calcite-marcasite vug that has weathered at low temperatures to oxides and sulfates at the Haughton impact structure in the Canadian High Arctic. This vug formed in the impact melt rocks as a result of the impact-generated hydrothermal system and weathered at ambient temperatures after cooling of the hydrothermal system. Evolving aqueous conditions are inferred from the

spectroscopy and validated by chemistry and mineralogy measurements, with formation of marcasite at high temperatures under reducing conditions and then weathering with progressively more oxidizing and complex aqueous solutions.

Chapter 5 synthesizes the results of this thesis and highlights a few applications of imaging spectroscopy at the thick section, hand sample, and outcrop scales. Imaging spectroscopy at these scales is a powerful non-destructive tool for mineralogic and petrologic analyses. This chapter is intended for a broader audience and is targeted for submission in *GSA Today*. For the reader unfamiliar with imaging spectroscopy, this chapter could provide an introduction to the technique.

References

Arvidson, R.E., Squyres, S.W., Bell, J.F., Catalano, J.G., Clark, B.C., Crumpler, L.S., Souza, P.A. de, Fairén, A.G., Farrand, W.H., Fox, V.K., Gellert, R., Ghosh, A., Golombek, M.P., Grotzinger, J.P., Guinness, E.A., Herkenhoff, K.E., Jolliff, B.L., Knoll, A.H., Li, R., McLennan, S.M., Ming, D.W., Mittlefehldt, D.W., Moore, J.M., Morris, R.V., Murchie, S.L., Parker, T.J., Paulsen, G., Rice, J.W., Ruff, S.W., Smith, M.D., Wolff, M.J., 2014. Ancient Aqueous Environments at Endeavour Crater, Mars. Science 343, 1248097. doi:10.1126/science.1248097

Baker, V.R., Carr, M.H., Gulick, V.C., Williams, C.R., Marley, M.S., 1992. Channels and valley networks. Mars -1, 493–522.

Bandfield, J.L., Glotch, T.D., Christensen, P.R., 2003. Spectroscopic Identification of Carbonate Minerals in the Martian Dust. Science 301, 1084–1087. doi:10.1126/science.1088054

Bibring, J.-P., Langevin, Y., Gendrin, A., Gondet, B., Poulet, F., Berthé, M., Soufflot, A., Arvidson, R., Mangold, N., Mustard, J., Drossart, P., the OMEGA team, 2005. Mars Surface Diversity as Revealed by the OMEGA/Mars Express Observations. Science 307, 1576 –1581. doi:10.1126/science.1108806

Bibring, J.-P., Langevin, Y., Mustard, J.F., Poulet, F., Arvidson, R., Gendrin, A., Gondet, B., Mangold, N., Pinet, P., Forget, F., the OMEGA team, 2006. Global Mineralogical and Aqueous Mars History Derived from OMEGA/Mars Express Data. Science 312, 400 –404. doi:10.1126/science.1122659

Bishop, J.L., Dobrea, E.Z.N., McKeown, N.K., Parente, M., Ehlmann, B.L., Michalski, J.R., Milliken, R.E., Poulet, F., Swayze, G.A., Mustard, J.F., Murchie, S.L., Bibring, J.-P., 2008. Phyllosilicate Diversity and Past Aqueous Activity Revealed at Mawrth Vallis, Mars. Science 321, 830 –833. doi:10.1126/science.1159699

Bishop, J.L., Englert, P.A.J., Patel, S., Tirsch, D., Roy, A.J., Koeberl, C., Böttger, U., Hanke, F., Jaumann, R., 2014. Mineralogical analyses of surface sediments in the Antarctic Dry Valleys: coordinated analyses of Raman spectra, reflectance spectra and elemental abundances. Philos. Trans. R. Soc. Math. Phys. Eng. Sci. 372, 20140198. doi:10.1098/rsta.2014.0198

Bishop, J.L., Franz, H.B., Goetz, W., Blake, D.F., Freissinet, C., Steininger, H., Goesmann, F., Brinckerhoff, W.B., Getty, S., Pinnick, V.T., Mahaffy, P.R., Dyar, M.D., 2013. Coordinated analyses of Antarctic sediments as Mars analog materials using reflectance spectroscopy and current flight-like instruments for CheMin, SAM and MOMA. Icarus, Terrestrial Analogs for Mars: Mars Science Laboratory and Beyond 224, 309–325. doi:10.1016/j.icarus.2012.05.014

Bishop, J.L., Murad, E., Lane, M.D., Mancinelli, R.L., 2004. Multiple techniques for mineral identification on Mars:: a study of hydrothermal rocks as potential analogues for astrobiology sites on Mars. Icarus 169, 311–323. doi:10.1016/j.icarus.2003.12.025

Bishop, J.L., Schiffman, P., Southard, R., 2002. Geochemical and mineralogical analyses of palagonitic tuffs and altered rinds of pillow basalts in Iceland and applications to Mars. Geol. Soc. Lond. Spec. Publ. 202, 371 –392. doi:10.1144/GSL.SP.2002.202.01.19

Cabrol, N.A., Grin, E.A., 1999. Distribution, Classification, and Ages of Martian Impact Crater Lakes. Icarus 142, 160–172. doi:10.1006/icar.1999.6191

Carter, J., Loizeau, D., Mangold, N., Poulet, F., Bibring, J.-P., 2015. Widespread surface weathering on early Mars: A case for a warmer and wetter climate. Icarus 248, 373–382. doi:10.1016/j.icarus.2014.11.011

Christensen, P.R., Bandfield, J.L., Clark, R.N., Edgett, K.S., Hamilton, V.E., Hoefen, T., Kieffer, H.H., Kuzmin, R.O., Lane, M.D., Malin, M.C., Morris, R.V., Pearl, J.C., Pearson, R., Roush, T.L., Ruff, S.W., Smith, M.D., 2000. Detection of crystalline hematite mineralization on Mars by the Thermal Emission Spectrometer: Evidence for near-surface water. J. Geophys. Res. 105, PP. 9623–9642. doi:200010.1029/1999JE001093

Christensen, P.R., Bandfield, J.L., Hamilton, V.E., Ruff, S.W., Kieffer, H.H., Titus, T.N., Malin, M.C., Morris, R.V., Lane, M.D., Clark, R.L., Jakosky, B.M., Mellon, M.T., Pearl, J.C., Conrath, B.J., Smith, M.D., Clancy, R.T., Kuzmin, R.O., Roush, T., Mehall, G.L., Gorelick, N., Bender, K., Murray, K., Dason, S., Greene, E.,

Silverman, S., Greenfield, M., 2001. Mars Global Surveyor Thermal Emission Spectrometer experiment: Investigation description and surface science results. J. Geophys. Res. Planets 106, 23823–23871. doi:10.1029/2000JE001370

Cousins, C.R., Crawford, I.A., Carrivick, J.L., Gunn, M., Harris, J., Kee, T.P., Karlsson, M., Carmody, L., Cockell, C., Herschy, B., Joy, K.H., 2013. Glaciovolcanic hydrothermal environments in Iceland and implications for their detection on Mars. J. Volcanol. Geotherm. Res. 256, 61–77. doi:10.1016/j.jvolgeores.2013.02.009

Craddock, R.A., Howard, A.D., 2002. The case for rainfall on a warm, wet early Mars. J. Geophys. Res. Planets 107, 21–1–21–36. doi:10.1029/2001JE001505

Ehlmann, B.L., Bish, D.L., Ruff, S.W., Mustard, J.F., 2012. Mineralogy and chemistry of altered Icelandic basalts: Application to clay mineral detection and understanding aqueous environments on Mars. J. Geophys. Res. 117, E00J16. doi:10.1029/2012JE004156

Ehlmann, B.L., Mustard, J.F., Murchie, S.L., Bibring, J.-P., Meunier, A., Fraeman, A.A., Langevin, Y., 2011. Subsurface water and clay mineral formation during the early history of Mars. Nature 479, 53–60. doi:10.1038/nature10582

Fassett, C.I., Head III, J.W., 2008a. The timing of martian valley network activity: Constraints from buffered crater counting. Icarus 195, 61–89. doi:10.1016/j.icarus.2007.12.009

Fassett, C.I., Head III, J.W., 2008b. Valley network-fed, open-basin lakes on Mars: Distribution and implications for Noachian surface and subsurface hydrology. Icarus 198, 37–56. doi:10.1016/j.icarus.2008.06.016

Gaudin, A., Dehouck, E., Mangold, N., 2011. Evidence for weathering on early Mars from a comparison with terrestrial weathering profiles. Icarus 216, 257–268. doi:10.1016/j.icarus.2011.09.004

Goudge, T.A., Head, J.W., Mustard, J.F., Fassett, C.I., 2012a. An analysis of open-basin lake deposits on Mars: Evidence for the nature of associated lacustrine deposits and post-lacustrine modification processes. Icarus 219, 211–229. doi:10.1016/j.icarus.2012.02.027

Goudge, T.A., Mustard, J.F., Head, J.W., Fassett, C.I., 2012b. Constraints on the history of open-basin lakes on Mars from the composition and timing of volcanic resurfacing. J. Geophys. Res. Planets 117, E00J21. doi:10.1029/2012JE004115

Greenberger, R.N., Mustard, J.F., Kumar, P.S., Dyar, M.D., Breves, E.A., Sklute, E.C., 2012. Low temperature aqueous alteration of basalt: Mineral assemblages of Deccan basalts and implications for Mars. J. Geophys. Res. 117, E00J12. doi:10.1029/2012JE004127

Grotzinger, J.P., Sumner, D.Y., Kah, L.C., Stack, K., Gupta, S., Edgar, L., Rubin, D., Lewis, K., Schieber, J., Mangold, N., Milliken, R., Conrad, P.G., DesMarais, D., Farmer, J., Siebach, K., Calef, F., Hurowitz, J., McLennan, S.M., Ming, D., Vaniman, D., Crisp, J., Vasavada, A., Edgett, K.S., Malin, M., Blake, D., Gellert, R., Mahaffy, P., Wiens, R.C., Maurice, S., Grant, J.A., Wilson, S., Anderson, R.C., Beegle, L., Arvidson, R., Hallet, B., Sletten, R.S., Rice, M., Bell, J., Griffes, J., Ehlmann, B., Anderson, R.B., Bristow, T.F., Dietrich, W.E., Dromart, G., Eigenbrode, J., Fraeman, A., Hardgrove, C., Herkenhoff, K., Jandura, L., Kocurek, G., Lee, S., Leshin, L.A., Leveille, R., Limonadi, D., Maki, J.,

McCloskey, S., Meyer, M., Minitti, M., Newsom, H., Oehler, D., Okon, A., Palucis, M., Parker, T., Rowland, S., Schmidt, M., Squyres, S., Steele, A., Stolper, E., Summons, R., Treiman, A., Williams, R., Yingst, A., and MSL Science Team, 2014. A Habitable Fluvio-Lacustrine Environment at Yellowknife Bay, Gale Crater, Mars. Science 343, 1242777. doi:10.1126/science.1242777

Head, J.W., Wordsworth, R., Forget, F., Madeleine, J.-B., Halevy, I., 2014. Late Noachian ``Cold and Icy Highlands'' Model: Geological Predictions for Equilibrium Environments and Equilibrium/Non-Equilibrium Melting Scenarios, in: Lunar and Planetary Science Conference. Presented at the Lunar and Planetary Science Conference, Abstract 1412.

Howard, A.D., Moore, J.M., Irwin, R.P., 2005. An intense terminal epoch of widespread fluvial activity on early Mars: 1. Valley network incision and associated deposits. J. Geophys. Res. Planets 110, E12S14. doi:10.1029/2005JE002459

Meunier, A., Petit, S., Ehlmann, B.L., Dudoignon, P., Westall, F., Mas, A., Albani, A.E., Ferrage, E., 2012. Magmatic precipitation as a possible origin of Noachian clays on Mars. Nat. Geosci. 5, 739–743. doi:10.1038/ngeo1572

Morris, R.V., Ruff, S.W., Gellert, R., Ming, D.W., Arvidson, R.E., Clark, B.C., Golden, D.C., Siebach, K., Klingelhöfer, G., Schröder, C., Fleischer, I., Yen, A.S., Squyres, S.W., 2010. Identification of Carbonate-Rich Outcrops on Mars by the Spirit Rover. Science 329, 421–424. doi:10.1126/science.1189667

Murchie, S., Arvidson, R., Bedini, P., Beisser, K., Bibring, J.-P., Bishop, J., Boldt, J., Cavender, P., Choo, T., Clancy, R.T., Darlington, E.H., Marais, D.D., Espiritu, R., Fort, D., Green, R., Guinness, E., Hayes, J., Hash, C., Heffernan, K., Hemmler, J.,

Heyler, G., Humm, D., Hutcheson, J., Izenberg, N., Lee, R., Lees, J., Lohr, D., Malaret, E., Martin, T., McGovern, J.A., McGuire, P., Morris, R., Mustard, J., Pelkey, S., Rhodes, E., Robinson, M., Roush, T., Schaefer, E., Seagrave, G., Seelos, F., Silverglate, P., Slavney, S., Smith, M., Shyong, W.-J., Strohbehn, K., Taylor, H., Thompson, P., Tossman, B., Wirzburger, M., Wolff, M., 2007. Compact Reconnaissance Imaging Spectrometer for Mars (CRISM) on Mars Reconnaissance Orbiter (MRO). J. Geophys. Res. 112, 57 PP. doi:200710.1029/2006JE002682

Murchie, S.L., Mustard, J.F., Ehlmann, B.L., Milliken, R.E., Bishop, J.L., McKeown, N.K., Dobrea, E.Z.N., Seelos, F.P., Buczkowski, D.L., Wiseman, S.M., Arvidson, R.E., Wray, J.J., Swayze, G., Clark, R.N., Marais, D.J.D., McEwen, A.S., Bibring, J.-P., 2009. A synthesis of Martian aqueous mineralogy after 1 Mars year of observations from the Mars Reconnaissance Orbiter. J. Geophys. Res. 114, 30 PP. doi:200910.1029/2009JE003342

Mustard, J.F., Murchie, S.L., Pelkey, S.M., Ehlmann, B.L., Milliken, R.E., Grant, J.A., Bibring, J.-P., Poulet, F., Bishop, J., Dobrea, E.N., Roach, L., Seelos, F., Arvidson, R.E., Wiseman, S., Green, R., Hash, C., Humm, D., Malaret, E., McGovern, J.A., Seelos, K., Clancy, T., Clark, R., Marais, D.D., Izenberg, N., Knudson, A., Langevin, Y., Martin, T., McGuire, P., Morris, R., Robinson, M., Roush, T., Smith, M., Swayze, G., Taylor, H., Titus, T., Wolff, M., 2008. Hydrated silicate minerals on Mars observed by the Mars Reconnaissance Orbiter CRISM instrument. Nature 454, 305–309. doi:10.1038/nature07097

Salvatore, M.R., Mustard, J.F., Head, J.W., Cooper, R.F., Marchant, D.R., Wyatt, M.B., 2013. Development of alteration rinds by oxidative weathering processes in Beacon Valley, Antarctica, and implications for Mars. Geochim. Cosmochim. Acta 115, 137–161. doi:10.1016/j.gca.2013.04.002

Squyres, S.W., Arvidson, R.E., Bell, J.F., Calef, F., Clark, B.C., Cohen, B.A., Crumpler, L.A., Souza, P.A. de, Farrand, W.H., Gellert, R., Grant, J., Herkenhoff, K.E., Hurowitz, J.A., Johnson, J.R., Jolliff, B.L., Knoll, A.H., Li, R., McLennan, S.M., Ming, D.W., Mittlefehldt, D.W., Parker, T.J., Paulsen, G., Rice, M.S., Ruff, S.W., Schröder, C., Yen, A.S., Zacny, K., 2012. Ancient Impact and Aqueous Processes at Endeavour Crater, Mars. Science 336, 570–576. doi:10.1126/science.1220476

Squyres, S.W., Grotzinger, J.P., Arvidson, R.E., Bell, J.F., Calvin, W., Christensen, P.R., Clark, B.C., Crisp, J.A., Farrand, W.H., Herkenhoff, K.E., Johnson, J.R., Klingelhöfer, G., Knoll, A.H., McLennan, S.M., McSween, H.Y., Morris, R.V., Rice, J.W., Rieder, R., Soderblom, L.A., 2004. In Situ Evidence for an Ancient Aqueous Environment at Meridiani Planum, Mars. Science 306, 1709–1714. doi:10.1126/science.1104559

Vaniman, D.T., Bish, D.L., Ming, D.W., Bristow, T.F., Morris, R.V., Blake, D.F., Chipera, S.J., Morrison, S.M., Treiman, A.H., Rampe, E.B., Rice, M., Achilles, C.N., Grotzinger, J.P., McLennan, S.M., Williams, J., Bell, J.F., Newsom, H.E., Downs, R.T., Maurice, S., Sarrazin, P., Yen, A.S., Morookian, J.M., Farmer, J.D., Stack, K., Milliken, R.E., Ehlmann, B.L., Sumner, D.Y., Berger, G., Crisp, J.A., Hurowitz, J.A., Anderson, R., Marais, D.J.D., Stolper, E.M., Edgett, K.S., Gupta, S., Spanovich, N., and MSL Science Team 2014. Mineralogy of a Mudstone at

Yellowknife Bay, Gale Crater, Mars. Science 343, 1243480. doi:10.1126/science.1243480

Warner, N.H., Farmer, J.D., 2010. Subglacial Hydrothermal Alteration Minerals in Jökulhlaup Deposits of Southern Iceland, with Implications for Detecting Past or Present Habitable Environments on Mars. Astrobiology 10, 523–547. doi:10.1089/ast.2009.0425

Wyatt, M.B., McSween, H.Y., 2002. Spectral evidence for weathered basalt as an alternative to andesite in the northern lowlands of Mars. Nature 417, 263–266. doi:10.1038/417263a

TABLE OF CONTENTS

CHAPTER 1

Serpentinization, iron oxidation, and aqueous conditions in an ophiolite: implications for hydrogen production and habitability on Mars

Rebecca N. Greenberger[a], John F. Mustard[a], Edward A. Cloutis[b], Lisa M. Pratt[c], Peter E. Sauer[c], Paul Mann[b], Kathryn Turner[d], M. Darby Dyar[e], and David L. Bish[c]

[a]Department of Earth, Environmental, and Planetary Sciences
Brown University, Providence, RI, USA 02912

[b]Department of Geography, University of Winnipeg
Winnipeg, Manitoba, Canada R3B 2E9

[c]Department of Geological Sciences
Indiana University, Bloomington, IN, USA 47405-1405

[d]Department of Physics, University of Winnipeg
Winnipeg, Manitoba, Canada R3B 2E9

[e]Mount Holyoke College, Department of Astronomy
South Hadley, MA, USA

Published in its current form in:
Earth and Planetary Science Letters
doi: 10.1016/j.epsl.2015.02.002 (2015)

ABSTRACT

Molecular hydrogen produced through iron oxidation during formation of serpentine and magnetite can sustain terrestrial subsurface ecosystems. The Fe^{3+} in serpentine partitions into octahedral and tetrahedral sites differently as serpentinization proceeds, and tetrahedral Fe^{3+} is present toward the end of serpentinization. We map Fe oxidation states in a serpentinite to determine the degree to which serpentinization progressed and where hydrogen production has been maximized to assess habitability at an abandoned chrysotile mine in Norbestos, Quebec, in association with the Canadian Space Agency's Mars Methane Analogue Mission. We also analyzed stable isotopes of carbon and oxygen in carbonates to constrain the conditions of water-rock interaction during serpentinization. Iron oxidation and coordination was determined through field imaging of rock walls with a visible hyperspectral imager (420-720 nm), and samples collected from imaged rocks and elsewhere in the mine were imaged in the laboratory (420-1100 nm). Sample chemistry, mineralogy, and oxidation state were determined with laboratory measurements of visible through mid-infrared reflectance spectra, major element chemistry, mineralogy, and Mössbauer spectroscopy. Mapping with hyperspectral imaging of outcrops and hand samples shows that tetrahedral Fe^{3+} is common in serpentinites at this site, and results are confirmed through other measurements. Major element chemistry and mineralogy are consistent with serpentine plus minor carbonate. Carbonate samples show an exceptional range in $\delta^{13}C$ (-13.14 to +16.12‰ VPDB) and $\delta^{18}O$ (-15.48 to -3.20‰ VPDB) that vary with location in the mine. Carbonates south of a shear zone ($\delta^{13}C$ more positive) likely formed during periods of serpentinization in a carbon-limited reservoir closed to carbon addition but open to

methane escape. Carbonates in a shear zone ($\delta^{13}C$ more negative) probably formed later at low temperatures through CO_2-metasomatism or atmospheric weathering, and isotopic trends are consistent with kinetic fractionation. The extensive presence of tetrahedral Fe^{3+} in serpentine shows the system liberally produced H_2 while the isotope systematics have implications for preservation of indicators of the aqueous conditions that formed serpentinites on Mars and their habitability.

Keywords: habitability; Mars analog; serpentine; hyperspectral imaging; stable isotopes

1. INTRODUCTION

Evidence of atmospheric methane on Mars and localized, episodic release of methane detected by the Mars Science Laboratory *Curiosity* rover have generated significant interest because methane can be produced though biological processes (e.g., Formisano et al., 2004; Krasnopolsky et al., 2004; Oze and Sharma, 2005; Mumma et al., 2009; Webster et al., 2014). One plausible source of this methane could be serpentinization, where olivine and pyroxene are hydrated at elevated temperatures, producing molecular hydrogen that can be oxidized biotically or abiotically to methane (e.g., Horita and Berndt, 1999; Sleep et al., 2004; Oze and Sharma, 2005; Schulte et al., 2006). Further connecting methane and serpentinization, atmospheric methane on Mars may be spatially associated with serpentine-bearing deposits identified from orbit (Wray and Ehlmann, 2011). Serpentinization has even been proposed to explain the martian crustal dichotomy and magnetic anomalies (Quesnel et al., 2009) and loss of surface water after the Noachian period (Chassefière et al., 2013). The presence of serpentine and

carbonate on the Martian surface detected through orbital (e.g., Bandfield et al., 2003; Ehlmann et al., 2008, 2009, 2010) and surface (Boynton et al., 2009; Morris et al., 2010) investigations is important in assessing martian subsurface habitability.

Previous work has shown that H_2 produced during serpentinization can support microbial communities that use H_2 to produce CH_4 (e.g., Schulte et al., 2006; Cardace and Hoehler, 2009; McCollom and Seewald, 2013). Microbes on Earth live off H_2 and CH_4 produced via serpentinization of peridotite on the seafloor Lost City hydrothermal field (Kelley et al., 2001, 2005), and CH_4 fluxes have been detected at locations of continental serpentinization (e.g., Etiope et al., 2012; Cardace et al., 2013; Szponar et al., 2013). The gaseous and mineral products of serpentinization may have been important in the origin of life on Earth and other planets (Russell et al., 1989; Sleep et al., 2004; McCollom and Seewald, 2013; Schrenk et al., 2013 and references therein). The serpentinization reaction is exothermic and, once initiated, may heat fluids enough to allow serpentinization to continue in the absence of an external heat source (Lowell and Rona, 2002; Emmanuel and Berkowitz, 2006). The goals of this paper are to characterize conditions of water-rock interactions and formation of biologically important byproducts (e.g., H_2, CH_4) in a terrestrial serpentinizing system in order to better understand the habitability of such systems elsewhere in the solar system and the signatures of serpentinizing conditions that might be preserved in the geologic record. To do this, we use hyperspectral imaging of outcrops and samples to map Fe oxidation state and coordination environments as proxies for degrees of serpentinization and H_2 generation and isotopic analyses to understand fluid chemistries and alteration environments.

1.1 SERPENTINIZATION

H_2 production via serpentinization accompanies Fe oxidation in both magnetite and serpentine (O'Hanley and Dyar, 1993, 1998; Seyfried Jr. et al., 2007; Marcaillou et al., 2011; Neubeck et al., 2011; Andreani et al., 2013; Mayhew et al., 2013; Stander et al., 2013; Klein et al., 2014). Andreani et al. (2013) found that most Fe^{3+} was in serpentine in rocks that had been up to 75% serpentinized, after which serpentine became more Mg-rich with more Fe^{3+} in magnetite. They estimate that Fe oxidation within serpentine accounts for 80% of the total H_2 produced in 50% serpentinized rocks and 22-40% of the H_2 in 90% serpentinized rocks, with the remaining H_2 from Fe^{2+} oxidation that goes into magnetite (Andreani et al., 2013). At temperatures <150-200°C, thermodynamics does not favor magnetite formation, and Fe oxidation in serpentine may produce all of the H_2 (Andreani et al., 2013; Klein et al., 2014). During serpentinization, Fe^{3+} is produced and goes into both tetrahedral and octahedral sites in serpentine, and Fe^{3+} content increases in octahedral sites before tetrahedral sites (Marcaillou et al., 2011), as shown in Fig. 1a. Fe^{3+} in serpentine may stabilize the crystal structure, and coupled substitution of Fe^{3+} for Si^{4+} in tetrahedral sites and Fe^{3+} for Mg^{2+} in octahedral sites is one method of charge-balancing the structures (O'Hanley and Dyar, 1993; Evans et al., 2013). Fe^{3+} substitution in tetrahedral sites is favored in low Si environments such as where the protolith is ultramafic (O'Hanley and Dyar, 1993; Evans et al., 2013). Additionally, during advanced serpentinization as indicated by bulk rock water contents >10 wt %, enough Fe^{3+} can be produced that Fe^{3+}/Fe^{2+} ratios exceed 2, the ratio in magnetite, and the excess Fe^{3+} goes into serpentine (Evans et al., 2013). Throughout this Fe^{3+} production and substitution into the serpentine structure, first in octahedral and then in both octahedral and tetrahedral

sites, H_2 is produced (Marcaillou et al., 2011). Tetrahedral Fe^{3+} can be identified with visible and near infrared spectroscopy by a spin forbidden electronic transition near 450 nm as shown in Fig. 1b (e.g., Burns, 1993; Dyar, 2002; Cloutis et al., 2011b)**.** Building on these results by Marcaillou et al. (2011) and others, we argue that remote sensing can determine locations where the highest total H_2 has been produced by identifying tetrahedrally-coordinated Fe^{3+} in serpentine.

2. FIELD SITE

Field investigations were conducted at an abandoned open-pit chrysotile asbestos mine in Norbestos, Quebec, located at 45.82°N, 71.84°W in association with the 2012 deployment of the Canadian Space Agency's Mars Methane Analogue Mission (M3) (Cloutis et al., 2011c, 2013). M3 utilized a micro-rover to search for methane and explore the site geology in order to characterize the biological potential (Cloutis et al., 2013). Results of the 2011 M3 deployment at nearby Jeffrey Mine in Asbestos, Quebec, located ~10 km southwest of the Norbestos mine (Cloutis et al., 2012) include detection of methane and modeling of its source and dispersal (Olsen et al., 2012) and discrimination of peridotite and slate units using an electromagnetic induction sounder (Boivin et al., 2013).

The geologic history of the Asbestos Ophiolite Complex, in which the Jeffrey and Norbestos mines are located, has been described previously (e.g., Riordon, 1973; Laurent, 1975; Laurent and Hebert, 1979; O'Hanley, 1987, 1996; Pinet and Tremblay, 1995). The Norbestos mine is part of the Nicolet deposit described by Riordon (1973) where serpentinized Early Ordovician peridotites are in contact with Cambrian slates.

The Jeffrey Mine and Norbestos sites are in the ophiolite belt of the Quebec Appalachians obducted during the Taconian orogeny (Pinet and Tremblay, 1995; Schroetter et al., 2006). Dating of the nearby Thetford Mines ophiolite determined a 479 +3/-2 Ma crystallization age (Dunning and Pedersen, 1988), and the ophiolite was emplaced onto the continent 477±5 Ma (Whitehead et al., 1995). The ophiolite was serpentinized twice: first in an oceanic environment and then again after obduction (Laurent and Hebert, 1979), although it has been suggested that these events may not be distinct and the first may grade into the second because the ophiolite was emplaced onto the continent shortly after crystallization (O'Hanley, 1987). Laurent (1975) notes the presence of low temperature alteration near faults attributed to hydrothermal metasomatism after emplacement onto the continent. The deposit was later deformed during the Acadian orogeny (Pinet and Tremblay, 1995 and references therein). The protolith for the serpentinite studied here was harzburgite (Riordon, 1973). Most mineable chrysotile deposits formed in harzburgite, which was not fully serpentinized during the first serpentinization event, allowing chrysotile vein formation during the second period of serpentinization (Laurent and Hebert, 1979). Today, the main rock type present is serpentinite with minor carbonate.

3. METHODS

Points across all rock sample surfaces were measured with an ASD (Analytical Spectral Devices, Boulder, Colorado) FieldSpec 3 spectrometer (350-2500 nm, spectral resolution 3 nm at 700 nm and 10 nm at 1400 and 2100 nm) at Brown University using an external light source and bare fiber optic cable and were made relative to Spectralon®

(Labsphere, North Sutton, New Hampshire) and corrected for the absolute reflectance properties of Spectralon®. Measurements at these wavelengths show diagnostic absorption features due to electronic transitions and charge transfers of transition metal cations (e.g., Burns, 1993) and vibrational absorption features from OH, H_2O, and metal-OH overtones and combination tones (e.g., Clark et al., 1990; Bishop et al., 2002)

Descriptions of all samples analyzed further and analyses done on each are given in Table 1, and all data not online or in the text are available upon request. Six serpentine and carbonate samples were ground with a mortar and pestle and sieved to form <45, 45-75, 75-125, and >125 μm particle size separates. The 45-75 μm separates were measured in the Keck/NASA Reflectance Experiment Laboratory (RELAB) at Brown University on a Nicolet Nexus 870 Fourier Transform Infrared (FTIR; 800-25,000 nm) spectrometer relative to a gold standard (Pieters, 1983). Spectra at this wavelength range show fundamental vibrational absorption features and their combinations and overtones (e.g., Farmer, 1974; Strens, 1974). Wavelengths longer than 2500 nm permit identification of carbonates in mixtures with serpentine because the carbonate and serpentine absorption features do not overlap as they do at wavelengths <2500 nm (e.g., Hunt and Salisbury, 1971; Gaffey, 1987; King and Clark, 1989). These data will be available through the RELAB online database in accordance with their release procedures (http://www.planetary.brown.edu/relab/).

Bulk major element chemistry (Al, Ca, Cr, Fe, K, Mg, Mn, Na, P, Ni, Si, and Ti) was measured on five ground samples (Table 1) with three run in triplicate using Inductively Coupled Plasma – Atomic Emission Spectrometry (ICP-AES) after a flux fusion sample preparation using methods modified from Murray et al. (2000) at Brown

University's Environmental Chemistry Facility. Seven National Institute of Standards and Technology and U.S. Geological Survey standard reference materials were run (MAG-1, BIR-1, BCR-2, BHVO-2, NIST2711, NIST1646a, and SGR-1). Blanks were run after every 6 samples. For the flux fusion preparation, 40 mg of each sample were mixed with 160 mg lithium metaborate flux and fused at 1050°C for 10 minutes. The molten flux and samples were then poured into 10% HNO_3, agitated for at least 30 minutes, filtered through 0.45 µm filters, and diluted to achieve ~4000x dilutions. Major element concentrations were then measured on a JY2000 Ultrace ICP-AES using peak wavelengths given in Murray et al. (2000), and actual concentrations were calculated through linear regressions of standards with known concentrations to account for losses during the flux fusion process after correcting for ICP-AES drift and subtracting blanks. Carbon content was determined on the same five samples with three in triplicate using a CE Instruments Model NC2100 Elemental Analyzer. Samples were dried overnight at 60°C, and 8-10 mg of each were weighed into tin capsules. Concentrations were determined from regressions using acetanilide, cyclohexane, pine (SRM 1575), and Montana soil (SRM 2711) standards.

Mineralogies of Nor3-1 (coating), Nor3-6, Nor4-9, Nor4-12 (green), Nor4-12 (red), and Nor4-13 (<125 µm particle size separates) were determined with an inXitu Terra (#213) X-ray diffractometer (XRD) with a Co source at the University of Rhode Island, summing 250 exposures over 2500 seconds after drying samples at 50°C for 7 hours. Two-dimensional images were converted to conventional one-dimensional XRD patterns, with a 2θ range of 5.0 to 54.9°. Peak positions of XRD patterns were compared with known library minerals using the database within XPowder. Mineralogies of

carbonate samples Nor3-7, Nor3-8 (thinner), Nor4-2 (bottom), Nor4-7_1, and Nor5-1_2 (outside) were determined through powder XRD at Indiana University (Bloomington, Indiana) using a Bruker D8 Advance instrument with Cu radiation and a SolX point detector. Data were measured from 2 to 70° 2θ overnight (count times per 0.02° step of 8 to 15 seconds), using samples mounted as slurries on "zero-background" quartz plates. Data analysis used Bruker AXS EVA and Topas software.

Mössbauer spectra were acquired for <125 μm separates of three samples (Nor4-9, Nor4-12_green, Nor4-13) to determine the fraction of Fe in different oxidation states and coordination environments using a source of ~40 mCi ^{57}Co in Rh on a SEE Co. model WT302 spectrometer (Mount Holyoke College). Data were collected at 295K over a ±4 mm/s velocity range and at 4K over a ±10 mm/s velocity range in 2048 channels. Spectra were corrected for nonlinearity via interpolation to a linear velocity scale, which is defined by the spectrum of the 25 μm Fe foil used for calibration. All data were corrected to remove the fraction of the baseline due to Compton scattering of 122 keV gamma rays by electrons inside the detector. Mössbauer data were posted at www.mtholyoke.edu/courses/mdyar/database/. Spectra were fit using the Mexdisd program, which uses a line-shape-independent model for fitting spectra and solves the full hyperfine-interaction Hamiltonian, producing a distribution of values for the hyperfine field and using quadrupole shift, center shift, and line width as adjustable parameters. It does not presume any particular distribution shape. The area of the peaks that make up each doublet or sextet is proportional to the percentage of Fe in that site. If known, correction for the mineral-specific recoil-free fraction can be applied for optimum accuracy, but *f* has not yet been determined for serpentine minerals. Errors (accuracy) of

peak areas are roughly ±3% absolute, on Mössbauer parameters are ±0.03 mm/s, and on Bhf ~±0.2 Tesla for individual sextets or doublets.

Samples of carbonates precipitated on serpentinite (Table 1) were identified by reaction with dilute HCl, scraped off with a metal spatula, and ground for isotope analyses. Carbon and oxygen stable isotopes were analyzed by a Gas Bench II coupled with Delta Plus XP IRMS at the Stable Isotope Research Facility at Indiana University with 16 samples run in triplicate and one in duplicate. Standardization to the VPDB international scale was performed using NBS-19 and two internal carbonate reference materials, LC-1 and CM-A. Carbonate contents (as calcite) for each sample were calculated using the CO_2 yields assuming all carbonate present is calcite.

Rock samples were imaged at the University of Winnipeg with two Channel Systems hyperspectral imagers: a visible imager (1.3 megapixel sensor, 420-720 nm, 10 nm spectral resolution, 5 nm sampling interval) and a near-infrared (NIR) imager (1.3 megapixel sensor, 650-1100 nm, 10 nm spectral resolution; two images interleaved to achieve 5 nm sampling). Spatial resolutions depend on distances from imager to sample, but typical resolutions at the observing distances were sub-mm. Exposure times varied with wavelength and were adjusted to maximize signal to noise through the imagers' autoexpose feature. Images were calibrated to reflectance (R) using the following equation:

$$R = \frac{\frac{(S_t - S_d)}{t_t}}{\frac{S_s - S_d}{t_s}} * R_S \,, \qquad (1)$$

where S_t is the target sample image, S_d is the dark image, S_s is the Spectralon® image, t_t are the target sample image exposure times, t_s are the Spectralon® image exposure times, and R_s is the reflectance spectrum of Spectralon®. Dark values were independent of

exposure times, while tests of the imagers showed that signals where the sensor received light scaled linearly with exposure time. Since Spectralon® is not a perfect reflector (e.g., 100% reflectance), images were corrected for the absolute spectrum of Spectralon® using RELAB spectrum HL-JFM-012 of SRT-99-050 resampled to the wavelengths sampled by the imagers.

Hyperspectral images were collected in the field of rock outcrops on mine walls and samples collected around the mine with the same visible imager used in the laboratory. Images were calibrated through a dark object subtraction (Chavez Jr, 1996 and references therein) and ratio to in-scene calibration target (white poster board) with the following equation:

$$R = \frac{S_t - D}{C - D} * R_p \,, \tag{2}$$

where D is the average dark spectrum, C is the average calibration target spectrum, and R_p is the reflectance spectrum of the calibration target. All values except R_p are in digital number. These methods are similar to those of Clark et al. (2002) for AVIRIS data calibration. There is good agreement between field and laboratory imaging (Fig. S1).

Images were analyzed with parameters to map various spectral features (e.g., Clark and Roush, 1984; Pelkey et al., 2007) with formulas and interpretations in Table 2. Images were resampled to Pancam and Mastcam bandpasses using transmission profiles given by Bell et al. (2003, 2012) to compare these hyperspectral measurements with multispectral systems on the *Opportunity* and *Curiosity* rovers currently operating on the surface of Mars. This was done by assuming that the bandpass shape for these hyperspectral imagers is a $\mathrm{sinc}^2(x)$ function as has been reported for acousto-optic tunable filter systems (Georgiev et al., 2002) with full width at half maximum equal to the 10 nm

spectral resolution.

4. RESULTS

Laboratory measurements (spectroscopy, chemistry, and mineralogy) show samples dominated by serpentine with minor carbonate and magnetite that differ in the iron oxidation states and coordination environments within serpentine. These results scale to the outcrop. The samples also differ with location within the mine in the stable isotopic signatures of thin carbonate precipitates.

ASD spectra of samples are generally consistent with serpentine with some variations (Fig. 1b). FTIR spectra of select samples further resolve absorption features near 1390 and between 2000 and 2600 nm into several sharp bands (Fig. 2). In one piece of sample Nor4-9, which is serpentinite with no discernible carbonate, narrow absorption features at 1382, 1388, 1390, and 1392 nm are due to the first Mg_3-OH stretching overtone, consistent with published serpentine spectra (e.g., King and Clark, 1989; Clark et al., 1990; Bishop et al., 2008). The presence of multiple absorption features may result from OH coordinated by multiple cations (Mustard, 1992) or differences in vibrational frequencies of inner and outer OH groups (e.g., King and Clark, 1989). An asymmetric Mg_3-OH combination tone near 2320-2330 nm is seen in most ASD spectra (e.g., Clark et al., 1990; Post and Borer, 2000; Bishop et al., 2008) and is further resolved into distinct features at 2326 and 2337 nm in FTIR data. Most spectra also have vibrational absorption features at 2100 and 2130 nm typical of serpentine (e.g., Hunt and Evarts, 1981; King and Clark, 1989; Ehlmann et al., 2009) but not formally assigned to specific molecular vibrations. While H_2O is not present in ideal serpentine mineral structures,

spectra of all serpentine samples measured here have broad OH stretch and H-O-H bend combination bands near 1900 nm (e.g., Clark et al., 1990). This absorption feature commonly seen in serpentine (e.g., Hunt and Evarts, 1981) may be due to adsorbed water, a H_2O-bearing phase such as another phyllosilicate mixed with serpentine, or trace water incorporated into the serpentine structure. In FTIR data (Fig. 2), an absorption feature near 2500 nm in a few spectra is due to a C-O combination often used to distinguish carbonates (Hunt and Salisbury, 1971). Additional features at 3350-3500 and 3800-4000 nm are diagnostic of carbonates (e.g., Schroeder et al., 1962).

The visible and near infrared wavelengths of ASD spectra (Fig. 1b) provide insight into Fe oxidation states within serpentine or other Fe-bearing minerals. In some spectra, a spin-forbidden electronic transition of tetrahedrally-coordinated Fe^{3+} in serpentine is seen near 450 nm (e.g., Burns, 1993; Dyar, 2002; Cloutis et al., 2011b). A Fe^{2+}/Fe^{3+} intervalence charge transfer at 700-750 nm and octahedral Fe^{2+} electronic transitions within serpentine at 900-940 and 1100-1200 nm also are seen (e.g., Clark et al., 1990; Cloutis et al., 2011a, 2011b). The charge transfer and Fe^{2+} electronic transitions are present in most spectra but vary in strength and spectral contrast, and overall slopes of spectra differ. These variations may be due to textures, coatings, the presence of magnetite, or oxidation state or coordination (Singer and Roush, 1983; Fischer and Pieters, 1993; Cloutis et al., 2011a). Minor magnetite in rocks disproportionately reduces reflectance and lowers spectral contrast (Hunt and Evarts, 1981). Red slopes are likely due to Fe^{3+} in phases other than serpentine and formation of ferric oxides such as hematite, goethite, and ferrihydrite (e.g., Hunt and Ashley, 1979; Cloutis et al., 2011a).

Other sample analyses are consistent with mineralogies dominated by serpentine.

Major element chemistries of samples without significant carbonate fractions are mostly Fe, Mg, and Si, consistent with the ultramafic protolith (Table 3). The chemistry of sample Nor4-9, which is typical of serpentinites at this site, is similar in composition to other reported serpentinites in Canada (e.g., Wares and Martin, 1980; O'Hanley and Wicks, 1995), and mineralogy (Table 3) determined by XRD shows antigorite, lizardite, and magnetite, consistent with other analyses. Other samples also contain calcite (Nor 4-12_red, Nor4-12_green, Nor4-13), hydromagnesite and magnesite (Nor3-1, Nor3-6), brucite (Nor3-6), and ferric oxides (Nor4-12_red). Note that XRD did not identify chrysotile in these samples because chrysotile veins were intentionally avoided when grinding the rocks. Carbonate samples that were analyzed contain calcite (Nor4-2, Nor5-1_2 outside), hydromagnesite and dolomite/ankerite (Nor3-7, Nor3-8 thinner), and pyroaurite (Nor3-7, Nor3-8 thinner, Nor4-7_1, Nor5-1_2 outside) as well as serpentine and, for some, talc or smectite.

Mössbauer spectra provide insights into the iron oxidation state and coordination, and fits are given in Table S1. These spectra can have multiple interpretations because tetrahedral and octahedral Fe^{3+} peaks are close together, but despite these limitations are consistent with interpretations from visible-NIR spectroscopy of tetrahedral and octahedral Fe^{3+} in Nor4-9 and Nor4-12_green and only octahedral Fe^{3+} in Nor4-13. In the parameters for fits of Mössbauer spectra, tetrahedral Fe^{3+} has an isomer shift <0.25, and octahedral Fe^{3+} has an isomer shift of 0.25-0.50 (Dyar et al., 2006).

Carbon stable isotope measurements show a range of nearly 30‰ ($\delta^{13}C$), extending from -13.14 to +16.12‰ VPDB (Fig. 3; Table S2). Standard deviations where enough material was present to run replicates are <0.62‰, with most <0.3‰. While

carbonate morphologies show no discernible correlation with isotope values, spatial distributions within the mine suggest that carbonates formed under different conditions and from different carbon reservoirs. With one exception, samples with $\delta^{13}C$ values lower than +2‰ were collected within a shear zone that ran through the mine. Samples with $\delta^{13}C$ values higher than 0‰ are from massive serpentinites located ~100-200 m south of the shear zone. Oxygen isotopic values ($\delta^{18}O$) are -15.48 to -3.20‰ VPDB with a reproducibility of 0.24‰ based on the standards, while larger standard deviations in some samples result from sample heterogeneity. Generally, samples with the most negative and most positive $\delta^{13}C$ values have the most negative $\delta^{18}O$ values (Fig. 3). Carbonate contents were calculated with an error of ±10%, range from 9.6% to pure carbonate, and do not correlate with $\delta^{13}C$ or $\delta^{18}O$.

Hyperspectral imaging maps different oxidation states within samples at high spatial resolutions. In the laboratory image of sample Nor4-9 (Fig. 4), a spatial resolution <100 μm/pixel was achieved. Laboratory measurements were done under controlled lighting conditions with little to no contribution from atmospheric scattering. Absorption features due to tetrahedral Fe^{3+}, Fe^{2+}/Fe^{3+} charge transfers, octahedral Fe^{2+}, H_2O/OH, and slopes from Fe^{3+} were all mapped (Fig. 4, S4c), and the sample surface shows high variability despite the entire sample being serpentinite. Locations highlighted by the BD450 parameter generally also have high green peak parameter values and appear white or magenta in Fig. 4c (scatterplot in Fig. 4d). This correlation is expected because the peak at green wavelengths occurs due to absorptions from tetrahedral Fe^{3+} at shorter wavelengths and an Fe^{2+}/Fe^{3+} charge transfer at longer wavelengths (e.g., Burns, 1993; Dyar, 2002; Cloutis et al., 2011a, 2011b). Tetrahedral Fe^{3+} has also been shown to

correlate with octahedral Fe^{3+} in lizardite (O'Hanley and Dyar, 1993). Spectra with the highest values for the green peak parameter have the deepest absorptions on either side of the peak, both of which require Fe^{3+}. Spectra with blue slopes differ texturally from other parts of the sample, there may be thin coatings transparent at longer wavelengths that contribute to the spectrum at shorter wavelengths, or the texture at the surface may be smooth, resulting in the surface scattering light differently at different wavelengths (Singer and Roush, 1983; Fischer and Pieters, 1993). Magnetite can also cause the spectrum to have a blue slope (Fischer and Pieters, 1993; Cloutis et al., 2011a). Redder parts of samples highlighted by the red slope parameter likely have Fe^{3+}-oxides present and have undergone oxidation unrelated to serpentinization (e.g., Hunt and Ashley, 1979; Cloutis et al., 2011a).

Other samples show similar results to Nor4-9, with red slope, green peak, and blue slope spectral parameters mapping discrete areas and correlations between the green peak and BD450 parameters. Samples Nor4-13 (Fig. S2) and Nor4-14 (Fig. S3) were collected from an imaged rock wall of the mine (Fig. 5) and show similar trends in laboratory imaging, although the 450 nm band depth is generally weaker or absent in Nor4-13 spectra. Nor4-13 is mostly serpentine with some calcite, and the green peak spectral parameter dominates most of the sample's surface in laboratory and field images (Figs. 5, S2). ASD spectra of the ground portion of Nor4-13 and Mössbauer spectra indicate no tetrahedral Fe^{3+} present, although laboratory imaging shows that small areas of the sample contain tetrahedral Fe^{3+} in serpentine. At the outcrop-scale (Fig. 5), imaging highlights spectra of the sample's surface overall as being dominated by the green peak, as in laboratory data. Sample Nor4-14 (Fig. S3) from elsewhere within the

same outcrop image has red coatings on half its surface and green serpentine on the other half. Both the laboratory (Fig. S3) and field imaging data (Fig. 5) show these trends, and laboratory data show a correlation between the 450 nm band depth and the green peak parameter.

NIR images show spatial correlations between Fe^{3+} and the degree of hydration (Fig. S4). While work by O'Hanley and Dyar (1998) shows that octahedral Fe^{3+} substitutions can be charge-balanced by H^+ vacancies, predicting a negative correlation between these spectral features, the substitutions in samples analyzed here of Fe^{3+} for Si^{4+} in tetrahedral sites require a different process to charge balance the structure. Two possibilities are coupled substitutions of Fe^{3+} into the tetrahedral and octahedral sheets with no change in H^+ content (Evans et al., 2013; O'Hanley and Dyar, 1993) or additions of H^+ into the structure, either of which could explain the spectral observations here. These results are consistent with other work showing that advanced serpentinization produces serpentines with both high H_2O and high Fe^{3+} contents (Evans et al., 2013).

In field imaging data (Fig. 5), tetrahedral Fe^{3+} is better inferred using the green peak parameter and visually inspecting spectra rather than mapping directly via the BD450 parameter. The imager's spectral performance degrades at the long and short wavelength ends of the detector, particularly at the shortest wavelengths. This effect is present in both laboratory and field data, but the shortest wavelengths are further complicated by downwelling atmospheric scattering in the field, which adds to the spectra and contributes most in blue wavelengths where the 450 nm feature occurs, lowering the imaging system's signal-to-noise. For these reasons, it is difficult to use the BD450 parameter in field data. However, as already shown, laboratory data of samples

including some from within field images show good correlations between BD450 and the green peak (Figs. 4, S2-3), and the green peak can therefore be used as an indirect indicator of oxidation state and possible tetrahedral Fe^{3+}. Inspecting averages as small as 5-10 pixels (~11-24 cm in Fig. 5) confirms the presence of the 450 nm feature above the level of noise.

Using laboratory data as confirmation, spectral units are mapped across the outcrop wall (Fig. 5). Variability is seen at this scale, with discrete redder, greener, and bluer units that represent formation of Fe^{3+}-oxides, Fe^{3+} oxidation within serpentine, and the presence of magnetite or a textural property of the serpentine, respectively. Limited yellow or cyan areas may be due to sub-pixel mixing where multiple materials are present within a single pixel or spectra of one material exhibiting properties mapped by multiple spectral parameters. Overall, the wall is dominated by the green peak, and the results and interpretations are consistent with the known serpentine lithology.

5. DISCUSSION

The results of hyperspectral imaging and stable isotope analyses characterize conditions of water-rock interactions and habitability during serpentinization. We infer extents of serpentinization and relative amounts of biologically-important H_2 produced with spectroscopy from Fe oxidation states and coordination environments in serpentine (e.g., Marcaillou et al., 2011; Evans et al., 2013). At this site, much of the protolith has been extensively serpentinized at elevated temperatures, with high H_2 production based on the presence of tetrahedral Fe^{3+}. The nature of the system (e.g., open/closed, fluid chemistry and source, timing) is further illuminated from stable isotope analyses of

carbonates, and signatures from the production and removal of CH_4 formed as a byproduct of serpentinization are present. These complementary analyses present a fuller picture of the ancient serpentinization events and suggest the presence of a habitable subsurface environment.

Field and laboratory hyperspectral imaging shows differences in Fe oxidation state and coordination environments within this serpentinite deposit. These results are consistent with laboratory measurements of individual samples by O'Hanley and Dyar (1993, 1998) finding different Fe oxidation states and coordination among samples from the same localities. The identification of tetrahedrally-coordinated Fe^{3+} directly through a 450 nm spin-forbidden electronic transition and indirectly through a peak near 580 nm related to both octahedral and tetrahedral Fe^{3+} that generally correlates with the 450 nm absorption feature indicates that the sample or outcrop has undergone advanced serpentinization where there has been the highest cumulative H_2 production. In a planetary mission searching for habitable environments, biomarkers, and evidence of past life in a serpentine terrain, areas with tetrahedral Fe^{3+} are important candidates for additional in situ analyses because the H_2 produced could have been an energy source for microbes (e.g., Schulte et al., 2006). Calculating total volumes of H_2 produced requires quantification of Fe^{3+} content and is beyond the scope of this work but has been done for other serpentinites by Stander et al. (2013). While primary olivine and pyroxene were not found in these samples, previous work has shown that visible-NIR spectroscopy can be used to distinguish lower degrees of serpentinization in samples with low magnetite contents (Hunt and Evarts, 1981). It is unclear whether CO_2-metasomatism or atmospheric weathering could change the Fe oxidation state within serpentine. We feel

that these processes are unlikely to introduce new tetrahedral Fe^{3+} since Fe^{2+} within serpentine should only be in octahedral sites, but a complete discussion of this question is beyond the scope of this work. We do note that low temperature weathering of serpentinite can generate H_2 and CH_4 (Okland et al., 2012).

Our data resampled to the bandpasses of multispectral imaging systems such as Pancam and Mastcam on current Mars rovers (Bell et al., 2003, 2006, 2012) show variability within images (Fig. 6), but precise mineralogical or oxidative differences causing spectral variability cannot be determined. Fig. 6 shows that neither multispectral system is capable of identifying tetrahedrally-coordinated Fe^{3+} because neither samples short enough wavelengths nor has sufficient bands between ~400 and 480 nm. Hyperspectral systems that sample such short wavelengths not only show the presence of a feature at 450 nm but also have sufficient bands covering the feature to provide confidence that the feature exists above the level of noise. Chemcam on *Curiosity* should be able to identify this feature in passive reflectance mode, if it is present (Johnson et al., 2014). Also notable in the resampled multispectral data is that band centers and shapes for the same spectrum sampled with different bandpasses appear differently depending on the wavelengths of the multispectral bands. The loss of critical information in multispectral systems was also seen by Cousins et al. (2010, 2012), who tried to design a multispectral imaging system that could identify the diversity of minerals potentially present on Mars. Swayze et al. (2003) noted that minerals with distinct absorption features can appear the same if the sampling interval of a spectrometer is too broad. Expanding the wavelength range of this hyperspectral system into the infrared would allow for more sophisticated analyses of astrobiological potential, could distinguish

serpentine from other green-colored minerals, show where other interesting minerals may be present, and allow for remote identification of the mineral assemblages.

Stable isotope measurements further illuminate the serpentinization conditions beyond what is possible with spectroscopy alone. These measurements show a wide range of carbon and oxygen isotope ratios within carbonate coatings on serpentinites collected around the mine and show two distinct trends in isotopic compositions reflecting different alteration scenarios within and outside the shear zone (Fig. 3). Carbonate samples from the wall imaged ~100-200 m south of the shear zone (Fig. 5) likely precipitated during serpentinization in a relatively closed system with a deep groundwater source similar to that described by Neal and Stanger (1985) and Mervine et al. (2014) to explain observations of the Semail ophiolite in Oman. This model is supported in our investigations by high $\delta^{13}C$ values likely resulting from reaction of H_2 from serpentinization with CO_2 to produce CH_4 enriched in ^{12}C (Ohmoto, 1972), leaving the remaining carbon reservoir enriched in ^{13}C if the system was closed to carbon addition but open to CH_4 escape. In this scenario, the carbonates formed when the fluids became saturated in Ca^{2+} removed from the ophiolite and the pH rose during serpentinization (Neal and Stanger, 1985). While the ophiolite likely had low overall Ca content, harzburgites in nearby Thetford Mines, Quebec, contain up to 6% clinopyroxene, and orthopyroxenes there have up to 1.8 wt % CaO (Pagé et al., 2008). The presence of Ca from primary mineralogies released by weathering combined with the absence of Ca in typical serpentinization products (i.e., serpentine, magnetite, brucite) could have allowed Ca^{2+} to build up in the fluids until the system saturated and calcite precipitated (Neal and Stanger, 1985). The carbonates with the highest ^{13}C proportion probably

formed last from the most evolved fluids under the most water-limited conditions as volume expansion during serpentinization reduced fluid flow (O'Hanley, 1992 and references therein). The carbonate mineralogies determined with XRD from this portion of the mine are dominated by calcite with less magnesite and/or pyroaurite. This scenario for evolving conditions during serpentinization is shown conceptually in Fig. 7. We note that these data cannot distinguish carbonate formed during serpentinization in oceanic versus continental environments because environmental conditions leading to these high $\delta^{13}C$ values required little or no input from the ocean or atmosphere above. Even in oceanic environments with significant calcite precipitation near the seafloor, less calcite is seen at depth (Schwarzenbach et al., 2013).

The isotopic trend for shear zone samples matches the overall trends and ranges in isotopic compositions previously reported for carbonates in ophiolites in Oman and elsewhere attributed to kinetic fractionation (e.g., Clark et al., 1992; Kelemen et al., 2011; Mervine et al., 2014). Radiocarbon dates of carbonate veins in Oman reported by Kelemen et al. (2011) and Mervine et al. (2014) range from 4 to 36 ka, showing that carbonates there formed recently, and stable isotope analyses of monomineralic carbonate samples show that carbonates formed at temperatures <60°C and are not associated with the serpentinization (Mervine et al., 2014). Similarly, carbonates in the shear zone in Norbestos likely formed after serpentinization ended, overprinting most isotopic signatures of the original serpentinizing fluids, although one sample has high ^{13}C and may be related to these primary serpentinizing fluids. Carbonate mineralogies of analyzed shear zone samples are hydromagnesite and pyroaurite with dolomite/ankerite and/or magnesite. Magnesite often forms in serpentinites through CO_2-metasomatism (Klein and

Garrido, 2011; Klein and McCollom, 2013), and hydromagnesite can be a product of atmospheric weathering (e.g., Power et al., 2009). These mineralogies support our interpretation that these carbonates formed through later processes after serpentinization ceased. Carbonate in one shear zone sample with the most negative $\delta^{13}C$ measured, Nor4-2 (bottom), is calcite, suggesting that there is not a perfect correlation between mineralogy and stable isotopes.

Although no biological isotopic fractionations have been found in these data, isotopic signatures of samples from the imaged wall south of the shear zone suggest that some carbonates present formed during serpentinization events in close association with methane production. The methane could have formed biotically or abiotically through CO_2 reduction by H_2 (e.g., Horita and Berndt, 1999; Oze and Sharma, 2005; Schulte et al., 2006), which, along with the CH_4, is important in microbial metabolisms (e.g., Schulte et al., 2006; Cardace and Hoehler, 2009; McCollom and Seewald, 2013). Signatures of carbonates formed through CH_4 oxidation by microbes were not found, but those signatures were also absent in nearby ophicalcites in Quebec with deposits thought to be fossilized microbial communities that are the same age as the Norbestos serpentinites (Lavoie and Chi, 2010). In fact, the samples here have a broader $\delta^{13}C$ range than the samples analyzed at that site by Lavoie and Chi (2010). Thus, in the ancient serpentinite deposit in Norbestos there is still an isotopic signature of the original serpentinization event and the gases produced as a byproduct that potentially could have sustained life (Fig. 7). On Mars, where there has been limited recent aqueous activity (e.g., Bibring et al., 2006), these signatures are more likely to have been preserved if they were once present. Parnell et al. (2010) analyzed methane preserved in ancient terrestrial

serpentinites and suggest that the carbon and hydrogen isotopes in the methane, as well as sulfur isotopes in sulfides within serpentinites, may contain microbial signatures (Parnell et al., 2010). Therefore, serpentinites can preserve isotopic signatures of ancient habitable environments in which microbial communities were supported by gases formed during serpentinization, and hyperspectral imaging can determine the most habitable locations within the serpentinite and guide further sampling.

6. CONCLUSION

In serpentinite terrains, Fe oxidation within serpentine, in addition to magnetite production, produces H_2 that microbes can use as an energy source, and tetrahedrally-coordinated Fe^{3+} in serpentine is produced at the end stages of serpentinization (Marcaillou et al., 2011). Therefore, identification of tetrahedral Fe^{3+} in serpentine through diagnostic absorptions at visible wavelengths indicates maximum H_2 production during serpentinization and the highest astrobiological potential. In the Norbestos serpentinite studied here, tetrahedral Fe^{3+} is common, suggesting high H_2 production during serpentinization. Analyses of carbon and oxygen stable isotopes in carbonates precipitated on serpentine show that some carbonates likely formed during the original serpentinization events when H_2 and CH_4 were produced and illuminate aqueous conditions of alteration at elevated temperatures and low water/rock ratios in a carbon-limited system. The retention of signatures of serpentinization and methane production is promising for the detection of ancient biosignatures in similar environments on Mars, if they were ever present.

ACKNOWLEDGMENTS

We would like to thank the Canadian Space Agency's Mars Methane Analogue Mission for field and logistical support. We also thank Dawn Cardace, Dan Carnevale, Taki Hiroi, Dave Murray, and Joe Orchardo for assistance with measurements and Tim Goudge and Kevin Cannon for comments on a draft of this manuscript. We thank Jim Bell and Melissa Rice for providing the Pancam and Mastcam transmission profiles and Dawn Cardace for helpful discussions. Finally, we want to thank Frieder Klein and an anonymous reviewer for their helpful comments that improved this manuscript and Christophe Sotin for editorial handling. This work was supported by NASA and the Mars Data Analysis Program grant NNX13AK72G. E.A.C. thanks the Canada Foundation for Innovation, Manitoba Research Innovations Fund, Canadian Space Agency, NSERC, and University of Winnipeg for supporting the establishment and operation of the Planetary Spectrophotometer Facility at the University of Winnipeg. The funding sources had no involvement in this study.

AUTHOR CONTRIBUTIONS

RNG, JFM, EAC, and LMP designed the research; RNG, PM, KT, PES, MDD, and DLB did the measurements; RNG, JFM, EAC, LMP, and PES analyzed the data; RNG, JFM, and MDD wrote the paper; all authors provided comments on the paper and approved the final version.

REFERENCES

Andreani, M., Muñoz, M., Marcaillou, C., Delacour, A., 2013. μXANES study of iron

redox state in serpentine during oceanic serpentinization. Lithos 178, 70–83. doi:10.1016/j.lithos.2013.04.008

Bandfield, J.L., Glotch, T.D., Christensen, P.R., 2003. Spectroscopic Identification of Carbonate Minerals in the Martian Dust. Science 301, 1084–1087. doi:10.1126/science.1088054

Bell, J.F., Joseph, J., Sohl-Dickstein, J.N., Arneson, H.M., Johnson, M.J., Lemmon, M.T., Savransky, D., 2006. In-flight calibration and performance of the Mars Exploration Rover Panoramic Camera (Pancam) instruments. J. Geophys. Res. 111, E02S03. doi:10.1029/2005JE002444

Bell, J.F., Malin, M.C., Caplinger, M.A., Ravine, M.A., Godber, A.S., Jungers, M.C., Rice, M.S., Anderson, R.B., 2012. Mastcam Multispectral Imaging on the Mars Science Laboratory Rover: Wavelength Coverage and Imaging Strategies at the Gale Crater Field Site, in: Lunar and Planetary Institute Science Conference Abstracts. Presented at the Lunar and Planetary Institute Science Conference Abstracts, p. 2541.

Bell, J.F., Squyres, S.W., Herkenhoff, K.E., Maki, J.N., Arneson, H.M., Brown, D., Collins, S.A., Dingizian, A., Elliot, S.T., Hagerott, E.C., Hayes, A.G., Johnson, M.J., Johnson, J.R., Joseph, J., Kinch, K., Lemmon, M.T., Morris, R.V., Scherr, L., Schwochert, M., Shepard, M.K., Smith, G.H., Sohl-Dickstein, J.N., Sullivan, R.J., Sullivan, W.T., Wadsworth, M., 2003. Mars Exploration Rover Athena Panoramic Camera (Pancam) investigation. J. Geophys. Res. 108, 8063. doi:10.1029/2003JE002070

Bibring, J.-P., Langevin, Y., Mustard, J.F., Poulet, F., Arvidson, R., Gendrin, A., Gondet,

B., Mangold, N., Pinet, P., Forget, F., the OMEGA team, 2006. Global Mineralogical and Aqueous Mars History Derived from OMEGA/Mars Express Data. Science 312, 400 –404. doi:10.1126/science.1122659

Bishop, J.L., Lane, M.D., Dyar, M.D., Brown, A.J., 2008. Reflectance and emission spectroscopy study of four groups of phyllosilicates: smectites, kaolinite-serpentines, chlorites and micas. Clay Miner. 43, 35 –54. doi:10.1180/claymin.2008.043.1.03

Bishop, J., Murad, E., Dyar, M.D., 2002. The influence of octahedral and tetrahedral cation substitution on the structure of smectites and serpentines as observed through infrared spectroscopy. Clay Miner. 37, 617 –628. doi:10.1180/0009855023740064

Boivin, A., Lai, P., Samson, C., Cloutis, E., Holladay, S., Monteiro Santos, F.A., 2013. Electromagnetic induction sounding and 3D laser imaging in support of a Mars methane analogue mission. Planet. Space Sci. 82-83, 27–33. doi:10.1016/j.pss.2013.03.005

Boynton, W.V., Ming, D.W., Kounaves, S.P., Young, S.M.M., Arvidson, R.E., Hecht, M.H., Hoffman, J., Niles, P.B., Hamara, D.K., Quinn, R.C., Smith, P.H., Sutter, B., Catling, D.C., Morris, R.V., 2009. Evidence for Calcium Carbonate at the Mars Phoenix Landing Site. Science 325, 61–64. doi:10.1126/science.1172768

Burns, R.G., 1993. Mineralogical applications of crystal field theory. Cambridge University Press.

Cardace, D., Hoehler, T.M., 2009. Serpentinizing Fluids Craft Microbial Habitat. Northeast. Nat. 16, 272–284. doi:10.1656/045.016.0520

Cardace, D., Hoehler, T., McCollom, T., Schrenk, M., Carnevale, D., Kubo, M., Twing, K., 2013. Establishment of the Coast Range ophiolite microbial observatory (CROMO): drilling objectives and preliminary outcomes. Sci. Drill. 16, 45–55. doi:10.5194/sd-16-45-2013

Chassefière, E., Langlais, B., Quesnel, Y., Leblanc, F., 2013. The fate of early Mars' lost water: The role of serpentinization. J. Geophys. Res. Planets 118, 1123–1134. doi:10.1002/jgre.20089

Chavez Jr, P.S., 1996. Image-Based Atmospheric Corrections-Revisited and Improved. Photogramm. Eng. Remote Sens. 62, 1025–1036.

Clark, I.D., Fontes, J.-C., Fritz, P., 1992. Stable isotope disequilibria in travertine from high pH waters: Laboratory investigations and field observations from Oman. Geochim. Cosmochim. Acta 56, 2041–2050. doi:10.1016/0016-7037(92)90328-G

Clark, R.N., King, T.V.V., Klejwa, M., Swayze, G.A., Vergo, N., 1990. High Spectral Resolution Reflectance Spectroscopy of Minerals. J. Geophys. Res. 95, 12653–12680. doi:10.1029/JB095iB08p12653

Clark, R.N., Roush, T.L., 1984. Reflectance Spectroscopy: Quantitative Analysis Techniques for Remote Sensing Applications. J. Geophys. Res. 89, PP. 6329–6340. doi:198410.1029/JB089iB07p06329

Clark, R.N., Swayze, G.A., Livo, K.E., Kokaly, R.F., King, T.V., Dalton, J.B., Vance, J.S., Rockwell, B.W., Hoefen, T., McDougal, R.R., 2002. Surface reflectance calibration of terrestrial imaging spectroscopy data: a tutorial using AVIRIS, in: Proceedings of the 10th Airborne Earth Science Workshop. pp. 02–1.

Cloutis, E.A., Hiroi, T., Gaffey, M.J., Alexander, C.M.O., Mann, P., 2011a. Spectral

reflectance properties of carbonaceous chondrites: 1. CI chondrites. Icarus 212, 180–209. doi:10.1016/j.icarus.2010.12.009

Cloutis, E.A., Hudon, P., Hiroi, T., Gaffey, M.J., Mann, P., 2011b. Spectral reflectance properties of carbonaceous chondrites: 2. CM chondrites. Icarus 216, 309–346. doi:10.1016/j.icarus.2011.09.009

Cloutis, E., Vrionis, H., Qadi, A., Bell, J.F., Berard, G., Boivin, A., Ellery, A., Jamroz, W., Kruzelecky, R., Mann, P., Samson, C., Stromberg, J., Strong, K., Tremblay, A., Whyte, L., Wing, B., 2011c. Mars Methane Analogue Mission (M3): Analytical Techniques and Operations, in: Lunar and Planetary Institute Science Conference Abstracts. Presented at the Lunar and Planetary Institute Science Conference Abstracts, p. 1174.

Cloutis, E., Whyte, L., Qadi, A., Anderson-Trocme, L., Bell, J.F., Berard, G., Boivin, A., Ellery, A., Greenberger, R., Haddad, E., Jamroz, W., Kruzelecky, R., Mann, P., Mustard, J., Olsen, K., Perrot, M., Popa, D., Ralchenko, M., Rhind, T., Samson, C., Sharma, R., Stromberg, J., Strong, K., Tremblay, A., Wing, B., 2013. The Mars Methane Analogue Mission (M3): Results of the 2012 Field Deployment, in: Lunar and Planetary Institute Science Conference Abstracts. Presented at the Lunar and Planetary Institute Science Conference Abstracts, p. 1579.

Cloutis, E.A., Whyte, L., Qadi, A., Bell, J.F., Berard, G., Boivin, A., Ellery, A., Haddad, E., Jamroz, W., Kruzelecky, R., Mann, P., Olsen, K., Perrot, M., Popa, D., Rhind, T., Samson, C., Sharma, R., Stromberg, J., Strong, K., Tremblay, A., Wilhelm, R., Wing, B., Wong, B., 2012. The Mars Methane Analogue Mission (M3): Results of the 2011 Field Deployment, in: Lunar and Planetary Institute Science

Conference Abstracts. Presented at the Lunar and Planetary Institute Science Conference Abstracts, p. 1569.

Cousins, C.R., Griffiths, A.D., Crawford, I.A., Prosser, B.J., Storrie-Lombardi, M.C., Davis, L.E., Gunn, M., Coates, A.J., Jones, A.P., Ward, J.M., 2010. Astrobiological Considerations for the Selection of the Geological Filters on the ExoMars PanCam Instrument. Astrobiology 10, 933–951. doi:10.1089/ast.2010.0517

Cousins, C.R., Gunn, M., Prosser, B.J., Barnes, D.P., Crawford, I.A., Griffiths, A.D., Davis, L.E., Coates, A.J., 2012. Selecting the geology filter wavelengths for the ExoMars Panoramic Camera instrument. Planet. Space Sci. 71, 80–100. doi:10.1016/j.pss.2012.07.009

Dunning, G.R., Pedersen, R.B., 1988. U/Pb ages of ophiolites and arc-related plutons of the Norwegian Caledonides: implications for the development of Iapetus. Contrib. Mineral. Petrol. 98, 13–23. doi:10.1007/BF00371904

Dyar, M.D., 2002. Optical and Mössbauer Spectroscopy of Iron in Micas. Rev. Mineral. Geochem. 46, 313–349. doi:10.2138/rmg.2002.46.06

Dyar, M.D., Agresti, D.G., Schaefer, M.W., Grant, C.A., Sklute, E.C., 2006. Mössbauer Spectroscopy of Earth and Planetary Materials. Annu. Rev. Earth Planet. Sci. 34, 83–125. doi:10.1146/annurev.earth.34.031405.125049

Ehlmann, B.L., Mustard, J.F., Murchie, S.L., 2010. Geologic setting of serpentine deposits on Mars. Geophys. Res. Lett. 37, L06201. doi:10.1029/2010GL042596

Ehlmann, B.L., Mustard, J.F., Murchie, S.L., Poulet, F., Bishop, J.L., Brown, A.J., Calvin, W.M., Clark, R.N., Marais, D.J.D., Milliken, R.E., Roach, L.H., Roush,

T.L., Swayze, G.A., Wray, J.J., 2008. Orbital Identification of Carbonate-Bearing Rocks on Mars. Science 322, 1828–1832. doi:10.1126/science.1164759

Ehlmann, B.L., Mustard, J.F., Swayze, G.A., Clark, R.N., Bishop, J.L., Poulet, F., Marais, D.J.D., Roach, L.H., Milliken, R.E., Wray, J.J., Barnouin-Jha, O., Murchie, S.L., 2009. Identification of hydrated silicate minerals on Mars using MRO-CRISM: Geologic context near Nili Fossae and implications for aqueous alteration. J. Geophys. Res. 114, 33 PP. doi:200910.1029/2009JE003339

Emmanuel, S., Berkowitz, B., 2006. Suppression and stimulation of seafloor hydrothermal convection by exothermic mineral hydration. Earth Planet. Sci. Lett. 243, 657–668. doi:10.1016/j.epsl.2006.01.028

Etiope, G., Ehlmann, B.L., Schoell, M., 2012. Low temperature production and exhalation of methane from serpentinized rocks on Earth: A potential analog for methane production on Mars. Icarus. doi:10.1016/j.icarus.2012.05.009

Evans, B.W., Hattori, K., Baronnet, A., 2013. Serpentinite: What, Why, Where? Elements 9, 99–106. doi:10.2113/gselements.9.2.99

Farmer, V., 1974. The layer silicates. Infrared Spectra Miner. 4, 331–363.

Fischer, E.M., Pieters, C.M., 1993. The Continuum Slope of Mars: Bidirectional Reflectance Investigations and Applications to Olympus Mons. Icarus 102, 185–202. doi:10.1006/icar.1993.1043

Formisano, V., Atreya, S., Encrenaz, T., Ignatiev, N., Giuranna, M., 2004. Detection of Methane in the Atmosphere of Mars. Science 306, 1758–1761. doi:10.1126/science.1101732

Gaffey, S.J., 1987. Spectral reflectance of carbonate minerals in the visible and near

infrared (0.35–2.55 um): Anhydrous carbonate minerals. J. Geophys. Res. 92, 1429–1440. doi:10.1029/JB092iB02p01429

Gao, B.-C., Goetz, A.F.H., 1990. Column atmospheric water vapor and vegetation liquid water retrievals from Airborne Imaging Spectrometer data. J. Geophys. Res. Atmospheres 95, 3549–3564. doi:10.1029/JD095iD04p03549

Georgiev, G., Glenar, D.A., Hillman, J.J., 2002. Spectral Characterization of Acousto-Optic Filters Used in Imaging Spectroscopy. Appl. Opt. 41, 209–217. doi:10.1364/AO.41.000209

Horita, J., Berndt, M.E., 1999. Abiogenic Methane Formation and Isotopic Fractionation Under Hydrothermal Conditions. Science 285, 1055–1057. doi:10.1126/science.285.5430.1055

Hunt, G.R., Ashley, R.P., 1979. Spectra of altered rocks in the visible and near infrared. Econ. Geol. 74, 1613–1629. doi:10.2113/gsecongeo.74.7.1613

Hunt, G.R., Evarts, R.C., 1981. The use of near-infrared spectroscopy to determine the degree of serpentinization of ultramafic rocks. GEOPHYSICS 46, 316–321. doi:10.1190/1.1441202

Hunt, G.R., Salisbury, J.W., 1971. Visible and near infrared spectra of minerals and rocks. II. Carbonates. Mod. Geol. 2, 23–30.

Johnson, J.R., Bell III, J.F., Bender, S., Blaney, D., Cloutis, E., DeFlores, L., Ehlmann, B., Gasnault, O., Gondet, B., Kinch, K., Lemmon, M., Le Mouélic, S., Maurice, S., Rice, M., Wiens, R.C., 2014. ChemCam passive reflectance spectroscopy of surface materials at the Curiosity landing site, Mars. Icarus. doi:10.1016/j.icarus.2014.02.028

Kelemen, P.B., Matter, J., Streit, E.E., Rudge, J.F., Curry, W.B., Blusztajn, J., 2011. Rates and Mechanisms of Mineral Carbonation in Peridotite: Natural Processes and Recipes for Enhanced, in situ CO2 Capture and Storage. Annu. Rev. Earth Planet. Sci. 39, 545–576. doi:10.1146/annurev-earth-092010-152509

Kelley, D.S., Karson, J.A., Blackman, D.K., Früh-Green, G.L., Butterfield, D.A., Lilley, M.D., Olson, E.J., Schrenk, M.O., Roe, K.K., Lebon, G.T., Rivizzigno, P., the AT3-60 Shipboard Party, 2001. An off-axis hydrothermal vent field near the Mid-Atlantic Ridge at 30° N. Nature 412, 145–149. doi:10.1038/35084000

Kelley, D.S., Karson, J.A., Früh-Green, G.L., Yoerger, D.R., Shank, T.M., Butterfield, D.A., Hayes, J.M., Schrenk, M.O., Olson, E.J., Proskurowski, G., Jakuba, M., Bradley, A., Larson, B., Ludwig, K., Glickson, D., Buckman, K., Bradley, A.S., Brazelton, W.J., Roe, K., Elend, M.J., Delacour, A., Bernasconi, S.M., Lilley, M.D., Baross, J.A., Summons, R.E., Sylva, S.P., 2005. A Serpentinite-Hosted Ecosystem: The Lost City Hydrothermal Field. Science 307, 1428–1434. doi:10.1126/science.1102556

King, T.V.V., Clark, R.N., 1989. Spectral characteristics of chlorites and Mg-serpentines using high-resolution reflectance spectroscopy. J. Geophys. Res. Solid Earth 94, 13997–14008. doi:10.1029/JB094iB10p13997

Klein, F., Bach, W., Humphris, S.E., Kahl, W.-A., Jöns, N., Moskowitz, B., Berquó, T.S., 2014. Magnetite in seafloor serpentinite—Some like it hot. Geology 42, 135–138. doi:10.1130/G35068.1

Klein, F., Garrido, C.J., 2011. Thermodynamic constraints on mineral carbonation of serpentinized peridotite. Lithos 126, 147–160. doi:10.1016/j.lithos.2011.07.020

Klein, F., McCollom, T.M., 2013. From serpentinization to carbonation: New insights from a CO2 injection experiment. Earth Planet. Sci. Lett. 379, 137–145. doi:10.1016/j.epsl.2013.08.017

Krasnopolsky, V.A., Maillard, J.P., Owen, T.C., 2004. Detection of methane in the martian atmosphere: evidence for life? Icarus 172, 537–547. doi:10.1016/j.icarus.2004.07.004

Laurent, R., 1975. Occurrences and Origin of the Ophiolites of Southern Quebec, Northern Appalachians. Can. J. Earth Sci. 12, 443–455. doi:10.1139/e75-038

Laurent, R., Hebert, Y., 1979. Paragenesis of serpentine assemblages in harzburgite tectonite and dunite cumulate from the Quebec Appalachians. Can. Mineral. 17, 857–869.

Lavoie, D., Chi, G., 2010. An Ordovician "Lost City" — venting serpentinite and life oases on Iapetus seafloor. Can. J. Earth Sci. 47, 199–207. doi:10.1139/E10-013

Lowell, R.P., Rona, P.A., 2002. Seafloor hydrothermal systems driven by the serpentinization of peridotite. Geophys. Res. Lett. 29, 1531. doi:10.1029/2001GL014411

Marcaillou, C., Muñoz, M., Vidal, O., Parra, T., Harfouche, M., 2011. Mineralogical evidence for H2 degassing during serpentinization at 300 °C/300 bar. Earth Planet. Sci. Lett. 303, 281–290. doi:10.1016/j.epsl.2011.01.006

Mayhew, L.E., Ellison, E.T., McCollom, T.M., Trainor, T.P., Templeton, A.S., 2013. Hydrogen generation from low-temperature water-rock reactions. Nat. Geosci. 6, 478–484. doi:10.1038/ngeo1825

McCollom, T.M., Seewald, J.S., 2013. Serpentinites, Hydrogen, and Life. Elements 9,

129–134. doi:10.2113/gselements.9.2.129

Mervine, E.M., Humphris, S.E., Sims, K.W.W., Kelemen, P.B., Jenkins, W.J., 2014. Carbonation rates of peridotite in the Samail Ophiolite, Sultanate of Oman, constrained through 14C dating and stable isotopes. Geochim. Cosmochim. Acta 126, 371–397. doi:10.1016/j.gca.2013.11.007

Morris, R.V., Ruff, S.W., Gellert, R., Ming, D.W., Arvidson, R.E., Clark, B.C., Golden, D.C., Siebach, K., Klingelhöfer, G., Schröder, C., Fleischer, I., Yen, A.S., Squyres, S.W., 2010. Identification of Carbonate-Rich Outcrops on Mars by the Spirit Rover. Science 329, 421–424. doi:10.1126/science.1189667

Mumma, M.J., Villanueva, G.L., Novak, R.E., Hewagama, T., Bonev, B.P., DiSanti, M.A., Mandell, A.M., Smith, M.D., 2009. Strong Release of Methane on Mars in Northern Summer 2003. Science 323, 1041–1045. doi:10.1126/science.1165243

Murray, R., Miller, D.J., Kryc, K., 2000. Analysis of major and trace elements in rocks, sediments, and interstitial waters by inductively coupled plasma–atomic emission spectrometry (ICP-AES). ODP Tech. Note 29, 1–27.

Mustard, J.F., 1992. Chemical analysis of actinolite from reflectance spectra. Am. Mineral. 77, 345–358.

Neal, C., Stanger, G., 1985. Past And Present Serpentinisation of Ultramafic Rocks; An Example from the Semail Ophiolite Nappe of Northern Oman, in: Drever, J.I. (Ed.), The Chemistry of Weathering, NATO ASI Series. Springer Netherlands, pp. 249–275.

Neubeck, A., Duc, N.T., Bastviken, D., Crill, P., Holm, N.G., 2011. Formation of H2 and CH4 by weathering of olivine at temperatures between 30 and 70°C. Geochem.

Trans. 12, 1–10. doi:10.1186/1467-4866-12-6

O'Hanley, D.S., 1987. The origin of the chrysolite asbestos veins in southeastern Quebec. Can. J. Earth Sci. 24, 1–9. doi:10.1139/e87-001

O'Hanley, D.S., 1992. Solution to the volume problem in serpentinization. Geology 20, 705–708. doi:10.1130/0091-7613(1992)020<0705:STTVPI>2.3.CO;2

O'Hanley, D.S., 1996. Serpentinites: Records of tectonic and petrological history. Oxford University Press New York.

O'Hanley, D.S., Dyar, M.D., 1993. The composition of lizardite 1T and, the formation of magnetite in serpentinites. Am. Mineral. 78, 391–404.

O'Hanley, D.S., Dyar, M.D., 1998. The composition of chrysotile and its relationship with lizardite. Can. Mineral. 36, 727–739.

O'Hanley, D.S., Wicks, F.J., 1995. Conditions of formation of lizardite, chrysotile and antigorite, Cassiar, British Columbia. Can. Mineral. 33, 753–773.

Ohmoto, H., 1972. Systematics of Sulfur and Carbon Isotopes in Hydrothermal Ore Deposits. Econ. Geol. 67, 551–578. doi:10.2113/gsecongeo.67.5.551

Okland, I., Huang, S., Dahle, H., Thorseth, I.H., Pedersen, R.B., 2012. Low temperature alteration of serpentinized ultramafic rock and implications for microbial life. Chem. Geol. 318–319, 75–87. doi:10.1016/j.chemgeo.2012.05.015

Olsen, K.S., Cloutis, E., Strong, K., 2012. Small-scale methane dispersion modelling for possible plume sources on the surface of Mars. Geophys. Res. Lett. 39, L19201. doi:10.1029/2012GL052922

Oze, C., Sharma, M., 2005. Have olivine, will gas: Serpentinization and the abiogenic production of methane on Mars. Geophys. Res. Lett. 32, L10203.

doi:10.1029/2005GL022691

Pagé, P., Bédard, J.H., Schroetter, J.-M., Tremblay, A., 2008. Mantle petrology and mineralogy of the Thetford Mines Ophiolite Complex. Lithos 100, 255–292. doi:10.1016/j.lithos.2007.06.017

Parnell, J., Boyce, A.J., Blamey, N.J.F., 2010. Follow the methane: the search for a deep biosphere, and the case for sampling serpentinites, on Mars. Int. J. Astrobiol. 9, 193–200. doi:10.1017/S1473550410000200

Pelkey, S.M., Mustard, J.F., Murchie, S., Clancy, R.T., Wolff, M., Smith, M., Milliken, R., Bibring, J.-P., Gendrin, A., Poulet, F., Langevin, Y., Gondet, B., 2007. CRISM multispectral summary products: Parameterizing mineral diversity on Mars from reflectance. J. Geophys. Res. 112, 18 PP. doi:200710.1029/2006JE002831

Pieters, C.M., 1983. Strength of Mineral Absorption Features in the Transmitted Component of Near-Infrared Reflected Light: First Results From RELAB. J. Geophys. Res. 88, PP. 9534–9544. doi:198310.1029/JB088iB11p09534

Pinet, N., Tremblay, A., 1995. Tectonic evolution of the Quebec-Maine Appalachians; from oceanic spreading to obduction and collision in the Northern Appalachians. Am. J. Sci. 295, 173–200. doi:10.2475/ajs.295.2.173

Post, J.., Borer, L., 2000. High-resolution infrared spectra, physical properties, and micromorphology of serpentines. Appl. Clay Sci. 16, 73–85. doi:10.1016/S0169-1317(99)00047-2

Power, I.M., Wilson, S.A., Thom, J.M., Dipple, G.M., Gabites, J.E., Southam, G., 2009. The hydromagnesite playas of Atlin, British Columbia, Canada: A

biogeochemical model for CO2 sequestration. Chem. Geol. 260, 286–300. doi:10.1016/j.chemgeo.2009.01.012

Quesnel, Y., Sotin, C., Langlais, B., Costin, S., Mandea, M., Gottschalk, M., Dyment, J., 2009. Serpentinization of the martian crust during Noachian. Earth Planet. Sci. Lett. 277, 184–193. doi:10.1016/j.epsl.2008.10.012

Riordon, P.H., 1973. Geology of the Asbestos Deposits of Southern Quebec /[by] P.H. Riordon. Department of Natural Resources.

Russell, M.J., Hall, A.J., Turner, D., 1989. In vitro growth of iron sulphide chimneys: possible culture chambers for origin-of-life experiments. Terra Nova 1, 238–241. doi:10.1111/j.1365-3121.1989.tb00364.x

Schrenk, M.O., Brazelton, W.J., Lang, S.Q., 2013. Serpentinization, Carbon, and Deep Life. Rev. Mineral. Geochem. 75, 575–606. doi:10.2138/rmg.2013.75.18

Schroeder, R.A., Weir, C.E., Lippincott, E.R., 1962. Lattice Frequencies and Rotational Barriers for Inorganic Carbonates and Nitrates from Low Temperature Infrared Spectroscopy. J Res. Natl Bur Stand. Vol: 66A.

Schroetter, J.-M., Tremblay, A., Bédard, J.H., Villeneuve, M.E., 2006. Syncollisional basin development in the Appalachian orogen—The Saint-Daniel Mélange, southern Québec, Canada. Geol. Soc. Am. Bull. 118, 109–125. doi:10.1130/B25779.1

Schulte, M., Blake, D., Hoehler, T., McCollom, T., 2006. Serpentinization and Its Implications for Life on the Early Earth and Mars. Astrobiology 6, 364–376. doi:10.1089/ast.2006.6.364

Schwarzenbach, E.M., Früh-Green, G.L., Bernasconi, S.M., Alt, J.C., Plas, A., 2013.

Serpentinization and carbon sequestration: A study of two ancient peridotite-hosted hydrothermal systems. Chem. Geol. 351, 115–133. doi:10.1016/j.chemgeo.2013.05.016

Seyfried Jr., W.E., Foustoukos, D.I., Fu, Q., 2007. Redox evolution and mass transfer during serpentinization: An experimental and theoretical study at 200 °C, 500 bar with implications for ultramafic-hosted hydrothermal systems at Mid-Ocean Ridges. Geochim. Cosmochim. Acta 71, 3872–3886. doi:10.1016/j.gca.2007.05.015

Singer, R.B., Roush, T.L., 1983. Spectral reflectance properties of particulate weathered coatings on rocks: Laboratory modeling and applicability to Mars, in: Lunar and Planetary Institute Science Conference Abstracts. pp. 708–709.

Sleep, N.H., Meibom, A., Fridriksson, T., Coleman, R.G., Bird, D.K., 2004. H2-rich fluids from serpentinization: Geochemical and biotic implications. Proc. Natl. Acad. Sci. U. S. A. 101, 12818–12823. doi:10.1073/pnas.0405289101

Stander, A., Nelms, M., Wilkinson, K., Dyar, M.D., Cardace, D., 2013. Potential Hydrogen Yields from Ultramafic Rocks of the Coast Range Ophiolite and Zambales Ophiolite: Inferences from Mössbauer Spectroscopy. AGU Fall Meet. Abstr. -1, 0482.

Strens, R.G.J., 1974. The common chain, ribbon, and ring silicates. Infrared Spectra Miner. Mineral. Soc. Lond. UK 305–330.

Swayze, G.A., Clark, R.N., Goetz, A.F.H., Chrien, T.G., Gorelick, N.S., 2003. Effects of spectrometer band pass, sampling, and signal-to-noise ratio on spectral identification using the Tetracorder algorithm. J. Geophys. Res. 108, 5105.

doi:10.1029/2002JE001975

Szponar, N., Brazelton, W.J., Schrenk, M.O., Bower, D.M., Steele, A., Morrill, P.L., 2013. Geochemistry of a continental site of serpentinization, the Tablelands Ophiolite, Gros Morne National Park: A Mars analogue. Icarus, Terrestrial Analogs for Mars: Mars Science Laboratory and Beyond 224, 286–296. doi:10.1016/j.icarus.2012.07.004

Wares, R.P., Martin, R.F., 1980. Rodingitization of granite and serpentinite in the Jeffrey Mine, Asbestos, Quebec. Can. Mineral. 18, 231–240.

Webster, C.R., Mahaffy, P.R., Atreya, S.K., Flesch, G.J., Mischna, M.A., Meslin, P.-Y., Farley, K.A., Conrad, P.G., Christensen, L.E., Pavlov, A.A., Martín-Torres, J., Zorzano, M.-P., McConnochie, T.H., Owen, T., Eigenbrode, J.L., Glavin, D.P., Steele, A., Malespin, C.A., Archer, P.D., Sutter, B., Coll, P., Freissinet, C., McKay, C.P., Moores, J.E., Schwenzer, S.P., Bridges, J.C., Navarro-Gonzalez, R., Gellert, R., Lemmon, M.T., the MSL Science Team, 2014. Mars methane detection and variability at Gale crater. Science 1261713. doi:10.1126/science.1261713

Whitehead, J., Reynolds, P.H., Spray, J.G., 1995. The sub-ophiolitic metamorphic rocks of the Québec Appalachians. J. Geodyn. 19, 325–350. doi:10.1016/0264-3707(94)00021-M

Wray, J.J., Ehlmann, B.L., 2011. Geology of possible Martian methane source regions. Planet. Space Sci. 59, 196–202. doi:10.1016/j.pss.2010.05.006

Table 1: Samples, descriptions, and analyses done. Reflectance spectra (ASD) and hyperspectral images were obtained of all samples.

Sample name	Description	FTIR	Chemistry	Mineralogy[a]	Mössbauer	Stable isotopes[a]
Nor3-1_white	Coating of fine white powder on dark serpentinite; float	x		1		1
Nor3-6[b]	Vein of bendable serpentine and hydromagnesite from shear zone	x	x	1		
Nor3-7	Serpentinite with carbonate blebs from shear zone			1		1
Nor3-8	Serpentinite from shear zone with carbonate coatings			1		3
Nor4-2	Blue-colored serpentinite with carbonate coatings from shear zone			1		1
Nor4-3	Serpentinite with carbonate blebs on top and thick white carbonate coating on side from shear zone					2
Nor4-4	Vein of green serpentine from shear zone with thin carbonate coatings					1
Nor4-5	Massive serpentinite with patchy carbonate coating from shear zone					1
Nor4-7	Green-white coating on massive serpentinite rock from shear zone			1		2
Nor4-9[b]	Green and dark blue serpentinite with rare carbonate coatings from shear zone	x	x	1	x	1
Nor4-12_red[b]	Red coating on serpentinite rock from outcrop 100-200 m S of shear zone	x	x	1		1
Nor4-12_green[b]	Green coating on serpentinite rock from outcrop 100-200 m S of shear zone	x	x	1	x	1
Nor4-13[b]	Brittle light green serpentine from outcrop 100-200 m S of shear zone	x	x	1	x	1
Nor4-14	Serpentinite with bright red and green coatings from outcrop 100-200 m S of shear zone					1
Nor4-16	Massive serpentinite rock with thin patchy carbonate coatings from outcrop 100-200 m S of shear zone					1
Nor5-1	Serpentinite with patchy thin films and crystals of carbonate from outcrop 100-200 m S of shear zone			1		3
Nor5-2	Serpentinite with patchy thin coatings of carbonate from outcrop 100-200 m S of shear zone					1

[a]Number of distinct samples from each single hand sample that were analyzed. Note that carbonate samples were often thin coatings on serpentinite rock.
[b]Sample was ground and sieved to <45, 45-75, 75-125, and >125 µm separates.

Table 2: Spectral parameters calculated to analyze data

Spectral parameter	Formula[a]	Cause of spectral feature
BD450	$1 - \frac{R445 + R450 + R455 + R460}{R430 + R435 + R475 + 480}$	Spin forbidden electronic transition of tetrahedral Fe^{3+} (e.g., Burns, 1993; Dyar, 2002; Cloutis et al., 2011a)
Red slope	$\frac{R690 + R700 + R710}{R445 + R450 + R455}$	More oxidized surface (e.g., Hunt and Ashley, 1979; Cloutis et al., 2011b)
Green peak	$\frac{R575 + R580 + R585 + R590}{R465 + R470 + R695 + R700}$	Enhanced by presence of Fe^{3+}/Fe^{2+} charge transfer and spin forbidden tetrahedral Fe^{3+} transition (e.g., King and Clark, 1989; Burns, 1993; Cloutis et al., 2011a)
Blue slope	$\frac{R445 + R450 + R455}{R690 + R700 + R710}$	Textural property, coating or magnetite (Singer and Roush, 1983; Fischer and Pieters, 1993; Cloutis et al., 2011a)
BD740	$1 - \frac{2 * (R730 + R735 + R740 + R745)}{R680 + R685 + R690 + R695 + R805 + R810 + R815 + R820}$	Fe^{2+}/Fe^{3+} charge transfer absorption (e.g., King and Clark, 1989; Burns, 1993; Cloutis et al., 2011a)
BD940	$1 - \frac{2 * (R920 + R925 + R965 + R970)}{R825 + R830 + R835 + R840 + R1020 + R1025 + R1030 + R1035}$	Octahedral Fe^{2+} in serpentine (King and Clark, 1989; Clark et al., 1990; Cloutis et al., 2011a)
BD945	$1 - \frac{2 * (R945 + R950)}{R925 + R930 + R965 + R970}$	Hydration, similar in wavelength to an atmospheric water absorption (e.g., Gao and Goetz, 1990)

[a]R# = reflectance at wavelength # nm

Table 3: Major element chemistry determined through ICP-AES and elemental analyses and mineralogy from XRD.

Sample name	Mineralogy	Al_2O_3	CaO	Cr_2O_3	Fe_2O_3	K_2O	MgO	MnO	Na_2O	NiO	P_2O_5	SiO_2	TiO_2	C
Nor3-1_white[a,b]	serpentine, magnetite, hydromagnesite, magnesite													
Nor3-6[c]	serpentine, magnetite, hydromagnesite, magnesite, brucite	0.33	0.03	0.05	7.45	0.04	40.48	0.20	0.18	0.11	0.01	31.06	0.03	2.42
Nor3-7[a,c]	serpentine, talc, hydromagnesite, dolomite/ankerite, pyroaurite													
Nor3-8 (thinner)[a,c]	serpentine, talc, pyroaurite, hydromagnesite, dolomite/ankerite													
Nor4-2 (bottom)[a,c]	calcite, serpentine													
Nor4-7_1[a,c]	pyroaurite/sjogrenite, serpentine, smectite													
Nor4-9[c]	serpentine, magnetite	0.42	0.06	0.63	10.68	0.01	39.11	0.10	0.14	0.33	0.01	40.79	0.01	0.08
Nor4-12_red[d]	serpentine, calcite, magnesite, iron oxide	0.17	31.19	0.04	3.67	0.02	15.54	0.16	0.08	0.08	0.01	14.55	0.02	5.39
Nor4-12_green[d]	serpentine, calcite, magnesite	0.40	10.27	0.01	2.86	0.02	34.94	0.09	0.04	0.15	0.01	34.38	0.03	2.23
Nor4-13[d]	serpentine, magnetite, calcite	0.21	5.49	0.00	4.00	0.01	37.93	0.08	0.00	0.09	0.01	39.39	0.01	1.43
Nor5-1_2 [a,d]	serpentine, calcite, pyroaurite													

[a]Major element chemistry was not measured for this sample due to the limited amount of sample
[b]Sample is float
[c]Sample is from shear zone
[d]Sample is from imaged wall 100-200 m south of shear zone

FIGURE CAPTIONS

Fig. 1. a. Diagram showing relative proportions of Fe^{2+} and tetrahedral and octahedral Fe^{3+} in serpentine with time during serpentinization determined experimentally by Marcaillou et al. (2011). H_2 is produced during this process. Numbers correspond with absorption features in b. **b.** Reflectance spectra of two points on the surfaces of samples with arrows showing locations of absorption features in serpentines. 1: spin-forbidden electronic transition of tetrahedrally-coordinated Fe^{3+}. 2: Fe^{2+}/Fe^{3+} intervalence charge transfer. 3: electronic transition of octahedrally-coordinated Fe^{2+}. Also shown is the wavelength coverage of the visible imager (labeled visible) and NIR imager (labeled NIR). Band assignments are from Bishop et al. (2002, 2008), Burns (1993), Cloutis et al. (2011a, b), Dyar (2002), King and Clark (1989), and Post and Borer (2000).

Fig. 2. FTIR spectra of samples Nor4-9 (black) and Nor4-13 (grey). Close up views of key absorptions in the 1400, 2300, and 3400-4000 nm regions are also shown, and spectrum Nor4-9 has been multiplied by 2 for clarity in all close up plots.

Fig. 3. Plot of $\delta^{18}O$ vs $\delta^{13}C$, both in ‰ vs VPDB, for carbonates precipitated on serpentine. Standard deviations of measurements of both isotopes are shown for samples where enough material was present to run replicates, but standard deviations on $\delta^{13}C$ measurements are generally less than the width of the symbol. Samples are categorized based on the location from which they were collected within the mine: a shear zone (dark gray), a wall of serpentinite that was imaged south of the shear zone (black), and one sample of float (light gray).

Fig. 4. a. Color composite image of sample Nor4-9 using three bands from the hyperspectral image to approximate a true color image. Red: 660 nm, green: 530 nm, blue: 450 nm. **b.** Spectral parameter map. Red: red slope (Fe^{3+}, likely in iron oxide minerals), green: green peak (correlates with Fe^{3+} in serpentine), blue: blue slope (magnetite, a coating, or a textural property of serpentine). **c.** Spectral parameters BD450 (tetrahedral Fe^{3+}) in magenta and green peak in green. White areas indicate the presence of both the 450 nm band depth and the green peak, and regions highest in both parameters are outlined in white. **d.** Density-sliced scatterplot of BD450 parameter versus the green peak parameter. Red is high density and blue is low density. Points with a BD450 feature present have a calculated parameter value greater than 0, and points with a green peak feature have values greater than 1. The linear correlation coefficient for all points with a green peak value greater than or equal to 1 is 0.761.

Fig. 5. a. Approximate true color image of rock wall of mine from the visible hyperspectral imager. Red: 660 nm, green: 530 nm, blue: 450 nm. Locations where samples Nor4-13 and Nor4-14 (Figs. S2 and S3) were collected are shown. **b.** Spectral parameter map of wall of mine. Red: red slope, green: green peak, blue: blue slope. Vegetation and the calibration target have been masked.

Fig. 6. a. Spectra from the visible hyperspectral imager in the field and **b.** from the visible and NIR imagers in the laboratory shown at hyperspectral resolution (left plots) and resampled to Mastcam and Pancam bandpasses (right plots) for comparison (Bell et

al., 2003, 2012). Spectra at Mastcam resolution are dashed with diamonds at each bandpass, and spectra at Pancam resolution are solid lines. Laboratory NIR spectra have been scaled to the visible spectra at 680 nm.

Fig. 7. Conceptual figure showing fluid flow, hydrogen and methane production, and carbonate formation with different C isotope ratios during early (left) and late (right) stages of serpentinization in the subsurface out of contact with the overlying atmosphere or ocean. This figure describes formation of carbonates with the isotopic signatures of samples from outside the shear zone, and oceanic and continental serpentinization events cannot be distinguished. Rectangles are carbonate veins, and ovals are carbonate coatings. Large, light blue arrows are fluid flow paths. In the right panel, the fluid flow path is wavy to signify decreased water/rock ratios and decreased permeability in the serpentinite, likely due to volume expansion (O'Hanley, 1992 and references therein). As serpentinization proceeded and the system evolved, available carbon decreased, water-rock ratios decreased, and $\delta^{13}C$ values became heavier. Throughout this process, H_2 and CH_4 were produced, and these gases could have been important energy sources for microbes (e.g., Schulte et al., 2006; Cardace and Hoehler, 2009; McCollom and Seewald, 2013).

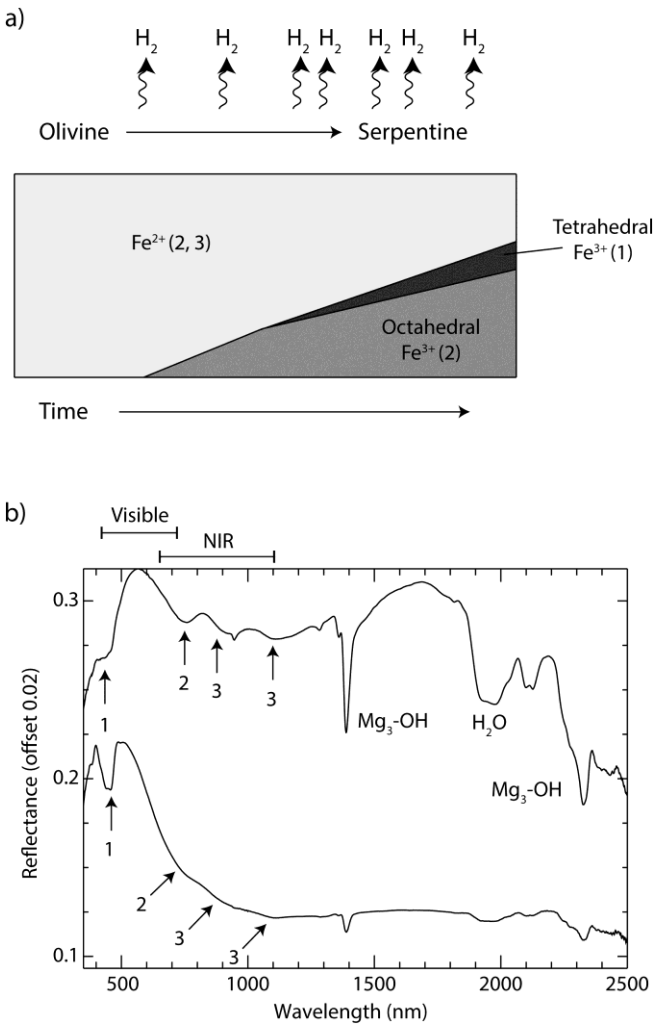
a)
H2
H2
H2 H2
H2 H2
H2
Olivine
Serpentine
Fe2+ (2, 3)
Tetrahedral
Fe3+ (1)
Octahedral
Fe3+ (2)
Time
b)
Visible
NIR
0.3
0.2
0.1
Reflectance (offset 0.02)
1
2
3
3
Mg3-OH
H2O
Mg3-OH
1
2
3
3
500
1000
1500
2000
2500
Wavelength (nm)

Figure 1.

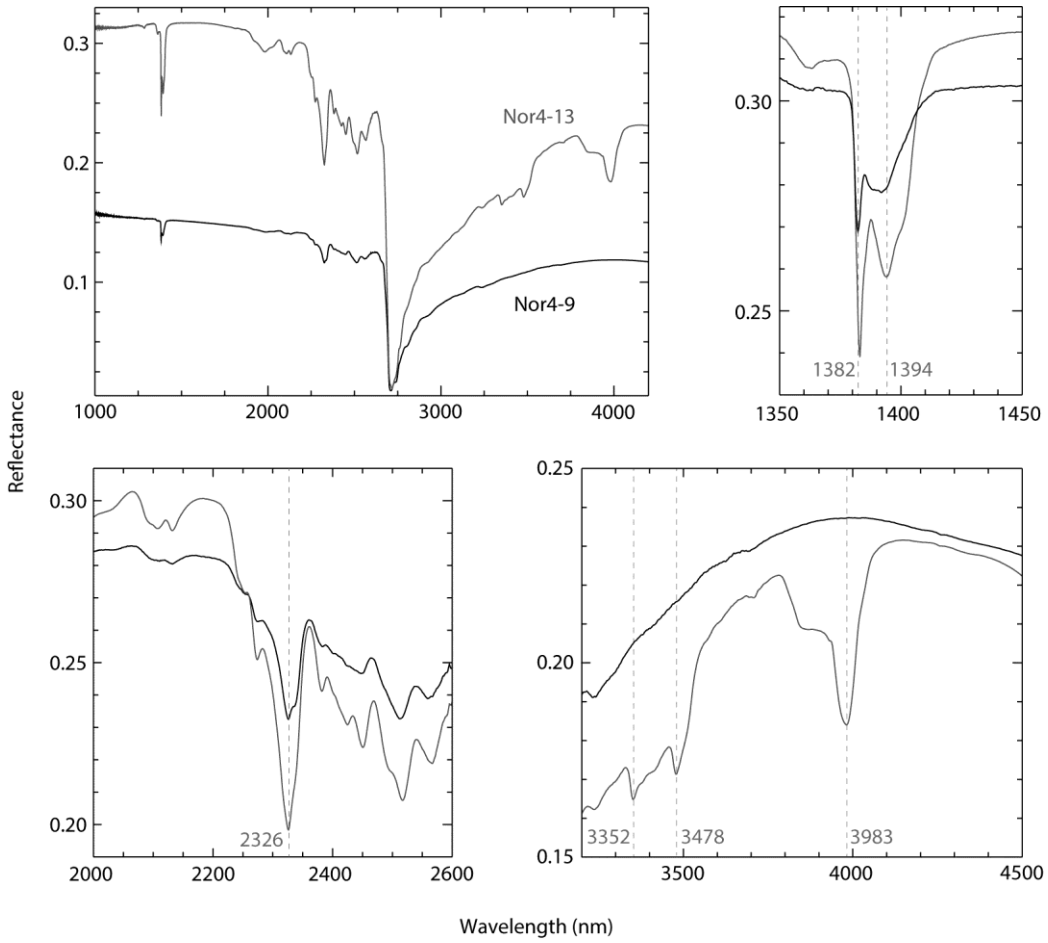
Nor4-13
Nor4-9
1382
1394
2326
3352
3478
3983
Reflectance
Wavelength (nm)

Figure 2.

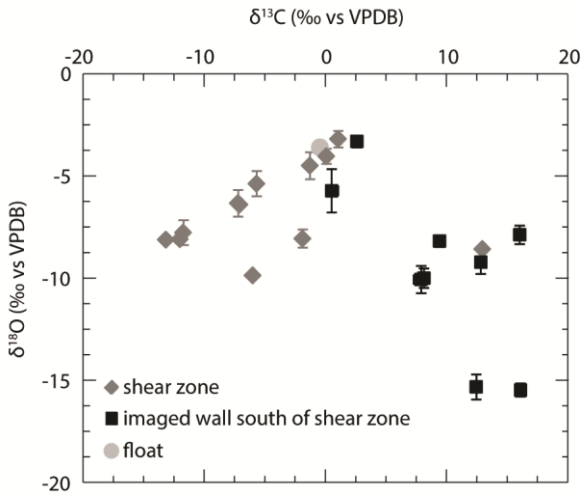
δ13C (‰ vs VPDB)
-20
-10
0
10
20
0
-5
-10
-15
-20
δ18O (‰ vs VPDB)
shear zone
imaged wall south of shear zone
float

Figure 3.

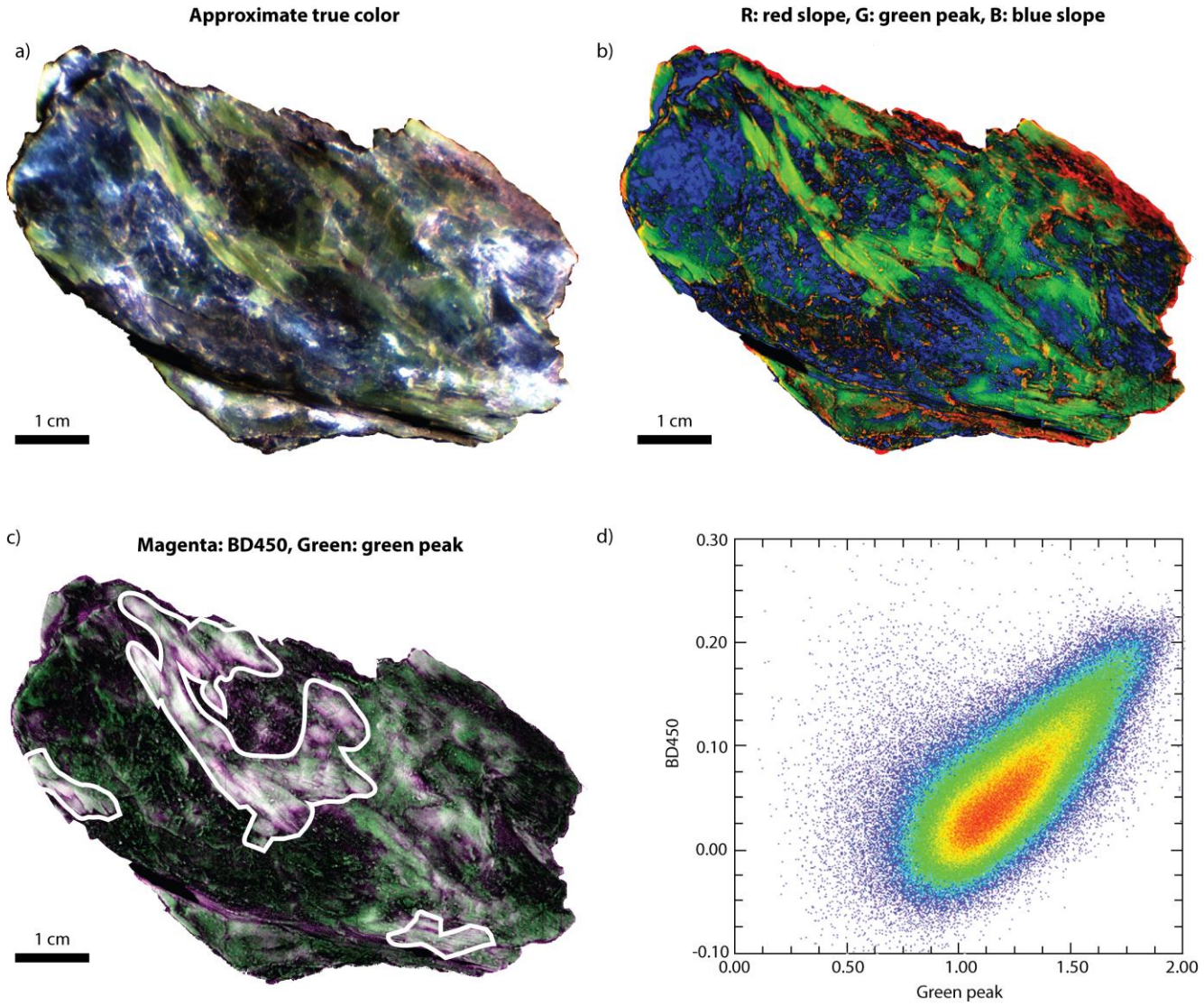
Approximate true color
a)
1 cm
R: red slope, G: green peak, B: blue slope
b)
1 cm
c)
Magenta: BD450, Green: green peak
1 cm
d)
BD450
0.30
0.20
0.10
0.00
-0.10
0.00
0.50
1.00
1.50
2.00
Green peak

Figure 4.

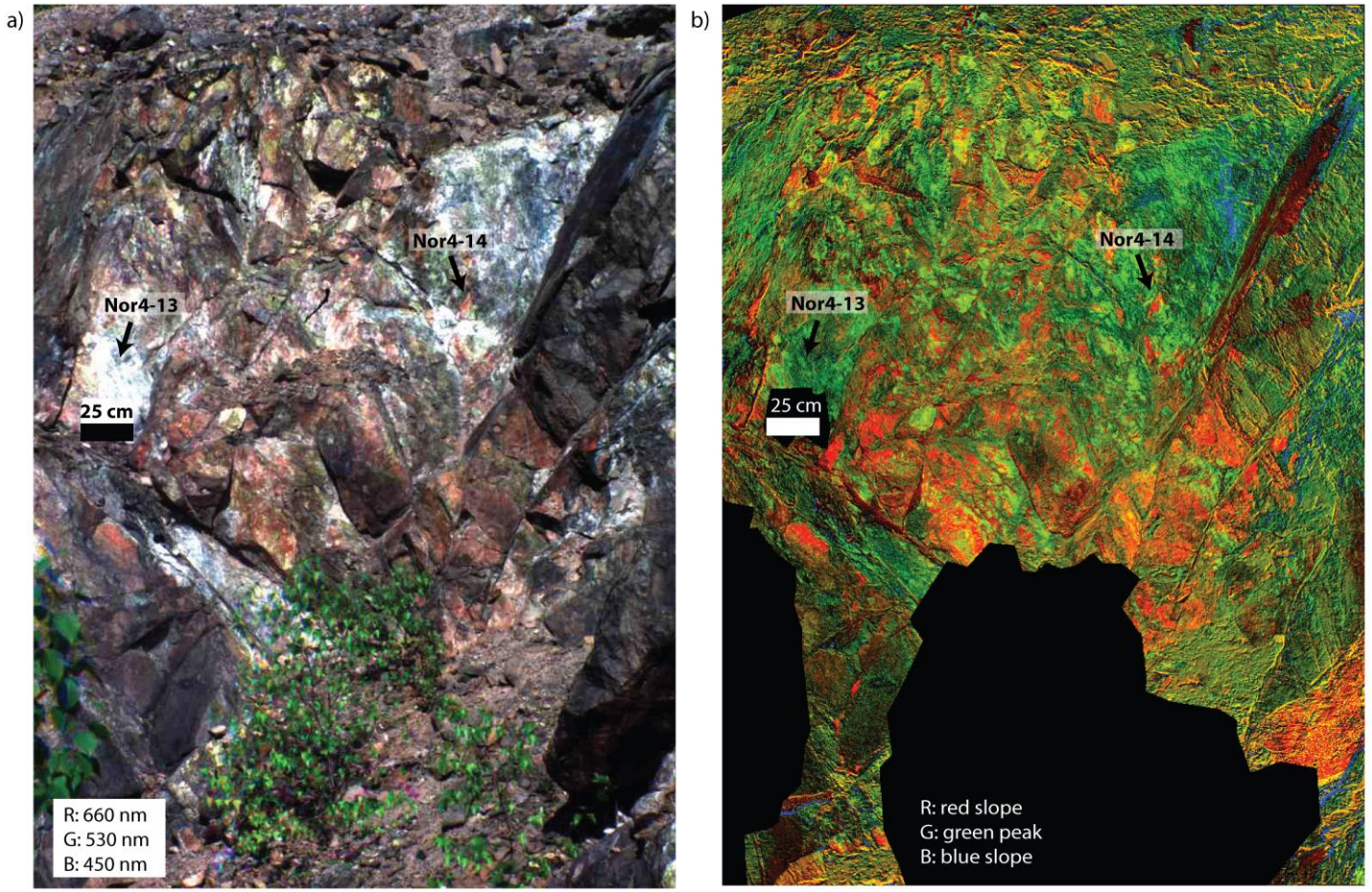
a)
Nor4-14
Nor4-13
25 cm
R: 660 nm
G: 530 nm
B: 450 nm
b)
Nor4-14
Nor4-13
25 cm
R: red slope
G: green peak
B: blue slope

Figure 5.

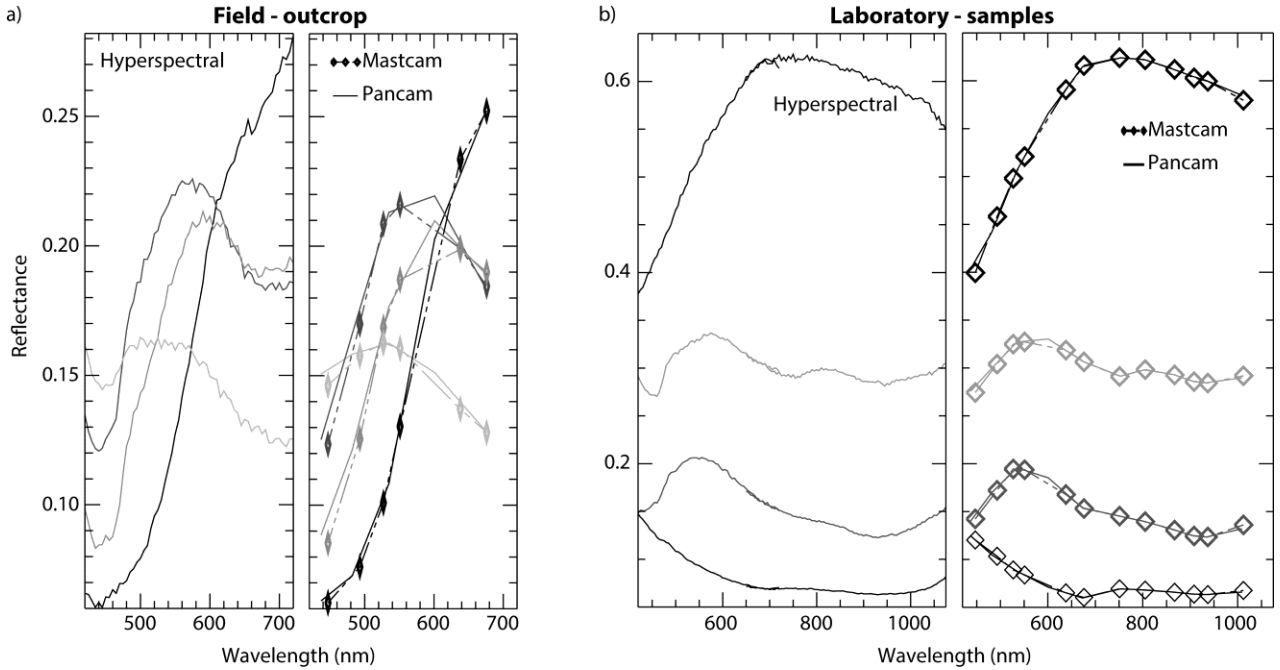
a)
Field - outcrop
Hyperspectral
Mastcam
Pancam
Reflectance
0.25
0.20
0.15
0.10
500
600
700
Wavelength (nm)
b)
Laboratory - samples
Hyperspectral
Mastcam
Pancam
0.6
0.4
0.2
600
800
1000
Wavelength (nm)

Figure 6.

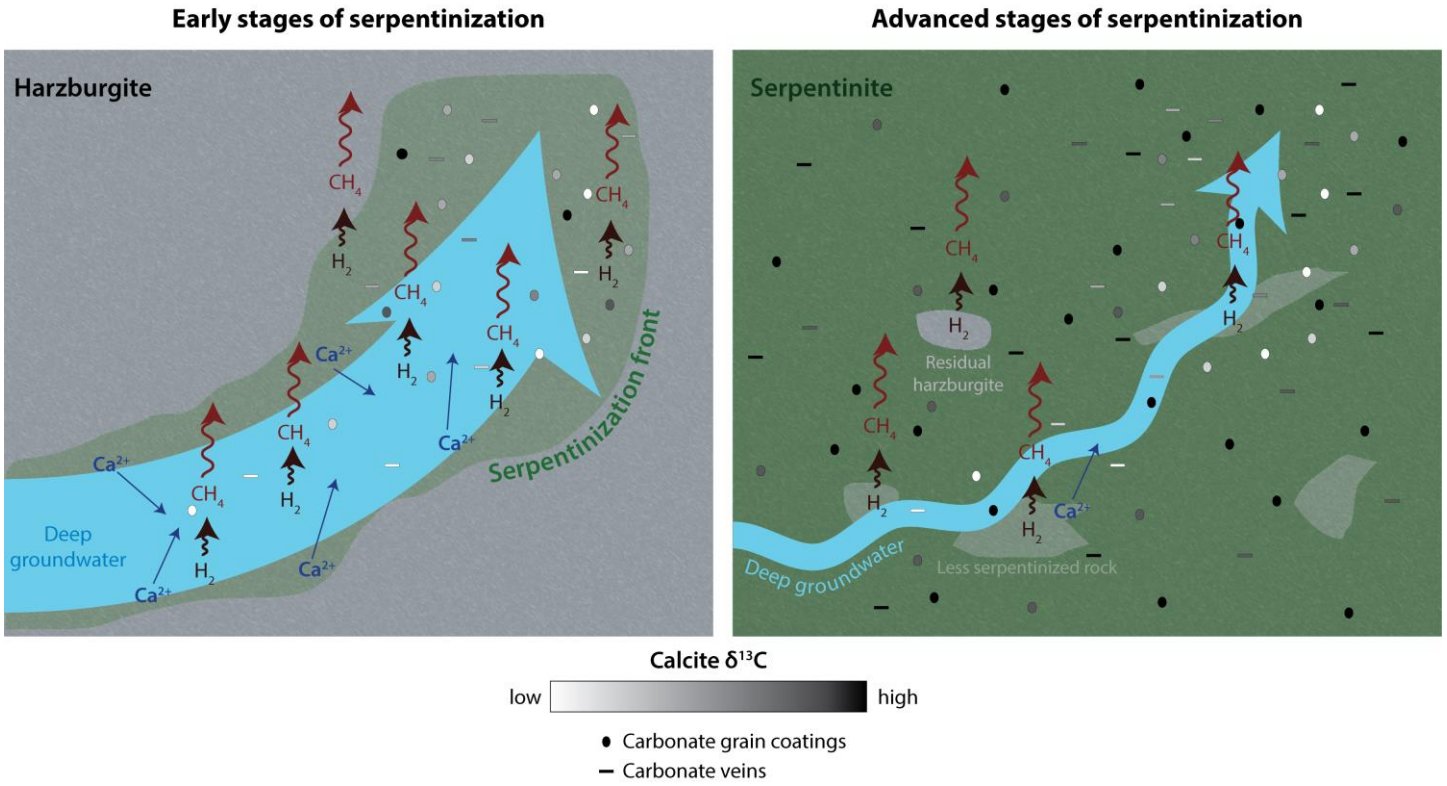
Early stages of serpentinization
Advanced stages of serpentinization
Harzburgite
Serpentinite
Deep groundwater
Serpentinization front
Residual harzburgite
Deep groundwater
Less serpentinized rock
Calcite δ13C
low
high
Carbonate grain coatings
Carbonate veins

Figure 7.

SUPPLEMENTAL MATERIAL

Table S1: Mössbauer parameters for the three samples analyzed.

	Parameters[a]	Nor4-9	Nor4-12_green	Nor4-13
Fe^{3+} (tetrahedral)	IS	0.25	0.19	
	QS	0.45	0.38	
	Width	0.40	0.42	
	Area	3	43	
Fe^{3+} (octahedral)	IS	0.35	0.37	0.31
	QS	0.76[b]	0.75	0.62
	Width	1.02	0.41	0.62
	Area	8	45	17
Fe^{2+} (octahedral)	IS	1.14	1.14	1.15
	QS	2.68	2.70	2.71
	Width	0.38	0.31	0.37
	Area	10	11	21
Magnetite	IS	0.66		0.67
	QS	0.02		0.01
	Field	45.78		46.04
	Width	0.40		0.31
	Area	49		31
Magnetite	IS	0.30		0.31
	QS	0.01		-0.01
	Field	49.23		49.42
	Width	0.35		0.42
	Area	31		31
	χ^2	3243.8	1194.8	897.5
	χ^2_{norm}	6.3	2.3	1.8

[a]IS = isomer shift (mm/s). QS = quadrupole splitting (mm/s). Width is the FWHM (mm/s). Hyperfine Field (B_{Hf}) is in units of kOe. Area is the percentage of the total area.
[b]Parameter fixed

Table S2. Results of stable isotope analyses of carbonates.

Sample ID	Sampling location	Replicates	$\delta^{13}C$ (‰ vs VPDB)	$\delta^{13}C$ Std Dev.	$\delta^{18}O$ (‰ vs VPDB)	$\delta^{18}O$ Std Dev.	% Carbonate (as CaCO3)
Nor3-1 (coating)	float	3	-0.44	0.18	-3.61	0.29	39.7%
Nor3-7	shear zone	3	-7.19	0.17	-6.33	0.65	24.5%
Nor3_8 (thicker)	shear zone	3	1.08	0.26	-3.20	0.41	58.5%
Nor3-8 (thinner)	shear zone	3	-1.26	0.05	-4.50	0.65	29.9%
Nor3-8_3	shear zone	3	0.11	0.24	-4.04	0.37	51.7%
Nor4-2 (bottom)	shear zone	1	-13.14		-8.12		114.9%
Nor4-3 (side)	shear zone	1	12.99		-8.58		96.1%
Nor4-3 (top)	shear zone	3	-11.71	0.19	-7.77	0.61	47.9%
Nor4-4	shear zone	1	-11.98		-8.09		27.1%
Nor4-5	shear zone	1	-7.07		-6.40		17.4%
Nor4-7_1	shear zone	3	-5.66	0.08	-5.37	0.62	28.5%
Nor4-7_2	shear zone	1	-5.98		-9.87		33.6%
Nor4-9 (back)	shear zone	3	-1.86	0.22	-8.06	0.45	54.6%
Nor4-12 (green)	imaged wall	3	16.12	0.17	-15.48	0.32	17.1%
Nor4-12 (red)	imaged wall	3	8.15	0.11	-10.01	0.47	47.3%
Nor4-13	imaged wall	3	7.91	0.59	-10.07	0.67	9.6%
Nor4-14	imaged wall	3	9.44	0.27	-8.19	0.29	93.6%
Nor4-16	imaged wall	3	0.53	0.53	-5.72	1.07	31.7%
Nor5-1 (small crystals)	imaged wall	3	16.05	0.11	-7.88	0.45	93.0%
Nor5-1_1 (inside)	imaged wall	2	2.62	0.62	-3.31	0.29	33.4%
Nor5-1_2 (outside)	imaged wall	3	12.84	0.27	-9.22	0.58	10.7%
Nor5-2	imaged wall	3	12.47	0.29	-15.32	0.61	56.5%

SUPPLEMENTAL CAPTIONS

Fig. S1. Spectra of approximately the same spots on samples Nor4-14 (top) and Nor4-13 (bottom) from the visible hyperspectral imager in the laboratory (black solid lines) and field (gray dashed lines). Spectra from laboratory data are averages of at least 100 pixels, and spectra from field data are averages of 4-16 pixels. More pixels were averaged in laboratory data than field data to account for the higher spatial resolution of the laboratory data.

Fig. S2. (a) Color composite image of sample Nor4-13 using three bands from the hyperspectral image to approximate a true color image. Red: 660 nm, green: 530 nm, blue: 450 nm. **(b)** Spectral parameter map of Nor4-13. Red: red slope, green: green peak, blue: blue slope. **(c)** Spectral parameter map of Nor4-13 with BD450 shown as magenta and the green peak as green. Locations with both the green peak and BD450 present appear white, and locations with the highest values of both parameters are outlined in white. **(d)** Density-sliced scatterplot of the BD450 parameter versus the green peak parameter. Red is high density and blue is low density. The linear correlation coefficient for all points with a green peak value greater than or equal to 1 is 0.575.

Fig. S3. (a) Color composite image of sample Nor4-14 using three bands from the hyperspectral image to approximate a true color image. Red: 660 nm, green: 530 nm, blue: 450 nm. **(b)** Spectral parameter map of Nor4-14. Red: red slope, green: green peak, blue: blue slope. **(c)** Spectral parameter map of Nor4-14 with BD450 shown as magenta and the green peak as green. Locations with both the green peak and BD450 present appear white, and locations with the highest values in both parameters are outlined. **(d)**

Density-sliced scatterplot of the BD450 parameter versus the green peak parameter. Red is high density and blue is low density. The linear correlation coefficient for all points with green peak values between 1 and 5 and BD450 values between -1 and 1.1 is 0.586. Subsetting the range of points that were included in the regression removed 72 points with extreme values out of 767,807 total points, or 0.0094% of the points.

Fig. S4. NIR spectral parameter maps of **(a)** Nor4-3, **(b)** Nor4-14, and **(c)** Nor4-9. Red: BD740 (Fe^{2+}/Fe^{3+} charge transfer), green: BD940 (octahedral Fe^{2+} electronic transition), blue: BD950 (hydration). All parameters are stretched such that the strengths of features mapped are greater than ~3%. Magenta regions are regions with both the 740 nm charge transfer and 950 nm hydration feature present. Yellow regions have both the 740 nm charge transfer and 940 nm electronic transition.

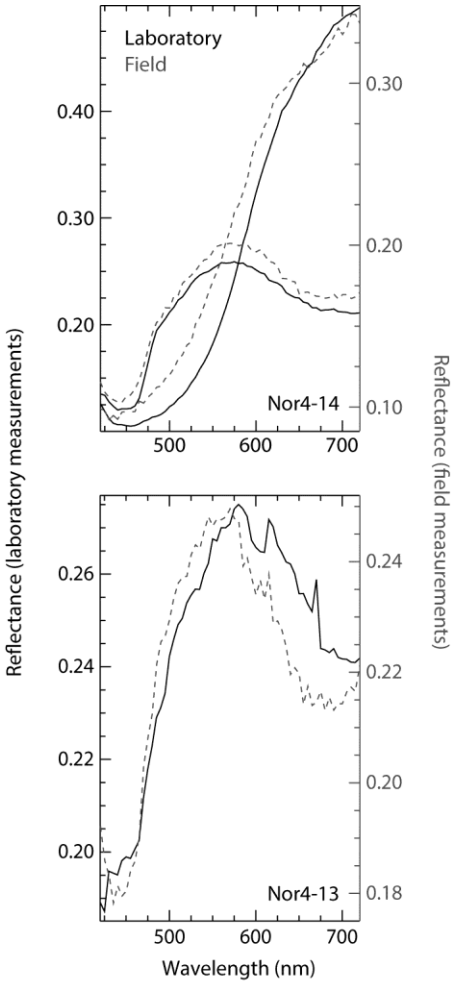
Laboratory
Field
Nor4-14
Nor4-13
Reflectance (laboratory measurements)
Reflectance (field measurements)
Wavelength (nm)
0.40
0.30
0.20
0.26
0.24
0.22
0.30
0.20
0.10
0.24
0.22
0.20
0.18
500
600
700

Figure S1.

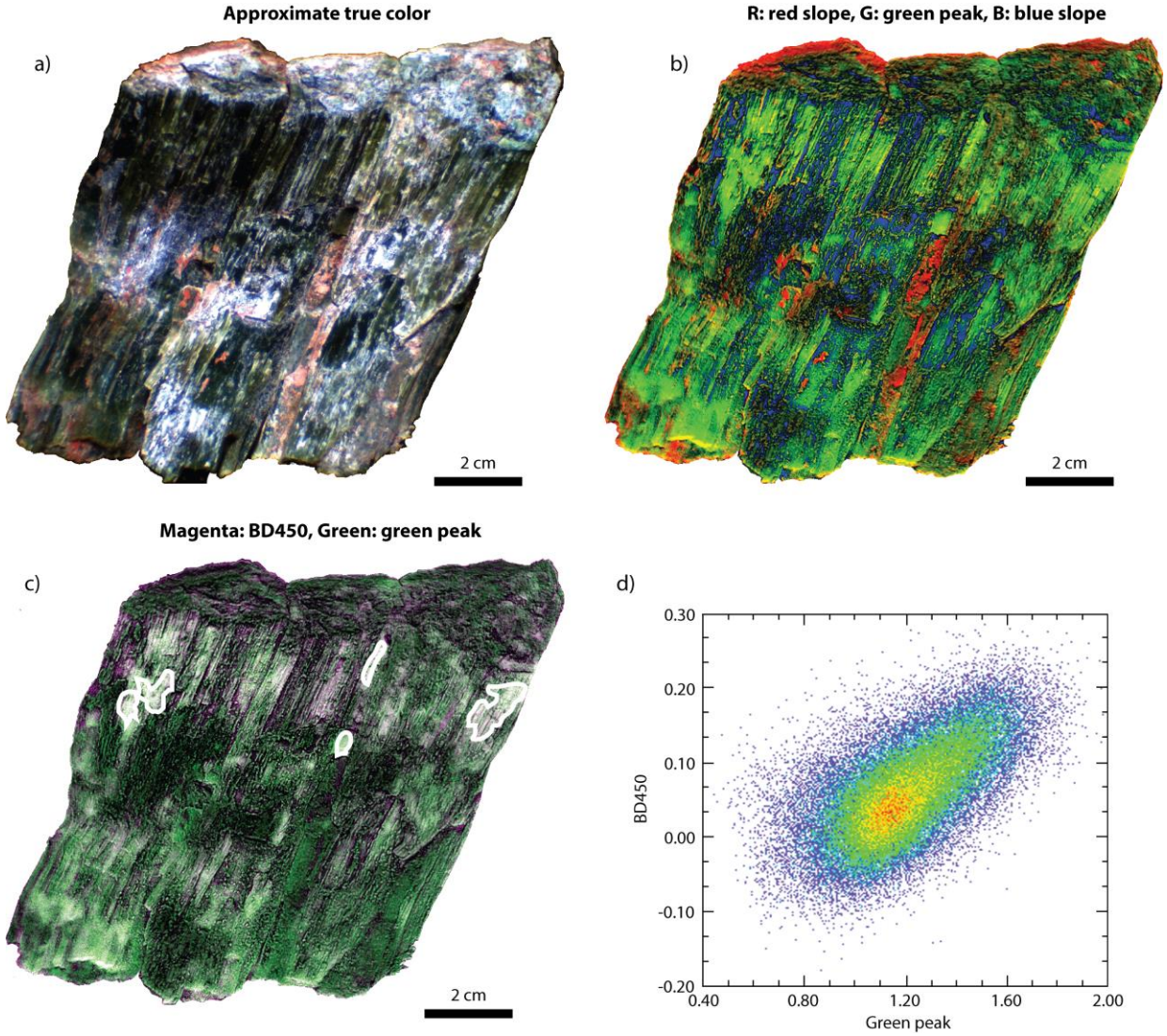
Approximate true color
a)
2 cm
R: red slope, G: green peak, B: blue slope
b)
2 cm
Magenta: BD450, Green: green peak
c)
2 cm
d)
BD450
0.30
0.20
0.10
0.00
-0.10
-0.20
0.40
0.80
1.20
1.60
2.00
Green peak

Figure S2.

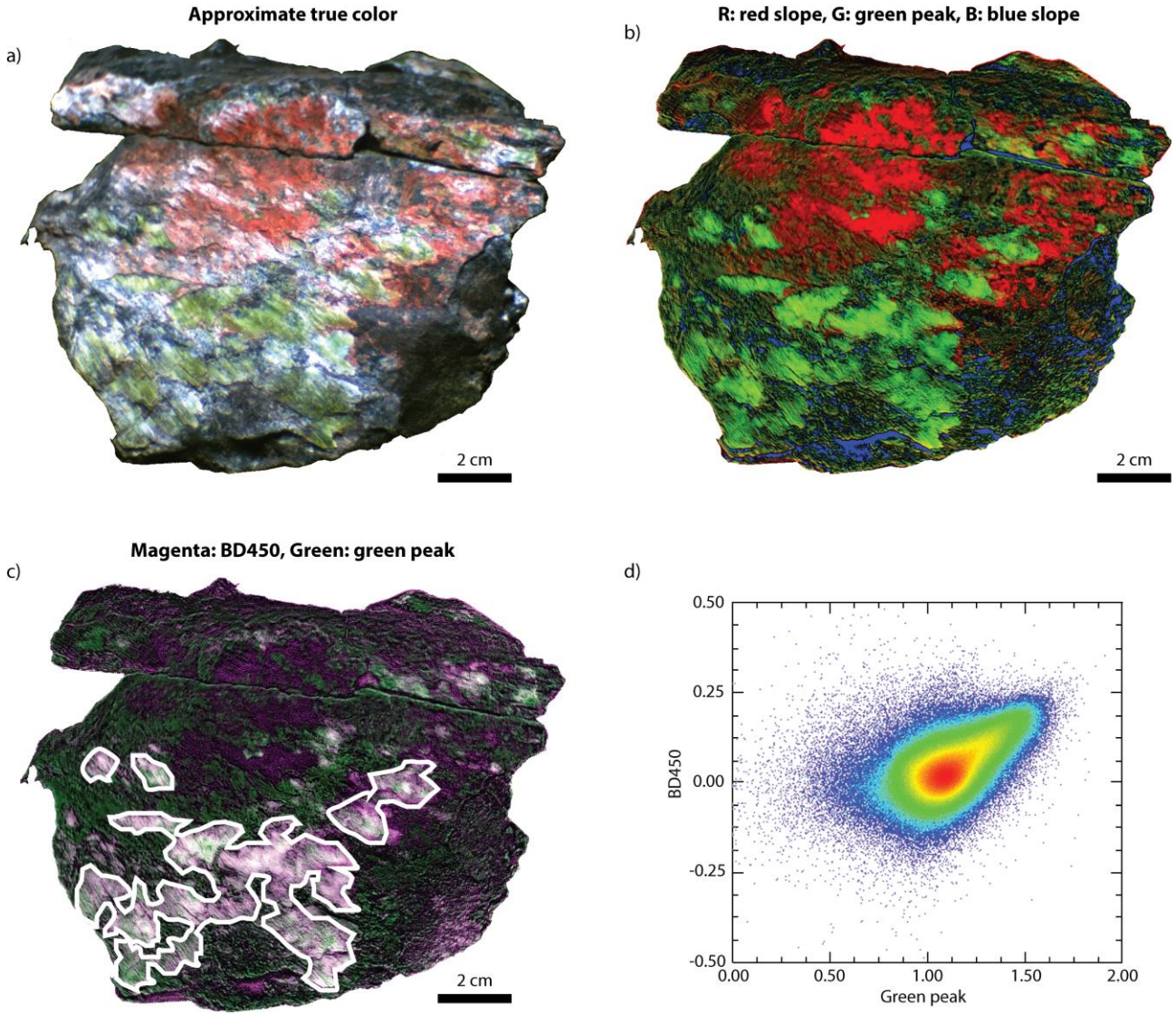
Approximate true color
a)
2 cm
R: red slope, G: green peak, B: blue slope
b)
2 cm
Magenta: BD450, Green: green peak
c)
2 cm
d)
BD450
0.50
0.25
0.00
-0.25
-0.50
0.00
0.50
1.00
1.50
2.00
Green peak

Figure S3.

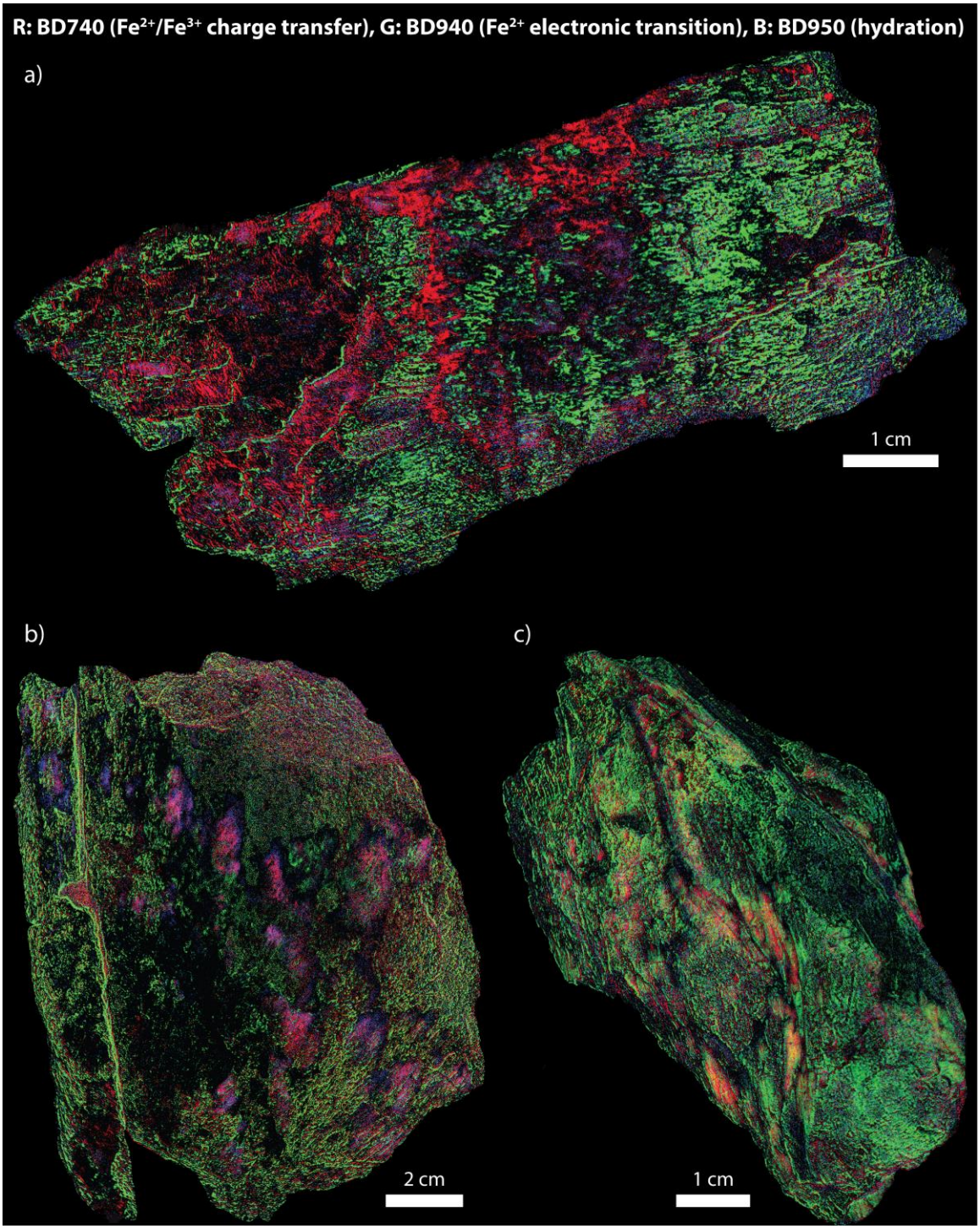
R: BD740 (Fe2+/Fe3+ charge transfer), G: BD940 (Fe2+ electronic transition), B: BD950 (hydration)
a)
1 cm
b)
2 cm
c)
1 cm

Figure S4.

CHAPTER 2

Hydrothermal alteration and diagenesis of terrestrial lacustrine pillow basalts: coordination of hyperspectral imaging with laboratory measurements

Rebecca N. Greenberger[a], John F. Mustard[a], Edward A. Cloutis [b], Paul Mann[b], Janette H. Wilson[c], Roberta L. Flemming[d], Kevin M. Robertson[a], Mark R. Salvatore[e], and Christopher S. Edwards[f]

[a]Department of Earth, Environmental, and Planetary Sciences, Brown University
Providence, RI, USA 02912

[b]Department of Geography, University of Winnipeg
Winnipeg, Manitoba, Canada R3B 2E9

[c]Headwall Photonics, Inc.
Fitchburg, MA, USA 01420

[d]Department of Earth Sciences, University of Western Ontario
London, Ontario, Canada, N6A 5B7

[e]School of Earth and Space Exploration, Arizona State University
Tempe, AZ, USA 85287-6305

[f]United States Geological Survey, Astrogeology Science Center
Flagstaff, AZ, USA 86001

In revision in its current form in:
Geochimica et Cosmochimica Acta

ABSTRACT

We investigate an outcrop of ~187 Ma lacustrine pillow basalts of the Talcott Formation exposed in Meriden, CT, focusing on coordinated analyses of one pillow lava to characterize the aqueous history of these basalts in the Hartford Basin. Analyses completed include hyperspectral imaging of a thick section and hand sample in the laboratory (0.4-2.5 μm), hyperspectral imaging of an outcrop in the field (0.42-1.1 μm), point reflectance spectroscopy, microscopic thermal emission spectroscopy, microscopic Raman spectroscopy, electron microprobe analyses, inductively-coupled plasma – atomic emission spectrometry, elemental analyses, microscopic x-ray diffraction, and powder x-ray diffraction.

The phases identified in the sample are albite, large iron oxides, and titanite throughout; calcite in vesicles; calcic clinopyroxene, aegirine, and Fe/Mg-bearing clay in the rind; and fine-grained hematite and pyroxenes in the interior. Imaging spectroscopy successfully scales results of mineralogy and chemistry analyses from thick section to hand sample to outcrop scales. From all of the analyses, we suggest that the pillow basalts were altered initially after emplacement, either by heated lake water or magmatic fluids, at temperatures of at least 400-600°C, and the calcic clinopyroxenes and aegirine identified in the rind are a preserved record of that alteration. As the hydrothermal system cooled to slightly lower temperatures, clays formed in the rind, and, during this alteration, the sample oxidized to form hematite in the matrix of the interior and Fe^{3+} in the pyroxenes in the rind. During the waning stages of the hydrothermal system, calcite precipitated in vesicles within the rind. Later, diagenetic processes albitized the sample, with albite replacing plagioclase, lining vesicles, and accreting onto the exterior of the

sample. This albitization or Na-metasomatism occurred when the lake within the Hartford Basin evaporated during a drier past climatic era, resulting in Na-rich brines. As plagioclase altered to albite, Ca was released into solution, eventually precipitating in previously-unfilled vesicles, dominantly in the interior of the pillow. Coordinated analyses of this sample permit identification of the alteration phases and help synthesize the aqueous history of pillow lavas of the Talcott formation. These results are also relevant to Mars, where volcanically-resurfaced open basin lakes have been found, and this Hartford Basin outcrop may be a valuable analog for any potential volcano-lacustrine interactions. The results can also help to inform the utility and optimization of potentially complementary, synergistic, and uniquely-suited techniques for characterization of hydrothermally-altered terrains.

1 INTRODUCTION

Hydrothermal systems occur in a variety of settings where hot rocks, often volcanic, interact with water. Understanding the nature of these water-rock interactions provides insights into the associated heat fluxes and modes of cooling, mass fluxes, and ore deposits (e.g., Von Damm et al., 1985; Alt et al., 1986; Hedenquist and Lowenstern, 1994; Lowell et al., 1995), and the resulting mineral assemblages are key to understanding the temperatures, fluid chemistries, and evolution of the hydrothermal system. Additionally, hydrothermal systems may be important in the origin of life on Earth and perhaps elsewhere in the solar system (e.g., Holm, 1992; Shock, 1997; Nisbet and Sleep, 2001; Martin et al., 2008).

Hydrothermal alteration of seafloor basalts driven by igneous processes has been

extensively studied (e.g., Seyfried Jr. and Mottl, 1982; Von Damm et al., 1985; Alt et al., 1986; Seyfried, 1987; Seyfried et al., 1988; Alt et al., 1992; Gillis et al., 1993; Lowell et al., 1995). Lower temperature alteration of these basalts is characterized by Mg-metasomatism and progressive acidification of altering solutions until all Mg is removed from the fluids. At water/rock ratios less than 50 and temperatures less than 350°C, all Mg^{2+} is removed from solution (Seyfried, 1987). Ca-metasomatism dominates at higher water/rock ratios (Seyfried, 1987). Alt et al. (1986) characterized hydrothermal alteration of a 1 km core of basalts through the upper oceanic crust and found distinct zones of alteration that depended on depth, temperature, and type of primary rock (pillow, dike, or massive basalt). Secondary phases identified include Fe-hydroxides, saponite, chlorite, pyrite, zeolites, and carbonates, with zeolites and carbonates generally forming last (Alt et al., 1986).

Hydrothermal alteration of basalts that erupt within a lake differ from oceanic systems due to differences in the chemistries of the altering fluids, the durations of the systems, and the depths of burial. For example, the Lower Basaltic Formation and Inter Basaltic Formation in Northern Ireland have zones of pillow lavas and hyaloclastites interpreted to result from interaction with freshwater with secondary minerals including phyllosilicates, which formed at higher temperatures, and zeolites and calcite, which formed at lower temperatures (Robert, 2001). Zeolites that formed through hydrothermal alteration within a basin were also found in pillow basalts in the Siletz River Volcanics in Oregon, though the fluid source there may have been all or partly seawater (Keith and Staples, 1985).

In the Newark and Hartford basins of the U.S., basalts erupted within lakes, and a

variety of secondary minerals have been reported (e.g., Heald, 1956; Puffer et al., 1981; Cummings, 1987; Laskowich and Puffer, 1990; Puffer and Student, 1992; Kolleeny, 1996; Puffer and Benimoff, 1997; Puffer and Laskowich, 2012). Secondary minerals in Newark Basin basalts include quartz, calcite, prehnite, chalcopyrite, clays, zeolites, pectolite, pyrrhotite, and datolite (Cummings, 1987; Laskowich and Puffer, 1990; Puffer and Student, 1992; Puffer and Benimoff, 1997; Puffer and Laskowich, 2012), and these phases have been attributed to low temperature weathering near erosional surfaces, salt-water reactions from groundwater and brackish waters, hydrothermal alteration, assimilation of sediments leading to a layer with high Na, and metasomatism (Cummings, 1987; Puffer and Student, 1992). Secondary minerals that have been reported in the Hartford Basin basalts are discussed in Section 2. These lacustrine hydrothermal systems are relevant for Mars, where volcanically-resurfaced open basin lakes have been identified (Goudge et al., 2012), raising the possibility of potential volcano-lacustrine interactions during the early history of Mars. Alteration of pillow basalts has also been studied in other environments using reflectance spectroscopy as an analog for Mars (e.g., Bishop et al., 2002).

Unique insights into these types of high temperature water-rock interactions can be provided by hyperspectral imaging, a relatively new tool for petrographic analysis of rocks in the laboratory and field. Airborne and satellite multispectral and hyperspectral imagers have been used previously to study and map hydrothermally altered deposits (e.g., Thomas and Walter, 2002; Clark et al., 2003; Kruse et al., 2012; Launeau et al., 2004; Swayze et al., 2004; Swayze et al., 2014), but these spatial resolutions of these systems often average larger, heterogeneous areas within single pixels. A few studies

have used hyperspectral imagers or customized systems that raster point measurements to approximate imager data at the scales of outcrops, drill-cores, or samples in a variety of environments where there has been water-rock interaction (e.g., Roach et al., 2006; Kruse et al., 2012; Kurz et al., 2012; Yang et al., 2013; Yokoyama et al., 2015), and a similar imaging spectrometer is being developed for planetary missions (Van Gorp et al., 2014). Work by *Kruse et al.*, (2012) integrated spectral measurements of samples and drill-cores, as well as outcrops in the field and from aerial measurements that compared favorably with core logs and suggested where mineable deposits might be located. The outcrop of pillow basalts in the Hartford Basin studied here has a complex history of hydrothermal alteration, metamorphism, and diagenesis. Micro- and macro-scale hyperspectral imaging combined with other measurements of chemistry and mineralogy at the same scale can provide unique insights into past aqueous environments and extend those results to the larger outcrop. We present a detailed study of an altered lacustrine pillow basalt using hyperspectral imaging and a coordinated suite of micro-scale measurements to understand the alteration history, the resulting changes in chemistry and mineralogy, and the spectral signatures of that alteration at a sub-mm scale. Then, we scale those results to the hand sample and outcrop to understand the broader aqueous processes, which are traceable across scales.

2 GEOLOGIC SETTING

In the Hartford Basin, four sedimentary formations (New Haven Arkose, Shuttle Meadow Formation, East Berlin Formation, and Portland Arkose) are separated by three basaltic units (Talcott, Holyoke, and Hampden Basalt formations) (e.g., Hanshaw, 1968;

Puffer et al., 1981). These basalts are similar to Newark Basin basalts in chemistry (Puffer et al., 1981) and time (Seidemann et al., 1984) and are correlated with other Mesozoic basalts in North America through magnetic measurements (McHone, 1996). The eruption of these rift basalts is related to the breakup of Pangea and opening of the Atlantic Ocean and can be connected with basalts elsewhere in the world, including in Africa, South America, and Siberia, with differences between basalts likely due to fractionation and the degree of melting (e.g., Philpotts, 1978; McHone and Butler, 1984; Cummins et al., 1992; Puffer, 1992).

The oldest of the basalt formations, the Talcott basalt, was likely fed by the Higganum dike and erupted into a lake (Philpotts and Martello, 1986; Philpotts, 1992). Similar to the initial flows of other Mesozoic basalts, Talcott formation basalts were not fractionated and are classified as high-TiO_2 quartz-normative (Puffer et al., 1981; Philpotts and Reichenbach, 1985; Puffer, 1992). K/Ar dating has placed the age of the Talcott basalts at 187±3 Ma (Seidemann, 1988). Here, we present results from analysis of an outcrop of the Talcott basalt exposed in Meriden, CT (Hanshaw, 1968).

The Talcott formation has an average thickness of ~61 m in the Meriden quadrangle and contains massive, vesicular, and pillow basalts (Hanshaw, 1968). After eruption, the basalts and sediments in the Hartford Basin were altered through low and high temperature aqueous processes. Alteration minerals reported in the New Haven Arkose that underlies the Talcott Formation include epidote, grossular-andradite garnet, chlorite, other clay minerals, albite, calcite, and copper sulfides (Heald, 1956; Kolleeny, 1996). Thermal anomalies attributed to the igneous activity and resulting hydrothermal circulation have been noted in the Hartford basin through studies of the thermal maturity

of organics and the textures of alteration minerals (Pratt et al., 1988; Merino et al., 1997; Wolela and Gierlowski-Kordesch, 2007). Secondary phases in the Talcott basalt including chlorite, sericite, palagonite, quartz, albite, fluorite, barite, and zeolites have been identified along with enrichments in Fe^{3+} relative to Fe^{2+}, Na, and H_2O and depletions in Ca, Mg, and Si (Hanshaw, 1968; Robinson Jr and Woodruff, 1988; Puffer, 1992). Homogenization temperatures of fluid inclusions in Hartford Basin basalts and diabases are 90-210°C and constrain the temperatures of the hydrothermal system (Robinson Jr and Woodruff, 1988). There is also a carbonate deposit at Coe's Quarry in Connecticut that has been interpreted to be a hot spring deposit formed through flash-boiling of supersaturated fluids associated with the Talcott basalt (Steinen et al., 1987).

This paper focuses on a portion of a pillow lava outcrop characterized by green alteration significantly above the contact with the underlying New Haven Arkose in Meriden, Connecticut, through the investigation of a single representative sample collected at the base of the outcrop. The pillow has a green alteration rind surrounding a purple, oxidized interior and is highly vesicular with nearly all vesicles and fractures filled through secondary mineralization, dominantly calcite. Alteration rinds can be used to understand aqueous processes at a range of water-rock ratios since the degree of interaction with water varies with distance from the rind edge (Hausrath et al., 2008). There is also pink-hued material cutting through the pillow, and the morphology of this material suggests that it was emplaced before the basalt fully solidified.

3 METHODS

3.1 Sample preparation and analysis strategy

The sample analysis strategy employed here focused on a coordinated suite of spectral, chemical, and mineralogical measurements of a thick section that are then scaled to a hand sample and outcrop using imaging spectroscopy. The altered pillow basalt was cut open with a rock saw to expose a cross-section of the pillow and was imaged with a hyperspectral imager in the laboratory. A thick section was then made from the material on the cut face adjacent to the imaged face (Fig. 1a). The thick section was polished with coarse grit until it was an appropriate thickness for electron microprobe analysis and was imaged with the hyperspectral imaging spectrometer in the laboratory before being fully polished and carbon coated. The rougher surface is more optimal for hyperspectral imaging measurements because of greater volume scattering that results in stronger absorptions than are typically achieved with polished surfaces. Electron microprobe measurements of the carbon-coated and polished surface were acquired for bulk chemical analyses. The carbon coat was then removed, and the same face of the sample was analyzed for mineralogy and phase identification with a nine point transect from the rind to the interior (Fig. 1b) using microscopic x-ray diffraction (μXRD) (Flemming, 2007) and microscopic Raman spectroscopy. Microscopic thermal emission spectra (Edwards and Christensen, 2013) were measured for a 5x5 point grid spanning the interior and the rind of the thick section (Fig. 1c). These measurements of spectroscopy, chemistry, and mineralogy of the same sample at the same scales were integrated to better understand the aqueous processes that altered the sample. Imaging of the cut face of the full cross-section in the laboratory and outcrops in the field allow micro-scale measurements to be scaled to the hand sample and outcrop to understand the broader alteration processes and contexts. The types of analyses, their spatial resolutions, and the goals of each are

summarized in Table 1. While others have used coordinated analyses of powdered samples to characterize Mars-relevant materials (e.g., Bishop et al., 2013; Bishop et al., 2014), our methods differ by coordinating micro-scale analyses of unground samples, which preserves the mineralogic and petrologic contexts.

3.2 Point spectroscopy

Point spectra were measured on the surface of the sample with an Analytical Spectral Devices, Inc. (ASD) FieldSpec 3. This spectrometer has a spectral resolution of 3 nm at 0.7 µm and 10 nm at 1.4 and 2.1 µm and sampling intervals of 1.4 nm for wavelengths 0.35-1.0 µm and 2 nm for wavelengths 1.0-2.5 µm. Data are internally resampled to 1 nm sampling by the ASD software. The sample was illuminated by an Oriel Instruments® external light source with a model 66181 quartz tungsten halogen lamp housing with F/0.85 condenser and Model 68735 DC regulated power supply. Measurements were made relative to Spectralon® with a bare fiber optic cable at 30° from vertical, and an external light source at 0° (nadir). Spectra were corrected for the absolute reflectance properties of Spectralon® using the Reflectance Experiment Laboratory (RELAB, Brown University) spectrum HL-JFM-012 of SRT-99-050 after resampling to ASD wavelengths. ASD measurements have higher spectral resolution and signal to noise than the imaging data and provide an independent means of validating the image calibration.

3.3 Hyperspectral imaging

3.3.1 Laboratory

Hyperspectral images of the samples were acquired at the Headwall Photonics, Inc. (Fitchburg, MA USA) laboratory in the visible-near infrared (VNIR) and shortwave infrared (SWIR) wavelength ranges with two of their pushbroom hyperspectral imagers that consist of a foreoptic lens, spectrograph, and focal plane array. The samples are moved across the field of view of the pushbroom sensors on a computer-controlled motorized scanning table illuminated by a quartz tungsten halogen bulb comprising the Headwall Hyperspec® Starter Kit™. This results in a three-dimensional image with two spatial dimensions and one spectral dimension. Such three-dimensional data cubes are also referred to as hypercubes, where each pixel or data point in the two-dimensional image has a full resolution spectrum.

The Headwall High Efficiency Hyperspec® VNIR E-Series hyperspectral imager, configured to measure 338 spectral channels at a spectral resolution of 7 nm (defined as the full width at half maximum of the intensity of the slit image) and sampling interval of 1.785 nm/channel, was used to scan the samples in the VNIR region from 0.4-1.0 μm with an instantaneous field of view (IFOV) of 0.382 mrad. The distance between the sensor and the sample varied with each image, but spatial resolutions on the samples up to ~43.5 μm/pixel were achieved. The Headwall High Efficiency Hyperspec® SWIR X-Series hyperspectral imager, configured to measure 138 spectral channels at a spectral resolution of 12 nm and sampling interval of 12.0656 nm/channel, was used to scan samples in the SWIR region from 1.0-2.5 μm. The SWIR sensor has an IFOV of 1.2 mrad that translates to up to ~133 μm/pixel for these laboratory measurements.

Calibration of the instrument signal to reflectance requires that the background dark current is subtracted and corrections are made for any spectral or spatial non-

uniformities. The dark current was measured by acquiring one measurement with the lens cap covering the lens. A 99% reflectance Spectralon® block from Labsphere (North Sutton, NH, USA) was used as the white reference, and calibration was performed with the following equation:

$$R = \frac{S_t - S_d}{S_s - S_d} * R_s \quad (1)$$

where R is reflectance, S_t is the signal from the target, S_d is the signal from the dark current, S_s is the signal from the Spectralon® panel, and R_s is the reflectance spectrum of Spectralon®. For the reflectance spectrum of Spectralon®, spectrum HL-JFM-012 from RELAB of SRT-99-050, the same type of material used in these measurements, was used after resampling to the wavelengths sampled by the imagers. VNIR and SWIR images were co-registered through manual selection of control points, and SWIR images were warped to VNIR images using a first degree polynomial and nearest neighbor resampling with Exelis Visual Information Systems ENVI® software. VNIR and SWIR data were then joined by scaling SWIR to VNIR data at 0.997 µm (VNIR) and 0.998 µm (SWIR) assuming the inherent reflectance at those two wavelengths is equal, and deleting overlapping VNIR and SWIR bands to create a single image cube.

3.3.2 Field

Outcrops in the field were imaged with Channel Systems visible and near infrared (NIR) acousto-optic tunable filter hyperspectral imagers. The visible imager covers 0.42-0.72 µm with 10 nm spectral resolution and 5 nm sampling and has a 1280x1024 pixel detector. The NIR imager covers 0.65-1.10 µm with 10 nm spectral resolution and sampling and has a 1390x1024 pixel detector. Images were calibrated first with a dark

current subtraction and a flat field correction. The flat field correction was done by dividing the entire image by an image of Spectralon® held directly in front of the imager covering the entire field of view. These corrections removed instrumental effects. Exposure times for both imagers were determined with the software's autoexpose function, which chooses exposure times at each wavelength to maximize the signal without saturating. The dark signal is independent of exposure time, while signal in images where light reaches the sensor (flat field and outcrop images) scales linearly with exposure time. These corrections were calculated with the following equation:

$$R_{ff} = \frac{\frac{(S_o - S_d)}{t_o}}{\frac{S_{ff} - S_d}{t_{ff}}}, \quad (2)$$

where R_{ff} is the dark current and flat field corrected image, S_o is the image of the outcrop, S_d is the dark current image, t_o is the exposure times for the image of the outcrop, S_{ff} is the flat field image, and t_{ff} is the exposure times of the flat field image. Atmospheric effects were then corrected with a dark object subtraction to remove down-welling atmospheric scattering (Chavez Jr, 1996 and references therein) and ratio to the average spectrum of a Spectralon® panel (S_s) that was placed on the outcrop and therefore was illuminated similarly to the outcrop with a similar path length between the imager and the outcrop. These methods are similar to the methods of Clark et al. (2002). The dark object spectrum (D) was the average spectrum of the darkest points in the image. These corrections were calculated with the following equation:

$$R = \frac{R_{ff} - D}{S_s - D} * R_s, \quad (3)$$

where R is reflectance, and R_s is the reflectance spectrum of Spectralon®.

3.3.3 Image analysis

Images were analyzed through calculation of spectral and mineral indicator parameters (e.g., Clark and Roush, 1984; Pelkey et al., 2007; Viviano-Beck et al., 2014). Spectral parameters map depths of absorption features and strengths of slopes or downturns, and mineral indicator parameters use combinations of spectral parameters to map likely mineral phases. Formulas and interpretations for all parameters shown or discussed in this paper are given in Table 2.

3.4 Microscopic Thermal Infrared Emission Spectroscopy (micro-emission spectroscopy)

Microscopic thermal infrared emission spectra were obtained using the Micro Spectroscopy Laboratory instrument at Arizona State University using an instrument developed and described by Edwards and Christensen (2013). Twenty five points on the thick section were measured in a 5x5 grid that contained points within the green alteration rind, purple matrix of the interior, and calcite amygdules. The methods and data processing steps were described by Edwards and Christensen (2013). Measured sample radiances were ratioed to blackbody spectra of the same temperature to derive emissivity values. Individual spectra were categorized into six groups based on similar spectral characteristics. Each group was linearly unmixed using a non-negative least squares fitting algorithm described in Rogers and Aharonson (2008) and an endmember library of 44 laboratory-derived spectra of natural and synthetic mineral specimens. Only solid and coarse particulate endmembers were included in the unmixing library for better comparison with our sample. Linear unmixing is possible at thermal infrared wavelengths

due to the high absorption coefficients of geologically relevant materials in this wavelength region, resulting in areal (checkerboard) spectral mixing with minimal volumetric effects (Ramsey and Christensen, 1998).

3.5 Microscopic Raman Spectroscopy

Microscopic Raman (μRaman) spectra were measured on approximately the same points as the μXRD and micro-emission spectroscopy measurements with a B&WTek iRaman instrument at the University of Winnipeg Planetary Spectroscopy Facility using a 532 nm laser excitation and 10x microscope objective providing an 80 μm spot size and measured the Raman shifts from 174 to 4004 cm^{-1} with a spectral resolution of ~4 cm^{-1} at 614 cm^{-1}. The instrument consists of a thermoelectrically-cooled Glacier^{TM} T CCD detector and BAC102 fiber optic probe attached to a BAC151B video microscope. The automatic integration time function, which increases integration time incrementally until the response is close to saturation, was used, yielding an optimal signal-to-noise ratio. The dark current was measured before the acquisition of each spectrum using the same integration time as determined by the automatic function. Each spectrum is an average of five measurements. The background of each resulting spectrum and spikes due to cosmic rays were removed with CrystalSleuth, and spectra were compared with library Raman spectra in CrystalSleuth (Laetsch and Downs, 2006). High-frequency noise was removed by using a moving average of 3-4 points in wavenumber space.

3.6 Electron Microprobe Analyses

Electron microprobe analyses of the thick section were done at the Brown

University Electron Microprobe Research Facility using a Cameca SX-100 microprobe. Quantitative abundances of eight elements (Al, Ca, Fe, Mg, Mn, Na, Si, and Ti) were measured for 99 points in transects from exterior to interior. We used a 20 μm beam for glass and calcite phases to average the signal over a larger area and a point beam for all other mineral phases. Included in this transect are 15 measurements of calcites, 33 measurements of glass, 32 measurements of albite, and 19 measurements of other phases (iron oxides, titanite, and unknown phases). Separate calibrations were performed for glass, calcite, and silicates. Mineral phases were determined by comparing chemistries of points measured with chemistries of known minerals. Elemental mapping of Al, Ca, Fe, Mg, Mn, Na, Si, Ti, and K was done at a spatial resolution of 13 μm/pixel to cover nearly the entire sample.

To connect the elemental mapping results with the hyperspectral imaging, imaging and microprobe data were co-registered, and microprobe data were warped to the hyperspectral data using a degree 1 polynomial and bilinear interpolation to down-sample the image in ENVI. Minerals were then mapped from elemental data using a linear unmixing algorithm and selecting endmembers from the original (larger) unwarped microprobe image using glass, interior albite, exterior albite, calcite, iron oxide, titanite, dark (all values 0), and copper tape endmembers. Values for each endmember are given in Table 3. Errors in fits were lower using an interior and exterior endmember, and slight differences in composition discussed in section 4.1.5 may explain the differences in elemental mapping results. After unmixing the image, interior and exterior albite values were then summed to get the total albite content of that pixel. A dark endmember is common in linear unmixing of spectral data (Adams et al., 1986; Sabol et al., 1992) and

was included here to account for holes in the thick section (e.g., unfilled vesicles) and slight offsets between mapping tiles. Without this endmember, the algorithm would attempt to fit pixels with no material present with real components, resulting in incorrect phase identifications in the final product and higher errors.

3.7 Inductively coupled plasma – atomic emission spectrometry (ICP-AES)

Quantitative bulk major element chemistry (Al, Ca, Fe, K, Mg, Mn, Na, P, Si, and Ti for all, Cr and Ni for interior and rind samples only) was determined for 37 samples from this site with inductively coupled plasma – atomic emission spectrometry (ICP-AES) after a flux fusion sample preparation at the Brown University Environmental Chemistry Facility using methods modified from Murray et al. (2000). One sample of the interior, one of the alteration rind, and one sample of the pink material cutting through the pillow were ground with a mortar and pestle, and 35-45 mg of each was mixed with 155-165 mg lithium metaborate flux in graphite crucibles. All of the individual analyses of samples reported here are averages of measurements run in triplicate. However, the average value for all samples measured from the outcrop includes analyses that will be reported in a future paper, some of which were run with no replicates. Samples, standard reference materials (NIST2711, Mag-1, DTS-2B, NIST1646a, BIR-1, SGR-1, BHVO-2, NIST2702 and BCR-2 for all; G-2 and SRM-1c in addition for the interior and exterior samples), and blanks (only flux) were fused at 1050°C for 10 minutes. The molten beads were then quenched in 20 ml of 10% nitric acid, agitated for at least 30 minutes, filtered through a 0.45 μm filter, and diluted by pipetting 5 ml of the solution into 35 ml of 10% nitric acid. Diluted solutions were analyzed on a JY2000 Ultrace ICP-AES with a JY AS

421 autosampler and 2400 g/mm holographic grating. Concentrations were determined using the intensities of emission peaks at wavelengths given by Murray et al. (2000) with linear regressions using the standard reference materials. Concentrations have been corrected for drift during ICP-AES measurements, and a median background value determined from analysis of the blanks has been subtracted. Concentrations are reported in oxide weight percentages following geochemical convention.

3.8 Carbon, nitrogen, and sulfur analyses

Carbon contents of the same bulk samples analyzed with ICP-AES were determined on a CE Instruments Model NC2100 Elemental Analyzer at the Brown University Environmental Chemistry Facility after drying the samples overnight at 60°C. Concentrations were calculated from a linear regression using known concentrations of standards acetanilide, cyclohexanone, pine, and MT2711 for the sample of pink material and sulfanilide and NIST 2702 for the interior and exterior samples, and standards were also run every 10 samples and at the beginning and end to check for consistency during the run. All samples reported here were run in triplicate.

3.9 Microscopic x-ray diffraction (μXRD)

μXRD measurements were done at the University of Western Ontario with a Bruker D8 Discover instrument with a 60 mm Co Gobel mirror and a 300 μm snout (Flemming, 2007). Measurements were obtained from 9.5 to 90° 2θ by combining two frames. The first frame for each point was acquired with parameters θ_1=9.5°, θ_2=21°, and w=11° over 45 minutes. The second frame was done with parameters θ_1=29.5°, θ_1=40°,

and w=20° and was acquired for 60 minutes. The nominal beam diameter for each measurement is 300 µm. Nine points were analyzed in a transect from the rind to the interior, and one additional point was analyzed to identify an unknown phase. The resulting µXRD patterns were merged in Bruker Corporation's Diffrac.Suite EVA software, the background was subtracted, and mineral phases were identified by comparison to standard peak phases in the International Centre for Diffraction Data (ICDD) Database. Relative peak heights for various targets are qualitatively related to the abundances of various mineral phases, but quantitative analyses cannot be performed on these data. A few high peaks result from larger oriented crystals.

3.10 Powder x-ray diffraction (bulk)

Mineralogy was determined for bulk samples of the interior and rind using ~750 mg of ground sample with particle size <45 µm at Brown University on a Bruker D2 Phaser with a Cu Kα source and Lynx-eye 1D-detector (<680 eV energy resolution at 8 keV). A 0.6 mm divergence slit was used along with a 0.3 mm anti-scatter shield, a 2.5° soller slit and a Ni-filter to minimize iron fluorescence. Roughly, 750 mg of ground sample with particle size <45 µm were loaded into PMMA polymer sample mounts for analysis. Samples were scanned for 12 hours from 5 to 70° 2θ with 0.02° 2θ step size and rotated 15 full revolutions per minute.

The crystalline phases present were determined by comparing the XRD pattern obtained here with the ICDD database (PDF-2 release 2013) in Diffrac.EVA V3.1. Semi-quantitative analyses of interior and exterior samples were performed with the Rietveld Refinement method (Rietveld, 1969; Bish and Howard, 1988; Young, 1995) in

Diffrac.Suite TOPAS using structure files for aegirine (Redhammer et al., 2006), albite (Harlow, 1982), calcite (Markgraf and Reeder, 1985), chlorite (Zanazzi et al., 2007), diopside (Cameron et al., 1973), hematite (Blake et al., 1966), nontronite (Manceau et al., 1998), and titanite (Speer and Gibbs, 1976). Instrumental parameters used in the refinements included a 6^{th} order Chebychev background correction and a Berger CuKα emission profile. The high order Chebychev coefficient was used to improve the background modeling at low angles, which in turn improves the fit of the clay phases in this region. A sample displacement correction accounted for inconsistent sample loading. The refined specimen parameters included unit cell parameters, crystallite size and strain (lorentzian peak shape), preferred orientation (PO spherical harmonics) and site occupancy (where applicable).

4. RESULTS

4.1 Thick section

4.1.1 Point Reflectance Spectroscopy

Reflectance spectra measured with the ASD are used to identify dominant mineralogies within different units in the sample, specifically the interior matrix, the pink material that cuts through the sample, the rind, and calcite amygdules. The ASD spectra are similar to spectra obtained with the hyperspectral imager (Fig. 2), validating the wavelength and reflectance calibration of the Headwall Photonics imaging data. Small patches of datolite were identified with hyperspectral imaging (Fig. 2), but the ASD does not have sufficient spatial resolution to resolve them. The only indications of the presence of datolite in the ASD data are weak absorption features near 1.47 μm and 2.4 μm

superposed on a spectrum of calcite. The ASD measurements better resolve electronic transitions of Fe^{2+} in type A pyroxenes near 0.97 and 1.19 μm (Cloutis and Gaffey, 1991) than the hyperspectral imaging because the VNIR and SWIR hyperspectral measurements are joined in the middle of those features, leading to artifacts that make the spectral features difficult to resolve. The features seen in the spectra are discussed further in Section 4.1.2.

4.1.2 Hyperspectral imaging

Hyperspectral imaging across the alteration rind shows changes in mineralogy at sub-mm spatial resolution from interior to exterior of the sample (Figures 3, 4). Spectra of the interior matrix of the sample (Figures 2, 3) are consistent with anhydrous, oxidized mafic material and display a complex series of crystal field absorption features that are centered at approximately 0.50-0.51, 0.66, and 0.90 μm. The feature near 0.50-0.51 μm is likely due to a spin-forbidden electronic transition of octahedral Fe^{3+} in an oxide such as hematite, although the exact wavelength of this feature is slightly shorter than the typical absorption in hematite and slightly longer than the feature in other oxide minerals (Hunt and Ashley, 1979; Burns, 1993a; Scheinost et al., 1998). The feature near 0.66 μm also results from a spin-forbidden electronic transition of octahedral Fe^{3+} (e.g., Burns, 1993a; Scheinost et al., 1998). The absorption feature near 0.90 μm is either a spin-forbidden electronic transition of Fe^{3+} (Burns, 1993a; Scheinost et al., 1998; Crowley et al., 2003) or a spin-allowed electronic transition of Fe^{2+} in pyroxene in the M2 site (e.g., Adams, 1974; Adams, 1975; Cloutis and Gaffey, 1991; Burns, 1993a). The overall concavity of the spectrum in the SWIR may also be affected by Fe^{2+} in basaltic glass, which has

absorption features at 1.0 μm from octahedral Fe^{2+} and 1.9 μm from tetrahedral Fe^{2+} (Bell et al., 1976). The overall low reflectance of interior spectra and negative slope longward of ~0.76 μm suggest the presence of fine-grained iron oxides such as magnetite (Hunt and Evarts, 1981; Morris et al., 1985; Cloutis et al., 1990; Cloutis et al., 2011) or could be a textural property (Fischer and Pieters, 1993). The slope could also result from the presence of glass (e.g., Horgan and Bell III, 2012; Horgan et al., 2014). The spectra lack features at 1.4 and 1.9 μm that would indicate OH or H_2O (e.g., Clark et al., 1990), and the interior matrix is therefore assumed to be anhydrous.

Spectra of the rind (Figures 2, 3) are consistent with oxidized pyroxenes with high calcium content and hydration of some phase. A Fe^{2+}/Fe^{3+} intervalence charge transfer absorption feature is centered near 0.80-0.82 μm and is seen in Fe^{3+}-bearing clinopyroxenes (Adams, 1975; Cloutis and Gaffey, 1991; Burns, 1993a; Burns, 1993b). Electronic transitions of Fe^{2+} near 0.95 and 1.1-1.2 μm likely indicate the presence of a type A clinopyroxene, which typically have Wo>0.5 (Adams, 1975; Cloutis and Gaffey, 1991; Burns, 1993a; Burns, 1993b). In these calcic clinopyroxenes, Ca occupies nearly all M2 sites, and crystal field transitions seen in the spectra result from electronic transitions of Fe^{2+} in M1 sites that split into two features in the wavelength range observed here (Adams, 1975; Cloutis and Gaffey, 1991; Burns, 1993a; Burns, 1993b). The ~2 μm feature often seen in pyroxenes is absent in these spectra due to a lack of Fe^{2+} in the M2 site, consistent with type A pyroxenes in Cloutis and Gaffey (1991). Spectra of the rind also show overtones and combination tones of OH and H_2O consistent with a hydrated Fe/Mg-bearing clay. Some spectra exhibit weak bands at 1.39-1.42 μm from the first overtone of the OH stretch, likely coordinated by Fe and/or Mg (e.g., Clark et al.,

1990; Bishop et al., 2008), and nearly all spectra have an absorption feature at 1.9 μm from an H-O-H combination bend and stretch (e.g., Hunt and Ashley, 1979; Clark et al., 1990). These spectra also show an Fe/Mg-OH combination band at 2.30-2.31 μm (e.g., Hunt and Ashley, 1979; Clark et al., 1990; Bishop et al., 2008). As seen in Fig. 3, the strengths of all of these features increase from the inner to outer parts of the rind due to increasing hydration.

Calcite-filled amygdules are identified by an absorption feature at 2.34 μm and a downturn toward 2.5 μm (a full absorption feature would be seen if the wavelength range of this imager extended beyond 2.5 μm) due to the third overtone of the C-O asymmetric stretching mode and a C-O combination band, respectively (Fig. 2) (Hunt and Salisbury, 1971). The outer portion of some calcites in the rind show a broad absorption feature centered near 1 μm and a positive slope from 1 to 2 μm. These spectral characteristics could result from Fe in the carbonates, but microprobe data show no FeO in the outer portion of one such calcite analyzed compared with 0.29 wt % FeO in the interior. This signature may result from complex interactions of light due to volume scattering or another process with the calcite crystal and the surrounding altered matrix of the rind, which has those spectral features due to Fe. Calcites in the rind have stronger 1.9 μm H-O-H combination bands (e.g., Hunt and Ashley, 1979; Clark et al., 1990) than any other phase in the image, and the strength of this band decreases for more interior calcite amydules such that the most interior calcites show no evidence for hydration (Fig. 4). Stoichiometric calcite has no H_2O and therefore should have no 1.9 μm band. This H_2O could either be incorporated into the mineral structure or could be present as fluid inclusions.

A pink-colored material can be seen in the sample (Fig. 4), and context from the larger hand-sample suggests that this material cuts through the pillow. The presence of calcite is confirmed by the same 2.34 and 2.5 μm absorption features used to identify amygdular calcite (Fig. 2). A 1.9 μm H-O-H combination (e.g., Hunt and Ashley, 1979; Clark et al., 1990) indicates that the material is hydrated. Absorption features near 0.50, 0.66, and 0.87-0.90 μm due to Fe^{3+} electronic transitions suggest that there is an iron oxide such as hematite or goethite (e.g., Hunt and Ashley, 1979; Burns, 1993b; Scheinost et al., 1998). These spectra have a negative slope from 1.0 to 2.5 μm and absorption features are weaker relative to other carbonates, likely from a fine-grained opaque mineral (Hunt and Evarts, 1981; Morris et al., 1985; Cloutis et al., 1990; Cloutis et al., 2011).

Along the outer edge of the sample, a small patch of the hydrated borosilicate datolite (labeled in Fig. 4a) is present. Datolite is identified by the first overtone of the OH stretch at 1.47 μm, which is longer than other phases present in this sample, and a complex set of absorption features from 2.0 to 2.5 μm due to B-OH combinations (Clark et al., 1990). Datolite is an extremely minor component that would be difficult to identify through visual examination of the hand sample without hyperspectral imaging data.

The alteration rind is mapped (Fig. 4) by the indicator parameter for the Fe/Mg-OH-bearing phase and spectral parameters that measure a positive slope from 1.15 to 1.8 μm and is also mapped by the height of the peak in reflectance at 0.56-0.57 μm (the positive SWIR slope and green peak respectively in Table 2). Fig. 5 shows that the green peak is correlated with the positive SWIR slope. The green peak results from the Fe^{2+}/Fe^{3+} intervalence charge transfer that reduces reflectance at the longer visible

wavelengths in oxidized pyroxenes (Adams, 1975; Cloutis and Gaffey, 1991; Burns, 1993a; Burns, 1993b). Calcite is mapped where a 2.34 μm (BD2340) feature and a downturn to 2.5 μm (D2500) are present. In visible data, calcite is significantly brighter than every other component and can be mapped simply by the reflectance at 0.7 μm. The pink material that cuts through the pillow has weaker absorption features and is mapped by the same calcite mineral indicator parameter, although at lower values than for calcite amygdules, and an increase in reflectance from blue to red visible wavelengths (red slope parameter). The interior matrix of the sample is spectrally featureless in SWIR data and is best mapped by parameters in the visible and NIR due to the spectral signatures of oxidation (e.g., the red slope parameter). The red slope parameter in particular maps this oxidation. Datolite is well-mapped by a mineral indicator parameter that is positive where both the 1.48 μm (BD1480) and 2.41 μm (BD2410) features are present.

The boundary between the oxidized, anhydrous interior and the hydrated, calcic clinopyroxene-bearing rind is evident in spectral and mineral indicator parameter maps (Fig. 4). The boundary is not particularly sharp. Most of the rind is pervasively-altered, but there are additional patches of alteration present below the rind. Calcite amygdules occur throughout the sample, and the calcites in the rind have higher H_2O content, evident in the BD1900 parameter. The correlation between the green peak and the SWIR slope parameters (Fig. 5) allow altered zones to be mapped in field imaging data, which only extend to 1.1 μm.

4.1.3 Microscopic Thermal Emission Spectroscopy

Fig. 6 shows the measured MicroLab emission spectra and the modeled spectra

using the techniques described in Section 3.4. Modeled abundances for each spectrally-similar class, given in Table 4, are rounded to the nearest 5% and are only reported for phases modeled at abundances greater than or equal to 10% by volume, which is the accepted detection limit for most phases in the thermal infrared (Ramsey and Christensen, 1998; Christensen et al., 2000). These abundances are mathematical fits to the emission spectra. Mineral phases present at less than 10% volumetric abundances may not be accurately modeled in the thermal infrared, precluding direct comparison with more vetted laboratory-based mineralogical analyses. Class 1 includes points in the matrix of the interior and exterior of the sample, which have no obvious spectral differences, and is modeled as containing sheet silicate or amorphous material, feldspar, and carbonate. Class 2 contains only points in the green rind that are modeled similar to Class 1 but with a significant proportion of pyroxene. Four points in the matrix surrounding a large calcite amygdule make up class 3, and these fits include both carbonate and olivine components. The modeled olivine may be fitting a mixture of carbonate and other phases. Class 4 points fall within calcite amygdules, and fits of the spectra are dominated by carbonate. The measurement of the point that is class 5 included part of a large black crystal, likely hematite, and is modeled with a significant oxide component. Class 6 is one point that lies within the pink material and is modeled with carbonate, feldspar, and sheet silicate or amorphous material. We interpret these model results as best fits to the spectral shape, which are in general agreement with the sample compositions and mineral components present as measured by other laboratory techniques. It is difficult to distinguish sheet silicates and amorphous materials such as glass in mixtures at the frequencies sampled here. The abundances of sheet silicates are

higher than estimates from other measurements and may result from low spectral contrast of library endmember clays, the broad, non-unique absorption features associated with clays in the thermal infrared wavelengths, modeling of those broad spectral shapes and not necessarily individual unique absorption features, microstructural effects that disrupt long-range crystallographic order, or orientation effects of crystals or grains. They may also result from ideal endmember spectra not being available for inclusion in our spectral library. Relative abundances of other phases are consistent with other measurements, and these measurements are identifying the major phases present in the sample.

4.1.4 Microscopic Raman Spectroscopy (µRaman)

Microscopic Raman Spectroscopy (µRaman) measurements show albite, calcite, and hematite in the samples, and there is variability among the 9 different spots measured (Fig. 7). Spectra of the most interior and most exterior spots on the sample are dominated by albite and points on the interior have peaks from hematite. Spots 1 and 4 have features due to calcite (labeled Cal in Fig. 7): lattice mode at 280 cm^{-1}, ν_4 (asymmetric in-plane bend) at 704 cm^{-1}, and ν_1 (symmetric CO_3 stretch) at 1087 cm^{-1} (Griffith, 1969; Griffith, 1970; White, 1974). These spots are likely offset slightly from the spots measured with µXRD. Peaks identified as albite are seen at the following Raman shift: 205, 290, 329, 412, 456, 478, 505-508, 754-762, 815-820, 973-978, 1040-1045, 1099-1105, 1152, and 1172 cm^{-1} (McKeown, 2005). These features are due to tetrahedral ring and cage shear, breathing, expansion, compression, rotation, and deformation, Si-O-Si bending, Na-O stretching, O-Al-O bending, Al-O stretching, and Si-O stretching (see McKeown, 2005 for specific band assignments). A feature near 1320 cm^{-1} is seen in points 6-9 only and is

consistent with hematite (e.g., de Faria et al., 1997; de Faria and Lopes, 2007). These are the same points for which hematite is identified with μXRD (Section 4.1.7). The spectra lack obvious peaks from either clays or pyroxenes despite the presence of those phases in low abundances in the samples.

4.1.5 Electron microprobe

At the scale of the microprobe, the entire sample has a glassy matrix that is more microcrystalline in the interior than the exterior rind. Abundant albite, calcite amygdules, and minor iron oxide and titanite are also identified (Fig. 8). A transect of quantitative analyses through the glassy matrix shows higher Fe, Ca, Mg, and Mn and lower Al, Na, and Si in the rind (zones I-III) and the glassier portion of the interior adjacent to the rind (zone IV) than further in the interior (Table 5), and these relationships can be seen in Fig. 9. Feldspars in the sample are nearly pure albite with Na_2O contents of 11.0-12.2 wt %, in some cases slightly higher than stoichiometric albite. Si and Al and the totals of measured oxides within the albite decrease from interior to exterior, suggesting hydration and alteration of the albite toward the exterior. Calcites in the interior of the sample are surrounded by varying amounts of albite, while calcites in the rind are not surrounded by albite, and calcites throughout the sample are zoned, with outer calcites more pure (higher Ca content) and inner calcites having trace Mn, Fe, and Mg. The texture of the sample changes from interior to exterior along boundaries mirroring the pillow edge and reflecting both primary textures and aqueous processes.

We split the thick section into five zones based on textural and visual properties. The section furthest from the pillow edge (zone V) has a microcrystalline texture with

fine crystals of albite in a glassy matrix (Fig. 8f). There are also iron oxides intergrown with larger albite crystals. Quantitative analyses of glass in this zone show higher Al, Na, and Si and lower Fe, Ca, Mg, and Mn than more exterior portions of the sample (Fig. 9). The next zone (zone IV), still in the interior, purple-hued portion of the sample, visually appears to have a higher proportion of glass, though some microcrystalline albite is seen. There are also larger iron oxide and albite intergrowths. Chemically, the points analyzed in this zone are more similar to the rind than more interior points, though still with higher Al and Na than the rind (Fig. 9). Some amygdules have large proportions of albite concentrated on the side of the amygdule closest to the exterior of the sample. Large iron oxide crystals seem to concentrate at and line the base of the rind (red in Fig. 8b).

Zone III shows a distinct green color change (Fig. 4a and 8), has the glassiest texture at the scale of the microprobe, and likely indicates the base of the quenched rind of the pillow (Fig. 8e). Quantitative chemistry measurements show little change in the composition of the matrix from the outer zone of the interior (zone IV) into the rind. Further toward the exterior in the middle of the rind (zone II), there are larger grains of albite within the glassy matrix. This zone has fewer calcite-filled vesicles and more void space. Finally, the exterior-most portion of the rind (zone I) is heavily overprinted by albite (Fig. 8d). The glassy matrix is still visible in places, but void spaces are either empty, filled with albite, or calcite amygdules. Minor phases are present, including a small patch of datolite identified through spectroscopy that is consistent with microprobe measurements. There is also a phase that cuts through some of the calcite amygdules composed primarily of Si, Ca, and Fe, though the exact mineralogy is not known. Titanite occurs as a minor phase in the sample.

The pink material (e.g., right side of Fig. 8e) that cuts through the pillow is seen in three distinct portions of the sample and is a mixture of albite and calcite with minor titanite and iron oxide based on inferences from compositions determined from microprobe measurements. The texture, composition, and context of this material are distinct and suggest that this material formed through a different process than other alteration phases.

4.1.6 Inductively coupled plasma – atomic emission spectrometry (ICP-AES) and carbon content analyses

Powdered samples of the interior and rind material were analyzed for major element chemistry. Results (Table 6) show higher Al, Si, and Na in the interior and lower Fe and Mg when the calcite is subtracted (assuming all C is in calcite) and when concentrations are ratioed to Ti, which is often assumed to be immobile in aqueous systems (e.g., Nesbitt and Wilson, 1992). These trends are subtle in the bulk sample but are confirmed with the microprobe transects (Section 4.1.5). The bulk chemistry of this sample differs markedly from average unaltered Talcott basalts reported by Puffer et al. (1981) and given in Table 6: Ca, Na, and Mn concentrations are higher, while concentrations of all other measured elements are lower. These results suggest significant chemical mobility due to aqueous processes. The pink material cutting through the pillow is dominated by CaO (31.7 wt %) and CO_2 (24.64 wt %), likely almost entirely in calcite, and also has significant Al, Na, and Si. Fe and Ti concentrations are very low (1.5 and 0.11 wt %, respectively).

4.1.7 Micro x-ray diffraction (μXRD)

The μXRD results along the transect through the matrix (Fig. 1b) show the presence of albite and diopside in varying proportions (Fig. 10). The four points in the purple interior show peaks for hematite. Peak heights in μXRD data can be used to make qualitative inferences about the relative proportions of each phase (Fig. 11). The relative peak height of albite is highest at the most exterior portion of the rind and decreases toward the base of the rind before increasing toward the most interior part of the sample. Diopside displays the reverse trend, with the highest normalized peak heights for diopside occurring in the rind and the lowest at the most interior and exterior points. Calcite and datolite are not resolved by the μXRD because those areas were not selected as targets. Points were deliberately selected to be representative of the matrix, and areas of clearly-recognizable phases were avoided.

4.1.8 Powder X-ray Diffraction (XRD)

Powder XRD analyses for samples of the rind and interior are consistent with μXRD and other results (albite, diopside, hematite, calcite, trace titanite) showing few changes in mineralogy between the interior and rind samples (Fig. 12) with hematite in the rind likely confined to large grains. Minor variations in peak heights and position are observed between the interior and exterior, suggesting small differences in concentrations and site occupancy of mineral components. One significant difference between the samples is clear detection of clay in the rind sample as indicated by the chlorite (001) and (002) reflections at 14.32° 2θ and 7.16° 2θ respectively. Clays were not identified in μXRD because these very low 2θ angles could not be sampled with μXRD. Rietveld

refinements of the powder XRD data calculate approximate abundances of minerals in the interior as ~53% albite, ~30% calcite, ~3% hematite, ~11% pyroxene, and ~2% titanite, with no detectable clays. In the exterior, calculated abundances are as follows: ~42% albite, ~21% calcite, ~18% clay, ~15% pyroxene, ~1% hematite, and ~2% titanite. The clays identified are consistent with chlorite and smectite, though oriented mounts were not measured to definitively identify the clays present. The best matching clay phases were clinochlore and nontronite. These results also suggest that both aegirine and diopside are present in the interior and exterior samples. The weighted profile R-factors (R_{wp}) are 4.455 for the interior sample and 5.563 for the exterior. Some of the problems with the fit as seen from the residual (Fig. 12) are related to the clays and the pyroxenes. Intensity issues are observed for the chlorites and are most likely attributed to the non-oriented quality of the sample mounts, although the peak positions are consistent with previous detections. Some of the misfits observed for the pyroxenes are related to the unknown cation occupancy, which will affect both peak positions and peak intensities. The pyroxenes were not resolved on the microprobe, and, while the cation occupancies of the pyroxenes were allowed to vary in the refinement, the exact stoichiometric values are unknown.

4.2 Full cross-section of the pillow lava (hand-sample)

Hyperspectral imaging of the full cross-section of the pillow lava (Fig. 13) provides measurements consistent with the high resolution imaging of the thick section (Fig. 4). The spectra from the interior are consistent with anhydrous, oxidized, mafic material (Figures 3 and 13). The center portions of the pillow visually appear to be

slightly more crystalline, and spectra show higher brightness, a peak in reflectance at shorter wavelengths (0.73 versus 0.76 μm), and a crystal field absorption feature centered near 0.80-0.81 μm. As with the thick section imaging, spectra of the rind are consistent with oxidized calcic clinopyroxene and an Fe/Mg-clay, and calcite amygdules occur throughout the sample with interior calcites generally less hydrated than those in the rind. There are small regions in the interior that are spectrally similar to the rind. The context of the pink material that cuts through the pillow is more clearly defined in the larger hand sample, where this material is volumetrically more important. It is seen through much of the center of the sample with no difference between the interior and exterior, and there are smaller patches in other parts of the sample. Small patches of datolite are also identified in the rind. As with the thick section, the major units can be mapped in the visible spectral range: the green peak parameter maps the rind, the red slope parameter maps the oxidized interior, and the high reflectance at 700 nm correlates with calcite amygdules (Table 2).

4.3 Visible and NIR hyperspectral imaging of the outcrop

The detailed analyses of the thick section and hand-sample provide the basis for mineral mapping using spectroscopy at the outcrop scale (Fig. 14). Much of the scene is highlighted by the green peak parameter, which quantitatively maps green alteration rinds of pillow lavas as well as some altered hyaloclastite breccias with a green matrix. The outcrop-scale spectral properties are consistent with the high-resolution rind mapping. Areas of the outcrop highlighted by the red slope parameter have oxidized surfaces and likely are less altered than the green areas. The red areas may expose fresher (although

oxidized) basalt. The reflectance at 0.7 μm corresponds to carbonate in amygdules and veins since calcite is generally the brightest material in the scene. This method of mapping calcite in field data is imperfect because brightness is not a diagnostic mineral property and can be influenced by photometric effects such as illumination and outcrop orientation relative to the sun. However, at this outcrop, calcite is correlated to some bright areas and serves as a useful guide to further investigate spectrally-featureless areas in this wavelength range. An imager extending to longer wavelengths would be able to map absorption features due to mineral components directly and would allow for more definitive identifications (e.g., thick section and hand sample scale analyses).

5 DISCUSSION

5.1 Summary of results

The major phases present throughout the samples (Table 7) are calcite, calcic and sodic pyroxenes, and albite. Fine-grained hematite is present throughout the matrix of the interior of the pillow, and clays are present in the rind. While the sample appears to have interacted extensively with water and primary minerals have often been replaced by secondary minerals, the original igneous textures of the glassy rind and microcrystalline interior remain intact. Most primary vesicles are now filled with calcite and/or albite. While microprobe and thin section analyses suggest that glass is present in both the interior and the rind, the glass is likely cryptocrystalline, possibly through devitrification (Marshall, 1961), and individual crystals cannot be resolved by the microprobe. Providing additional evidence for these micro- or nano-crystalline phases is the fact that hematite, pyroxene, and phyllosilicates were all identified through multiple other

measurements, though there were no morphologies or chemistries consistent with those phases in the matrix resolved by the microprobe. Through different aqueous processes discussed in section 5.2, primary pyroxenes were replaced with extremely high Ca pyroxenes and aegirine, primary plagioclase was replaced with nearly pure albite, secondary albite lined vesicles and fractures and accreted in the outer portion of the rind, calcite precipitated in vesicles and fractures, phyllosilicates formed in the rind, and the entire sample was oxidized, forming fine-grained hematite in the interior as well as larger grains throughout the sample and leading to Fe^{3+} in pyroxenes in the rind.

5.2 Inferred aqueous history

The aqueous history of this sample and similar Talcott pillow lavas proposed here is summarized in Fig. 15. First, basaltic lava erupted within a lake (Philpotts and Martello, 1986; Philpotts, 1992), forming pillow morphologies with rapidly quenched, glassy rinds and microcrystalline to crystalline interiors (Fig. 15a) and associated hyaloclastite breccias. Vesicles formed in the pillows, with the uppermost pillows having the highest concentration of vesicles. Microcrystalline pyroxenes likely formed during the initial solidification of the pillow lavas. Soon after eruption but before the pillow fully solidified, the material that now is pink cut through the still-molten pillow (Fig. 15b). The rounded contact between this material and the basaltic matrix suggest that it was emplaced prior to pillow solidification. The distinct mineralogy and texture indicate that it has a different origin than the basaltic magma and likely did not form through replacement of primary igneous phases. This material was probably unoxidized initially, and the albite in it may have originally been more calcic plagioclase.

The primary pyroxenes present in the rind likely altered first at high temperature and were replaced with calcic clinopyroxenes and aegirine that have higher Ca and Na contents (Fig. 15c). This inference is based on spectroscopic analyses consistent with type A pyroxenes, which generally have Wo>0.5 (Cloutis and Gaffey, 1991), diopside identified with μXRD and powder XRD, aegirine identified with powder XRD, and high Na contents of the matrix from microprobe transects. Calcic clinopyroxenes and aegirine have been identified in other hydrothermally-altered deposits including the Skaergard intrusion, the oceanic crust, the Ann-Mason porphyry Cu deposit (a skarn deposit with calcic pyroxenes near the contact with a granitic pluton), and buried basalts in Iceland (e.g., Bird et al., 1984; Manning and Bird, 1986; Laverne, 1987; Dilles and Einaudi, 1992; Gillis et al., 1993; Laverne et al., 1995; Vanko et al., 1996; Marks et al., 2010; Alt et al., 2010). In some of these deposits, igneous pyroxenes are replaced with secondary pyroxenes with higher Ca and Fe content and likely formed at temperatures greater than 400°C, with some forming at significantly higher temperatures (Bird et al., 1984; Manning and Bird, 1986; Dilles and Einaudi, 1992; Gillis et al., 1993; Vanko et al., 1996; Marks et al., 2010). Secondary Na-rich pyroxenes such as aegirine have been interpreted to form at temperatures <500 to 600°C (Laverne et al., 1995). Alternatively, the secondary calcic clinopyroxene and aegirine in the rind of the sample analyzed here may have formed through deuteric alteration and possibly with a small component of non-magmatic hydrothermal fluids, as has been suggested for formation of similar minerals in the oceanic crust (Laverne, 1987; Laverne et al., 1995). The context of this and other samples with green rinds, some of which have few vesicles, suggest that they formed where flow of high temperature fluids was enhanced.

With development of hydrothermal circulation, fine-grained Fe/Mg-bearing phyllosilicates (probably chlorite and a Fe-bearing smectite) formed in the rind, probably through hydration of the original microcrystalline matrix (Fig. 15c). In oceanic crust, these phases have been interpreted to form at 250-320°C (Laverne et al., 1995). The planar boundary between the green rind with calcic and sodic clinopyroxenes and clays and the anhydrous, microcrystalline interior suggests that alteration processes were controlled by kinetics. The duration of the hydrothermal system and the mechanics of fluid flow through the system concentrated alteration in the rind, where water-rock ratios were higher. Coarse Fe oxide grains seem to concentrate at the base of the rind and likely indicate how far these higher volumes of heated fluids penetrated. Glass is very susceptible to weathering (e.g., Eggleton et al., 1987; Nesbitt and Wilson, 1992), possibly explaining why the rind is more altered than the microcrystalline interior. During the hydrothermal alteration, there was significant mobility or leaching of cations based on the microprobe and bulk chemistry analyses.

During the hydrothermal activity, the entire pillow oxidized, suggesting that the whole pillow interacted with some volume of water (Fig. 15c). While mafic rocks can oxidize in the absence of any water (Salvatore et al., 2013), the abundance of lake water above the basalts coupled with variations in the character of the oxidation around the outcrop suggest that the oxidation here was tied to aqueous processes. The matrix of the interior of the sample has fine-grained hematite, pyroxenes in the rind have Fe^{3+} identified through a Fe^{2+}/Fe^{3+} charge transfer absorption feature in spectroscopy, and the Fe-bearing clays probably have some component of Fe^{3+} in them, consistent with identification of nontronite with XRD. From this, we conclude that the hydrothermal

fluids were oxidizing such that Fe^{2+} in the glass and pyroxenes was far enough from equilibrium that it oxidized relatively quickly and was not subject to the kinetic controls on alteration that other secondary phases were.

During the final stages of hydrothermal alteration, calcite precipitated in vesicles and fractures in the pillow rinds (Fig. 15d). The rind calcites here are distinct from interior calcites because they have higher water content as determined through the depth of the 1.9 μm feature and are not surrounded by albite. These differences suggest that rind calcites and interior calcites did not form through the same processes. Calcites commonly precipitate during later stages of hydrothermal alteration (e.g., Alt et al., 1986; Robert, 2001). For calcite to form in the Hartford basin, fluids must have been rich in HCO_3^-, making them slightly acidic. A carbonate deposit associated with the Talcott basalts at Coe's Quarry in nearby North Branford, CT, has been interpreted to be a hot spring deposit formed through flash-boiling of supersaturated fluids (Steinen et al., 1987). Rapid precipitation of calcite through a process such as flash-boiling could potentially have trapped water within the calcite crystals and explain the hydration seen with spectroscopy.

After the hydrothermal system ceased and the basalts were buried, the outcrop was albitized (Fig. 15e). During this phase of alteration, albite replaced primary Ca-rich plagioclase in microcrystalline glass and larger crystals, coated or filled previously-unfilled vesicles, and precipitated in the outer portion of the rind where water/rock ratios were highest. For vesicles in the interior of the sample, albite always surrounds calcite, suggesting that the albite formed first, consistent with interpretations of sediments in the Hartford, Newark and Deerfield basins that similarly have albite overgrowths and albite

replacement of plagioclase (Hubert et al., 1992; van de Kamp and Leake, 1996; Wolela and Gierlowski-Kordesch, 2007). Complete replacement of plagioclase with albite has been reported in Hartford Basin sediments (Wolela and Gierlowski-Kordesch, 2007). In these regions, the Na_2O content of the sediments is 4-7%, higher than the 2-3% typical in sandstones and shales elsewhere (van de Kamp and Leake, 1996). The reported Na contents of sediments in the region (van de Kamp and Leake, 1996) are comparable with Na contents of altered basalts analyzed here (Table 6). The albitization or Na-metasomatism in the sediments likely occurred from lakes evaporating during drier climatic periods, creating Na-rich brines (Hubert et al., 1992; van de Kamp and Leake, 1996). These brines may have had a pH greater than 9, and alteration occurred at depths less than 2 km (van de Kamp and Leake, 1996).

The pervasive albitization seen here must have released significant Ca from the primary plagioclase into solution. In sediments elsewhere in the region, calcite is interpreted to have formed after albitization because Na originally in the fluids was removed through formation of albite while Ca was released from the primary mineralogy, forming to Ca-rich fluids (van de Kamp and Leake, 1996). We invoke a similar process for formation of calcites in interior vesicles of this basaltic pillow (Fig. 15f; the exterior vesicles were previously filled with calcite as shown in Fig. 15d). The average CaO content of all basalt samples analyzed from this outcrop is 10.83 wt%, which is remarkably similar to the average CaO content in unaltered Talcott basalts of 11.05 wt% reported by Puffer et al. (1981), though we note that the samples selected for chemistry analyses here were not intended to be representative of this heterogeneous outcrop. Some samples analyzed have significantly lower than average CaO contents, while others

including the pillow analyzed here have high CaO. It is possible that Ca is conserved in the system and in any available fractures and pores. In vesicular samples, Ca content is high because there was significant void space for calcite to precipitate. Less vesicular samples often have low Ca because there was nowhere for calcite to precipitate. We suggest that Ca was transported short distances but could not leave the system because it rapidly precipitated within the altering basalt. We also note that both the albite and calcite likely precipitated during single episodes, filling nearly all remaining void space in the sample, because albite and calcite do not form multiple concentric rings that would be expected with multiple cycles of albitization and calcite formation.

Small amounts of datolite were also identified in this sample. Boron is very mobile and is preferentially leached during hydrothermal fluid flow, concentrating boron in the fluids, and can be sourced from magmatic fluids (e.g., Leeman and Sisson, 1996; Garrett, 1998). Datolite is often found in regional or contact metamorphic or skarn deposits (Kistler and Helvaci, 1994). In one deposit in Hungary that has undergone very low-grade metamorphism, datolite occurs in veins and has been shown to form at temperatures between 160° and 210°C at 5-6 km depth (Kiss et al., 2012). In these Hartford Basin basalts, the datolite likely formed through similar hydrothermal processes.

5.3 Implications

Because pillow lavas erupt within a body of water, are generally fractured and more porous than basalt, and contain significant glass that is susceptible to weathering, some of the pillows here have undergone intense alteration, while there is unaltered or minimally altered Mesozoic basalt reported elsewhere in Connecticut (e.g., Puffer et al.,

1981). The rich information revealed through all of these complementary, coordinated measurements records the aqueous evolution from a hydrothermal system driven by heat from volcanism to diagenetic processes resulting from changes in climate affecting subsurface aqueous conditions in a rift basin. Previous work in the Hartford Basin has documented albitization of sediments (Hubert et al., 1992; van de Kamp and Leake, 1996; Wolela and Gierlowski-Kordesch, 2007), subsequent calcite formation (Hubert et al., 1992; van de Kamp and Leake, 1996) and evidence for thermal events (e.g., Pratt et al., 1988; Kolleeny, 1996; Merino et al., 1997; Wolela and Gierlowski-Kordesch, 2007), and there has been limited work on alteration minerals in the basalt (Hanshaw, 1968; Puffer et al., 1981; Steinen et al., 1987; Robinson Jr and Woodruff, 1988). Our work uses analyses of one sample to better constrain the types and sequences of alteration in the context of this previous work. In addition, to our knowledge, hydrothermal calcic clinopyroxenes and aegirine have not previously been identified in the Hartford Basin, and these minerals preserve a record of the initial >400°C hydrothermal system present initially after emplacement of the basalts or eruption of a subsequent volcanic flow on top of the one sampled here. We are also able to distinguish two distinct periods of calcite formation, one hydrothermal and the other diagenetic, through spectroscopy with additional evidence from electron microprobe analyses. Altered oceanic pillow basalts often have zeolites and Mg-bearing clays such as saponite (e.g., Seyfried Jr. and Mottl, 1982; Alt et al., 1986). Differences between the assemblages observed here and oceanic pillow basalts likely result from differences in fluid chemistry between freshwater lakes and the ocean. In addition, the precise diagenetic processes due to evaporation of nearly all of the overlying fluids that affected this sample are not observed in oceanic

environments.

Volcanically-resurfaced open basin lakes identified on Mars suggest the possibility of lava-lake interactions, though no morphologies consistent with those processes have been observed (Goudge et al., 2012). Nevertheless, if those interactions took place, the Hartford Basin pillow basalts could be a good analog. There could be similar secondary mineralogies preserved on Mars, with evidence for a hydrothermal system declining in temperature as well as late stage diagenetic processes that could be expected as the basalts were buried and the lake dried up with changing climate (e.g., Bibring et al., 2006). Unraveling the signatures of alteration under various conditions could shed light on the sequence of environmental change on Mars.

By integrating coordinated measurements of mineralogy, chemistry, and spectroscopy, hyperspectral imaging can be used to scale the results of many detailed measurements, some at the sub-cm and sub-mm scales to hand samples and outcrops quickly and non-destructively to understand the context and aqueous history of an outcrop. The results here could not be obtained with any single measurement, and there are features in VNIR and SWIR reflectance spectroscopy that connect with results of the other measurements. Although plagioclase cannot be seen in mixtures with more than minor proportions of other minerals (Cheek and Pieters, 2014), the presence of albite in outer portions of the rind can be inferred with spectroscopy because the green peak parameter has lower values (that portion of the rind is less green) owing to the presence of the albite. All of the analyses here are critical to understanding the alteration history of these basalts.

6. CONCLUSIONS

Coordinated analyses of the mineralogy, chemistry, and spectral signatures of an altered basaltic pillow lava reveal signatures of a complex aqueous history. The phases identified are albite, calcic clinopyroxene, aegirine, hematite, titanite, calcite, and, in the rind only, Fe/Mg-phyllosilicates. First, alteration at temperatures greater than 400°C replaced igneous pyroxenes with calcic and sodic clinopyroxenes having a distinct spectral signature. As the hydrothermal system cooled, fine-grained Fe/Mg-bearing clay minerals formed in the rind. In addition, during the hydrothermal alteration, the entire sample oxidized, forming fine-grained hematite in the matrix of the interior and oxidizing some Fe in pyroxenes and clays in the rind. During the late stages of hydrothermal alteration, calcite precipitated in vesicles in the rind, trapping enough H_2O to be seen spectrally either as fluid inclusions or within the calcite structure. After the basalts were buried, the lake in the Hartford Basin evaporated due to changes to the regional or global climate, forming Na-rich brines and leading to albitization or Na-metasomatism replacing primary plagioclase with albite and precipitating albite lining vesicles and on the exterior of the pillow. Destruction of igneous plagioclase released Ca into solution, and precipitation of albite removed Na from the fluids, causing Ca-rich fluids that precipitated calcite in any remaining unfilled vesicles and fractures.

The results here further illuminate the aqueous history of the Hartford Basin and have implications for exploration of Mars. We propose that this site is an analog for volcanically-resurfaced open basin lakes on Mars if water were present when the lavas first erupted, and similar mineralogies might be expected there. Each measurement acquired here was essential to unraveling the aqueous history of this sample, and

spectroscopy allows us to understand the context of each of the other measurements and scale the results and interpretations to the hand sample and outcrop scales.

ACKNOWLEDGMENTS

We would like to thank Anthony Philpotts for showing us potential field sites and Kevin Cannon, Tim Goudge, Mary Peterson, and Sandra Wiseman for field assistance. We also thank David Bannon and Kwok Wong at Headwall Photonics, Inc. for assistance with laboratory hyperspectral imaging measurements; Joe Boesenberg, Bill Collins, and Terik Daly for help with thin and thick section preparation and electron microprobe analyses; David Murray and Joe Orchardo for help with bulk chemistry analyses; Alex Pontefract and Gordon Osinski for setting up μXRD analyses; Phil Christensen for his effort in building Arizona State University's MicroSpectroscopy Lab in which the microscopic thermal emission measurements were made and Rebecca Smith for help with those measurements; and Reid Cooper for helpful discussions. Finally, we thank Target in Meriden, CT, for allowing us to work on their property and the city of Meriden for permitting sampling. This work was supported by NASA and the Mars Data Analysis Program grant NNX13AK72G. E.A.C. thanks CFI, MRIF, and CSA for supporting the establishment of the University of Winnipeg Planetary Spectrophotometer Facility, as well as these agencies and NSERC and University of Winnipeg for funding to support this study.

REFERENCES

Adams J. B. (1975) Interpretation of visible and near-infrared diffuse reflectance spectra of pyroxenes and other rock-forming minerals. *Infrared Raman Spectrosc. Lunar Terr. Miner.*, 91–116.

Adams J. B. (1974) Visible and Near-Infrared Diffuse Reflectance Spectra of Pyroxenes as Applied to Remote Sensing of Solid Objects in the Solar System. *J. Geophys. Res.* **79**, 4829–4836.

Adams J. B., Smith M. O. and Johnson P. E. (1986) Spectral mixture modeling: A new analysis of rock and soil types at the Viking Lander 1 Site. *J. Geophys. Res. Solid Earth* **91**, 8098–8112.

Alt J. C., France-Lanord C., Floyd P. A., Castillo P. and Galy A. (1992) Low-Temperature Hydrothermal Alteration of Jurassic Ocean Crust, Site 801. *Proc. Ocean Drill. Program Sci. Results* **129**, 415–427.

Alt J. C., Honnorez J., Laverne C. and Emmermann R. (1986) Hydrothermal alteration of a 1 km section through the upper oceanic crust, Deep Sea Drilling Project Hole 504B: Mineralogy, chemistry and evolution of seawater-basalt interactions. *J. Geophys. Res. Solid Earth* **91**, 10309–10335.

Alt J. C., Laverne C., Coggon R. M., Teagle D. A. H., Banerjee N. R., Morgan S., Smith-Duque C. E., Harris M. and Galli L. (2010) Subsurface structure of a submarine hydrothermal system in ocean crust formed at the East Pacific Rise, ODP/IODP Site 1256. *Geochem. Geophys. Geosystems* **11**, Q10010.

Andrieux P. and Petit S. (2010) Hydrothermal synthesis of dioctahedral smectites: The Al–Fe3+ chemical series. *Appl. Clay Sci.* **48**, 5–17.

Bell P. M., Mao H. K. and Weeks R. A. (1976) Optical spectra and electron paramagnetic resonance of lunar and synthetic glasses - A study of the effects of controlled atmosphere, composition, and temperature. In Lunar and Planetary Science Conference Proceedings. 2543–2559.

Bibring J.-P., Langevin Y., Mustard J. F., Poulet F., Arvidson R., Gendrin A., Gondet B., Mangold N., Pinet P., Forget F., and the OMEGA team (2006) Global Mineralogical and Aqueous Mars History Derived from OMEGA/Mars Express Data. *Science* **312**, 400 –404.

Bird D. K., Schiffman P., Elders W. A., Williams A. E. and McDowell S. D. (1984) Calc-silicate mineralization in active geothermal systems. *Econ. Geol.* **79**, 671–695.

Bish D. L. and Howard S. A. (1988) Quantitative phase analysis using the Rietveld method. *J. Appl. Crystallogr.* **21**, 86–91.

Bishop J. L., Englert P. A. J., Patel S., Tirsch D., Roy A. J., Koeberl C., Böttger U., Hanke F. and Jaumann R. (2014) Mineralogical analyses of surface sediments in the Antarctic Dry Valleys: coordinated analyses of Raman spectra, reflectance spectra and elemental abundances. *Philos. Trans. R. Soc. Math. Phys. Eng. Sci.* **372**, 20140198.

Bishop J. L., Franz H. B., Goetz W., Blake D. F., Freissinet C., Steininger H., Goesmann F., Brinckerhoff W. B., Getty S., Pinnick V. T., Mahaffy P. R. and Dyar M. D. (2013) Coordinated analyses of Antarctic sediments as Mars analog materials using reflectance spectroscopy and current flight-like instruments for CheMin, SAM and MOMA. *Icarus* **224**, 309–325.

Bishop J. L., Lane M. D., Dyar M. D. and Brown A. J. (2008) Reflectance and emission

spectroscopy study of four groups of phyllosilicates: smectites, kaolinite-serpentines, chlorites and micas. *Clay Miner.* **43**, 35 –54.

Bishop J. L., Schiffman P. and Southard R. (2002) Geochemical and mineralogical analyses of palagonitic tuffs and altered rinds of pillow basalts in Iceland and applications to Mars. *Geol. Soc. Lond. Spec. Publ.* **202**, 371 –392.

Blake R. L., Zoltai T., Hessevick R. E. and Finger L. W. (1966) Refinement of hematite crystal structure. *Am. Mineral.* **51**, 123–129.

Burns R. G. (1993a) *Mineralogical applications of crystal field theory*., Cambridge University Press, Cambridge.

Burns R. G. (1993b) Origin of electronic spectra of minerals in the visible to near-infrared region. *Remote Geochem. Anal. Elem. Mineral. Compos.* **4**, 3–29.

Cameron M., Sueno S., Prewitt C. T. and Papike J. J. (1973) High-Temperature Crystal Chemistry of Acmite, Diopside, Hedenbergite, Jadeite, Spodumine, and Ureyite. *Am. Mineral.* **58**, 594–618.

Chavez Jr P. S. (1996) Image-Based Atmospheric Corrections-Revisited and Improved. *Photogramm. Eng. Remote Sens.* **62**, 1025–1036.

Cheek L. C. and Pieters C. M. (2014) Reflectance spectroscopy of plagioclase-dominated mineral mixtures: Implications for characterizing lunar anorthosites remotely. *Am Miner.* **99**, 1871-1892.

Clark R. N., King T. V. V., Klejwa M., Swayze G. A. and Vergo N. (1990) High Spectral Resolution Reflectance Spectroscopy of Minerals. *J. Geophys. Res.* **95**, 12653–12680.

Clark R. N. and Roush T. L. (1984) Reflectance Spectroscopy: Quantitative Analysis

Techniques for Remote Sensing Applications. *J. Geophys. Res.* **89**, 6329–6340.

Clark R. N., Swayze G. A., Livo K. E., Kokaly R. F., King T. V., Dalton J. B., Vance J. S., Rockwell B. W., Hoefen T. and McDougal R. R. (2002) Surface reflectance calibration of terrestrial imaging spectroscopy data: a tutorial using AVIRIS. In *Proceedings of the 10th Airborne Earth Science Workshop* pp. 02–1.

Clark R. N., Swayze G. A., Livo K. E., Kokaly R. F., Sutley S. J., Dalton J. B., McDougal R. R. and Gent C. A. (2003) Imaging spectroscopy: Earth and planetary remote sensing with the USGS Tetracorder and expert systems. *J. Geophys. Res. Planets* **108**, 5131.

Cloutis E. A. and Gaffey M. J. (1991) Pyroxene Spectroscopy Revisited: Spectral-Compositional Correlations and Relationship to Geothermometry. *J. Geophys. Res.* **96**, 22,809–22,826.

Cloutis E. A., Gaffey M. J., Smith D. G. W. and Lambert R. S. J. (1990) Reflectance spectra of mafic silicate-opaque assemblages with applications to meteorite spectra. *Icarus* **84**, 315–333.

Cloutis E. A., Hiroi T., Gaffey M. J., Alexander C. M. O. and Mann P. (2011) Spectral reflectance properties of carbonaceous chondrites: 1. CI chondrites. *Icarus* **212**, 180–209.

Crowley J. K., Williams D. E., Hammarstrom J. M., Piatak N., Chou I.-M. and Mars J. C. (2003) Spectral reflectance properties (0.4–2.5 μm) of secondary Fe-oxide, Fe-hydroxide, and Fe-sulphate-hydrate minerals associated with sulphide-bearing mine wastes. *Geochem. Explor. Environ. Anal.* **3**, 219–228.

Cummings W. (1987) Mineralization at the Fanwood & Summit Quarries, New Jersey.

Rocks Miner. **62**, 150–159.

Cummins L. E., Arthur J. D. and Ragland P. C. (1992) Classification and tectonic implications for early Mesozoic magma types of the Circum-Atlantic. *Geol. Soc. Am. Spec. Pap.* **268**, 119–136.

Von Damm K. L., Edmond J. M., Grant B., Measures C. I., Walden B. and Weiss R. F. (1985) Chemistry of submarine hydrothermal solutions at 21 °N, East Pacific Rise. *Geochim. Cosmochim. Acta* **49**, 2197–2220.

Dilles J. H. and Einaudi M. T. (1992) Wall-rock alteration and hydrothermal flow paths about the Ann-Mason porphyry copper deposit, Nevada; a 6-km vertical reconstruction. *Econ. Geol.* **87**, 1963–2001.

Edwards C. S. and Christensen P. R. (2013) Microscopic emission and reflectance thermal infrared spectroscopy: instrumentation for quantitative in situ mineralogy of complex planetary surfaces. *Appl. Opt.* **52**, 2200.

Eggleton R. A., Foudoulis C. and Varkevisser D. (1987) Weathering of basalt; changes in rock chemistry and mineralogy. *Clays Clay Miner.* **35**, 161–169.

De Faria D. L. A. and Lopes F. N. (2007) Heated goethite and natural hematite: Can Raman spectroscopy be used to differentiate them? *Vib. Spectrosc.* **45**, 117–121.

De Faria D. L. A., Venâncio Silva S. and de Oliveira M. T. (1997) Raman microspectroscopy of some iron oxides and oxyhydroxides. *J. Raman Spectrosc.* **28**, 873–878.

Fischer E. M. and Pieters C. M. (1993) The Continuum Slope of Mars: Bidirectional Reflectance Investigations and Applications to Olympus Mons. *Icarus* **102**, 185–202.

Flemming R. L. (2007) Micro X-ray diffraction (μXRD): a versatile technique for characterization of Earth and planetary materials. *Can. J. Earth Sci.* **44**, 1333–1346.

Garrett D. E. (1998) *Borates: Handbook of Deposits, Processing, Properties, and Use*., Academic Press.

Gillis K. M., Thompson G. and Kelley D. S. (1993) A view of the lower crustal component of hydrothermal systems at the Mid-Atlantic Ridge. *J. Geophys. Res. Solid Earth* **98**, 19597–19619.

Van Gorp B., Mouroulis P., Blaney D., Green R. O., Ehlmann B. L. and Rodriguez J. I. (2014) Ultra-compact imaging spectrometer for remote, in situ, and microscopic planetary mineralogy. *J. Appl. Remote Sens.* **8**, 084988–084988.

Goudge T. A., Head J. W., Mustard J. F. and Fassett C. I. (2012) An analysis of open-basin lake deposits on Mars: Evidence for the nature of associated lacustrine deposits and post-lacustrine modification processes. *Icarus* **219**, 211–229.

Griffith W. P. (1970) Raman studies on rock-forming minerals. Part II. Minerals containing MO3, MO4, and MO6 groups. *J. Chem. Soc. Inorg. Phys. Theor.*, 286.

Griffith W. P. (1969) Raman studies on rock-forming minerals. Part I. Orthosilicates and cyclosilicates. *J. Chem. Soc. Inorg. Phys. Theor.*, 1372.

Hanshaw P. (1968) Bedrock Geologic Map of the Meriden Quadrangle, New Haven, Hartford, and Middlesex Counties, Connecticut. *US Geol. Surv. Geol. Quadrang. Maps U. S.*, 4 pp.

Harlow G. E. (1982) The anorthoclase structures; the effects of temperature and composition. *Am. Mineral.* **67**, 975–996.

Hausrath E. M., Navarre-Sitchler A. K., Sak P. B., Steefel C. I. and Brantley S. L. (2008) Basalt weathering rates on Earth and the duration of liquid water on the plains of Gusev Crater, Mars. *Geology* **36**, 67–70.

Heald M. T. (1956) Cementation of Triassic Arkoses in Connecticut and Massachusetts. *Geol. Soc. Am. Bull.* **67**, 1133–1154.

Hedenquist J. W. and Lowenstern J. B. (1994) The role of magmas in the formation of hydrothermal ore deposits. *Nature* **370**, 519–527.

Holm N. G. (1992) Why are Hydrothermal Systems Proposed as Plausible Environments for the Origin of Life? In *Marine Hydrothermal Systems and the Origin of Life* (ed. D. N. G. Holm). Springer Netherlands. pp. 5–14.

Horgan B. and Bell III J. F. (2012) Widespread weathered glass on the surface of Mars. *Geology* **40**, 391–394.

Horgan B. H. N., Cloutis E. A., Mann P. and Bell III J. F. (2014) Near-infrared spectra of ferrous mineral mixtures and methods for their identification in planetary surface spectra. *Icarus* **234**, 132–154.

Hubert J. F., Feshbach-Meriney P. E. and Smith M. A. (1992) The Triassic-Jurassic Hartford Rift Basin, Connecticut and Massachusetts: Evolution, Sandstone Diagenesis, and Hydrocarbon History (1). *AAPG Bull.* **76**, 1710–1734.

Hunt G. R. and Ashley R. P. (1979) Spectra of altered rocks in the visible and near infrared. *Econ. Geol.* **74**, 1613–1629.

Hunt G. R. and Evarts R. C. (1981) The use of near-infrared spectroscopy to determine the degree of serpentinization of ultramafic rocks. *GEOPHYSICS* **46**, 316–321.

Hunt G. R. and Salisbury J. W. (1971) Visible and near infrared spectra of minerals and

rocks. II. Carbonates. *Mod. Geol.* **2**, 23–30.

Van de Kamp P. C. and Leake B. E. (1996) Petrology, geochemistry, and Na metasomatism of Triassic-Jurassic non-marine clastic sediments in the Newark, Hartford, and Deerfield rift basins, northeastern USA. *Chem. Geol.* **133**, 89–124.

Keith T. E. C. and Staples L. W. (1985) Zeolites in Eocene basaltic pillow lavas of the Siletz River volcanics, central Coast Range, Oregon. *Clays Clay Miner.* **33**, 135–144.

Kiss G., Molnár F. and Zaccarini F. (2012) Fluid inclusion studies in datolite of low grade metamorphic origin from a Jurassic pillow basalt series in northeastern Hungary. *Cent. Eur. J. Geosci.* **4**, 261–274.

Kistler R. B. and Helvaci C. (1994) Boron and borates. *Ind. Miner. Rocks* **6**, 171–186.

Kolleeny J. (1996) Contact Metamorphism of Calcrete in New Haven Arkose (TR/J): Role of Infiltration Metasomatism and Hydrothermal Boiling. In Long Island Geologists Conference on "Geology of Long Island and Metropolitan New York." State University of New York at Stony Brook. pp. 73–82.

Kruse F. A., Bedell R. L., Taranik J. V., Peppin W. A., Weatherbee O. and Calvin W. M. (2012) Mapping alteration minerals at prospect, outcrop and drill core scales using imaging spectrometry. *Int. J. Remote Sens.* **33**, 1780–1798.

Kurz T. H., Dewit J., Buckley S. J., Thurmond J. B., Hunt D. W. and Swennen R. (2012) Hyperspectral image analysis of different carbonate lithologies (limestone, karst and hydrothermal dolomites): the Pozalagua Quarry case study (Cantabria, North-west Spain). *Sedimentology* **59**, 623–645.

Laetsch T. and Downs R. T. (2006) Software for identification and refinement of cell

parameters from powder diffraction data of minerals using the RRUFF Project and American Mineralogist Crystal Structure Databases. In *19th General Meeting of the International Mineralogical Association, Kobe, Japan* pp. 23–28.

Laskowich C. and Puffer J. H. (1990) Volcanic diapirs of the Orange Mountain Basalt, New Jersey. *NJ Acad Sci Bull* **35**, 1–9.

Launeau P., Girardeau J., Sotin C. and Tubia J. M. (2004) Comparison between field measurements and airborne visible and infrared mapping spectrometry (AVIRIS and HyMap) of the Ronda peridotite massif (south-west Spain). *Int. J. Remote Sens.* **25**, 2773–2792.

Laverne C. (1987) Unusual occurrences of aegirine-augite, fassaite and melanite in oceanic basalts (DSDP Hole 504B). *Lithos* **20**, 135–151.

Laverne C., Vanko D. A., Tartarotti P. and Alt J. C. (1995) 15. CHEMISTRY AND GEOTHERMOMETRY OF SECONDARY MINERALS FROM THE DEEP SHEETED DIKE COMPLEX, HOLE 504B1. In *Proceedings of the Ocean Drilling Program, Scientific Results* p. 140.

Leeman W. P. and Sisson V. B. (1996) Geochemistry of boron and its implications for crustal and mantle processes. *Rev. Mineral. Geochem.* **33**, 645–707.

Lowell R. P., Rona P. A. and Von Herzen R. P. (1995) Seafloor hydrothermal systems. *J. Geophys. Res. Solid Earth* **100**, 327–352.

Manceau A., Chateigner D. and Gates W. P. (1998) Polarized EXAFS, distance-valence least-squares modeling (DVLS), and quantitative texture analysis approaches to the structural refinement of Garfield nontronite. *Phys. Chem. Miner.* **25**, 347–365.

Manning C. E. and Bird D. K. (1986) Hydrothermal clinopyroxenes of the Skaergaard

intrusion. *Contrib. Mineral. Petrol.* **92**, 437–447.

Markgraf S. A. and Reeder R. J. (1985) High-temperature structure refinements of calcite and magnesite. *Am. Mineral.* **70**, 590–600.

Marks N., Schiffman P., Zierenberg R. A., Franzson H. and Fridleifsson G. Ó. (2010) Hydrothermal alteration in the Reykjanes geothermal system: Insights from Iceland deep drilling program well RN-17. *J. Volcanol. Geotherm. Res.* **189**, 172–190.

Marshall R. R. (1961) Devitrification of Natural Glass. *Geol. Soc. Am. Bull.* **72**, 1493–1520.

Martin W., Baross J., Kelley D. and Russell M. J. (2008) Hydrothermal vents and the origin of life. *Nat. Rev. Microbiol.* **6**, 805–814.

McHone J. G. (1996) Broad-terrane Jurassic flood basalts across northeastern North America. *Geology* **24**, 319–322.

McHone J. G. and Butler J. R. (1984) Mesozoic igneous provinces of New England and the opening of the North Atlantic Ocean. *Geol. Soc. Am. Bull.* **95**, 757–765.

McKeown D. A. (2005) Raman spectroscopy and vibrational analyses of albite: From 25 °C through the melting temperature. *Am. Mineral.* **90**, 1506–1517.

Merino E., Girard J.-P., May M. T. and Ranganathan V. (1997) Diagenetic mineralogy, geochemistry, and dynamics of Mesozoic arkoses, Hartford rift basin, Connecticut, U.S.A. *J. Sediment. Res.* **67**, 212–224.

Morris R. V., Jr H. V. L., Lawson C. A., Jr E. K. G., Nace G. A. and Stewart C. (1985) Spectral and Other Physicochemical Properties of Submicron Powders of Hematite (α-Fe2O3), Maghemite (γ-Fe2O3), Magnetite (Fe3O4), Goethite (α-

FeOOH), and Lepidocrocite (γ-FeOOH). *J. Geophys. Res.* **90**, PP. 3126–3144.

Murray R., Miller D. J. and Kryc K. (2000) Analysis of major and trace elements in rocks, sediments, and interstitial waters by inductively coupled plasma–atomic emission spectrometry (ICP-AES). *ODP Tech Note* **29**, 1–27.

Nesbitt H. W. and Wilson R. E. (1992) Recent chemical weathering of basalts. *Am. J. Sci.* **292**, 740 –777.

Nisbet E. G. and Sleep N. H. (2001) The habitat and nature of early life. *Nature* **409**, 1083–1091.

Pelkey S. M., Mustard J. F., Murchie S., Clancy R. T., Wolff M., Smith M., Milliken R., Bibring J.-P., Gendrin A., Poulet F., Langevin Y. and Gondet B. (2007) CRISM multispectral summary products: Parameterizing mineral diversity on Mars from reflectance. *J. Geophys. Res.* **112**, 18 PP.

Philpotts A. R. (1992) A model for emplacement of magma in the Mesozoic Hartford basin. *Geol. Soc. Am. Spec. Pap.* **268**, 137–148.

Philpotts A. R. (1978) Rift-Associated Igneous Activity in Eastern North America. In *Petrology and Geochemistry of Continental Rifts* (eds. E.-R. Neumann and I. B. Ramberg). NATO Advanced Study Institutes Series. Springer Netherlands. pp. 133–154.

Philpotts A. R. and Martello A. (1986) Diabase feeder dikes for the Mesozoic basalts in southern New England. *Am. J. Sci.* **286**, 105–126.

Philpotts A. R. and Reichenbach I. (1985) Differentiation of Mesozoic basalts of the Hartford basin, Connecticut. *Geol. Soc. Am. Bull.* **96**, 1131–1139.

Pratt L. M., Shaw C. A. and Burruss R. C. (1988) Thermal histories of the Hartford and

Newark basins inferred from maturation indices of organic matter. *Stud. Early Mesoz. Basins East. U. S.*, 58–62.

Puffer J. H. (1992) Eastern North American flood basalts in the context of the incipient breakup of Pangea. *Geol. Soc. Am. Spec. Pap.* **268**, 95–118.

Puffer J. H. and Benimoff A. I. (1997) Fractionation, Hydrothermal Alteration, and Wall-Rock Contamination of an Early Jurassic Diabase Intrusion: Laurel Hill, New Jersey. *J. Geol.* **105**, 99–110.

Puffer J. H., Hurtubise D. O., Geiger F. J. and Lechler P. (1981) Chemical Composition and Stratigraphic Correlation of the Mesozoic Basalt units of the Newark Basin, New Jersey, and the Hartford Basin, Connecticut. *Geol. Soc. Am. Bull.* **92**, 515–553.

Puffer J. H. and Laskowich C. (2012) Volcanic diapirs in the Orange Mountain flood basalt: New Jersey, USA. *J. Volcanol. Geotherm. Res.* **237–238**, 1–9.

Puffer J. H. and Student J. J. (1992) Volcanic structures, eruptive style, and posteruptive deformation and chemical alteration of the Watchung flood basalts, New Jersey. *Geol. Soc. Am. Spec. Pap.* **268**, 261–278.

Ramsey M. S. and Christensen P. R. (1998) Mineral abundance determination: Quantitative deconvolution of thermal emission spectra. *J. Geophys. Res.* **103**, PP. 577–596.

Redhammer G. J., Amthauer G., Roth G., Tippelt G. and Lottermoser W. (2006) Single-crystal X-ray diffraction and temperature dependent 57Fe Mössbauer spectroscopy on the hedenbergite-aegirine (Ca,Na)(Fe2+,Fe3+)Si2O6 solid solution. *Am. Mineral.* **91**, 1271–1292.

Rietveld H. M. (1969) A profile refinement method for nuclear and magnetic structures. *J. Appl. Crystallogr.* **2**, 65–71.

Roach L. H., Mustard J., Gendrin A., Fernández-Remolar D., Amils R. and Amaral-Zettler L. (2006) Finding mineralogically interesting targets for exploration from spatially coarse visible and near IR spectra. *Earth Planet. Sci. Lett.* **252**, 201–214.

Robert C. (2001) Hydrothermal alteration processes of the Tertiary lavas of Northern Ireland. *Mineral. Mag.* **65**, 543–557.

Robinson Jr G. R. and Woodruff L. G. (1988) Characteristics of base-metal and barite vein deposits associated with rift basins, with examples from some early Mesozoic basins of eastern North America. *US Geol Surv. Bull* **1776**, 377–390.

Rogers A. D. and Aharonson O. (2008) Mineralogical composition of sands in Meridiani Planum determined from Mars Exploration Rover data and comparison to orbital measurements. *J. Geophys. Res. Planets* **113**, E06S14.

Sabol D. E., Adams J. B. and Smith M. O. (1992) Quantitative subpixel spectral detection of targets in multispectral images. *J. Geophys. Res. Planets* **97**, 2659–2672.

Salvatore M. R., Mustard J. F., Head J. W., Cooper R. F., Marchant D. R. and Wyatt M. B. (2013) Development of alteration rinds by oxidative weathering processes in Beacon Valley, Antarctica, and implications for Mars. *Geochim. Cosmochim. Acta* **115**, 137–161.

Scheinost A. C., Chavernas A., Barron V. and Torrent J. (1998) Use and limitations of second-derivative diffuse reflectance spectroscopy in the visible to near-infrared range to identify and quantify Fe oxide minerals in soils. *Clays Clay Miner.* **46**, 528 –536.

Seidemann D. E. (1988) The hydrothermal addition of excess 40Ar at the lava flows from the early Jurassic in the Hartford Basin (Northeastern U.S.A.): Implications for the time scale. *Chem. Geol. Isot. Geosci. Sect.* **72**, 37–45.

Seidemann D. E., Masterson W. D., Dowling M. P. and Turekian K. K. (1984) K-Ar dates and 40Ar/39Ar age spectra for Mesozoic basalt flows of the Hartford Basin, Connecticut, and the Newark Basin, New Jersey. *Geol. Soc. Am. Bull.* **95**, 594–598.

Seyfried Jr. W. E. and Mottl M. J. (1982) Hydrothermal alteration of basalt by seawater under seawater-dominated conditions. *Geochim. Cosmochim. Acta* **46**, 985–1002.

Seyfried W. E., Berndt M. E. and Seewald J. S. (1988) Hydrothermal alteration processes at mid-ocean ridges; constraints from diabase alteration experiments, hot spring fluids and composition of the oceanic crust. *Can. Mineral.* **26**, 787–804.

Seyfried W. E. Jr. (1987) Experimental and Theoretical Constraints on Hydrothermal Alteration Processes at Mid-Ocean Ridges. *Annu. Rev. Earth Planet. Sci.* **15**, 317.

Shock E. L. (1997) High-temperature life without photosynthesis as a model for Mars. *J. Geophys. Res. Planets* **102**, 23687–23694.

Speer J. A. and Gibbs G. V. (1976) The crystal structure of synthetic titanite, CaTiOSiO 4 , and the domain textures of natural titanites. *Am. Mineral.* **61**, 238–247.

Steinen R. P., Gray N. H. and Mooney J. (1987) A Mesozoic carbonate hot-spring deposit in the Hartford Basin of Connecticut. *J. Sediment. Res.* **57**, 319–326.

Swayze G. A., Clark R. N., Goetz A. F. H., Livo K. E., Breit G. N., Kruse F. A., Sutley S. J., Snee L. W., Lowers H. A., Post J. L., Stoffregen R. E. and Ashley R. P. (2014) Mapping Advanced Argillic Alteration at Cuprite, Nevada, Using Imaging

Spectroscopy. *Econ. Geol.* **109**, 1179–1221.

Swayze G. A., Higgins C. T., Clinkenbeard J. P., Kokaly R. F., Clark R. N., Meeker G. P. and Sutley S. J. (2004) Preliminary Report on Using Imaging Spectroscopy to Map Ultramafic Rocks, Serpentinites, and Tremolite-Actinolite-Bearing Rocks in California. *US Geol. Surv. Open-File Rep. 2004-1304*, 9 pp.

Thomas M. and Walter M. R. (2002) Application of Hyperspectral Infrared Analysis of Hydrothermal Alteration on Earth and Mars. *Astrobiology* **2**, 335–351.

Vanko D. A., Laverne C., Tartarotti P. and Alt J. C. (1996) Chemistry and origin of secondary minerals from the deep sheeted dikes cored during Leg 148 (Hole 504B). In *Proceedings-Ocean Drilling Program Scientific Results* National Science Foundation. pp. 71–86.

Viviano-Beck C. E., Seelos F. P., Murchie S. L., Kahn E. G., Seelos K. D., Taylor H. W., Taylor K., Ehlmann B. L., Wisemann S. M., Mustard J. F. and Morgan M. F. (2014) Revised CRISM spectral parameters and summary products based on the currently detected mineral diversity on Mars. *J. Geophys. Res. Planets* **119**, 2014JE004627.

White W. B. (1974) The carbonate minerals. *Infrared Spectra Miner.* **4**, 227–284.

Whitney D. L. and Evans B. W. (2010) Abbreviations for names of rock-forming minerals. *Am. Mineral.* **95**, 185–187.

Wolela A. M. and Gierlowski-Kordesch E. H. (2007) Diagenetic history of fluvial and lacustrine sandstones of the Hartford Basin (Triassic–Jurassic), Newark Supergroup, USA. *Sediment. Geol.* **197**, 99–126.

Yang K., Whitbourn L., Mason P. and Huntington J. (2013) Mapping the Chemical

Composition of Nickel Laterites with Reflectance Spectroscopy at Koniambo, New Caledonia. *Econ. Geol.* **108**, 1285–1299.

Yokoyama E., Nédélec A., Baratoux D., Trindade R. I. F., Fabre S. and Berger G. (2015) Hydrothermal alteration in basalts from vargeão impact structure, south brazil, and implications for recognition of impact-induced hydrothermalism on mars. *Icarus*.

Young R. A. (1995) The rietveld method. *Cryst. Res. Technol.* **30**.

Zanazzi P. F., Montagnoli M., Nazzareni S. and Comodi P. (2007) Structural effects of pressure on monoclinic chlorite: A single-crystal study. *Am. Mineral.* **92**, 655–661.

Table 1. Measurements completed, spatial resolutions, and goals of each measurement.

Measurement	Spatial resolution or field of view (FOV)	Goals
Point spectroscopy	Varies with distance from sample; 25 degree FOV	Quick characterization of mineralogy and spectral signatures of single points; also provides ground-truth points in the field
Hyperspectral imaging	0.382 mrad VNIR and 1.2 mrad SWIR (up to 44 µm/pixel VNIR and 133 µm/pixel SWIR)	Determine mineralogy and spectral signatures with high spatial resolution to assess changes with different degrees of water-rock interactions and variations across samples and outcrops
Micro thermal infrared emission spectroscopy	100 µm	Assess mineralogy in mid-IR at high spatial resolution; help distinguish phases that are not spectrally unique in the shortwave infrared
Micro Raman spectroscopy	80 µm	Determine mineralogy; measurements are complementary with infrared spectroscopy
Electron microprobe	Point beam for silicates; 20 µm beam for glass and calcite; 13 µm/pixel for elemental mapping	Assess mobility of cations during aqueous alteration in context and directly connect with imaging spectroscopy
Major element chemistry analyses	Bulk measurement	Assess average chemistry and mobility of cations across a broader set of samples
µX-ray diffraction	300 µm	Determine mineralogy in context and connect directly with spectral signature; assess qualitative changes in mineralogy with alteration
Powder x-ray diffraction	Bulk measurement	Identify crystalline phases in average sample

Table 2. Formulas for calculation of spectral and mineral or phase indicator parameters and their interpretations.

Parameter	Formula[a,b]	Interpretation
	Field imaging spectral parameters	
Red slope	$\frac{R0.690 + R0.700 + R0.710}{R0.445 + R0.450 + R0.455}$	More oxidized surface (e.g., Hunt and Ashley, 1979)
Green peak	$\frac{R0.575 + R0.580 + R0.585 + R0.590}{R0.465 + R0.470 + R0.695 + R0.700}$	Enhanced by presence of Fe^{3+}/Fe^{2+} charge transfer (Adams, 1975; Cloutis and Gaffey, 1991; Burns, 1993a; Burns, 1993b)
	Laboratory imaging spectral parameters	
Red slope	$\frac{\sum R(0.758\ to\ 0.769)}{\sum R(0.483\ to\ 0.494)}$	See above
Green peak	$\frac{2 * \sum R(0.558\ to\ 0.569)}{1.36 * \sum R(0.465\ to\ 0.476) + 0.64 * \sum R(0.747\ to\ 0.758)}$	See above
Positive SWIR slope	$\frac{R1.794 + R1.806 + R1.818}{R1.154 + R1.167 + R1.179}$	Likely Fe^{2+}, possibly in type A pyroxenes (Cloutis and Gaffey, 1991)
BD1390	$1 - \frac{2 * (R1.384 + R1.396)}{1.62 * (R1.345 + R1.360) + 0.38 * (R1.504 + R1.516)}$	First overtone of OH stretch; Mg_3-OH (e.g., Bishop et al., 2008)
BD1410	$1 - \frac{2 * (R1.408 + R1.420)}{0.72 * (R1.345 + R1.360) + 1.28 * (R1.504 + R1.516)}$	First overtone of OH stretch; Al_2-OH (e.g., Bishop et al., 2008)
BD1480	$1 - \frac{2 * (R1.468 + R1.481 + R1.492)}{0.88 * (R1.336 + R1.348 + R1.360) + 1.12 * (R1.577 + R1.589 + R1.601)}$	First OH stretching overtone in minerals such as prehnite (1.48 µm) and datolite (1.47 µm) (Clark et al., 1990)
BD1900	$1 - \frac{2 * (R1.915 + R1.927 + R1.939)}{1.34 * (R1.843 + R1.854 + R1.867) + 0.66 * (R2.036 + R2.047 + R2.060)}$	H-O-H combination bend and stretch (e.g., Clark et al., 1990)
BD2300	$1 - \frac{4/3 * (R2.289 + R2.301 + R2.313)}{R2.205 + R2.217 + R2.386 + R2.398}$	Fe/Mg-OH combination (e.g., Clark et al., 1990; Bishop et al., 2008; Andrieux and Petit, 2010)
BD2340	$1 - \frac{2 * (R2.337 + R2.349)}{0.48 * (R2.205 + R2.217) + 1.52 * (R2.386 + R2.398)}$	Mg_3-OH combination band or third overtone of the C-O asymmetric stretching mode (e.g., Hunt and Salisbury, 1971; Bishop et al., 2008)
BD2410	$1 - \frac{2 * (R2.3987 + R2.410)}{(2.361 + R2.374 + R2.434 + R2.446}$	B-OH combination band in datolite (Clark et al., 1990)
D2500	$1 - \frac{R2.482 + R2.494}{R2.410 + R2.422}$	C-O combination band in carbonates (Hunt and Salisbury, 1971)
	Laboratory imaging mineral or phase indicator parameters	
Calcite	BD2340>0 and D2500>0; Displayed value: BD2340	
Fe/Mg clay	(BD1390 or BD1410)>0, BD1900>0, BD2300>0, and D2500<0.1; Displayed value: BD2300	
Datolite	BD1480>0 and BD2410>0; Displayed value: BD2410	

[a]R# = Reflectance at wavelength # µm

[b]ΣR(X to Y) = Sum of all bands sampled between and including X and Y µm

Table 3. Pure phase endmembers for linear unmixing to map minerals and glass from elemental mapping data. Values are raw signal with a maximum of 255, and are related qualitatively to abundances.

Endmember	# pixels averaged	BSE	Al	Ca	Fe	K	Mg	Mn	Na	Si	Ti
Glass	49	198.3	9.0	42.2	34.2	44.8	39.9	22.3	33.1	138.7	18.7
Interior albite	64	117.9	90.7	-1.9[a]	0.3	7.0	0.7	3.4	108.1	177.9	12.0
Exterior albite	64	121.3	70.4	-2.2 [a]	0.7	46.5	1.0	14.5	60.3	173.2	10.1
Calcite	225	174.4	0.6	173.1	0.9	51.6	3.7	22.7	0.3	10.5	12.9
Iron oxide	25	255	1.3	0.7	185.0	59.6	0.7	15.8	-1.3 [a]	12.0	25.5
Titanite	25	254.3	20.3	100.0	9.8	42.1	0.7	14.4	5.4	86.4	161.0
Copper tape	225	255	0.1	-0.5 [a]	0.8	10.3	1.4	18.1	0.6	0.8	9.1
Dark	n/a	0	0	0	0	0	0	0	0	0	0

[a]Elemental mapping tiles for Al, Ca, K, Mn, and Na were color-balanced so that values in overlapping regions were the same across tiles to correct for minor differences. This process occasionally resulted in negative values.

Table 4. Abundances (rounded to the nearest 5%) of phases from linear unmixing of microscopic thermal infrared emission spectroscopy data. Phases modeled with abundances less than 10% have been omitted, and abundances of amorphous/mineral phases are normalized to subtract the blackbody.

Phase	Class 1	Class 2	Class 3	Class 4	Class 5	Class 6
Amorphous/sheet silicate	45	35	55	20	45	25
Feldspar	30	25	15		15	30
Pyroxene		15				
Carbonate	10	10	10	60		35
Oxide					30	
Olivine			15			
Al_2SiO_5						
Blackbody	-65	-32	-75	-75	-245	-95
RMS error	0.581	0.740	0.864	1.188	2.027	1.333

Table 5. Results of the microprobe analyses of glassy matrix ordered approximately from exterior (top) to interior (bottom) of the sample.

Al_2O_3	CaO	FeO	MgO	MnO	Na_2O	SiO_2	TiO_2	Total[a]
1.718	9.544	20.945	5.781	0.465	6.557	51.464	1.346	97.819
1.681	10.251	20.099	6.394	0.695	5.661	51.428	1.108	97.317
1.014	11.114	19.520	5.870	0.767	5.099	51.483	0.809	95.675
1.219	9.153	20.818	5.462	0.563	6.668	51.274	1.318	96.474
1.315	10.031	20.412	5.774	0.559	6.726	51.623	1.411	97.850
1.055	9.945	21.122	5.331	0.554	6.592	51.520	1.330	97.449
1.332	10.728	19.540	6.210	0.705	5.668	51.261	1.066	96.510
2.008	9.213	20.659	5.869	0.461	6.433	50.986	1.485	97.115
1.040	11.677	20.024	6.049	0.723	5.361	51.130	0.928	96.931
1.610	12.197	18.784	6.232	0.740	5.135	51.515	0.789	97.002
1.616	10.993	19.686	6.296	0.637	5.324	51.300	1.099	96.952
0.927	10.277	20.772	5.512	0.640	6.380	51.780	1.206	97.494
0.881	12.531	19.649	6.275	0.792	4.875	51.931	0.742	97.676
1.102	10.136	21.249	5.469	0.714	6.389	51.560	1.253	97.871
1.799[b]	11.551[b]	19.048[b]	5.687[b]	0.652[b]	5.771[b]	51.560[b]	1.395[b]	97.465[b]
1.083	9.643	20.925	5.379	0.545	6.582	51.307	1.429	96.892
1.050	8.271	21.665	4.796	0.395	7.489	51.427	1.745	96.837
3.730[b]	9.311[b]	17.061[b]	5.040[b]	0.498[b]	6.784[b]	53.891[b]	1.600[b]	97.915[b]
1.370	8.799	20.439	5.300	0.495	7.388	52.103	1.435	97.328
3.227	10.275	17.664	5.064	0.588	6.539	52.817	1.164	97.338
4.282[b]	12.555[b]	17.579[b]	4.530[b]	0.562[b]	5.716[b]	51.224[b]	1.158[b]	97.605[b]
1.014	9.012	20.597	5.334	0.501	6.991	52.085	1.404	96.936
6.261[b]	8.196[b]	15.181[b]	4.332[b]	0.428[b]	7.520[b]	55.068[b]	0.980[b]	97.967[b]
4.943	8.325	16.728	4.619	0.470	7.431	54.070	0.996	97.583
6.927	7.312	20.020	2.862	0.263	7.776	51.078	1.462	97.699
13.837[b]	2.585[b]	9.426[b]	1.297[b]	0.102[b]	10.277[b]	61.225[b]	0.923[b]	99.671[b]

[a]Totals are calculated assuming all Fe is in the form Fe^{2+}. Some component of Fe^{3+} is likely present in each measured point and would increase the totals slightly.

[b]These numbers are averages of 2-3 adjacent measurements to account for heterogeneity within the matrix.

Table 6. Bulk chemistry and standard deviations in wt % from ICP-AES and CN analyses.

Sample	Al_2O_3	CaO	Cr_2O_3	FeO	K_2O	MgO	MnO	Na_2O	NiO	P_2O_5	SiO_2	TiO_2	CO_2	Total
Interior	9.73 ±0.14	21.49 ±0.20	0.028 ±0.001	5.69 ±0.07	0.082 ±0.025	0.88 ±0.01	0.195 ±0.004	6.36 ±0.11	0.003 ±0.001	0.057 ±0.005	39.59 ±0.51	0.735 ±0.023	15.26 ±0.48	100.09
Exterior	9.51 ±0.12	17.30 ±0.27	0.036 ±0.000	6.73 ±0.07	0.121 ±0.005	3.27 ±0.03	0.180 ±0.002	5.72 ±0.10	0.014 ±0.000	0.031 ±0.006	40.76 ±0.17	0.807 ±0.010	11.53 ±0.26	96.01
Pink material[a]	7.89 ±0.10	31.68 ±0.84		2.32 ±0.15	0.038 ±0.012	2.04 ±0.06	0.217 ±0.003	4.09 ±0.04		0.013 ±0.005	27.63 ±0.17	0.114 ±0.004	24.64 ±0.028	100.68
Average of all measured samples[b]	13.61	10.83		9.02	0.652	5.27	0.19	4.81		0.140	45.15	1.13	7.354	95.74
Average unaltered Talcott basalt[c]	14.08	11.05		10.70	0.49	7.87	0.16	2.03			51.16	1.06		100.22

[a]Cr and Ni concentrations were not measured for this sample.
[b]Average of all 20 measurements of basaltic bulk samples and interiors and exteriors of samples from Meriden, CT, including those reported above. The additional analyses will be reported individually in a future paper.
[c]From Puffer et al. (1981).

Table 7. Mineralogy determined or inferred from each measurement

Analysis	Clay	Albite	Pyroxene	Calcite	Hematite	Titanite	Glass
ASD spectroscopy	x		x	x	x		?[a]
Hyperspectral imaging	x	Inferred[b]	x	x	x		?[a]
Micro-emission spectroscopy	x	x	x	x	x		?
µRaman spectroscopy		x		x	x		
Electron microprobe[c]		x		x	x	x	x
µXRD	[d]	x	x	[e]	x	[f]	
Powder XRD (interior/exterior)	x	x	x	x	x	x	

[a]Glass is consistent with VNIR spectra of the interior of the sample, though other explanations are possible
[b]Albite can be inferred in the outermost portion of the rind with hyperspectral imaging
[c]Mineralogy is inferred from composition and morphology using the electron microprobe, although this is not a mineralogical analysis technique
[d]µXRD measurements did not reach low enough 2θ to detect the clay reflections seen with powder XRD
[e]Calcite amygdules were not targeted for analysis with µXRD and thus were not identified
[f]Titanite was generally associated with the pink material cutting through the pillow, and these units were not analyzed with µXRD

FIGURE CAPTIONS

Fig. 1: Locations of measurements labeled on grayscale images of samples using the reflectance at 601 nm from the hyperspectral image. **a)** Cross section of the altered pillow basalt cut on a rock saw. Lower case Roman numeral numbers correspond to spectra in Fig. 2. The thick section in (b) was derived from the material directly above where the black outline is (not shown). **b)** Thick section across the alteration rind. Numbers correspond with points where μXRD (Fig. 10) and μRaman measurements (Fig. 7) were performed. **c)** Thick section with approximate location of microprobe transects through glassy matrix and albite (black line) and spots with micro-emission spectroscopy measurements (black and white circles). The numbers next to the spots correspond with spectral classes (Fig. 6) and are to the left of the points.

Fig. 2: Comparison of ASD point spectra (dark gray) and spectra of approximately the same spots from hyperspectral imaging (black) of the surface of the full cross section of the pillow for validation. Roman numerals correspond to the spots measured that are labeled in Fig. 1. Spectra are shown of the major units that are large enough to be measured with the ASD: (from bottom to top) the interior matrix, the pink material that cuts through the pillow, the matrix of the rind, and calcite amygdules. Slight apparent offsets in the wavelength positions of absorption features are generally due to differences in spectral sampling for the ASD (automatically resampled to 1 nm) and the imager (1.785 nm VNIR and 12.0656 nm SWIR). All of these spectra from the image are averages of 15x15 pixels, and locations of the spectra are shown in Fig. 1a. There is also one spectrum (light gray) of the rind matrix from the thick section image that is an

average of 10x10 pixels, though this spectrum is of a different spot than the other two rind spectra. A spectrum of datolite (top) from the image of the full cross section of the pillow is also shown and is a 3x3 average. There is no corresponding ASD spectrum because this material is too small to be measured with the large field of view of the ASD. Spectra are offset for clarity.

Fig. 3: Spectral transect from the interior to the exterior of the sample showing changes in spectroscopy that result from an evolution in mineralogy, chemistry, and oxidation state with alteration. Spectra are averages of regions of interest from the image of the full cross-section hand-sample, and the location of this transect is shown in Fig. 13. Results are similar to the image of the thick section, but those spectra are noisier and not shown here because some signal to noise was lost to achieve the high spatial resolution of that image.

Fig. 4: a) Hyperspectral image of the thick section across the alteration rind using bands from the hyperspectral image to approximate a true color image. Red: 0.662 µm, green: 0.531 µm, blue: 0.426 µm. **b)** VNIR spectral parameters for comparison with field imaging data. Red: red slope, green: green peak, blue: reflectance at 0.7 µm. **c)** SWIR spectral and mineral indicator parameters. Red: calcite, green: positive SWIR slope, blue: Fe/Mg-clay. **d)** BD1900 grayscale image highlighting hydration. Black is low and white is high.

Fig. 5: Scatterplot of the positive SWIR slope versus the green peak spectral parameters.

The data are density sliced, with blue being the least dense and red being the most dense. Regions are outlined that map to the rind (1), exterior calcite amygdules (2), interior calcite amygdules (3), and the interior matrix (4). Both parameters are present, or positive features, where their values are greater than 1.

Fig. 6: Average spectra (solid black lines) and fits (gray dashed lines) of each spectrally-similar class for the 25 measured micro-emission spectroscopy points offset for clarity. Modeled abundances of phases and errors are given in Table 4.

Fig. 7: µRaman spectra offset for clarity with peaks corresponding to different minerals labeled. Cal=calcite, Hem=hematite, and Ab=albite. The backgrounds have been subtracted, spikes due to cosmic rays have been removed, and spectra have been smoothed to remove high frequency noise using a 3-4 point moving average. The numbers correspond to the points labeled in Fig. 1b.

Fig. 8: Results from electron microprobe analyses of the thick section. Parts a-c are from elemental mapping data and have spatial resolutions of 13 µm/pixel. **a)** Backscattered electron (BSE) image. Dark areas have lower atomic weights (e.g., albite), and bright areas have higher atomic weights (e.g., iron oxides). Boxes show the locations of close-up views in d, e, and f. **b)** Elemental mapping color composite image. Red: Fe, green: Mg, blue: Na. Zones I, II, III, IV, and V are distinguished based on texture and composition and correspond with zones in the transect in Fig. 9. The values for Na have been color balanced using overlapping areas to remove slight differences in value

between mapping squares. **c)** Class image showing pixels that are at least 75% one phase generated from a linear unmixing algorithm. Red is calcite, green is albite, blue is glass, magenta is Fe oxide, and yellow is titanite. **d)** BSE close-up view of the exterior of the sample with large albite crystals, calcite, Fe-oxide, a little remnant glass. **e)** BSE close-up view of the base of the rind. The calcite on the left is in an amygdule, and the mixed albite and calcite on the right is the pink material the cuts through the sample. **f)** BSE close-up view of the interior of the sample with a microcrystalline matrix. All "glass" referred to here is likely devitrified and at least poorly crystalline.

Fig. 9: Compositional transect through the glassy matrix from the interior to the exterior of the sample using data from quantitative electron microprobe analyses ratioed to the interior-most point measured. Note that the y-axis is not scaled by distance, but the points are broken up by textural and compositional zones shown in Fig. 8.

Fig. 10: μXRD transect from exterior (point 1) to interior (point 9) with each XRD pattern offset for clarity. Locations of points measured are shown in Fig. 1b. The phases corresponding to each peak are labeled: Ab=albite, Di=diopside, Hem=hematite, and F=Fe and/or Ti oxide. Peaks that are high relative to the other peaks from the same phase are likely due to an orientation effect from relatively large crystals. Best matching ICDD cards are albite=01-083-1466, diopside=00-041-1370, hematite=01-089-0596, Fe/Ti-oxide=00-046-1391. Aegirine is difficult to distinguish from diopside in these data, but ICDD card number 01-075-8659 also fits some of the peaks marked as diopside well.

Fig. 11: Plot showing the intensity of peaks for diopside, albite, and hematite ratioed to the sum of peaks from all three phases at each point measured with μXRD from interior to exterior. This plot shows qualitative differences in the abundance of various phases. Spot numbers correspond to the points analyzed in Fig. 1b and the XRD patterns in Fig. 10. The peaks used for each phase were selected so that they did not overlap with peaks from another phase. The albite peak used is at 25.6-25.8° 2θ, the diopside peak is at 34.8-34.9° 2θ, and the hematite peak is at 38.6-38.7° 2θ.

Fig. 12: Powder (bulk) XRD results for <45 μm particle size separates of the interior and the exterior (rind) samples. The interior pattern is purple and the exterior is green. The exterior pattern is offset 150,000 counts. The fits from Rietveld Refinement (black dashed lines) are plotted with the measured XRD patterns for comparison. Residuals for the exterior (green) and interior (purple) fits are also shown. Two-theta values have been converted to the values that would have resulted with a Co source to allow for direct comparison with μXRD data (Fig. 10). Abbreviations with best matching ICDD card numbers in parentheses are as follows: Ab=albite (01-084-0752), Aeg=aegirine (01-075-8657), Cal=calcite (00-024-0027), Chl=chlorite (00-007-0078), D=diopside (00-041-1370), Hem=hematite (00-033-0664), and Sme=smectite (nontronite, 01-089-5692). All abbreviations conform with Whitney and Evans (2010) where possible.

Fig. 13: a) Near true color composite from the hyperspectral image of the full cross-section of the altered pillow basalt. Red: 0.662 μm, green: 0.531 μm, blue: 0.426 μm. **b)** VNIR spectral parameter image. Red: red slope, green: green peak, blue: reflectance at

0.7 µm. **c)** SWIR spectral parameter and mineral indicator image. Red: calcite, green: positive SWIR slope, blue: Fe/Mg-clay. **d)** BD1900 grayscale image. Stretches for every band or parameter displayed in this figure are nearly identical to Fig. 4 to allow for direct comparison.

Fig. 14: a) Near true color composite image of a portion of the outcrop with greener alteration of lacustrine pillow basalts in Meriden, CT. Red: 0.66 µm, green: 0.53 µm, blue: 0.45 µm. **b)** Spectral parameter image. Red: red slope, green: green peak, blue: reflectance at 700 nm. In both images, vegetation, the calibration target, and shadows have been masked.

Fig. 15: Conceptual figure showing the aqueous history of the basalt from emplacement through hydrothermal alteration and diagenesis. **a)** The basalt erupts into a lake, forming pillow lavas with glassy rinds. Hydrothermal circulation begins. **b)** Calcite and plagioclase-bearing material cuts through the pillow before the lava fully solidifies. **c)** Green alteration rinds with aegirine and calcic clinopyroxenes form at temperatures 400-600+°C. At slightly lower temperatures, Fe/Mg-bearing clays also form in the rind. During this time, the entire sample oxidizes, and fine-grained hematite in the interior forms. **d)** During the waning stages of the hydrothermal system, calcite precipitates in vesicles in the rind, completely filling them. The hydrothermal fluids likely have significant Ca^{2+} leached from the basalts and HCO_3^-, suggesting a mildly acidic system. **e)** Na-brines form as the lake evaporates during drier climatic periods. Nearly all plagioclase is replaced by albite (albitization or Na-metasomatism), releasing Ca^{2+} into

solution. Albite coats unfilled vesicles and veins and precipitates throughout outer parts of the rinds. **f)** High Ca^{2+} fluids that result from albitization lead to precipitation of calcite in unfilled vesicles and veins, generally in the interior of the sample since exterior vesicles were filled with calcite during earlier hydrothermal processes.

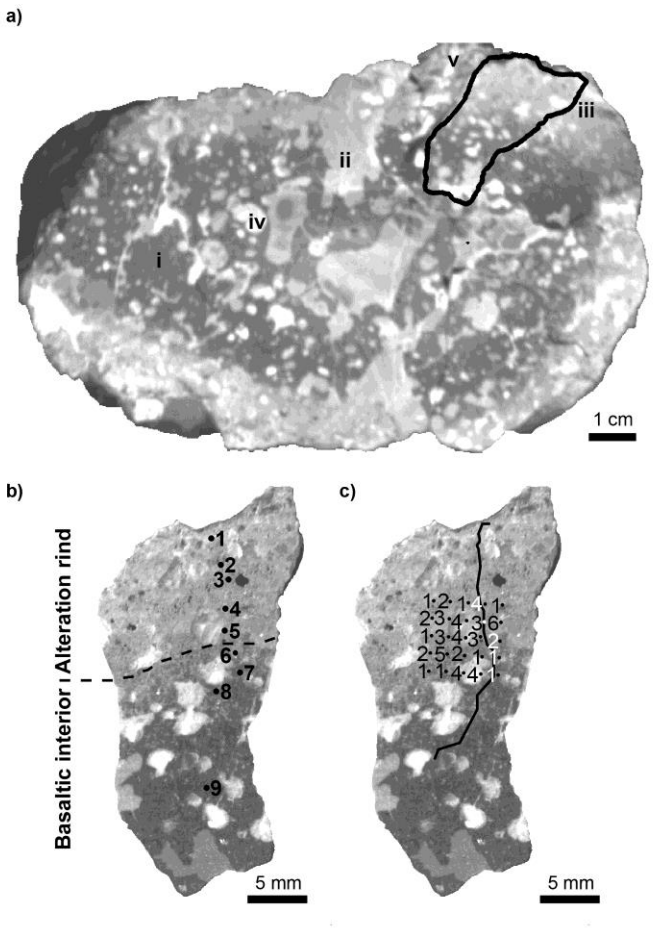
a)
v
iii
ii
iv
i
1 cm
b)
c)
Basaltic interior
Alteration rind
1
2
3
4
5
6
7
8
9
5 mm
5 mm

Figure 1.

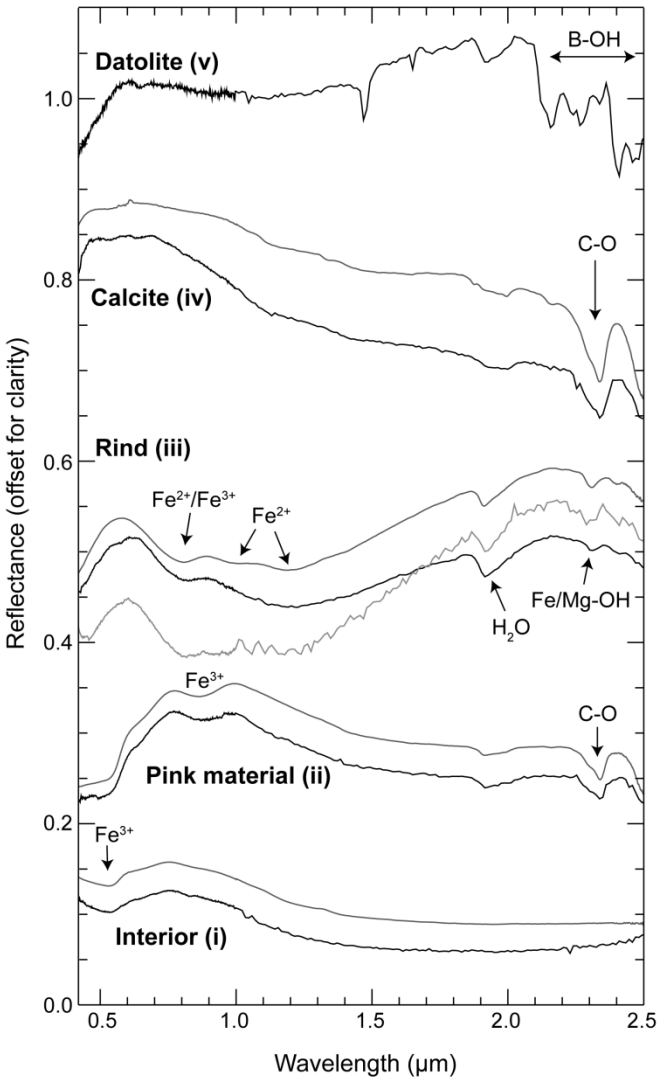
Datolite (v)
B-OH
Calcite (iv)
C-O
Rind (iii)
Fe2+/Fe3+
Fe2+
H2O
Fe/Mg-OH
Pink material (ii)
Fe3+
C-O
Interior (i)
Fe3+
Reflectance (offset for clarity)
Wavelength (μm)
0.0
0.2
0.4
0.6
0.8
1.0
0.5
1.0
1.5
2.0
2.5

Figure 2.

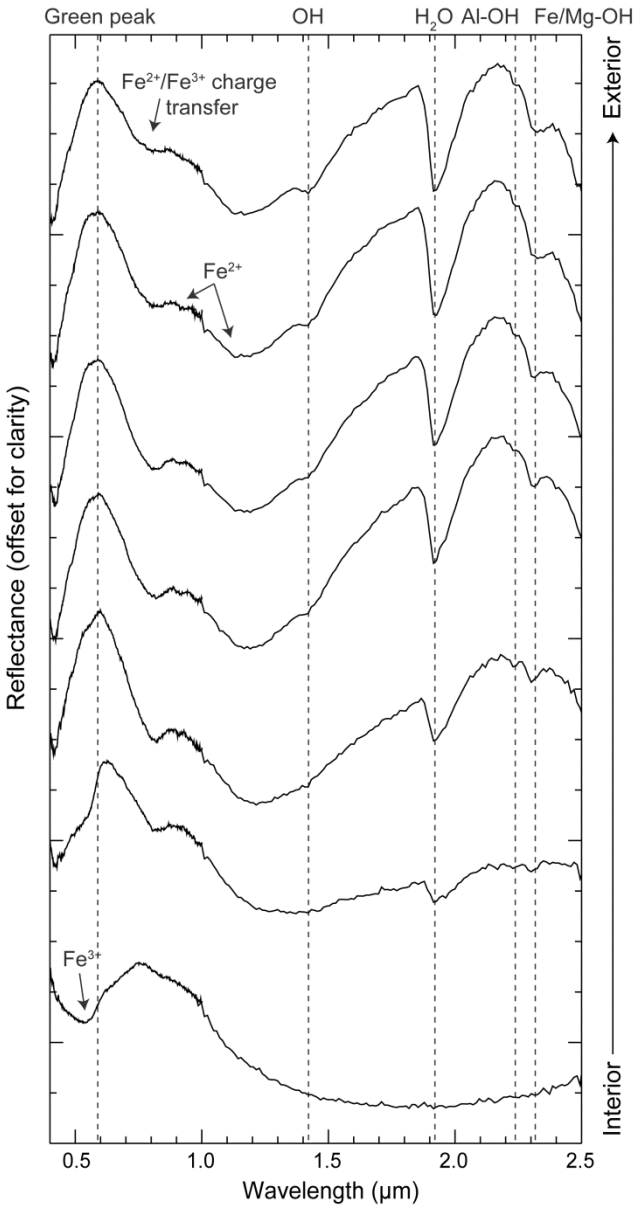
Green peak
OH
H2O
Al-OH
Fe/Mg-OH
Fe2+/Fe3+ charge transfer
Fe2+
Fe3+
Exterior
Interior
Reflectance (offset for clarity)
0.5
1.0
1.5
2.0
2.5
Wavelength (μm)

Figure 3.

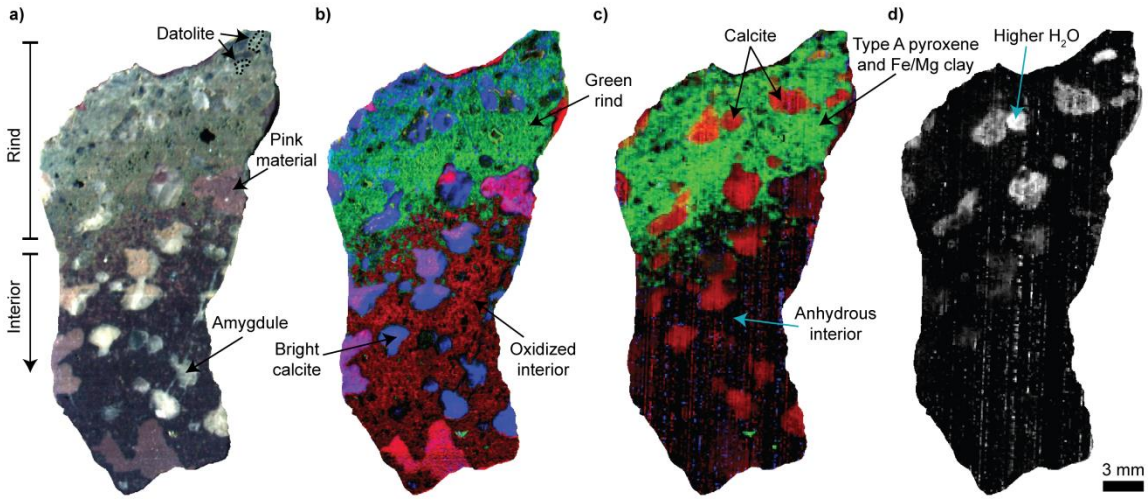
a)
b)
c)
d)
Datolite
Rind
Pink material
Interior
Amygdule
Bright calcite
Green rind
Oxidized interior
Calcite
Type A pyroxene and Fe/Mg clay
Anhydrous interior
Higher H_2O
3 mm

Figure 4.

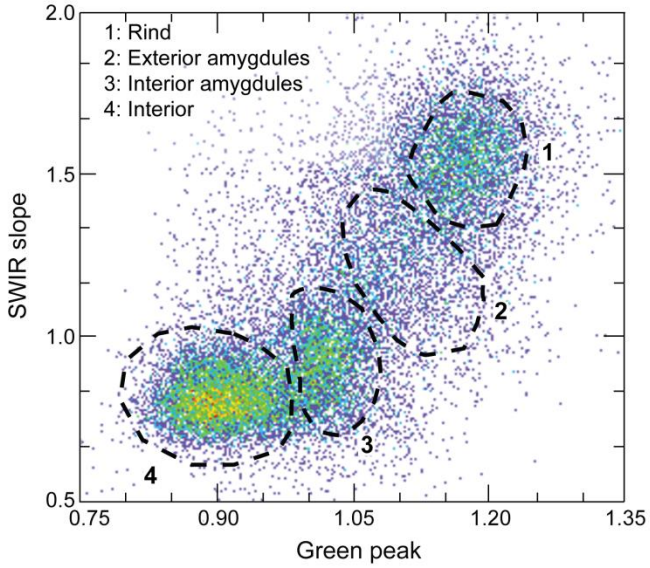
1: Rind
2: Exterior amygdules
3: Interior amygdules
4: Interior
SWIR slope
Green peak
2.0
1.5
1.0
0.5
0.75
0.90
1.05
1.20
1.35
1
2
3
4

Figure 5.

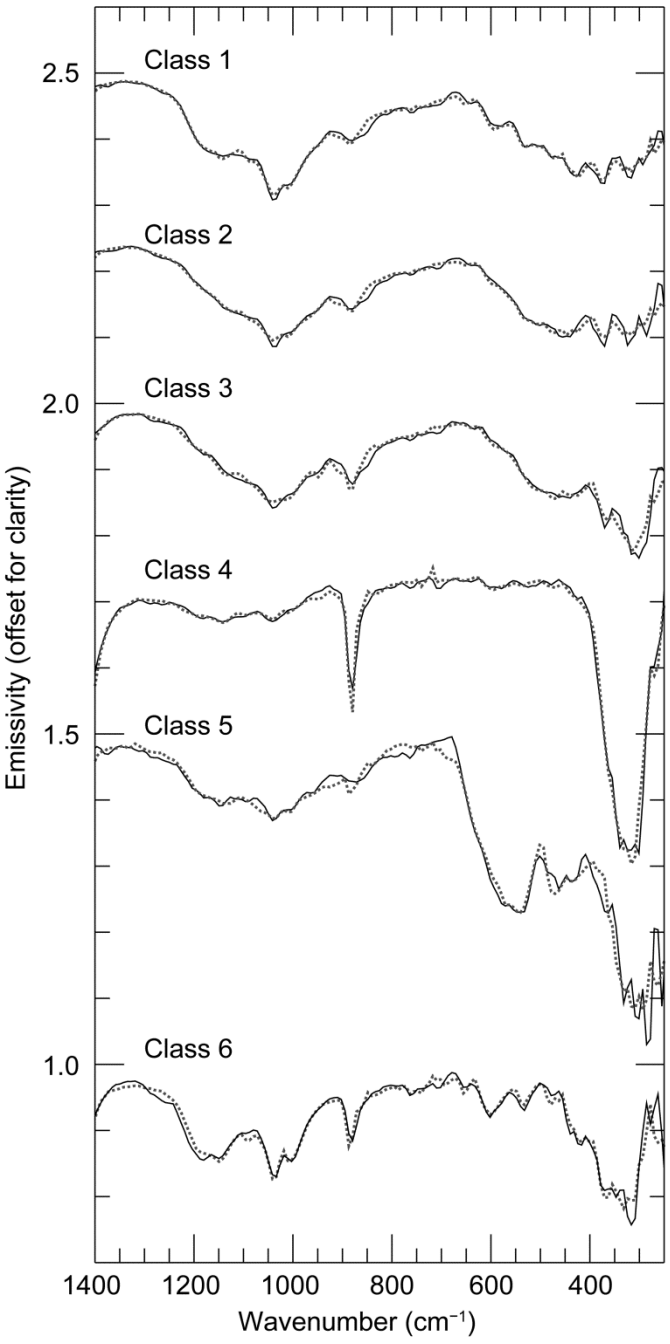
Class 1
Class 2
Class 3
Class 4
Class 5
Class 6
2.5
2.0
1.5
1.0
Emissivity (offset for clarity)
1400
1200
1000
800
600
400
Wavenumber (cm⁻¹)

Figure 6.

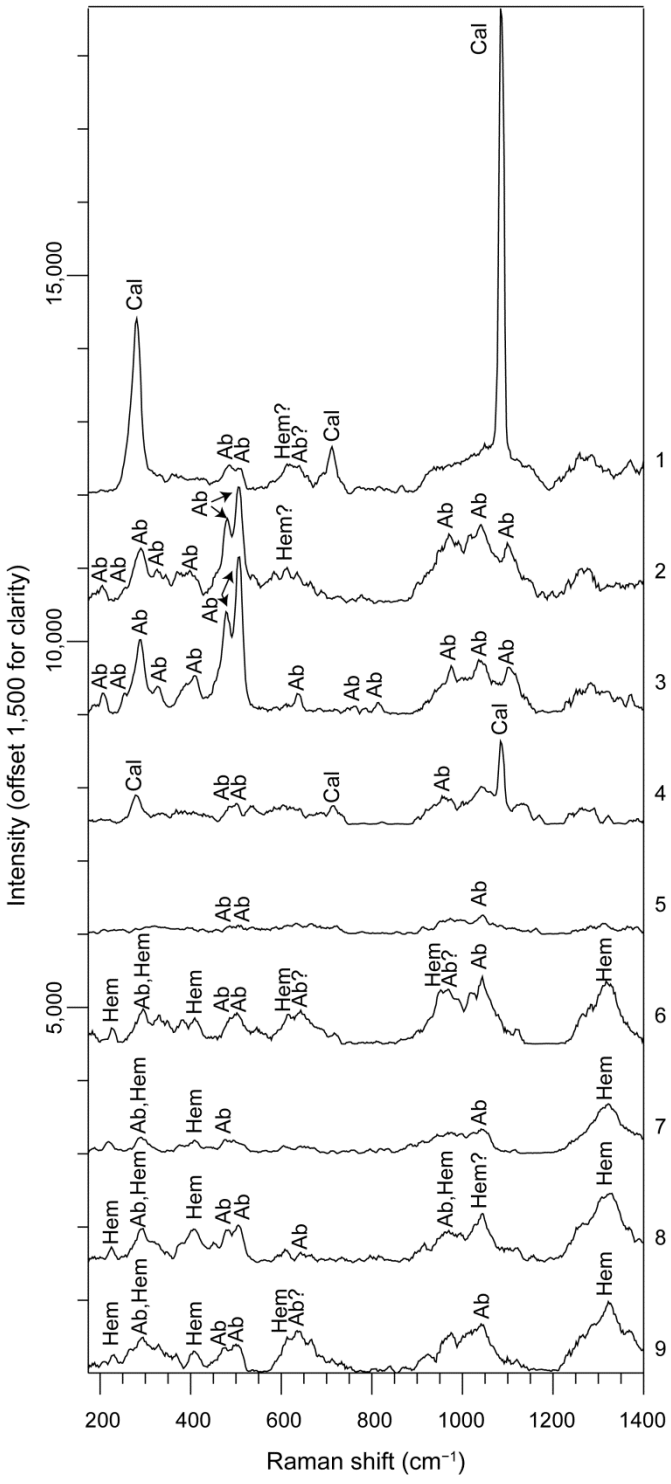
Intensity (offset 1,500 for clarity)
15,000
10,000
5,000
200
400
600
800
1000
1200
1400
Raman shift (cm⁻¹)
1
2
3
4
5
6
7
8
9
Cal
Ab
Hem
Hem?
Ab?
Ab,Hem

Figure 7.

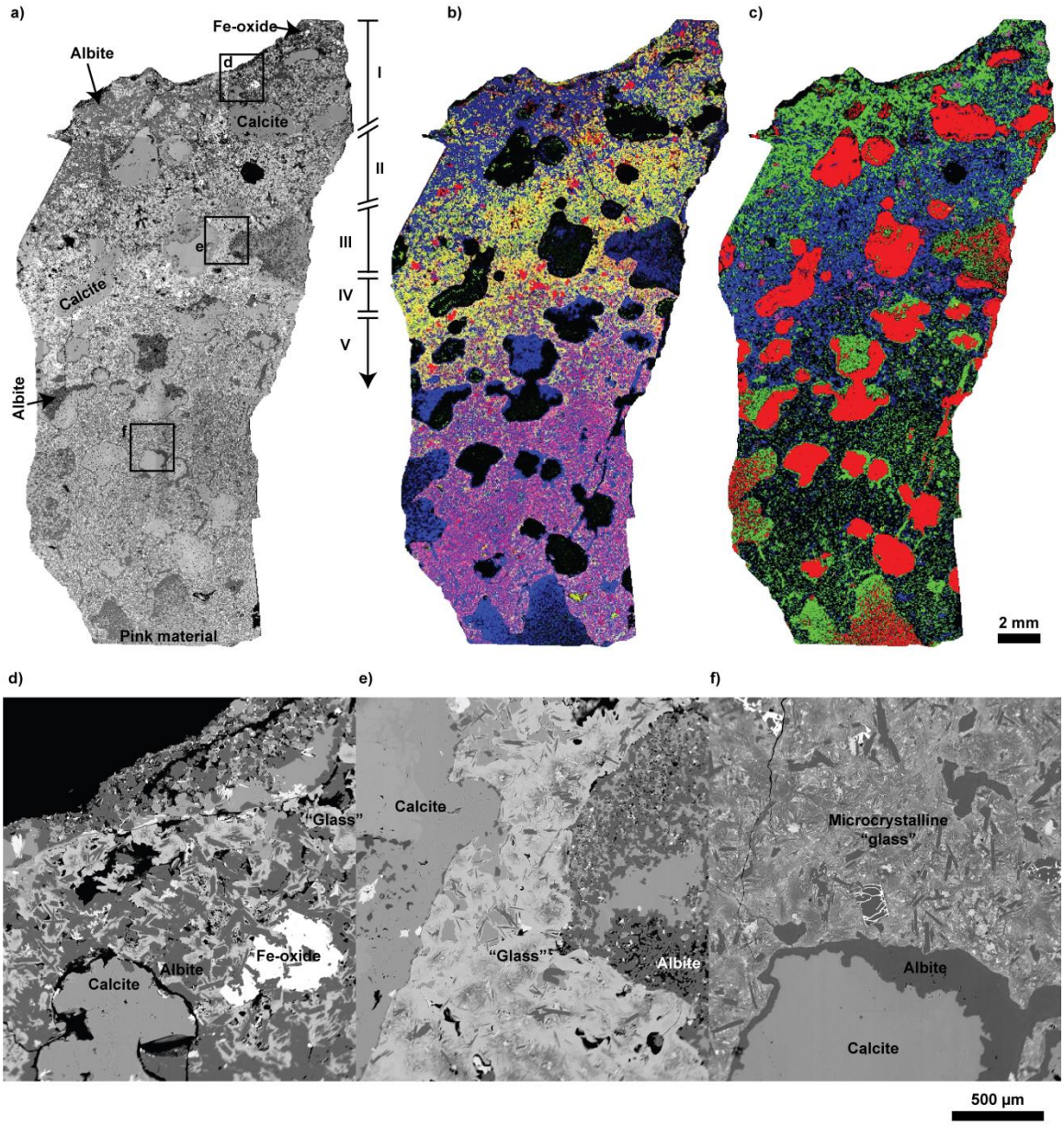
a)
b)
c)
Fe-oxide
Albite
d
Calcite
e
Calcite
Albite
f
Pink material
I
II
III
IV
V
2 mm
d)
e)
f)
"Glass"
Calcite
Albite
Fe-oxide
Calcite
"Glass"
Albite
Microcrystalline "glass"
Albite
Calcite
500 µm

Figure 8.

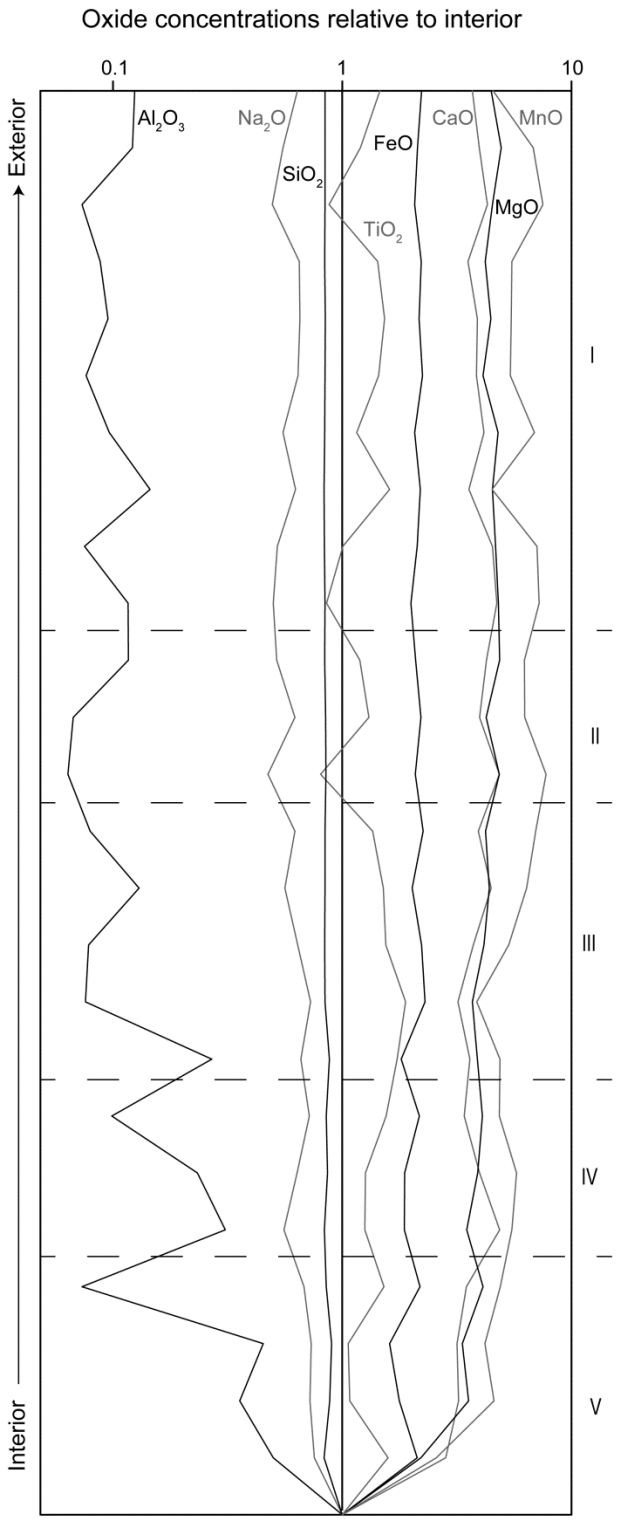
Oxide concentrations relative to interior
0.1
1
10
Exterior
Interior
Al_2O_3
Na_2O
SiO_2
FeO
TiO_2
CaO
MgO
MnO
I
II
III
IV
V

Figure 9.

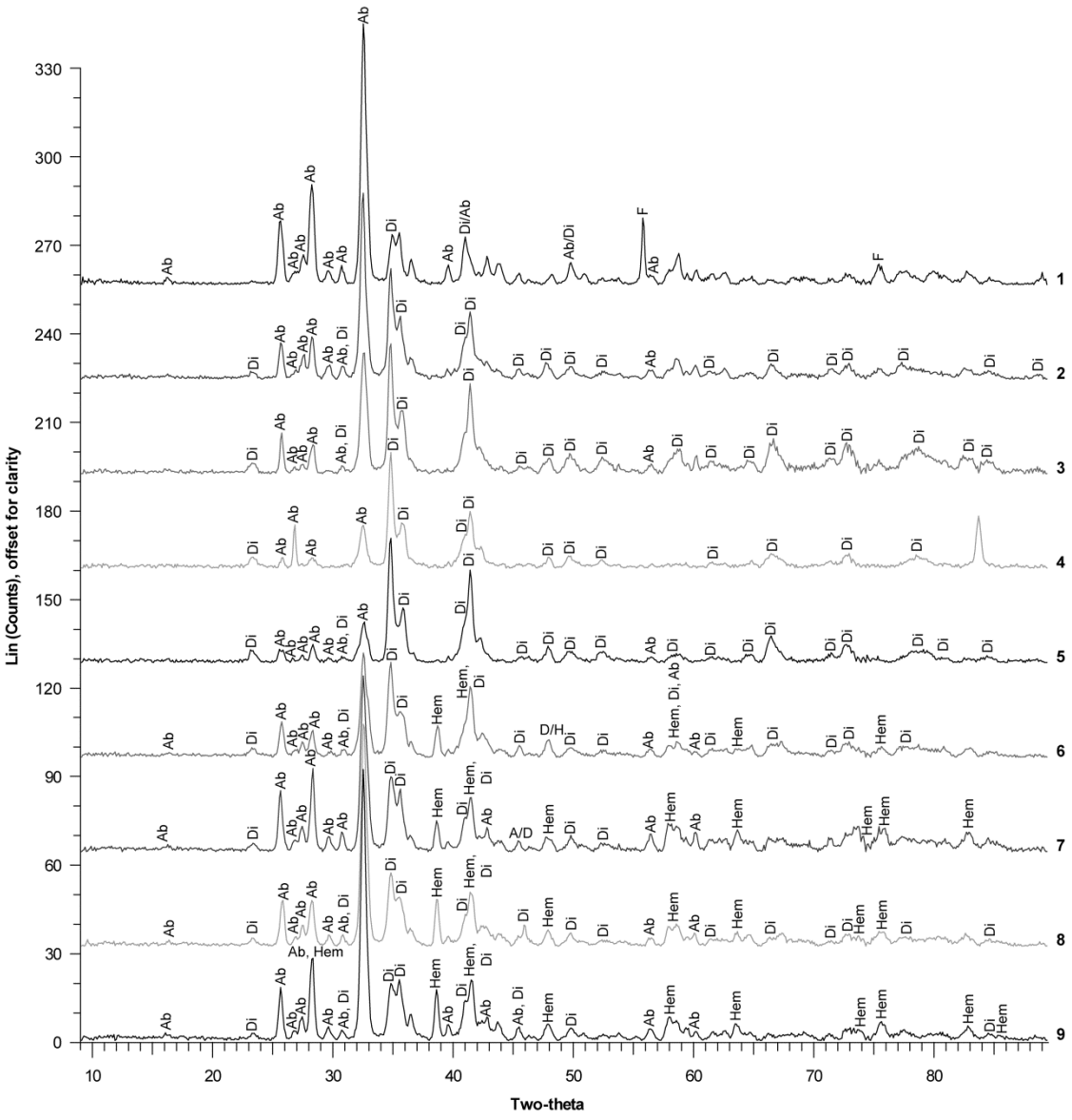
Lin (Counts), offset for clarity
Two-theta
330
300
270
240
210
180
150
120
90
60
30
0
10
20
30
40
50
60
70
80
1
2
3
4
5
6
7
8
9
Ab
Di
Hem
F
Ab/Di
Di/Ab
D/H
A/D
Ab, Di
Ab, Hem
Hem, Di
Hem, Di, Ab

Figure 10.

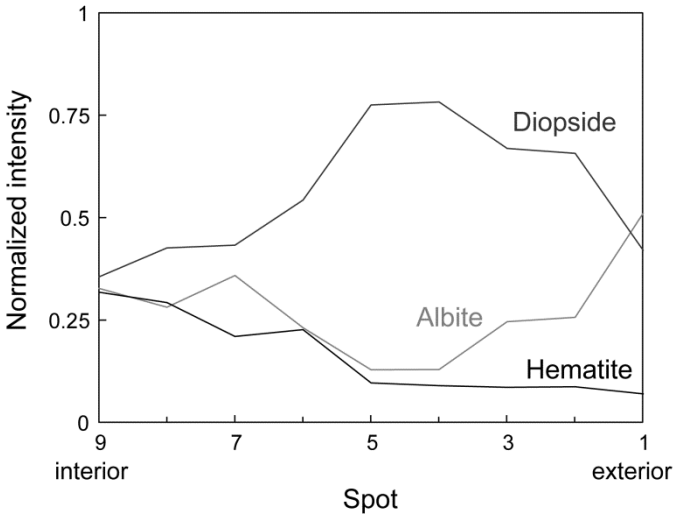
1
0.75
0.5
0.25
0
Normalized intensity
Diopside
Albite
Hematite
9
7
5
3
1
interior
exterior
Spot

Figure 11.

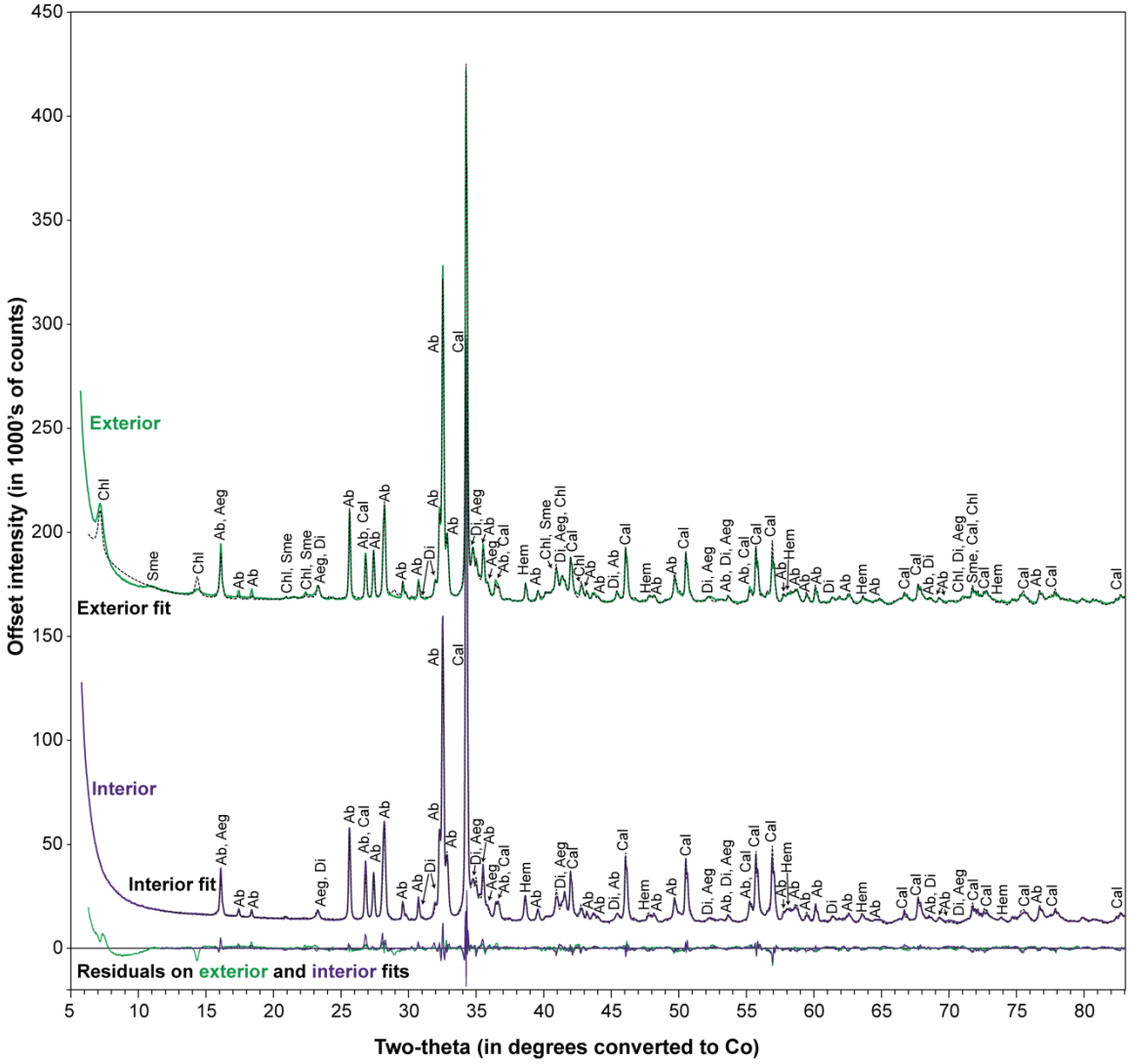
Offset intensity (in 1000's of counts)
Two-theta (in degrees converted to Co)
Exterior
Exterior fit
Interior
Interior fit
Residuals on exterior and interior fits

Figure 12.

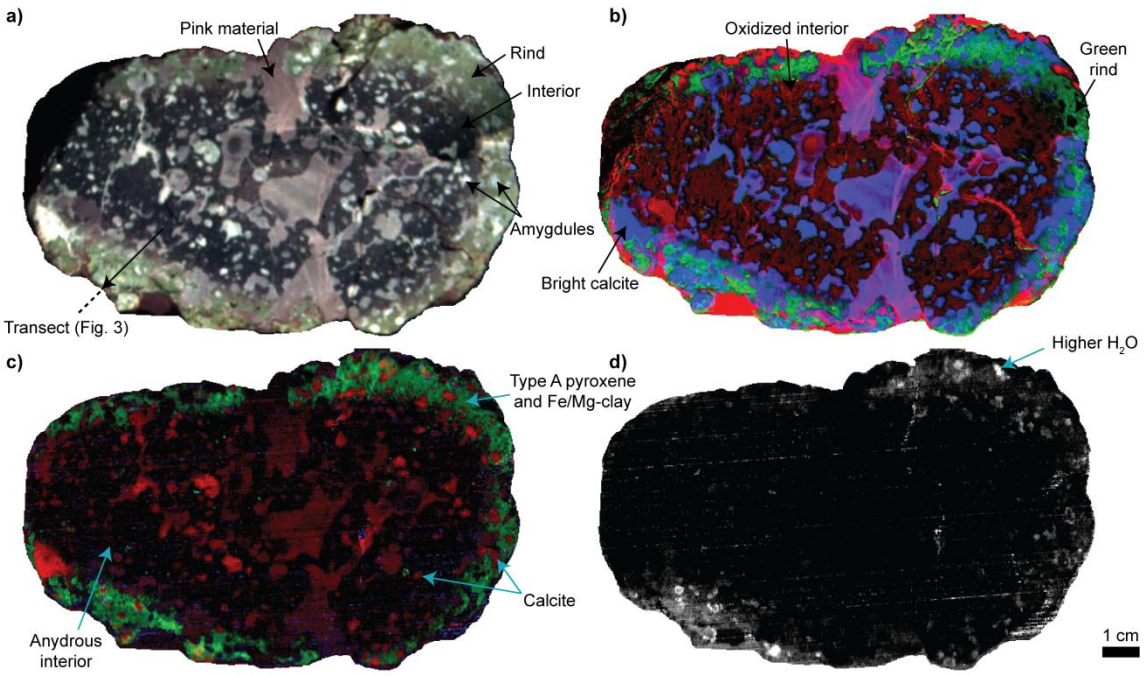
a)
Pink material
Rind
Interior
Amygdules
Transect (Fig. 3)
b)
Oxidized interior
Green rind
Bright calcite
c)
Type A pyroxene and Fe/Mg-clay
Calcite
Anydrous interior
d)
Higher H_2O
1 cm

Figure 13.

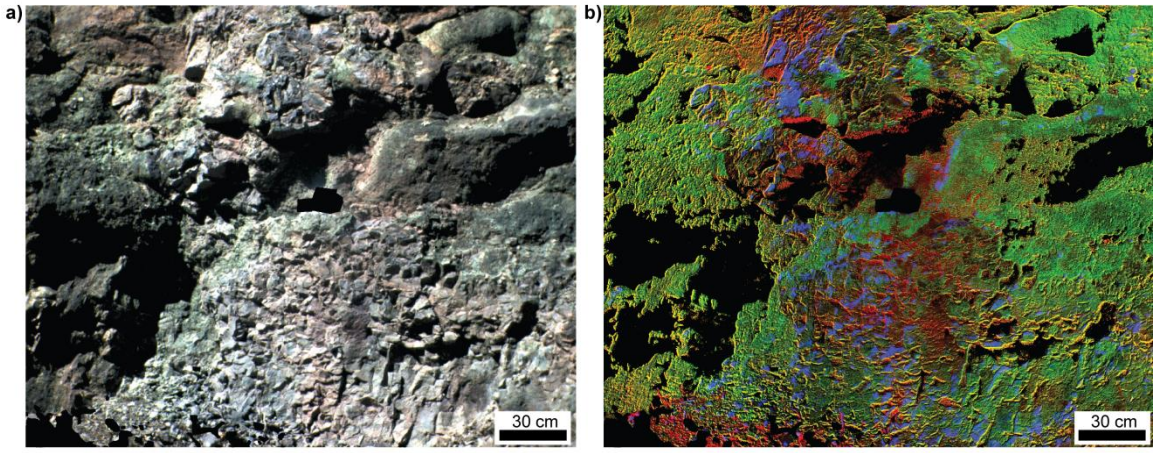

Figure 14.

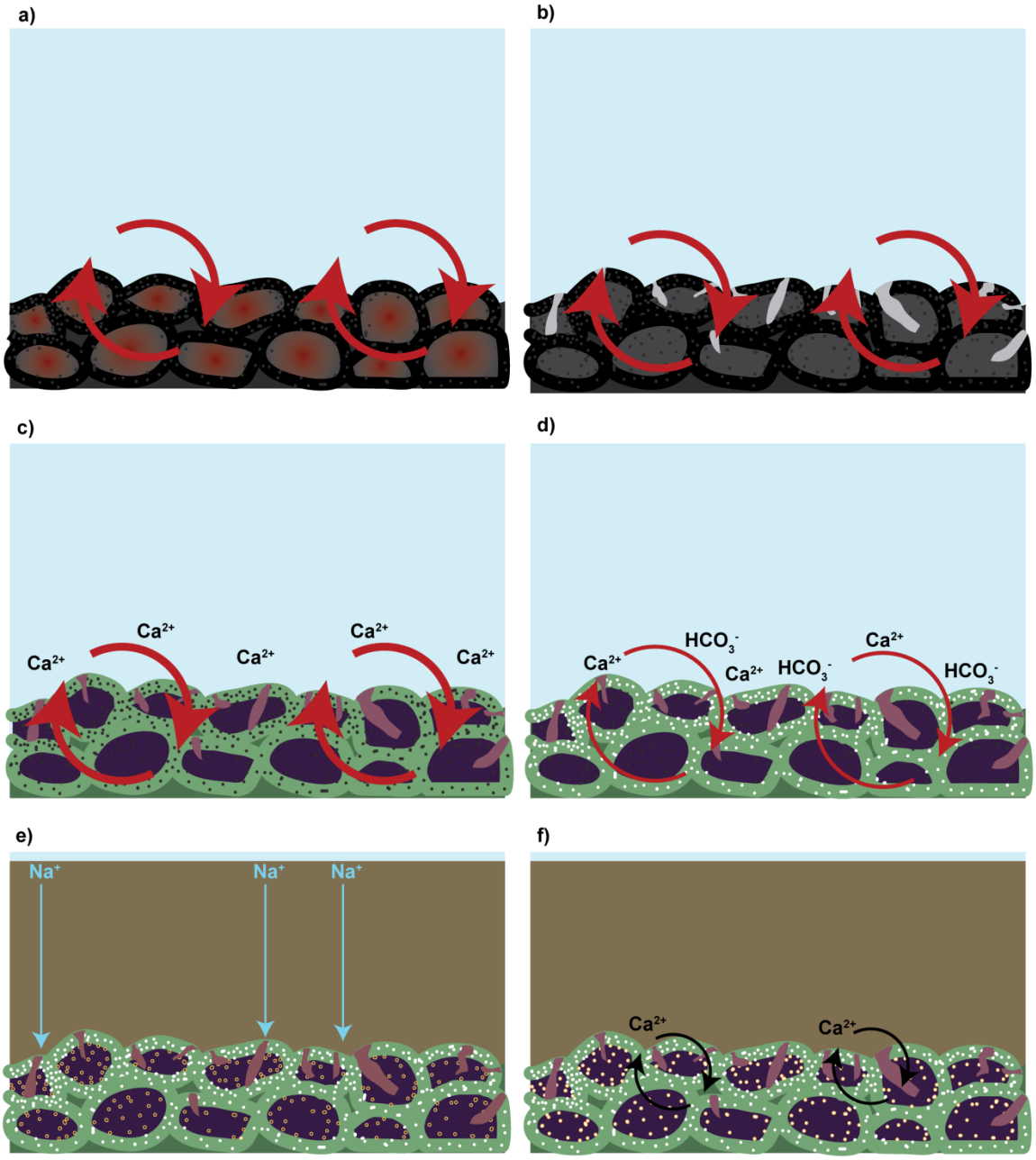
a)
b)
c)
d)
e)
f)
Ca2+
Ca2+
Ca2+
Ca2+
Ca2+
HCO3-
Ca2+
HCO3-
Ca2+
HCO3-
Na+
Na+
Na+
Ca2+
Ca2+

Figure 15.

CHAPTER 3

Characterization of aqueous alteration resulting from volcano-lacustrine interactions in the Hartford Basin: implications for Mars

Rebecca N. Greenberger[a], John F. Mustard[a], Edward A. Cloutis[b], Paul Mann[b], and Janette H. Wilson[c]

[a]Department of Earth, Environmental, and Planetary Sciences
Brown University, Providence, RI, USA 02912

[b]Department of Geography, University of Winnipeg
Winnipeg, Manitoba, Canada R3B 2E9

[c]Headwall Photonics, Inc.
Fitchburg, MA, USA 01420

In review in its current form in:
Chemical Geology

ABSTRACT

Volcanically-resurfaced open basin lakes identified on Mars suggest the possibility of volcano-lacustrine interactions in the past. We present the results of a study characterizing the mineral assemblages that resulted from these types of volcano-lacustrine interactions and later diagenesis at an outcrop of ~187 Ma Talcott Formation pillow basalts and the underlying sedimentary rocks of the New Haven Formation in Meriden, Connecticut. Analyses include hyperspectral imaging of the outcrop (0.42-1.1 μm), hyperspectral imaging of samples in the laboratory (0.4-2.5 μm), point spectroscopy (0.35-2.5 μm), inductively coupled plasma – atomic emission spectrometry and elemental analyses for major element chemistry, and x-ray diffraction for mineralogy. There are a variety of types of alteration at this outcrop: baking of and formation of coatings on sediments; oxidation of pillow lavas; formation of alteration rinds with clays, calcite, and/or sodic and calcic clinopyroxenes on pillows; and calcite, quartz, and prehnite mineralization of veins, vesicles, and hyaloclastite breccias. The secondary mineral phases identified are aegirine, albite, calcic clinopyroxene, calcite, chlorite, datolite, goethite, hematite, illite, montmorillonite, nontronite and/or saponite, prehnite, and quartz. While there is significant chemical heterogeneity in the sample analyses, there are distinct changes in chemistry from interior to coating or rind. For the sediment samples, coatings have higher Al, possibly from the basalts, and lower Mg. Red-altered pillow basalts have enrichments in Al, Na, and Si in the interior and depletions of those elements along with enrichments in Mg and Ca in the rinds. Green-altered pillow basalts have higher Na in the interior and significantly higher Mg with moderate increases in Fe in the rind. These results suggest high mobility of cations during alteration, and we

found no sample that was spectrally, chemically, and mineralogically consistent with an unaltered basalt. We hypothesize that this is likely due to the abundance of water during and after emplacement, the glassy nature of these pillow basalts, and the high porosity and permeability of this system. Similar heterogeneous assemblages might be expected for any similar outcrops on Mars.

1 INTRODUCTION

The minerals that result from water-rock interactions can illuminate past climates and environments on Mars and shed light on the habitability of these aqueous systems. Secondary minerals resulting from aqueous alteration have been identified on Mars through orbital (e.g., Bibring et al., 2006; Ehlmann et al., 2011a, 2011b; Murchie et al., 2009; Mustard et al., 2008) and rover (Arvidson et al., 2014; Morris et al., 2010; Squyres et al., 2012, e.g., 2004; Vaniman et al., 2014) investigations. Locations where there have been water-rock interactions at elevated temperatures have been suggested to be promising locations to search for biosignatures on Mars (Farmer and Des Marais, 1999; Summons et al., 2011 and references therein). There are also morphologic indicators of aqueous activity on Mars, including valley networks and lakes (e.g., Baker et al., 1992; Fassett and Head III, 2008a, 2008b; Goudge et al., 2012; Hynek and Phillips, 2003; Irwin et al., 2005), and many of these open-basin lakes have been volcanically resurfaced (Goudge et al., 2012). Although no morphologic evidence has been found for volcano-lacustrine interactions on Mars (Goudge et al., 2012), there has been no comprehensive study looking for mineralogic indicators, and, given the temporal overlap between volcanic and aqueous activity on Mars (e.g., Ehlmann et al., 2011b), these types of

interactions are likely to have occurred in the past.

On Earth, the hydrothermal systems that result from lavas erupting into large bodies of water have been well-characterized, particularly on the ocean seafloor (Alt et al., 1992, 1986; Gillis et al., 1993; Lowell et al., 1995; e.g., Seyfried Jr. and Mottl, 1982; Seyfried et al., 1988; Seyfried, 1987; Von Damm et al., 1985). Mg-metasomatism is common in these systems, and Ca-metasomatism is seen at higher water/rock ratios (Lowell et al., 1995; e.g., Seyfried Jr. and Mottl, 1982; Seyfried et al., 1988; Seyfried, 1987; Von Damm et al., 1985). Alt et al. (1986) characterized a core through 1 km of oceanic crust and found zones and progressions of alteration with depth, degree of water-rock interaction, and temperature, among other factors. While these types of interactions also occur in freshwater lacustrine environments, where phyllosilicates, zeolites, calcites, and other secondary minerals have been found, there has been limited study of these types of systems (e.g., Cummings, 1987; Heald, 1956; Keith and Staples, 1985; Kolleeny, 1996; Laskowich and Puffer, 1990; Puffer et al., 1981; Puffer and Benimoff, 1997; Puffer and Laskowich, 2012; Robert, 2001). Aqueous alteration of subglacial pillow basalts has been studied as an analog for alteration on Mars (e.g., Bishop et al., 2002; Cousins et al., 2013; Warner and Farmer, 2010). What remains unexamined is how the mineral assemblages that result from volcano-lacustrine alteration processes manifest at the outcrop scale that would be accessible to orbital and landed instrument packages.

We are studying an outcrop of hydrothermally-altered lacustrine pillow basalts of the Talcott formation and underlying sediments of the New Haven Formation exposed in Meriden, Connecticut, USA (Hanshaw, 1968). Our goals are to characterize the mineral assemblages that formed through alteration of pillow basalts erupted in a lacustrine

environment and understand how they vary spatially across an outcrop and are expressed in remotely-sensed data. We accomplish this using hyperspectral imaging of hand samples in the laboratory to map the mineralogies and other laboratory analyses to determine chemistries and validate spectrally-determined mineralogies. Then, we use hyperspectral imaging of the outcrop in the field to scale the results from the hand-samples to the larger outcrops.

2 GEOLOGICAL SETTING

The rift basalts of the Hartford Basin are related to basalts around the world that erupted as Pangea broke up and the Atlantic Ocean opened in the Mesozoic and have been correlated in time and chemistry with Newark Basin basalt formations (Cummins et al., 1992; McHone and Butler, 1984; e.g., Philpotts, 1978; Puffer, 1992; Seidemann et al., 1984). The outcrop studied here is part of the Talcott Formation, which is the oldest of three basaltic formations in the Hartford Basin and likely was fed by the Higganum dike, and overlies the New Haven Arkose (Hanshaw, 1968; Philpotts, 1992; Philpotts and Martello, 1986; Puffer et al., 1981). The Talcott Formation is 200 feet (61 m) thick on average in the Meriden quadrangle and is composed of pillow, massive, and vesicular, unfractionated, high-TiO_2 quartz-normative basalts (Hanshaw, 1968; Philpotts and Reichenbach, 1985; Puffer, 1992; Puffer et al., 1981). The Talcott basalts have been dated to be 187±3 Ma (Seidemann, 1988).

The Talcott basalt has been altered, and chlorite, sericite, palagonite, quartz, albite, fluorite, barite, and zeolites have all been identified along with enrichments in Fe^{3+}/Fe^{2+}, Na, and H_2O with depletions in Ca, Mg, and Si (Hanshaw, 1968; Puffer et al.,

1981; Robinson Jr and Woodruff, 1988). Fluid inclusion studies have determined homogenization temperatures in basalts and diabases in the Hartford Basin to be 90-210°C (Robinson Jr and Woodruff, 1988). Since the Hartford Basin basalts have been correlated with the three Newark Basin flows (Puffer et al., 1981; Seidemann et al., 1984), studies of hydrothermal alteration in the Newark Basin can also inform our understanding of alteration in the Hartford basin, and phases including quartz, calcite, prehnite, chalcopyrite, clays, zeolites, pectolite, pyrrhotite, and datolite have been identified (Cummings, 1987; Laskowich and Puffer, 1990; Puffer and Benimoff, 1997; Puffer and Laskowich, 2012; Puffer and Student, 1992). These secondary minerals formed through low and high temperature aqueous processes, and their distribution is controlled by porosity, permeability, and crystallinity of the rock (Cummings, 1987; Puffer and Student, 1992). Dome structures, described as diapirs, have been found in the Orange Mountain Basalt in the Newark Basin that are thought to be related to hydrothermal activity resulting from intrusion of the Palisade Sill below leading to increased alteration and the formation of carbonate-enriched basalt layers (Laskowich and Puffer, 1990; Puffer and Laskowich, 2012).

In the New Haven Arkose, secondary minerals have also been identified, including epidote, garnet, clay minerals, albite, calcite, and copper sulfides (Heald, 1956; Kolleeny, 1996). Merino et al. (1997) use the textures of alteration minerals to suggest that they formed during a sudden heating event. In this model, the fluids in the New Haven Arkose were dominated by Na, Al, and SiO_2 before the volcanism, and K, Mg, and Fe^{2+} derived from the basalt were added later (Merino et al., 1997). It has also been suggested that heat from the Talcott basalts caused the waters in the Hartford basin to

overturn for the first time (Gray, 1988), and the thermal maturity of organics in the region show anomalies from the volcanism and related hydrothermal circulation (Pratt et al., 1988; Wolela and Gierlowski-Kordesch, 2007). Partial and complete albitization of primary feldspar minerals has been reported (Wolela and Gierlowski-Kordesch, 2007). Generations of calcsilicates and calcite may result from pressure (and CO_2) release as hot fluids fractured the surrounding rock and boiled, then precipitated secondary minerals and sealed the system, allowing pressure and CO_2 to build again (Kolleeny, 1996). These sediments have also been altered before and after the igneous activity (Heald, 1956; Kolleeny, 1996). Elsewhere in the Hartford Basin, hematitic concretions within the New Haven Arkose that formed through pedogenic processes unrelated to the volcanic activity have been studied as an analog for Mars (Wilson et al., 2012). In the Newark Basin, the sedimentary Passaic Formation has been altered by the igneous activity in the region, and homogenization temperatures for the alteration range from 150 to 280°C with an average of 180°C (El-Tabakh et al., 1997). These temperatures are not attainable simply through diagenesis since these sediments were only buried to a maximum depth of 3 km, suggesting that the volcanic activity in the region played an important role in heating the altering fluids (El-Tabakh et al., 1997).

The interface between the Talcott basalt and underlying sediments has been found to contain phases indicative of contact metamorphism (Kolleeny, 1996). Concentrations of copper sulfides at the basalt-sediment boundary likely derived from the sediments (Gray, 1988). Here, copper was probably already dissolved in diagenetic fluids within the New Haven Arkose before volcanic activity began and then precipitated after the basalt was emplaced (Gray, 1988). It also has been suggested that the most permeable parts of

the Talcott basalt were altered by waters from underlying sediments (Puffer et al., 1981). Higher in the Hartford Basin stratigraphy, East Berlin Formation sediments within a few meters of the Hampden basalts are also altered, with calcite and interstratified chlorite/vermiculite present (April, 1980). Closest to the basalts, the chlorite-vermiculite is more abundant and well-ordered (April, 1980).

The outcrop studied here exposes the base of the Talcott Basalt overlying ~1 m of New Haven Arkose sediments. The sediments have been pushed up between basaltic pillows in places and baked (Fig. 1a). The basalts at the base of the outcrop often have red-orange coatings extending upward up to a few meters, and the interiors of some of the pillows have altered to a redder color. Alteration of the pillow basalts exposed at this outcrop that are stratigraphically higher are characterized by green alteration rinds and oxidized, purple interiors (Fig. 1b). Throughout the outcrop, calcite fills veins and vesicles (Fig. 1c). There is also quartz mineralization lower in the section and prehnite higher, and hyaloclastite breccias with angular glassy clasts and calcite are present in places (Fig. 1d). Higher in the section, these breccias are greener and contain significant chlorite. Descriptions of samples collected and analyses done on each are given in Table 1.

3 METHODS

Hyperspectral imaging of the outcrop was done with Channel Systems visible and near infrared (NIR) imagers, which are acousto-optic tunable filter systems equipped with 1.3 Mpixel detectors and 12 bit quantization. The visible imager covers wavelengths 0.42-0.72 μm with 5 nm sampling and 10 nm spectral resolution, and the NIR imager

covers 0.65-1.1 μm with 10 nm sampling and spectral resolution. Exposure times varied as a function of wavelength and were selected using the imaging software's autoexpose function to maximize exposure times without saturating the image. Dark current measurements were made periodically by taking images with the lens cap on and were subtracted from the image of the outcrop. Images were also taken with a uniform target (a Spectralon® panel) taking up the entire field of view to correct for spatial and spectral non-uniformities. These corrections were done using the following equation: $R_{ff} = \frac{\frac{(S_o - S_d)}{t_o}}{\frac{S_{ff} - S_d}{t_{ff}}}$, where R_{ff} is the reflectance following the flat field correction, S_o is the image of the outcrop, S_d is the dark current image, S_{ff} is the image of Spectralon for the flat field correction, t_o is the exposure times for the image of the outcrop, and t_{ff} is the exposure times for the flat field image. Then, an average spectrum of the darkest pixels in the image (D) was subtracted to remove atmospheric scattering (Chavez Jr, 1996 and references therein), and the image was divided by an average spectrum of a Spectralon® panel placed on the outcrop (S) within the field of view of the imager to complete the atmospheric correction: $R = \frac{R_{ff} - D}{S - D} * R_s$, where R is the fully calibrated reflectance image, and R_s is a spectrum of Spectralon®. Spectralon® is not a perfect reflector at all wavelengths, and the image was corrected for these non-Lambertian effects using spectrum HL-JFM-012 of SRT-99-050 from Labsphere acquired in the Reflectance Experiment Laboratory (RELAB; Brown University, RI, USA) and resampled to the wavelengths sampled by these imagers.

Samples from the outcrop were imaged in the laboratory at Headwall Photonics, Inc. (Fitchburg, MA, USA) using two pushbroom hyperspectral imagers. The Headwall

High Efficiency Hyperspec® Visible-Near Infrared (VNIR) E-Series imager scanned samples in 338 spectral channels from wavelengths 0.4-1.0 µm with a sampling interval of 1.785 nm and spectral resolution of 7 nm. The spectral resolution given here is the full width at half maximum of the slit width image intensity. The instantaneous field of view (IFOV) is 0.382 mrad, and exact spatial resolutions depended on the distance between the sensor and the sample. The Headwall High Efficiency Hyperspec® Shortwave Infrared (SWIR) X-Series imager measured samples in 138 spectral channels from wavelengths 0.950-2.603 µm with a spectral resolution of 12 nm and sampling interval of 12.0656 nm. The IFOV of this system is 1.2 mrad. Both systems have a foreoptic lens, spectrograph, and focal plane array. During imaging, samples were moved on a stage below the sensors at a controlled rate with the Headwall Hyperspec® Starter Kit™, which contains a controlled motorized stage and quartz tungsten halogen light source, in order to create three-dimensional image cubes or hypercubes.

The laboratory images were calibrated by subtracting a dark current measurement, ratioing to an image of Spectralon®, and correcting for the absolute reflectance properties of Spectralon®. The dark current measurement was done by taking an image with the lens cap on. Correction to reflectance (R) was done with the following equation: $R = \frac{S_t - S_d}{S_s - S_d} * R_s$, where S_t is the signal from the sample, S_d is the dark signal, S_s is signal from imaging Spectralon®, and R_s is the same reflectance spectrum of Spectralon® from RELAB as was used for the field measurements except resampled to the wavelength bands of these imaging systems.

VNIR and SWIR images were coregistered when possible, and the SWIR images were warped to the VNIR image size in Exelis Visual Information Systems ENVI®

software with a first degree polynomial and nearest neighbor resampling using manually-selected control points. The images were then stacked and joined by scaling SWIR to VNIR spectra at each pixel through a multiplicative factor assuming that the reflectance is the same at 996 nm (VNIR) and 997 nm (SWIR). Overlapping bands were then deleted. For some samples, VNIR and SWIR images could not be coregistered, generally where the samples were not flat. For those samples, VNIR and SWIR images were analyzed separately. Hyperspectral images were analyzed using spectral parameters (e.g., Clark and Roush, 1984; Pelkey et al., 2007) and mineral indicator parameters that are combinations of various spectral parameters. Equations used and interpretations are given in Table 2.

Spectra of points on samples and the outcrop were measured from 0.35-2.5 μm with an Analytical Spectral Devices, Inc. (ASD) Fieldspec 3 instrument. This instrument has a spectral resolution of 3 nm at 0.7 μm and 10 nm at 1.4 and 2.1 μm. Measurements are done with sampling intervals of 1.4 nm for wavelengths 0.35-1.0 μm and 2.0 nm for the remainder of the wavelength range, and output spectra are resampled to 1 nm sampling through ASD's internal software. All spectra were corrected for the spectrum of Spectralon® and were splice corrected to remove offsets between the ASD's three detectors. The field measurements were done with a contact probe, which illuminates the sample with a 0° incidence and measures the reflectance with a 30° emission angle, and the laboratory measurements were done using the bare fiber optic cable and an Oriel Instruments® model 66181 quartz tungsten halogen lamp housing with an F/0.85 condenser and model 68735 DC regulated power supply to illuminate the sample.

Major element chemistry (Al, C, Ca, Fe, K, Mg, Mn, N, Na, P, Si, and Ti) was

determined for 33 samples with 9 run in duplicate or triplicate at the Brown University Environmental Chemistry facilities. Concentrations of C and N were analyzed on a CE Instruments Model NC2100 Carbon-Nitrogen analyzer and were calculated using standards acetanilide, cyclohexanone, pine, and MT2711 and 2 blanks. For 14 of the samples, concentrations were analyzed by the same instrument setup but with varying amounts of sulfanilamide as a standard, 2 blanks, and both sulfanilamide and NIST2702 to check the quality of the measurements. To ensure the measurements were consistent, two standards were analyzed as unknowns after every ~10 samples and at the beginning and end of the run. For each of these measurements, samples were ground and dried overnight at 60°C. Approximately 10 mg of each were then weighed into tin capsules that were folded to seal and compress them and stored in a desiccator until analysis. The errors on these measurements (accuracy) determined from standards run as unknowns are <10% excluding one anomalous measurement and are <5% for samples with higher C. The precision determined from replicates are <4% (the standard deviation normalized to the average measured C for each set of replicates) or <0.2 wt% actual C except for one sample, which may have a higher standard deviation due to sample heterogeneity. The measured concentrations of N were 0 or near 0 for every sample and are not discussed further in this paper. The remaining major element concentrations were determined with Inductively Coupled Plasma-Atomic Emission Spectrometry (ICP-AES) after a flux fusion sample preparation using methods modified from Murray et al. (2000). Standard reference materials from the United States Geological Survey and National Institute of Standards and Technology (NIST2711, MAG-1, DTS-2B, NIST1646a, BIR-1, SGR-1, BHVO-2, NIST2702, and BCR-2) were run using the same methods as the unknown

samples. For a subset of samples, Cr and Ni were also analyzed, and SRM-1c and G-2 standards were run in addition to those listed above. Blanks containing only flux were run using the same methods, and the signal from these samples was subtracted. For the flux fusion preparation, 35-45 mg of sample mixed with 155-165 mg lithium metaborite flux in a graphite crucible were fused in a 1050°C oven for 10 minutes. The samples were then poured into 20 ml of 10% nitric acid, agitated for at least 30 minutes to fully dissolve the sample, and filtered to remove particulates with a 0.45 µm filter. The solutions were diluted further by adding 5 ml to 35 ml of 10% nitric acid. These ~4000x diluted solution were run on a JY2000 Ultrace ICP-AES with a JY AS 421 autosampler and 2400 g/mm holographic grating to determine element concentrations using emission peak wavelengths recommended by Murray et al. (2000). Final concentrations were determined using linear regressions of standards to convert intensities to concentration after subtracting blanks and correcting for drift during the ICP-AES measurements. Concentrations are reported in oxide weight percentages following geochemical convention, and all Fe is reported as FeO, the some Fe_2O_3 is also present. The accuracy of these methods was assessed using the calibration standards above from one of the three sets of analyses with values reported in this paper by calculating the linear regression converting intensity to concentration omitting one standard, then comparing the calculated values of the omitted standard with the actual values. This procedure was repeated for all standards. The average errors were <5% as a percentage of the actual concentrations or <0.03 wt% in actual concentrations for all elements except K, which had an average error of 7.5% or 0.11 wt%. The precision of these measurements was determined from standard deviations of replicates normalized to the average

concentrations in each sample. The variations were <5% with many <2% or <0.03 wt% in actual concentration for each element. All standards were used in the linear regression used to calculate element concentrations in unknown samples.

The mineral phases present were determined with x-ray diffraction (XRD) for 25 samples. Some of those samples were ground and dry-sieved to <45 μm particle size and analyzed on a Bruker D2 Phaser with a Cu Kα source and Lynx-eye 1D-detector with <680 eV energy resolution at 8 keV (designated BrU in Table 1). These samples were scanned from 5 to 70° 2θ for approximately 4 hours and rotated 15 times per minute. For smaller samples or coatings, the mineralogy was determined after grinding to particle sizes <150 μm on inXitu Terra XRD instruments. Some samples were measured from 5 to 54.75° 2θ on Terra #299 from the University of Winnipeg (designated UWin on Table 1) with a Cu Kα source and average 200 measurements with a total integration time of 2000 seconds. Other samples were analyzed using Terra #213 at the University of Rhode Island (designated URI on Table 1). This instrument has a Co Kα source and integrates for a total of 2500 seconds from 5 to 54.9° 2θ. XRD patterns were fit in Bruker Corporation's Diffrac.EVA V3.1 software through comparison with the ICDD PDF-2 release 2013 database.

4 RESULTS

4.1 Alteration of sediments

Sediments of the New Haven Arkose formation are exposed at the base of the outcrop. The contact between the sediments and the pillows is difficult to trace because the sediments have been pushed up between basaltic pillows, sometimes more than 1

meter. The baked sediments often have small green crystals that are not as apparent in sediments further from the basalts.

The top of sample Mer04-6 is from 12.5 cm below the nearest basalt. While this sample probably was still heated by emplacement of the basalts, it appears to be less baked than the sediments pushed up between the basalts. Reflectance spectra of this sample (not shown) are characterized by broad 1.4 and 1.9 μm absorption features due to an OH stretching vibration and an H-O-H combination band, respectively (e.g., Clark et al., 1990). The width of these bands suggests that there is water within the rock that is not structural. In places, there is also an absorption feature near 2.3 μm consistent with an Fe/Mg-clay (e.g., Clark et al., 1990). The bottom portion of that sample is a layer of coarse-grained orange sediment that shows hydration absorptions and additional spectral features at 2.23 and 2.34-2.35 μm. Mineralogic interpretation of these spectra are not unique and could result from either Al-OH combination bands in muscovite (Clark et al., 1990) or an Si-OH combination band in a hydrated silica such as opal (e.g., Aines and Rossman, 1984; Goryniuk et al., 2004) mixed with calcite, which has a third overtone of the C-O asymmetric stretching mode at 2.34 μm (Hunt and Salisbury, 1971), or chlorite, which has Mg-OH and/or Fe^{2+}-OH combination bands at 2.31-2.35 μm (Bishop et al., 2008; King and Clark, 1989). Muscovite, quartz, calcite, and chlorite are all identified in the sedimentary layer above this orange sediment by XRD, suggesting that all of these phases are likely contributing to the spectrum.

The key difference between Mer04-6 and the baked samples is that the baked samples are often finer grained and have larger green grains (Fig. 2). Infrared spectra of the matrix of sample Mer05-10 (Fig. 3a, spectrum 2) are relatively featureless, though

there may be weak features at 1.94 and 2.21-2.27 μm that are barely above the signal to noise of the imaging system. There are also spin-forbidden electronic transitions of Fe^{3+} at 0.53-0.54 and 0.68 μm likely due to hematite, though the feature that would be expected near 0.88 μm in hematite is weak to absent (Burns, 1993a; Scheinost et al., 1998). A few of the green crystals are visible in Fig. 2a-c (see green arrows in Fig. 2a), and spectrum 3 in Fig. 3 is of one such crystal. Spectral features at 2.23-2.26 μm and 2.34-2.36 μm suggest $AlFe^{3+}$-OH and Fe^{2+}-OH combination bands, respectively, in chamosite or another chlorite (Bishop et al., 2008), though the abundance of this component is too small to be isolated or distinguished from other clays in the sample with XRD. ASD spectra of other samples with similar green crystals that are large enough to get a clear spectrum of are also consistent with chlorite. There is a cluster of lighter grains (Fig. 2a; spectrum 1 in Fig. 3) that we interpret as likely hydrothermal or diagenetic based on its relationship cutting across sedimentary layers and what appears to be a reaction rim surrounding them. These grains consist of mostly calcite with its 2.34 μm C-O overtone (Hunt and Salisbury, 1971) along with some goethite based on electronic transitions of Fe^{3+} at 0.48 and 0.91-0.96 μm (Scheinost et al., 1998) and possible hydrated silica or quartz with minor water with an Si-OH combination band near 2.22 μm (Aines and Rossman, 1984; Goryniuk et al., 2004). This sample also has a coating with patches of red and pale yellow (Fig. 2d-f; spectra 4-5 in Fig. 3a). Spectra of the coating have absorption features at 2.20-2.23 and 2.34-2.35 μm and are consistent with chlorite, illite, and calcite. Spectrum 4 (Fig. 3a) of the redder part of the coating also contains iron oxides, probably both hematite and goethite.

Hyperspectral imaging of Mer05-10 (Fig. 2) shows that the interior is oxidized as

highlighted by the red slope parameter (red in Fig. 2b), and the coating is patchy with redder and greener areas (Fig. 2d, red slope and green peak parameters in Fig. 2e). This is a coating and not a rind based on the cross-section view of the sample (Fig.s 2a-c) showing that the coating is very thin and the contact between the sedimentary layers and the coating is sharp. There is little systematic mineralogic variation within the sedimentary layers. It may be that the combination of quartz, which is spectrally featureless in this wavelength range, and fine-grained iron oxides, which darken surfaces (Cloutis et al., 2011, 1990; Morris et al., 1985), overwhelm any differences in hydrated signatures from the clays. The coating is heterogeneous in the hyperspectral imaging with regions with more calcite and patches with more Al or Fe/Mg-rich clays.

XRD data (Table 3) show that these baked sediment samples generally contain albite, calcite, dolomite, quartz, muscovite, and chlorite, with some samples also having montmorillonite, goethite, or hematite. The proportions of each phase vary. For example, three portions of sample Mer0614-02 (Table 1) were analyzed. Mer0614-02-3 is heavily-altered sediment from closer to the basalts than the less altered Mer0614-02-2. Based on the relative peak heights from XRD and confirmed visually, Mer0614-02-3 has significantly more calcite. The hyaloclastite-like coating on the sample (Mer0614-02-1) in contact with the basalt appears to have glassy clasts and has more chlorite and less quartz than the other two samples.

Major element chemistry analyses (Table 3) show that these samples have high K, low Na, and generally lower Al, Mg, and Si contents relative to nearly all basaltic samples. As a result mostly of the low Na content, they plot on the right side of the compositional ternary diagram in Fig. 4. Fig. 4b shows three sets of samples of baked

sediments where both the interiors and coatings of the samples were analyzed. The coatings have higher Al and lower Mg than the interiors. For sample Mer0614-02, the hyaloclastite coating has higher Al and Fe and lower Mg contents than the interior, and the intermediate calcite-rich section has similar Al and Fe but lower Mg than the most interior sample. The high K concentrations in these coatings suggest that much of that material is derived from the sediments, though the high Al may result from interaction with the basalts.

4.2 Red alteration of basalts

The few meters of basaltic pillow lavas at the base of the section in closest contact with the sediments are red with red, white, and/or green coatings and rinds. Reflectance spectra of the interiors of these samples (Fig. 3b, spectra 4 and 7) show some weak crystal field transitions of Fe^{3+} at 0.53, 0.66, and 0.89 μm suggestive of hematite (Burns, 1993a; Scheinost et al., 1998). In spectrum 4, there is a weak 1.9 μm H-O-H combination as well as a weak feature at 2.34-2.35 μm that could be due to either chlorite or calcite, both of which are present in the sample. Spectra of the exterior such as spectra 3 and 6 (Fig. 3b) have Mg-OH and Fe^{2+}-OH combination bands consistent with chlorite (Bishop et al., 2008; King and Clark, 1989), while other areas (spectra 2 and 5) have bands at 2.20-2.24 μm suggestive of hydrated silica or an Al-OH combination in montmorillonite or another Al-rich clay (e.g., Aines and Rossman, 1984; Bishop et al., 2008; Clark et al., 1990). The presence of features near both 2.24 and 2.35 μm may also be partially due to illite, particularly in spectrum 5.

Hyperspectral imaging of two samples (Fig. 5) shows that clay and carbonate

minerals are generally confined to the alteration rinds and veins, and discrete areas with different mineralogies are mapped. In the samples shown in Fig. 5, the rinds contain considerable Al-bearing clays or hydrated silica (green). There is also likely some chlorite that appears to be confined to the inner (Mer04-19 in Fig.s 5d-f) or middle (Mer04-13 in Fig.s 5a-c) portions of the rinds. Calcite is difficult to distinguish in mixtures from chlorite due to overlapping absorption features at 2.34-2.35 μm but is almost certainly present in the rinds and in spectra 3-6 (Fig. 4) based on the high measured C contents of the rinds. In visible wavelengths, the interiors are strongly oxidized (high red slope, red color in Fig.s 5b and e). The green peak and BD660 parameters map the rinds well. We note that, for these samples, changes in color do not necessarily correlate with measurable changes in the mineralogy. Portions of the rind of Mer04-13 (Fig. 5a-c) are mapped by the green peak parameter but do not show signatures of secondary minerals seen further toward the exterior of the sample.

XRD measurements of these samples (Table 3 under basalts from bottom of section near sediments) show albite, clinopyroxene (diopside and/or aegirine) in some, and calcite in most samples. There are also clay minerals identified, including chlorite, illite, montmorillonite, and nontronite and muscovite in one. Some samples also have hematite. Chemical analyses of the samples show low K concentrations in all but one sample, Mer0614-04, which was friable material from between a pillow lava and the surrounding sediments. Most of these samples also have significantly higher Na_2O than average unaltered Talcott basalts which have 2.03 wt% as reported by Puffer et al. (1981). The Fe and Mg contents of these samples are lower than unaltered Talcott basalts (Puffer et al., 1981), while Si contents are variable. The interiors of samples Mer04-13

and Mer04-19 both have relatively high Si, while the exteriors of those samples have low Si. The interiors of the samples also have higher Na and Al and lower Ca, Mg, and Fe than the exteriors. As a result, the ternary diagram (Fig. 4c) shows that points move away from the Al_2O_3 and Na_2O+K_2O side with increasing alteration.

4.3 Green alteration of basalts

Stratigraphically higher in the section, there are zones that visibly appear to be more or differently altered. These are characterized by green alteration rinds and green breccias (Fig. 1b). One sample characteristic of this type of alteration (MerPillow) was analyzed by Greenberger et al. (in review), who found that the green alteration rind contains calcic and sodic clinopyroxenes interpreted to form in a 400-600+°C hydrothermal system or at high temperatures through deuteric alteration through comparisons with other reported contact metamorphic deposits (Bird et al., 1984; Dilles and Einaudi, 1992; Gillis et al., 1993; Laverne, 1987; Laverne et al., 1995; Manning and Bird, 1986; Marks et al., 2010; Vanko et al., 1996) and Fe/Mg-clays (likely chlorite and perhaps nontronite). The interior of this sample is purple and contains hematite.

Additional measurements of samples showing this type of alteration (in particular, Mer05-4, Mer05-7, and Mer05-9) are generally consistent with these results. Spectra of the interiors of these samples (Fig. 3c, spectra 3 and 5) show no clear indication of hydration above the signal to noise of the imaging system. These spectra do have electronic transitions near 0.65 and 0.85 μm that could be from Fe^{3+} within hematite (Burns, 1993a; Scheinost et al., 1998). The overall shape of the spectrum in the infrared could be due to Fe^{2+} in glass (e.g., Horgan and Bell III, 2012; Horgan et al., 2014) or

fine-grained iron oxides (Cloutis et al., 2011, 1990; Morris et al., 1985) or could be a textural effect (Fischer and Pieters, 1993). The exterior of the sample (Fig. 3c, spectra 1-2) shows spectral features due to chlorite or other Fe/Mg-clays and likely has contributions from Type A pyroxenes, which have such high Ca content that all Fe is in the M1 site, resulting in two bands near 1 μm and no 2 μm band (Cloutis and Gaffey, 1991). Spectrum 1 from Mer05-4 (Fig. 3c) in particular has an overall shape in the 1 μm region that seems to have contributions from these calcic clinopyroxenes. This spectrum also has a clay contribution based on the deep 1.9 μm H-O-H combination band and a complex absorption feature at 2.31-2.35 μm that could result from chlorite, smectite, or a mixed-layer chlorite/smectite (e.g., Bishop et al., 2008; Clark et al., 1990; Milliken and Bish, 2010). Both spectra 1 and 2 of the green rind have features due to Fe^{2+}/Fe^{3+} intervalence charge transfers at 0.73-0.74 μm commonly seen in chlorites and sometimes seen in partially oxidized calcic clinopyroxenes (e.g., Burns, 1993a; Cloutis and Gaffey, 1991). The relative peak heights at 0.55 and 0.8 μm in spectrum 2 are similar to spectra of coarser particle size separates of chlorites in King and Clark (1989) attributed to a particle size effect. That spectrum has an AlFe-OH or AlMg-OH combination band near 2.25 μm and Mg-OH or Fe^{2+}-OH combination bands at 2.31-2.35 μm consistent with chlorite (Bishop et al., 2008). There may also be contributions from nontronite in that spectrum (e.g., Bishop et al., 2008; Clark et al., 1990) or a mixed-layer chlorite/smectite (Milliken and Bish, 2010).

The spectra of the matrix and inner portions of the rind of Mer05-4 are particularly interesting. Spectra 5-7 (Fig. 3c) show a Fe^{2+} electronic transition near 1 μm. This feature is also present in ASD spectra and therefore is not an artifact of the join

between VNIR and SWIR images. Spectra 6 and 7 of inner portions of the rind also have a Fe^{2+}/Fe^{3+} charge transfer absorption feature around 0.80 μm, and both seem to have a second Fe^{2+} electronic transition centered around 2.35 μm. These spectra have similarities with high-Ca pyroxene-bearing (e.g., Cloutis and Gaffey, 1991) basalts but the peak in reflectance around 1.75 μm is at much longer wavelengths than a typical basalt (e.g., Adams, 1974). These crystal field transitions in the spectra are also similar to actinolite but lack the OH overtone and Fe/Mg-OH combination bands characteristic of those spectra (Mustard, 1992). It could be that the Fe^{2+} is in an altered pyroxene with sites and coordination more similar to actinolite or could be a mixture of pyroxene and actinolite.

The hyperspectral images (Fig. 6) show the relationships between hydrated phases (green in Fig.s 6c and f), calcite, and the anhydrous interior matrix. Similar to the red alteration, comparisons between the visible parameters (Fig.s 6b and e) and the infrared parameters (Fig. 6c and f) are not identical, but the green peak parameter maps the Fe/Mg-clay in the alteration rind fairly well. The clear Fe/Mg-clay signatures in Mer05-4 (Fig. 6c) are confined to the outermost portion of the rind.

XRD analyses of these samples show similar mineralogies in the interiors and exteriors with the addition of clays in the exterior. The samples have albite and clinopyroxene (diopside or aegirine), hematite in the interiors, and smectite and chlorite in the exteriors. The possible montmorillonite identified in the interior of Mer05-9 may be an artifact of the kapton window used during the measurements (e.g., Achilles et al., 2011). Most of these samples, with the exception of MerPillow interior and exterior, have lower CaO and all but some of the exterior samples have higher Na_2O than average unaltered Talcott basalts (Puffer et al., 1981). The Si contents, similar to samples with red

alteration, are generally either higher (up to 63 wt%) or lower (<40 wt%) than typical basalts. For samples where interiors and rinds were measured, Mg is 2-4 times higher in the rinds, and Fe is generally higher. Na concentrations are lower in the rinds. Mer05-7 has much higher Al in the interior than the exterior and also has K_2O content similar to the sediments measured. Differences in chemistry between the interior and exterior of sample MerPillow are much more subtle than for Mer05-4, Mer05-7, and Mer05-9. On the ternary diagram (Fig. 4d), the compositions move away from the Na_2O+K_2O apex and toward the FeO_T+MgO apex with alteration.

4.4 Mineralization of veins and vesicles

Mineralization of veins and vesicles is common throughout the outcrop, even in sections that have no other visible alteration. Calcite is ubiquitous, while quartz is identified lower in the section and prehnite is identified higher. Datolite is occasionally present. For example, there is a thick calcite vein in Mer04-13 (Fig. 5a-c), and there are pipe vesicles filled with calcite and lined with an Fe/Mg-clay, possibly saponite, in Mer05-4 (Fig. 6a-c). Mer05-9 (Fig. 6d-f) also has considerable calcite mineralization. MerPillow (Greenberger et al., in review) has calcite amygdules throughout the sample.

These phases are easily identified through spectroscopy. Calcite is identified (e.g., spectrum 1 in Fig. 3b and spectrum 4 in Fig. 3c) by the C-O overtone at 2.34 μm and a roll-off toward 2.5 μm (e.g., Hunt and Salisbury, 1971). Spectrum 1 in Fig. 3b shows contributions from an Fe^{3+}-oxide. Based on the positions of Fe^{3+} electronic transitions at 0.48, 0.67, and 0.92 μm, this is likely goethite (Burns, 1993a; Scheinost et al., 1998). Spectrum 4 in Fig. 3c from Mer05-4 (Fig. 6a-c) shows none of these electronic transitions

and is more consistent with a pure calcite. There is also datolite mineralization in a portion of Mer05-4 imaged before the rock was cut (not shown here) identified based on an OH stretching overtone at 1.47 μm and a complex set of absorption features from 2.0-2.5 μm due to boron-OH combination bands (Clark et al., 1990). Prehnite is identified in spectra and images by the 1.48 μm OH overtone and absorption features at 2.24, 2.29, and 2.35 μm (e.g., Clark et al., 2007; Ehlmann et al., 2009) and is mostly identified in small vugs or veins in the outcrop. Petrographic relationships are also seen with the hyperspectral images. For example, in Fig. 6c, Fe/Mg-clays rim the pipe vesicles filled with calcite. In visible imaging data, calcite is best identified by its brightness, since it is often the brightest phase in the sample.

Calcite is identified with XRD in most samples. XRD confirms field and spectral identifications of a vein of calcite (Mer05-8) and an area with prehnite (Mer05-38). Calcite was also identified in the field through reaction with dilute HCl. In chemical data, there are enrichments in CaO along with high CO_2 concentrations in some samples consistent with calcite mineralization.

4.5 Breccias

Throughout the section, there are breccias, with many appearing to be hyaloclastites with angular fragments of glass within a matrix of hydrothermal mineralization that is often calcite but occasionally quartz. Higher in the section near the green alteration, there is a breccia with a green matrix, calcite cement, and smaller, ripped up pillow lavas that may be a pillow breccia as described by Carlisle (1963). Samples Mer05-15 and Mer05-19 are from this unit. Spectra of the matrix of the green angular

clasts of Mer05-15 have a peak in reflectance at green wavelengths (green peak parameter), a weak absorption feature around 2.25 μm likely due to an $AlFe^{3+}$-OH or AlMg-OH combination band and a stronger feature at 2.33-2.36 from a Mg or Fe^{2+}-OH combination band typical of chlorite (Bishop et al., 2008; King and Clark, 1989). Calcite is identified by a C-O overtone at 2.34 μm and a decrease in reflectance toward 2.5 μm (Hunt and Salisbury, 1971). The calcite, bright in visible wavelengths (Fig. 7b-c), also has a positive slope in the SWIR and broad 1.4 and 1.9 μm features. This may be an optical effect, where the calcite is somewhat transparent, and spectral features from the surrounding chlorite contribute to what appears to be the calcite spectrum. There may also be minor Fe and water within the calcite. In the imaging data (Fig. 7), the calcite is mapped in veins between angular clasts that appear to be chlorite.

Albite, calcite, chlorite, and illite/muscovite are identified in both Mer05-15 and Mer05-19 through XRD analyses (Table 3). Mer05-19 also contains diopside and hematite. This mineralogy could result from alteration of volcanic glass. Relative to the unaltered Talcott basalt analyzed by Puffer et al. (1981), these samples have higher Mg and lower Al, Ca, and Si. Unlike most other basaltic samples analyzed, Na is not enriched in these samples.

4.6 Outcrop-scale hyperspectral imaging

Hyperspectral imaging of outcrops was done in VNIR wavelengths only, and comparisons of VNIR parameter maps of samples imaged in the laboratory with mineral mapping in SWIR wavelengths allow us to correlate VNIR data with types of alteration and mineralogy. Fig. 8 shows sediments of the New Haven Arkose at the base of the

formation and well-defined pillow basalts higher. There is considerable mixing spatially between the basalts and sediments. Of the samples labeled in Fig. 8, all but Mer05-11 are baked sediments. Mer05-11 is basalt, but identification of dolomite, muscovite, and quartz with XRD (Table 3) suggests some interaction with sediment. In Fig. 8b, the red slope and BD660 spectral parameters map the sediments. The red slope is likely due to oxidation and formation of hematite or other Fe^{3+}-oxides (e.g., Hunt and Ashley, 1979), and the 0.66 μm feature mapped by BD660 could be a spin-forbidden electronic transition of Fe^{3+} in oxides such as hematite or goethite (e.g., Burns, 1993a; Scheinost et al., 1998), a Fe^{2+}/Fe^{3+} charge transfer (e.g., Burns, 1993a), or an organic pigment. The coloration from those two parameters extends into the portion of the outcrop where pillow basalts are present, and many of these areas are sediments that were pushed up and baked by emplacement of the lavas. There are also red-orange coatings (Fig. 8a) that map in the parameters as orange and green due to the presence of both a red slope and a green peak (Fig. 8b). These coatings are often near or on the baked sediments, particularly where pillows have been removed (see Mer05-10 in Fig. 2 for an example of one of these samples), and field observations show that this association is correct. Higher, there are more areas that are just red in the parameters, and some of these are associated with oxidized cross-sections of pillow lavas. This red alteration is consistent with laboratory imaging of Mer04-13 and Mer04-19 (Fig. 5). On the left of the image, portions of a large pillow are relatively dark in the parameter map, suggesting that that material is less oxidized and altered in the ways that these parameters are mapping.

Stratigraphically higher, Fig. 9 shows a portion of the outcrop dominated by green alteration. Spectral parameters do indeed map most of the rocks with the green peak

parameter, and laboratory imaging (e.g., Fig.s 6-7) indicates that these greener areas have undergone more advanced alteration. There are a few areas that are redder, but the oxidation causing the reddening is much less intense than in Fig. 8. Portions of the image that are mapped as blue in Fig. 9b are either facing the sun and therefore are brighter or are calcite veins and amygdules.

5 DISCUSSION

Hydrothermal alteration and later diagenesis of pillow basalts and their underlying sediments in a lacustrine setting result in highly variable degrees and types of alteration. We identify at this outcrop large green grains (probably chlorite) within baked sediments, red coatings particularly on the baked sediments, red, white, and green rinds of basaltic pillow lavas, oxidation of pillow interiors to both red and purple colors, mineralization of vesicles and veins; hyaloclastite breccias and alteration of their clasts, and pervasive albitization. The secondary phases identified are aegirine, albite, calcic clinopyroxene, calcite, chlorite, datolite, goethite, hematite, illite, montmorillonite, nontronite and/or saponite, prehnite, and quartz. Some of these phases have been reported previously (e.g., Hanshaw, 1968; Puffer et al., 1981; Robinson Jr and Woodruff, 1988), but we add new mineral identifications and a discussion of these secondary mineral occurrences in context. We note that zeolites have been reported previously within the Talcott basalts (e.g., Hanshaw, 1968). However, we found little evidence of zeolites and found the mineralization at this particular site to be dominantly calcite with some quartz and prehnite. The prehnite, however, may have formed by reaction of zeolites such as laumontite with calcite and could potentially explain the lack of zeolites higher in the

section (Thompson, 1971). Prehnite facies are also stable at higher temperatures than zeolites (Frey and Robinson, 1999).

The compositions of the samples analyzed here are highly variable, and even measurements of interiors of pillow basalts are not consistent from sample to sample. Despite the heterogeneity, there are distinct trends with alteration seen in the elemental analyses (Fig. 4). Interiors of pillow basalts plot to the left of the exteriors on the ternary diagram (Fig. 4a) due to an enrichment in Na_2O in the interiors and a depletion in the exteriors relative to unaltered Talcott basalts reported by Puffer et al. (1981). FeO and MgO generally increase significantly from interior to exterior. For samples with green alteration rinds, the exteriors plot right and down (Fig. 4d) from the corresponding interior compositions because Na_2O decreases are coupled with large increases in MgO and often large increases in FeO_T. For samples with red alteration rinds, the trend on the ternary diagrams (Fig. 4c) is similar but does not dip as steeply downward due to lower MgO concentrations. In addition, the samples with less red alteration do not have such large Na_2O depletions as are often seen in the green alteration rinds. Coupled with generally lower FeO and MgO contents, the chemistries of these redder rinds do not plot near the FeO_T+MgO apex as the green rinds do. The sediments and their coatings show a very different trend: coatings plot more toward the Al_2O_3 apex as Al_2O_3 increases and MgO decreases. It is possible that the increased Al_2O_3 in at least some cases comes from the basalts. Puffer et al. (1981) note enrichments in Fe^{3+}, Na, and H_2O and depletions in Ca, Mg, and Si in altered Talcott Formation basalts. Our results agree with the enrichments that they found, but our data tell a more complicated story for Ca, Mg, and Si. There is significant mobility of nearly all elements in this system, and different

samples or different portions of the same sample show differences in enrichments and depletions of various elements.

The character of the alteration changes upward in the stratigraphy. The sediments at the base are baked and have larger green crystals that are probably chlorite, though they are too small to be identified with XRD. Sample Mer0614-02 shows calcite mineralization of the sediment closer to the basalt. This is a small-scale example of a larger trend observed in the Berlin Formation higher in the Hartford Basin stratigraphy by Kolleeny et al. (1996), where calcite is present, not dolomite, in the 2-3 m below the basalt. Several authors have reported contact metamorphism of sediments in the Hartford basin from Mesozoic volcanism (e.g., April, 1980; Gray, 1988; Heald, 1956; Kolleeny, 1996; Wolela and Gierlowski-Kordesch, 2007), consistent with our results. The lithified sediments analyzed here have variable compositions, but they have much lower SiO_2 content than the average New Haven Formation (63.71%) given by van de Kamp and Leake (1996) and higher CaO (2.75%) and CO_2 (2.06%). These differences may be due to the samples analyzed and the particular sedimentary facies selected; our samples are by no means representative of the entire New Haven Formation. Nevertheless, it is interesting that these samples are so enriched in CaO and CO_2 since that is an indicator of metamorphism elsewhere in the Hartford Basin (Kolleeny, 1996).

Within 2-3 m above the sediments, well-defined basalts are characterized by red alteration, oxidation, and clay formation. The spatial association of this alteration with the sediments suggests that the alteration is associated with the sediments, perhaps from fluids within wet sediments being driven off, and is supported by others who have noted alteration of the base of lava flows in the region and interpreted them as resulting from

interaction with sediments (Philpotts et al., 1996; Puffer et al., 1981). There is considerable mixing spatially between the basalts and sediments. Sediments were pushed up between pillows and dropped down to sit within depressions in the pillows. The clays identified in rinds here are more aluminous than those identified higher, with montmorillonite and even illite and muscovite more common. Dolomite, muscovite, illite, and quartz are seen with XRD in a few basaltic samples and coatings from this section and may be derived from the sediments. Stratigraphically higher, there are sections with more intense alteration with green rinds and purple interiors. This purple color is caused by fine-grained hematite and is similar to pillow lavas that underwent hydrothermal metamorphism in the Josephine Ophiolite described by Harper (1980). In the Hartford Basin, it has been suggested that the rocks oxidized at moderate to high temperatures because hematite is present and not maghemite (McIntosh et al., 1985). The green rinds contain Fe/Mg-clays, including chlorite and smectite, possibly a nontronite, and aegirine and calcic and sodic clinopyroxenes. These samples show larger changes in chemistry in Fig. 4 than the red-altered samples, suggesting more advanced alteration and water/rock interaction. Similarly, oceanic pillow basalts with green alteration have been interpreted to be more altered than samples with red halos of iron oxides (Alt et al., 1986), though there is no connection with sediments for altered seafloor basalts. In addition, we identify quartz mineralization in vesicles and veins only lower in the section and prehnite higher in the section, likely due to changes in fluid chemistry through time or changing pressures and temperatures of metamorphism. It is rare to see both prehnite and quartz with calcite and zeolites, and only prehnite or quartz is generally present with calcite (Thompson, 1971).

There are two secondary phases ubiquitous in this section: albite and calcite. The Na contents of these samples are higher than typical basalts, and sedimentary rocks from the Hartford, Newark, and Deerfield basins have been reported to be partially to completely albitized (Hubert et al., 1992; van de Kamp and Leake, 1996; Wolela and Gierlowski-Kordesch, 2007). It has been suggested that Na-rich brines formed during drier climatic periods that caused the lake in the Hartford Basin to dry up, and these brines then albitized the plagioclase in the sediments (Hubert et al., 1992; van de Kamp and Leake, 1996). We suggest that the Talcott Formation pillow basalts were albitized at the same time. Calcite also occurs throughout the section studied here and is present in nearly all samples analyzed, despite efforts to isolate matrices and avoid calcite when grinding some samples. Calcite likely formed through two processes. The first is low temperature hydrothermal alteration. Calcite is commonly seen as a late-stage product of hydrothermal alteration in lacustrine and oceanic pillow basalts (e.g., Alt et al., 1986; Robert, 2001). The second is as a result of the albitization, which would have liberated Ca from plagioclase and created Ca-rich brines, as has been suggested for some of the calcite within albitized sediments (van de Kamp and Leake, 1996). This interpretation is consistent with Greenberger et al. (in review) based on detailed micro-analyses of one sample from this outcrop that distinguished hydrothermal calcite amygdules in the rind and diagenetic calcite surrounded by albite in the interior. They also suggested that Ca is conserved in this system based on an average composition of all samples analyzed from this site (Table 3) close to the average unaltered Talcott basalt composition of Puffer et al. (1981). This interpretation requires significant HCO_3^- in the waters of the Hartford Basin.

With all of this alteration, no spectrum has been acquired here consistent with unaltered basalt or basaltic glass despite portions of the outcrop looking like crystalline basalts. The only spectrum reminiscent of basalt is from the pale blue, inner portion of the alteration rind of sample Mer05-4 (Fig. 3c, spectra 6 and 7), and this signature likely is not primary since it is only seen within the visibly altered rind and not in the interior of the sample. In addition, none of the samples analyzed are chemically consistent with basalts. The interiors of the samples have SiO_2 and Na_2O contents too high to be primary basalts, though some of this is explained by later albitization. In the exteriors, concentrations of those elements are low. All spectra also show signatures of oxidation, whether red oxidation to iron oxides or green resulting from Fe^{2+}/Fe^{3+} intervalence charge transfer bands within pyroxenes or clays. This hydrothermal system differed markedly from low temperature subaerial systems, where unaltered basalt remains deep in weathering profiles or within corestones despite formation of clays and oxides leached of any mobile cation (e.g., Nesbitt and Wilson, 1992; Nesbitt and Young, 1989). Here, there seems to be pervasive low-grade alteration with limited zones of more intense alteration in pillow rinds, fractures, and hyaloclastite breccias. Geochemical and petrological studies have been done on unaltered basalts collected in the Hartford Basin (e.g., Philpotts, 1998; Puffer et al., 1981). The outcrop here likely is so altered because these basalts erupted within a lake where there was ample water to alter the rocks, the resulting glass is more susceptible to weathering (e.g., Eggleton et al., 1987; Nesbitt and Wilson, 1992), and the system is more porous than subaerial basalts. In the Newark Basin, the porosity, permeability, and crystallinity of the igneous rocks are similarly thought to control the degrees and distributions of alteration (Cummings, 1987; Puffer and Student,

1992).

Hyperspectral imaging of outcrops in the field connects laboratory measurements with the types of alteration present. While there is not an exact correlation between mineralogy and spectroscopy at the limited wavelengths (0.42-1.1 μm) measured in the field, types of alteration including red oxidation, red-orange coatings, greener alteration, and calcite and other types of mineralization can be mapped, and these types of alteration often have characteristic mineral products that can be inferred. Mapping of outcrops in SWIR wavelengths, as was done in the laboratory, could map these mineralogies directly. On Mars, where there are volcanically-resurfaced lakes (Goudge et al., 2012), any past volcano-lacustrine interactions could have resulted in similar mineralogies and types of alteration, and this site in Connecticut is a good analog. Based on these results, this type of alteration on Mars would likely be heterogeneous: some areas would be more extensively altered, while others would be minimally-altered. This heterogeneity is seen here on scales of millimeters or centimeters, orders of magnitude below the 18 m/pixel spatial resolution of the Compact Reconnaissance Imaging Spectrometer for Mars (CRISM; Murchie et al., 2007) that is currently the orbital instrument capable of assessing mineralogy on the martian surface at highest spatial resolution. Identifying and understanding a system such as this one would require analyses with coordinated measurements of chemistry, mineralogy, and texture at multiple spatial scales as envisioned by the instrument suite on NASA's Mars rover planned for launch in 2020 (Mustard, 2013).

6 CONCLUSIONS

Hydrothermal alteration of pillow basalts erupted in a lacustrine setting and the underlying sediments results in varying types of alteration, and mineralogies and degrees of alteration vary on scales of millimeters to centimeters. Secondary minerals from the hydrothermal alteration and later diagenesis identified here are aegirine, albite, calcic clinopyroxene, calcite, chlorite, datolite, goethite, hematite, illite, montmorillonite, nontronite and/or saponite, prehnite, and quartz. The character of the alteration changes upward in the stratigraphy. At the base, the sediments are pushed up between pillow lavas and baked. These sediments have larger green grains in them that are likely chlorites as determined through spectroscopy and probably formed through hydrothermal or contact metamorphic processes. The basalts associated with these sediments are oxidized and altered, likely due to interaction with the sediments or fluids driven off the sediments. These pillow basalts have hematite in the interiors and Al- and Fe/Mg-bearing clays in their rinds, including chlorite, nontronite, montmorillonite, and occasionally illite. Stratigraphically higher, there are areas of more intense alteration with pillow basalts that have purple interiors and green rinds. The interiors of these samples have fine-grained hematite, and alteration minerals in the rinds contain aegirine, calcic clinopyroxenes, chlorite, and an Fe/Mg-smectite. Pillow basalt interiors generally have higher Na and Si than rinds, which are generally enriched in Fe and Mg. There are also calcite, quartz (lower in the section), prehnite (higher in the section), and datolite mineralization of vesicles and veins and hyaloclastite breccias that have in places been altered to chlorite and/or smectite. All parts of this section have been albitized. Every sample analyzed at this outcrop shows some evidence of alteration, including samples that visually appear to

be unaltered crystalline basalt. From this, we conclude there has been pervasive low-grade hydrothermal alteration and/or oxidation of these basalts with zones of more intense alteration usually confined to rims of pillow basalts, fractures, and veins. Similar mineralogies and spatial scales of alteration would be expected if there were past volcano-lacustrine interactions on Mars.

ACKNOWLEDGMENTS

We would like to thank Anthony Philpotts for showing us potential field sites in Connecticut. We also thank Kevin Cannon, Tim Goudge, Mary Peterson, Sandra Wiseman for field assistance. We are grateful to all of those who helped with various measurements: Dawn Cardace, Dave Murray, Joe Orchardo, Kevin Robertson, Amy Stander, Ken Wilkinson. We especially want to thank Kwok Wong and David Bannon at Headwall Photonics for the hyperspectral imaging measurements that were integral to this work. Finally, we thank Target in Meriden, CT, for allowing us to study this fantastic outcrop on their property and the City of Meriden, CT, for permitting sampling. This work was funded by the NASA Mars Data Analysis Program grant number NNX13AK72G and Brown University. EAC thanks the Canadian Space Agency, the Canada Foundation for Innovation, the Manitoba Research Innovations Fund, and the University of Winnipeg for supporting the acquisition of the University of Winnipeg facilities used in this study.

REFERENCES

Achilles, C., Ming, D.W., Morris, R.V., Blake, D.F., 2011. Detection Limit of Smectite

by Chemin IV Laboratory Instrument: Preliminary Implications for Chemin on the Mars Science Laboratory Mission. Lunar Planet. Sci. Conf., Abstract #2671.

Adams, J.B., 1974. Visible and Near-Infrared Diffuse Reflectance Spectra of Pyroxenes as Applied to Remote Sensing of Solid Objects in the Solar System. J. Geophys. Res. 79, PP. 4829–4836. doi:197410.1029/JB079i032p04829

Adams, J.B., 1975. Interpretation of visible and near-infrared diffuse reflectance spectra of pyroxenes and other rock-forming minerals. Infrared Raman Spectrosc. Lunar Terr. Miner. 91–116.

Aines, R.D., Rossman, G.R., 1984. Water in minerals? A peak in the infrared. J. Geophys. Res. Solid Earth 89, 4059–4071. doi:10.1029/JB089iB06p04059

Alt, J.C., France-Lanord, C., Floyd, P.A., Castillo, P., Galy, A., 1992. Low-Temperature Hydrothermal Alteration of Jurassic Ocean Crust, Site 801. Proc. Ocean Drill. Program Sci. Results 129, 415–427.

Alt, J.C., Honnorez, J., Laverne, C., Emmermann, R., 1986. Hydrothermal alteration of a 1 km section through the upper oceanic crust, Deep Sea Drilling Project Hole 504B: Mineralogy, chemistry and evolution of seawater-basalt interactions. J. Geophys. Res. Solid Earth 91, 10309–10335. doi:10.1029/JB091iB10p10309

Andrieux, P., Petit, S., 2010. Hydrothermal synthesis of dioctahedral smectites: The Al–Fe3+ chemical series. Appl. Clay Sci. 48, 5–17. doi:10.1016/j.clay.2009.11.019

April, R.H., 1980. Regularly interstratified chlorite/vermiculite in contact metamorphosed red beds, Newark Group, Connecticut Valley. Clays Clay Miner. 28, 1–11.

Arvidson, R.E., Squyres, S.W., Bell, J.F., Catalano, J.G., Clark, B.C., Crumpler, L.S.,

Souza, P.A. de, Fairén, A.G., Farrand, W.H., Fox, V.K., Gellert, R., Ghosh, A., Golombek, M.P., Grotzinger, J.P., Guinness, E.A., Herkenhoff, K.E., Jolliff, B.L., Knoll, A.H., Li, R., McLennan, S.M., Ming, D.W., Mittlefehldt, D.W., Moore, J.M., Morris, R.V., Murchie, S.L., Parker, T.J., Paulsen, G., Rice, J.W., Ruff, S.W., Smith, M.D., Wolff, M.J., 2014. Ancient Aqueous Environments at Endeavour Crater, Mars. Science 343, 1248097. doi:10.1126/science.1248097

Baker, V.R., Carr, M.H., Gulick, V.C., Williams, C.R., Marley, M.S., 1992. Channels and valley networks. Mars -1, 493–522.

Bibring, J.-P., Langevin, Y., Mustard, J.F., Poulet, F., Arvidson, R., Gendrin, A., Gondet, B., Mangold, N., Pinet, P., Forget, F., the OMEGA team, 2006. Global Mineralogical and Aqueous Mars History Derived from OMEGA/Mars Express Data. Science 312, 400 –404. doi:10.1126/science.1122659

Bird, D.K., Schiffman, P., Elders, W.A., Williams, A.E., McDowell, S.D., 1984. Calc-silicate mineralization in active geothermal systems. Econ. Geol. 79, 671–695. doi:10.2113/gsecongeo.79.4.671

Bishop, J.L., Lane, M.D., Dyar, M.D., Brown, A.J., 2008. Reflectance and emission spectroscopy study of four groups of phyllosilicates: smectites, kaolinite-serpentines, chlorites and micas. Clay Miner. 43, 35 –54. doi:10.1180/claymin.2008.043.1.03

Bishop, J.L., Schiffman, P., Southard, R., 2002. Geochemical and mineralogical analyses of palagonitic tuffs and altered rinds of pillow basalts in Iceland and applications to Mars. Geol. Soc. Lond. Spec. Publ. 202, 371 –392. doi:10.1144/GSL.SP.2002.202.01.19

Burns, R.G., 1993a. Mineralogical applications of crystal field theory. Cambridge University Press, 2nd ed, 576 pp.

Burns, R.G., 1993b. Origin of electronic spectra of minerals in the visible to near-infrared region. Remote Geochem. Anal. Elem. Mineral. Compos. 4, 3–29.

Carlisle, D., 1963. Pillow Breccias and Their Aquagene Tuffs, Quadra Island, British Columbia. J. Geol. 71, 48–71.

Chavez Jr, P.S., 1996. Image-Based Atmospheric Corrections-Revisited and Improved. Photogramm. Eng. Remote Sens. 62, 1025–1036.

Clark, R.N., King, T.V.V., Klejwa, M., Swayze, G.A., Vergo, N., 1990. High Spectral Resolution Reflectance Spectroscopy of Minerals. J. Geophys. Res. 95, 12653–12680. doi:199010.1029/JB095iB08p12653

Clark, R.N., Roush, T.L., 1984. Reflectance Spectroscopy: Quantitative Analysis Techniques for Remote Sensing Applications. J. Geophys. Res. 89, PP. 6329–6340. doi:198410.1029/JB089iB07p06329

Clark, R.N., Swayze, G.A., Wise, R., Livo, E., Hoefen, T., Kokaly, R., Sutley, S.J., 2007. "Usgs digital spectral library splib06a: US Geological Survey, data series 231.

Cloutis, E.A., Gaffey, M.J., 1991. Pyroxene Spectroscopy Revisited: Spectral-Compositional Correlations and Relationship to Geothermometry. J. Geophys. Res. 96, PP. 22,809–22,826. doi:199110.1029/91JE02512

Cloutis, E.A., Gaffey, M.J., Smith, D.G.W., Lambert, R.S.J., 1990. Reflectance spectra of mafic silicate-opaque assemblages with applications to meteorite spectra. Icarus 84, 315–333. doi:10.1016/0019-1035(90)90041-7

Cloutis, E.A., Hiroi, T., Gaffey, M.J., Alexander, C.M.O., Mann, P., 2011. Spectral

reflectance properties of carbonaceous chondrites: 1. CI chondrites. Icarus 212, 180–209. doi:10.1016/j.icarus.2010.12.009

Cousins, C.R., Crawford, I.A., Carrivick, J.L., Gunn, M., Harris, J., Kee, T.P., Karlsson, M., Carmody, L., Cockell, C., Herschy, B., Joy, K.H., 2013. Glaciovolcanic hydrothermal environments in Iceland and implications for their detection on Mars. J. Volcanol. Geotherm. Res. 256, 61–77. doi:10.1016/j.jvolgeores.2013.02.009

Cummings, W., 1987. Mineralization at the Fanwood & Summit Quarries, New Jersey. Rocks Miner. 62, 150–159.

Cummins, L.E., Arthur, J.D., Ragland, P.C., 1992. Classification and tectonic implications for early Mesozoic magma types of the Circum-Atlantic. Geol. Soc. Am. Spec. Pap. 268, 119–136. doi:10.1130/SPE268-p119

Dilles, J.H., Einaudi, M.T., 1992. Wall-rock alteration and hydrothermal flow paths about the Ann-Mason porphyry copper deposit, Nevada; a 6-km vertical reconstruction. Econ. Geol. 87, 1963–2001. doi:10.2113/gsecongeo.87.8.1963

Eggleton, R.A., Foudoulis, C., Varkevisser, D., 1987. Weathering of basalt; changes in rock chemistry and mineralogy. Clays Clay Miner. 35, 161–169.

Ehlmann, B.L., Mustard, J.F., Clark, R.N., Swayze, G.A., Murchie, S.L., 2011a. Evidence for Low-Grade Metamorphism, Hydrothermal Alteration, and Diagenesis on Mars from Phyllosilicate Mineral Assemblages. Clays Clay Miner. 59, 359–377. doi:10.1346/CCMN.2011.0590402

Ehlmann, B.L., Mustard, J.F., Murchie, S.L., Bibring, J.-P., Meunier, A., Fraeman, A.A., Langevin, Y., 2011b. Subsurface water and clay mineral formation during the

early history of Mars. Nature 479, 53–60. doi:10.1038/nature10582

Ehlmann, B.L., Mustard, J.F., Swayze, G.A., Clark, R.N., Bishop, J.L., Poulet, F., Marais, D.J.D., Roach, L.H., Milliken, R.E., Wray, J.J., Barnouin-Jha, O., Murchie, S.L., 2009. Identification of hydrated silicate minerals on Mars using MRO-CRISM: Geologic context near Nili Fossae and implications for aqueous alteration. J. Geophys. Res. 114, 33 PP. doi:200910.1029/2009JE003339

El-Tabakh, M., Riccioni, R., Schreiber, B.C., 1997. Evolution of late Triassic rift basin evaporites (Passaic Formation): Newark Basin, Eastern North America. Sedimentology 44, 767–790. doi:10.1046/j.1365-3091.1997.d01-47.x

Farmer, J.D., Des Marais, D.J., 1999. Exploring for a record of ancient Martian life. J. Geophys. Res. Planets 104, 26977–26995. doi:10.1029/1998JE000540

Fassett, C.I., Head III, J.W., 2008a. The timing of martian valley network activity: Constraints from buffered crater counting. Icarus 195, 61–89. doi:10.1016/j.icarus.2007.12.009

Fassett, C.I., Head III, J.W., 2008b. Valley network-fed, open-basin lakes on Mars: Distribution and implications for Noachian surface and subsurface hydrology. Icarus 198, 37–56. doi:10.1016/j.icarus.2008.06.016

Fischer, E.M., Pieters, C.M., 1993. The Continuum Slope of Mars: Bidirectional Reflectance Investigations and Applications to Olympus Mons. Icarus 102, 185–202. doi:10.1006/icar.1993.1043

Frey, M., Robinson, D., 1999. Low-grade metamorphism. Blackwell Science, Oxford, UK.

Gillis, K.M., Thompson, G., Kelley, D.S., 1993. A view of the lower crustal component

of hydrothermal systems at the Mid-Atlantic Ridge. J. Geophys. Res. Solid Earth 98, 19597–19619. doi:10.1029/93JB01717

Goryniuk, M.C., Rivard, B.A., Jones, B., 2004. The reflectance spectra of opal-A (0.5–25 μm) from the Taupo Volcanic Zone: Spectra that may identify hydrothermal systems on planetary surfaces. Geophys. Res. Lett. 31, L24701. doi:10.1029/2004GL021481

Goudge, T.A., Head, J.W., Mustard, J.F., Fassett, C.I., 2012. An analysis of open-basin lake deposits on Mars: Evidence for the nature of associated lacustrine deposits and post-lacustrine modification processes. Icarus 219, 211–229. doi:10.1016/j.icarus.2012.02.027

Gray, N.H., 1988. The origin of copper occurrences in the Hartford basin. Stud. Early Mesoz. Basins East. U. S. US Geol. Surv. Bull. 1776, 341–349.

Greenberger, R.N., Mustard, J.F., Cloutis, E.A., Mann, P., Wilson, J.H., Flemming, R.L., Robertson, K.M., Salvatore, M.R., Edwards, C.S., in review. Hydrothermal alteration and diagenesis of terrestrial lacustrine pillow basalts: coordination of hyperspectral imaging with laboratory measurements. Geochim. Cosmochim. Acta.

Hanshaw, P., 1968. Bedrock Geologic Map of the Meriden Quadrangle, New Haven, Hartford, and Middlesex Counties, Connecticut. US Geol. Surv. Geol. Quadrang. Maps U. S. 4 pp.

Harper, G.D., 1980. The Josephine Ophiolite—Remains of a Late Jurassic marginal basin in northwestern California. Geology 8, 333–337. doi:10.1130/0091-7613(1980)8<333:TJOOAL>2.0.CO;2

Heald, M.T., 1956. Cementation of Triassic Arkoses in Connecticut and Massachusetts. Geol. Soc. Am. Bull. 67, 1133–1154. doi:10.1130/0016-7606(1956)67[1133:COTAIC]2.0.CO;2

Horgan, B., Bell III, J.F., 2012. Widespread weathered glass on the surface of Mars. Geology 40, 391–394. doi:10.1130/G32755.1

Horgan, B.H.N., Cloutis, E.A., Mann, P., Bell III, J.F., 2014. Near-infrared spectra of ferrous mineral mixtures and methods for their identification in planetary surface spectra. Icarus 234, 132–154. doi:10.1016/j.icarus.2014.02.031

Hubert, J.F., Feshbach-Meriney, P.E., Smith, M.A., 1992. The Triassic-Jurassic Hartford Rift Basin, Connecticut and Massachusetts: Evolution, Sandstone Diagenesis, and Hydrocarbon History (1). AAPG Bull. 76, 1710–1734.

Hunt, G.R., Ashley, R.P., 1979. Spectra of altered rocks in the visible and near infrared. Econ. Geol. 74, 1613–1629. doi:10.2113/gsecongeo.74.7.1613

Hunt, G.R., Salisbury, J.W., 1971. Visible and near infrared spectra of minerals and rocks. II. Carbonates. Mod. Geol. 2, 23–30.

Hynek, B.M., Phillips, R.J., 2003. New data reveal mature, integrated drainage systems on Mars indicative of past precipitation. Geology 31, 757–760. doi:10.1130/G19607.1

Irwin, R.P., Craddock, R.A., Howard, A.D., 2005. Interior channels in Martian valley networks: Discharge and runoff production. Geology 33, 489–492. doi:10.1130/G21333.1

Keith, T.E.C., Staples, L.W., 1985. Zeolites in Eocene basaltic pillow lavas of the Siletz River volcanics, central Coast Range, Oregon. Clays Clay Miner. 33, 135–144.

King, T.V.V., Clark, R.N., 1989. Spectral characteristics of chlorites and Mg-serpentines using high-resolution reflectance spectroscopy. J. Geophys. Res. Solid Earth 94, 13997–14008. doi:10.1029/JB094iB10p13997

Kolleeny, J., 1996. Contact Metamorphism of Calcrete in New Haven Arkose (TR/J): Role of Infiltration Metasomatism and Hydrothermal Boiling. Presented at the Long Island Geologists Conference on "Geology of Long Island and Metropolitan New York," State University of New York at Stony Brook, pp. 73–82.

Laskowich, C., Puffer, J.H., 1990. Volcanic diapirs of the Orange Mountain Basalt, New Jersey. NJ Acad Sci Bull 35, 1–9.

Laverne, C., 1987. Unusual occurrences of aegirine-augite, fassaite and melanite in oceanic basalts (DSDP Hole 504B). Lithos 20, 135–151. doi:10.1016/0024-4937(87)90003-X

Laverne, C., Vanko, D.A., Tartarotti, P., Alt, J.C., 1995. 15. Chemistry and geothermometry of secondary minerals from the deep sheeted dike complex, hole 504B1, in: Proceedings of the Ocean Drilling Program, Scientific Results. p. 140.

Lowell, R.P., Rona, P.A., Von Herzen, R.P., 1995. Seafloor hydrothermal systems. J. Geophys. Res. Solid Earth 100, 327–352. doi:10.1029/94JB02222

Manning, C.E., Bird, D.K., 1986. Hydrothermal clinopyroxenes of the Skaergaard intrusion. Contrib. Mineral. Petrol. 92, 437–447. doi:10.1007/BF00374426

Marks, N., Schiffman, P., Zierenberg, R.A., Franzson, H., Fridleifsson, G.Ó., 2010. Hydrothermal alteration in the Reykjanes geothermal system: Insights from Iceland deep drilling program well RN-17. J. Volcanol. Geotherm. Res. 189, 172–190. doi:10.1016/j.jvolgeores.2009.10.018

McHone, J.G., Butler, J.R., 1984. Mesozoic igneous provinces of New England and the opening of the North Atlantic Ocean. Geol. Soc. Am. Bull. 95, 757–765. doi:10.1130/0016-7606(1984)95<757:MIPONE>2.0.CO;2

McIntosh, W.C., Hargraves, R.B., West, C.L., 1985. Paleomagnetism and oxide mineralogy of Upper Triassic to Lower Jurassic red beds and basalts in the Newark Basin. Geol. Soc. Am. Bull. 96, 463–480. doi:10.1130/0016-7606(1985)96<463:PAOMOU>2.0.CO;2

Merino, E., Girard, J.-P., May, M.T., Ranganathan, V., 1997. Diagenetic mineralogy, geochemistry, and dynamics of Mesozoic arkoses, Hartford rift basin, Connecticut, U.S.A. J. Sediment. Res. 67, 212–224. doi:10.1306/D4268536-2B26-11D7-8648000102C1865D

Milliken, R.E., Bish, D.L., 2010. Sources and sinks of clay minerals on Mars. Philos. Mag. 90, 2293–2308. doi:10.1080/14786430903575132

Morris, R.V., Jr, H.V.L., Lawson, C.A., Jr, E.K.G., Nace, G.A., Stewart, C., 1985. Spectral and Other Physicochemical Properties of Submicron Powders of Hematite (α-Fe2O3), Maghemite (γ-Fe2O3), Magnetite (Fe3O4), Goethite (α-FeOOH), and Lepidocrocite (γ-FeOOH). J. Geophys. Res. 90, PP. 3126–3144. doi:198510.1029/JB090iB04p03126

Morris, R.V., Ruff, S.W., Gellert, R., Ming, D.W., Arvidson, R.E., Clark, B.C., Golden, D.C., Siebach, K., Klingelhöfer, G., Schröder, C., Fleischer, I., Yen, A.S., Squyres, S.W., 2010. Identification of Carbonate-Rich Outcrops on Mars by the Spirit Rover. Science 329, 421–424. doi:10.1126/science.1189667

Murchie, S., Arvidson, R., Bedini, P., Beisser, K., Bibring, J.-P., Bishop, J., Boldt, J.,

Cavender, P., Choo, T., Clancy, R.T., Darlington, E.H., Marais, D.D., Espiritu, R., Fort, D., Green, R., Guinness, E., Hayes, J., Hash, C., Heffernan, K., Hemmler, J., Heyler, G., Humm, D., Hutcheson, J., Izenberg, N., Lee, R., Lees, J., Lohr, D., Malaret, E., Martin, T., McGovern, J.A., McGuire, P., Morris, R., Mustard, J., Pelkey, S., Rhodes, E., Robinson, M., Roush, T., Schaefer, E., Seagrave, G., Seelos, F., Silverglate, P., Slavney, S., Smith, M., Shyong, W.-J., Strohbehn, K., Taylor, H., Thompson, P., Tossman, B., Wirzburger, M., Wolff, M., 2007. Compact Reconnaissance Imaging Spectrometer for Mars (CRISM) on Mars Reconnaissance Orbiter (MRO). J. Geophys. Res. 112, 57 PP. doi:200710.1029/2006JE002682

Murchie, S.L., Mustard, J.F., Ehlmann, B.L., Milliken, R.E., Bishop, J.L., McKeown, N.K., Dobrea, E.Z.N., Seelos, F.P., Buczkowski, D.L., Wiseman, S.M., Arvidson, R.E., Wray, J.J., Swayze, G., Clark, R.N., Marais, D.J.D., McEwen, A.S., Bibring, J.-P., 2009. A synthesis of Martian aqueous mineralogy after 1 Mars year of observations from the Mars Reconnaissance Orbiter. J. Geophys. Res. 114, 30 PP. doi:200910.1029/2009JE003342

Murray, R., Miller, D.J., Kryc, K., 2000. Analysis of major and trace elements in rocks, sediments, and interstitial waters by inductively coupled plasma–atomic emission spectrometry (ICP-AES). ODP Tech Note 29, 1–27.

Mustard, J.F., 1992. Chemical analysis of actinolite from reflectance spectra. Am. Mineral. 77, 345–358.

Mustard, J.F., 2013. Scientific Objectives and Opportunities Associated with NASA's Mars 2020 Rover Mission, in: 2013 GSA Annual Meeting in Denver.

Mustard, J.F., Murchie, S.L., Pelkey, S.M., Ehlmann, B.L., Milliken, R.E., Grant, J.A., Bibring, J.-P., Poulet, F., Bishop, J., Dobrea, E.N., Roach, L., Seelos, F., Arvidson, R.E., Wiseman, S., Green, R., Hash, C., Humm, D., Malaret, E., McGovern, J.A., Seelos, K., Clancy, T., Clark, R., Marais, D.D., Izenberg, N., Knudson, A., Langevin, Y., Martin, T., McGuire, P., Morris, R., Robinson, M., Roush, T., Smith, M., Swayze, G., Taylor, H., Titus, T., Wolff, M., 2008. Hydrated silicate minerals on Mars observed by the Mars Reconnaissance Orbiter CRISM instrument. Nature 454, 305–309. doi:10.1038/nature07097

Nesbitt, H.W., Wilson, R.E., 1992. Recent chemical weathering of basalts. Am. J. Sci. 292, 740 –777. doi:10.2475/ajs.292.10.740

Nesbitt, H.W., Young, G.M., 1989. Formation and Diagenesis of Weathering Profiles. J. Geol. 97, 129–147.

Pelkey, S.M., Mustard, J.F., Murchie, S., Clancy, R.T., Wolff, M., Smith, M., Milliken, R., Bibring, J.-P., Gendrin, A., Poulet, F., Langevin, Y., Gondet, B., 2007. CRISM multispectral summary products: Parameterizing mineral diversity on Mars from reflectance. J. Geophys. Res. 112, 18 PP. doi:200710.1029/2006JE002831

Philpotts, A.R., 1978. Rift-Associated Igneous Activity in Eastern North America, in: Neumann, E.-R., Ramberg, I.B. (Eds.), Petrology and Geochemistry of Continental Rifts, NATO Advanced Study Institutes Series. Springer Netherlands, pp. 133–154.

Philpotts, A.R., 1992. A model for emplacement of magma in the Mesozoic Hartford basin. Geol. Soc. Am. Spec. Pap. 268, 137–148. doi:10.1130/SPE268-p137

Philpotts, A.R., 1998. Nature of a flood-basalt-magma reservoir based on the compositional variation in a single flood-basalt flow and its feeder dike in the Mesozoic Hartford Basin, Connecticut. Contrib. Mineral. Petrol. 133, 69–82. doi:10.1007/s004100050438

Philpotts, A.R., Carroll, M., Hill, J.M., 1996. Crystal-Mush Compaction and the Origin of Pegmatitic Segregation Sheets in a Thick Flood-Basalt Flow in the Mesozoic Hartford Basin, Connecticut. J. Petrol. 37, 811–836. doi:10.1093/petrology/37.4.811

Philpotts, A.R., Martello, A., 1986. Diabase feeder dikes for the Mesozoic basalts in southern New England. Am. J. Sci. 286, 105–126. doi:10.2475/ajs.286.2.105

Philpotts, A.R., Reichenbach, I., 1985. Differentiation of Mesozoic basalts of the Hartford basin, Connecticut. Geol. Soc. Am. Bull. 96, 1131–1139. doi:10.1130/0016-7606(1985)96<1131:DOMBOT>2.0.CO;2

Pratt, L.M., Shaw, C.A., Burruss, R.C., 1988. Thermal histories of the Hartford and Newark basins inferred from maturation indices of organic matter. Stud. Early Mesoz. Basins East. U. S. 58–62.

Puffer, J.H., 1992. Eastern North American flood basalts in the context of the incipient breakup of Pangea. Geol. Soc. Am. Spec. Pap. 268, 95–118. doi:10.1130/SPE268-p95

Puffer, J.H., Benimoff, A.I., 1997. Fractionation, Hydrothermal Alteration, and Wall-Rock Contamination of an Early Jurassic Diabase Intrusion: Laurel Hill, New Jersey. J. Geol. 105, 99–110.

Puffer, J.H., Hurtubise, D.O., Geiger, F.J., Lechler, P., 1981. Chemical Composition and

Stratigraphic Correlation of the Mesozoic Basalt units of the Newark Basin, New Jersey, and the Hartford Basin, Connecticut. Geol. Soc. Am. Bull. 92, 515–553. doi:10.1130/GSAB-P2-92-515

Puffer, J.H., Laskowich, C., 2012. Volcanic diapirs in the Orange Mountain flood basalt: New Jersey, USA. J. Volcanol. Geotherm. Res. 237–238, 1–9. doi:10.1016/j.jvolgeores.2012.05.010

Puffer, J.H., Student, J.J., 1992. Volcanic structures, eruptive style, and posteruptive deformation and chemical alteration of the Watchung flood basalts, New Jersey. Geol. Soc. Am. Spec. Pap. 268, 261–278. doi:10.1130/SPE268-p261

Robert, C., 2001. Hydrothermal alteration processes of the Tertiary lavas of Northern Ireland. Mineral. Mag. 65, 543–557.

Robinson Jr, G.R., Woodruff, L.G., 1988. Characteristics of base-metal and barite vein deposits associated with rift basins, with examples from some early Mesozoic basins of eastern North America. US Geol Surv. Bull 1776, 377–390.

Scheinost, A.C., Chavernas, A., Barron, V., Torrent, J., 1998. Use and limitations of second-derivative diffuse reflectance spectroscopy in the visible to near-infrared range to identify and quantify Fe oxide minerals in soils. Clays Clay Miner. 46, 528 –536.

Seidemann, D.E., 1988. The hydrothermal addition of excess 40Ar at the lava flows from the early Jurassic in the Hartford Basin (Northeastern U.S.A.): Implications for the time scale. Chem. Geol. Isot. Geosci. Sect. 72, 37–45. doi:10.1016/0168-9622(88)90035-8

Seidemann, D.E., Masterson, W.D., Dowling, M.P., Turekian, K.K., 1984. K-Ar dates

and 40Ar/39Ar age spectra for Mesozoic basalt flows of the Hartford Basin, Connecticut, and the Newark Basin, New Jersey. Geol. Soc. Am. Bull. 95, 594–598. doi:10.1130/0016-7606(1984)95<594:KDAAAS>2.0.CO;2

Seyfried Jr., W.E., Mottl, M.J., 1982. Hydrothermal alteration of basalt by seawater under seawater-dominated conditions. Geochim. Cosmochim. Acta 46, 985–1002. doi:10.1016/0016-7037(82)90054-0

Seyfried, W.E., Berndt, M.E., Seewald, J.S., 1988. Hydrothermal alteration processes at mid-ocean ridges; constraints from diabase alteration experiments, hot spring fluids and composition of the oceanic crust. Can. Mineral. 26, 787–804.

Seyfried, W.E., Jr., 1987. Experimental and Theoretical Constraints on Hydrothermal Alteration Processes at Mid-Ocean Ridges. Annu. Rev. Earth Planet. Sci. 15, 317. doi:10.1146/annurev.ea.15.050187.001533

Squyres, S.W., Arvidson, R.E., Bell, J.F., Brückner, J., Cabrol, N.A., Calvin, W., Carr, M.H., Christensen, P.R., Clark, B.C., Crumpler, L., Marais, D.J.D., d' Uston, C., Economou, T., Farmer, J., Farrand, W., Folkner, W., Golombek, M., Gorevan, S., Grant, J.A., Greeley, R., Grotzinger, J., Haskin, L., Herkenhoff, K.E., Hviid, S., Johnson, J., Klingelhöfer, G., Knoll, A.H., Landis, G., Lemmon, M., Li, R., Madsen, M.B., Malin, M.C., McLennan, S.M., McSween, H.Y., Ming, D.W., Moersch, J., Morris, R.V., Parker, T., Rice, J.W., Richter, L., Rieder, R., Sims, M., Smith, M., Smith, P., Soderblom, L.A., Sullivan, R., Wänke, H., Wdowiak, T., Wolff, M., Yen, A., 2004. The Opportunity Rover's Athena Science Investigation at Meridiani Planum, Mars. Science 306, 1698–1703. doi:10.1126/science.1106171

Squyres, S.W., Arvidson, R.E., Bell, J.F., Calef, F., Clark, B.C., Cohen, B.A., Crumpler, L.A., Souza, P.A. de, Farrand, W.H., Gellert, R., Grant, J., Herkenhoff, K.E., Hurowitz, J.A., Johnson, J.R., Jolliff, B.L., Knoll, A.H., Li, R., McLennan, S.M., Ming, D.W., Mittlefehldt, D.W., Parker, T.J., Paulsen, G., Rice, M.S., Ruff, S.W., Schröder, C., Yen, A.S., Zacny, K., 2012. Ancient Impact and Aqueous Processes at Endeavour Crater, Mars. Science 336, 570–576. doi:10.1126/science.1220476

Summons, R.E., Amend, J.P., Bish, D., Buick, R., Cody, G.D., Des Marais, D.J., Dromart, G., Eigenbrode, J.L., Knoll, A.H., Sumner, D.Y., 2011. Preservation of Martian Organic and Environmental Records: Final Report of the Mars Biosignature Working Group. Astrobiology 11, 157–181. doi:10.1089/ast.2010.0506

Thompson, A.B., 1971. P CO2 in low-grade metamorphism; zeolite, carbonate, clay mineral, prehnite relations in the system CaO-Al2O3-SiO2-CO2-H2O. Contrib. Mineral. Petrol. 33, 145–161. doi:10.1007/BF00386112

Van de Kamp, P.C., Leake, B.E., 1996. Petrology, geochemistry, and Na metasomatism of Triassic-Jurassic non-marine clastic sediments in the Newark, Hartford, and Deerfield rift basins, northeastern USA. Chem. Geol. 133, 89–124. doi:10.1016/S0009-2541(96)00071-X

Vaniman, D.T., Bish, D.L., Ming, D.W., Bristow, T.F., Morris, R.V., Blake, D.F., Chipera, S.J., Morrison, S.M., Treiman, A.H., Rampe, E.B., Rice, M., Achilles, C.N., Grotzinger, J.P., McLennan, S.M., Williams, J., Bell, J.F., Newsom, H.E., Downs, R.T., Maurice, S., Sarrazin, P., Yen, A.S., Morookian, J.M., Farmer, J.D., Stack, K., Milliken, R.E., Ehlmann, B.L., Sumner, D.Y., Berger, G., Crisp, J.A.,

Hurowitz, J.A., Anderson, R., Marais, D.J.D., Stolper, E.M., Edgett, K.S., Gupta, S., Spanovich, N., and MSL Science Team, 2014. Mineralogy of a Mudstone at Yellowknife Bay, Gale Crater, Mars. Science 343, 1243480. doi:10.1126/science.1243480

Vanko, D.A., Laverne, C., Tartarotti, P., Alt, J.C., 1996. Chemistry and origin of secondary minerals from the deep sheeted dikes cored during Leg 148 (Hole 504B), in: Proceedings-Ocean Drilling Program Scientific Results. National Science Foundation, pp. 71–86.

Von Damm, K.L., Edmond, J.M., Grant, B., Measures, C.I., Walden, B., Weiss, R.F., 1985. Chemistry of submarine hydrothermal solutions at 21 °N, East Pacific Rise. Geochim. Cosmochim. Acta 49, 2197–2220. doi:10.1016/0016-7037(85)90222-4

Warner, N.H., Farmer, J.D., 2010. Subglacial Hydrothermal Alteration Minerals in Jökulhlaup Deposits of Southern Iceland, with Implications for Detecting Past or Present Habitable Environments on Mars. Astrobiology 10, 523–547. doi:10.1089/ast.2009.0425

Whitney, D.L., Evans, B.W., 2010. Abbreviations for names of rock-forming minerals. Am. Mineral. 95, 185–187. doi:10.2138/am.2010.3371

Wilson, J.H., McLennan, S.M., Glotch, T.D., Rasbury, E.T., Gierlowski-Kordesch, E.H., Tappero, R.V., 2012. Pedogenic hematitic concretions from the Triassic New Haven Arkose, Connecticut: Implications for understanding Martian diagenetic processes. Chem. Geol. 312–313, 195–208. doi:10.1016/j.chemgeo.2012.04.013

Wolela, A.M., Gierlowski-Kordesch, E.H., 2007. Diagenetic history of fluvial and lacustrine sandstones of the Hartford Basin (Triassic–Jurassic), Newark

Supergroup, USA. Sediment. Geol. 197, 99–126. doi:10.1016/j.sedgeo.2006.09.006

Table 1. Descriptions of samples analyzed and analyses done on each.

Sample name	Sample description	Hyperspectral image	Chemistry analyses	Mineralogy analyses[a]
	Sediments from well below basalt-sediment contact			
Mer04-6	Sediments from 12.5+ cm below contact with basalts with a fine-grained, dark red layer on top, coarse-grained lighter red to red-white layer in the middle, and coarser-grained orange layer on bottom	Yes	Bulk	UWin
Mer04-16	Dark red sedimentary rock		Bulk	
	Sedimentary rocks and their coatings from basalt-sediment interface			
Mer04-2	Baked sediment with distinct orange and white coatings		Interior and coating	
Mer04-5	Sediment just below contact with basalt; purple color with thin brown-orange layers	Yes	Middle layer	UWin-middle layer and top coating
Mer04-11	Sediment surrounding pillow basalt with orange and green rind		Interior and red coating	
Mer05-10	Baked sediment directly against pillow basalt with orange-yellow coating	Yes	Interior	
Mer0614-01	Baked sediment between several pillow lavas with red, orange, and green coatings		Bulk	BrownU-bulk
Mer0614-02	Baked sediment (2) against basalt with coating of red hyaloclastite breccia with angular black clasts (1) and greener altered sediments below coating closest to basalts (3)		Hyaloclastite coating (1); sediments further from basalt (2); altered sediments from near basalt (3)	BrownU-all (1, 2, and 3)
	Basalts from bottom of section near sediments			
Mer04-3	Less-altered basalt with a few thin white veins and larger white crystals; red-brown coating on one side	Yes	Bulk	UWin-bulk
Mer04-13	Pillow basalt with red-pink interior and green and white rind	Yes	Interior and rind	UWin-interior; URI-exterior
Mer04-19	Pillow basalt with redder interior and whiter rind	Yes	Interior and rind	URI-exterior
Mer05-11	Basalt with orange, white, and black coatings		Bulk	Brown U-bulk
Mer0614-04	Extremely friable material from outermost rind of pillow basalt (where Mer04-13 was sampled) against surrounding sedimentary rocks		Bulk	BrownU-bulk

Sample name	Sample description	Hyperspectral image	Chemistry analyses	Mineralogy analyses[a]
	Basalts and breccias from greener altered area higher in section			
Mer05-4	Portion of larger pillow basalt with purple interior, light green-blue inner part of rind, and green outer part of rind; a few pipe vesicles with black rims and filled with white crystals	Yes	Interior, inner rind, and outer rind	
Mer05-6	Vesicular basalt with light purple matrix and vesicles filled with white and green crystals; redder rind	Yes	Bulk	
Mer05-7	Rock with purple matrix with green and black coating		Interior and rind	UWin-interior and rind
Mer05-9	Portion of pillow basalt with purple matrix with white coatings and more friable green coating	Yes	Interior and green coating	URI-interior and rind
Mer05-15	Breccia with green matrix and calcite veins	Yes	Matrix	UWin-matrix
MerPillow	Intact altered pillow basalt with oxidized purple interior, green rind, calcite amygdules and veins throughout, and pink material cutting through the pillow; float but representative of greener alteration	Yes	Interior, rind, and pink material	BrownU-interior and rind
	Miscellaneous samples			
Mer05-8	Transparent orange crystals from a 1-2 cm wide vein within the basalts			UWin
Mer05-38	Large green crystals with some white crystals			UWin
Mer05-F2	Basalt with brown matrix with thick white vein rimmed with a platy green mineral	Yes		
Mer05-F4	Breccia with dark blue, almost shiny clasts		Bulk	UWin
MerFloatV	Vesicular basalt with some vesicles filled with calcite and/or prehnite and many remaining unfilled vesicles	Yes		

[a]URI=XRD analyses done with Co source inXitu Terra at University of Rhode Island; UWin=XRD analyses done with Cu source inXitu Terra XRD from University of Winnipeg; BrownU=XRD analyses done on Bruker D2 Phaser at Brown University

Table 2. Formulas and interpretations of spectral and mineral indicator parameters shown or referenced in the text

Parameter	Formula[a,b]	Interpretation
	Field imaging spectral parameters	
Red slope	$\frac{R0.690 + R0.700 + R0.710}{R0.445 + R0.450 + R0.455}$	More oxidized surface (e.g., Hunt and Ashley, 1979)
Green peak	$\frac{R0.575 + R0.580 + R0.585 + R0.590}{R0.465 + R0.470 + R0.695 + R0.700}$	Enhanced by presence of Fe^{3+}/Fe^{2+} charge transfer (Adams, 1975; Burns, 1993a, 1993b; Cloutis and Gaffey, 1991)
BD660	$1 - \frac{2 * (R0.655 + R0.660 + R0.665)}{R0.590 + R0.595 + R0.600 + R0.710 + R0.715 + R0.720}$	Fe^{3+} electronic transition (Burns, 1993a; Scheinost et al., 1998) or Fe^{2+}/Fe^{3+} charge transfer (e.g., Burns, 1993a); also could highlight an organic pigment
	Laboratory imaging spectral parameters	
Red slope	$\frac{\sum R(0.758\ to\ 0.769)}{\sum R(0.483\ to\ 0.494)}$	See above
Green peak	$\frac{2 * \sum R(0.558\ to\ 0.569)}{1.36 * \sum R(0.465\ to\ 0.476) + \ 0.64 * \sum R(\ 0.747\ to\ 0.758)}$	See above
BD660	$1 - \frac{2 * \sum R(0.656\ to\ 0.667)}{\sum R(0.592\ to\ 0.603) + \sum R(\ 0.803\ to\ 0.813)}$	See above
Positive SWIR slope 1	$\frac{R1.794 + R1.806 + R1.818}{R1.154 + R1.167 + R1.179}$	Likely Fe^{2+}, possibly in type A pyroxenes (Cloutis and Gaffey, 1991) or chlorite (e.g., Bishop et al., 2008; King and Clark, 1989)
Positive SWIR slope 2	$\frac{R1.806 + R1.818}{R1.239 + R1.251}$	Likely Fe^{2+}, possibly in type A pyroxenes (Cloutis and Gaffey, 1991) or chlorite (e.g., Bishop et al., 2008; King and Clark, 1989)
BD1390	$1 - \frac{2 * (R1.384 + R1.396)}{1.62 * (R1.348 + R1.360) + 0.38 * (R1.505 + R1.517)}$	First overtone of OH stretch; Mg_3-OH (e.g., Bishop et al., 2008)
BD1410	$1 - \frac{2 * (R1.408 + R1.420)}{0.72 * (R1.348 + R1.360) + 1.28 * (R1.505 + R1.517)}$	First overtone of OH stretch; Al_2-OH (e.g., Bishop et al., 2008)
BD1480	$1 - \frac{2 * (R1.469 + R1.481 + R1.493)}{0.88 * (R1.336 + R1.348 + R1.360) + 1.12 * (R1.589 + R1.601 + R1.613)}$	First OH stretching overtone in minerals such as prehnite (1.48 μm) and datolite (1.47 μm) (Clark et al., 1990)
BD1900	$1 - \frac{2 * (R1.915 + R1.927 + R1.939)}{1.34 * (R1.843 + R1.855 + R1.867) + 0.66 * (R2.036 + R2.048 + R2.060)}$	H-O-H combination bend and stretch (e.g., Clark et al., 1990)

Parameter	Formula[a,b]	Interpretation
BD2220	$1-\frac{2*(R2.217+R2.229)}{0.66*(R2.156+R2.168)+1.34*(R2.253+R2.265)}$	Si-OH in hydrated silica (Aines and Rossman, 1984; Goryniuk et al., 2004) or Al-OH combination (e.g., Clark et al., 1990)
BD2240	$1-\frac{4/3*(R2.229+R2.241+R2.253)}{0.67*(R2.132+R2.144)+1.33*(R2.277+R2.289)}$	Si-OH in hydrated silica (Aines and Rossman, 1984; Goryniuk et al., 2004)
BD2260	$1-\frac{4/3*(R2.253+R2.265+R2.277)}{1.30*(R2.168+R2.180)+0.70*(R2.2.410+R2.422)}$	AlMg-OH or AlFe-OH in chlorite or other clays (Bishop et al., 2008)
BD2300	$1-\frac{{}^{4}/_{3}*(R2.289+R2.301+R2.313)}{R2.205+R2.217+R2.386+R2.398}$	Fe/Mg-OH combination (Andrieux and Petit, 2010; Bishop et al., 2008; e.g., Clark et al., 1990)
BD2340	$1-\frac{2*(R2.337+R2.349)}{0.48*(R2.205+R2.217)+1.52*(R2.386+R2.398)}$	Mg_3-OH combination band or third overtone of the C-O asymmetric stretching mode (Bishop et al., 2008; e.g., Hunt and Salisbury, 1971)
BD2370	$1-\frac{2*(R2.361+R2.2.374)}{0.39*(R2.168+R2.180)+1.61*(R2.410+R2.421)}$	Fe^{2+}-OH combination band (Bishop et al., 2008)
D2500	$1-\frac{R2.482+R2.494}{R2.410+R2.422}$	C-O combination band in carbonates (Hunt and Salisbury, 1971)
	Laboratory imaging mineral or phase indicator parameters	
Al-clay or hydrated silica	BD2220>0; Displayed value: BD2220	
Calcite	BD2340>0 and D2500>0; Displayed value: BD2340	
Chlorite	BD1900>0, BD2260>0, BD2370>0, and SWIR slope 2 >1 Displayed value: BD2370	
Fe/Mg clay	(BD1390 or BD1410)>0, BD1900>0, BD2300>0, and D2500<0.1; Displayed value: BD2300	
Hydrated silica (2.24)	BD1900>0 and BD2240>0; Displayed value: BD2240	
Prehnite	BD1480>0 and BD2340>0, D2500<0.15; Displayed value: BD2340	

[a]R#=reflectance at wavelength # µm

[b]ΣR(X to Y)=sum of reflectance values from wavelength X µm to wavelength Y µm

Table 3. Results of chemistry (ICP-AES and elemental analyses) and mineralogy (XRD) analyses for samples described in Table 1.

Sample Name	Al_2O_3	CaO	Cr_2O_3	FeO_{tot}	K_2O	MgO	MnO	Na_2O	NiO	P_2O_5	SiO_2	TiO_2	CO_2	Total	Mineralogy[a]
Sediments from well below basalt-sediment contact															
Mer04-6	8.07	26.60	n/a[d]	6.35	1.89	2.83	0.45	1.15	n/a[d]	0.05	27.96	0.61	23.57	99.52	Ab, Cal, Dol, En, Mtn, Ms, Qz
Mer04-16	9.23	11.31	0.01	6.78	2.86	7.09	0.22	1.10	0.01	0.08	40.66	0.52	17.62	97.48	Ab,Cal, Dol, Hem, Ms, Qz
Sediments and coatings on sedimentary rocks from basalt-sediment interface															
Mer04-2 interior	6.96	16.08	0.01	5.84	2.31	10.22	0.21	0.64	n.d.[e]	0.05	31.49	0.41	23.77	97.97	Ab, Cal, Chl, Dol, Hem, Ilt/Ms, Qz
Mer04-2 orange exterior	8.43	19.94	0.03	6.76	2.46	4.86	0.31	0.31	0.01	0.04	29.58	0.56	22.98	96.28	
Mer04-5 middle	7.53	29.71	n/a[d]	7.57	2.53	2.46	0.43	0.42	n/a[d]	0.06	23.23	0.38	23.86	98.15	Ab, Cal, Chl, En?, Gth, Mnt, Ms, Qz
Mer04-5 top coating															Cal, Chl, Sme, Qz
Mer04-11 interior	7.42	17.02	0.01	6.78	2.31	10.33	0.19	0.66	0.01	0.09	28.27	0.40	25.13	98.61	Ab, Cal, Chl, Dol, Hem, Ms, Qz, Ttn
Mer04-11 red coating	8.91	24.65	0.03	11.90	2.08	2.34	0.31	0.38	n.d.[e]	n.d.[e]	19.47	0.96	22.37	93.39	
Mer05-10[b]	10.57	11.92	0.01	8.04	3.30	7.09	0.24	1.02	n.d.[e]	0.07	38.67	0.54	17.08	98.56	
Mer0614-01[b]	9.83	10.99	0.01	7.57	3.32	7.43	0.18	0.84	0.01	0.09	40.58	0.54	16.60	97.99	Ab, Chl, Dol, Hem, Ms, Qz
Mer0614-02-1	13.51	16.21	0.05	11.77	2.72	3.22	0.18	0.64	0.01	0.03	26.93	1.26	13.48	90.00	Ab, Cal, Chl, Dol, Ms, Qz
Mer0614-02-2	6.91	19.08	0.01	6.09	2.37	11.42	0.31	0.56	n.d.[e]	0.07	22.63	0.36	27.36	97.18	Ab, Cal, Chl Dol, Ms, Qz
Mer0614-02-3	6.43	24.64	0.01	5.95	1.70	7.66	0.47	0.30	0.01	0.02	22.30	0.36	27.18	97.04	Ab, Cal, Chl, Dol, Ms, Qz
Basalts from bottom of section near sediments															
Mer04-3	13.59	11.64	n/a[d]	9.44	0.42	6.56	0.15	1.89	n/a[d]	0.09	45.94	1.04	6.52	97.28	Ab, Cal, Chl, Cpx, Qz, Sme?

Sample Name	Al_2O_3	CaO	Cr_2O_3	FeO_{tot}	K_2O	MgO	MnO	Na_2O	NiO	P_2O_5	SiO_2	TiO_2	CO_2	Total	Mineralogy[a]
Mer04-13 exterior	13.82	17.13	n/a[d]	8.72	0.483	2.73	0.41	3.60	n/a[d]	0.03	35.67	1.58	13.15	97.32	Ab, Cal, Chl, Mnt
Mer04-13 interior	16.90	5.93	n/a[d]	4.68	0.36	0.97	0.17	8.32	n/a[d]	0.28	55.27	1.47	4.24	98.56	Ab, Cal, Chl, Cpx, Hem, Sme, Zeo?
Mer04-19 exterior[b]	14.77	16.73	n/a[d]	5.62	0.86	1.42	0.26	4.78	n/a[d]	0.09	39.85	1.51	13.49	99.38	Ab, Cal, Chl, Ilt, Mnt
Mer04-19 interior[b]	17.82	6.56	0.05	3.03	0.48	0.54	0.09	8.95	n.d.[e]	0.53	59.68	1.29	5.06	104.08	
Mer05-11	11.84	12.09	0.04	6.56	0.34	1.77	0.28	5.25	0.01	0.26	47.35	1.04	10.06	96.88	Ab, Cal, Chl, Dol, Hem, Ms, Qz
Mer0614-04	18.01	11.90	0.05	7.90	3.64	1.19	0.21	1.20	0.01	0.04	35.65	1.72	9.31	90.82	Ab, Cal, Chl, Hem, Ilt, Ms
Basalts and breccias from greener altered area higher in section															
Mer05-4 exterior	13.61	4.00	0.05	18.27	0.39	13.65	0.19	1.72	0.01	0.19	40.26	1.47	0.18	94.00	
Mer05-4 inner rind	13.58	7.08	0.05	10.37	0.38	6.38	0.18	6.12	0.0	0.06	57.25	1.36	0.16	102.97	
Mer05-4 interior	14.43	5.03	0.04	11.69	0.29	6.45	0.11	6.63	0.01	0.18	55.73	1.07	0.27	101.94	
Mer05-6	13.10	7.95	n/a[d]	9.30	0.18	7.31	0.14	5.16	n/a[d]	0.12	47.47	1.01	3.39	95.12	
Mer05-7 exterior	13.07	8.75	n/a[d]	9.51	0.36	9.99	0.13	3.68	n/a[d]	0.02	40.38	0.66	6.36	92.91	Ab, Cal, Chl, Cpx, Sme
Mer05-7 interior	18.16	3.82	n/a[d]	4.26	2.20	2.55	0.05	8.40	n/a[d]	0.03	62.35	0.39	3.02	105.24	Ab, Chl, Cpx, Hem
Mer05-9 exterior[b]	12.62	5.28	n/a[d]	14.26	0.14	12.80	0.24	1.74	n/a[d]	0.20	38.35	2.24	1.54	89.40	Ab, Chl, Non, Zeo?
Mer05-9 interior[c]	13.41	7.54	n/a[d]	8.93	0.25	3.09	0.13	7.64	n/a[d]	0.31	57.47	1.08	2.28	102.13	Ab, Cal, Cpx, Hem, Mnt?
Mer05-15 (matrix)	13.73	5.70	n/a[d]	13.43	0.79	11.52	0.19	2.42	n/a[d]	0.11	39.99	1.22	2.39	91.49	Ab, Cal, Chl, Ms
Mer05-19	12.67	8.97	0.04	12.07	0.65	10.36	0.20	2.55	0.01	0.08	36.28	0.88	7.62	92.40	Ab, Cal, Chl, Cpx, Hem, Ilt
MerPillow exterior[b,f]	9.51	17.30	0.04	6.73	0.12	3.27	0.18	5.72	0.01	0.03	40.76	0.81	11.53	96.01	Aeg, Ab, Cal, Chl, Di, Hem, Sme, Ttn

Sample Name	Al_2O_3	CaO	Cr_2O_3	FeO_{tot}	K_2O	MgO	MnO	Na_2O	NiO	P_2O_5	SiO_2	TiO_2	CO_2	Total	Mineralogy[a]
MerPillow interior[b,f]	9.73	21.49	0.03	5.69	0.08	0.88	0.19	6.36	n.d.[e]	0.06	39.59	0.73	15.26	100.09	Aeg, Ab, Cal, Di, Hem, Ttn
MerPillow pink[b]	7.89	31.68		2.32	0.04	2.04	0.22	4.09		0.01	27.63	0.11	24.64	100.68	
						Miscellaneous									
Mer05-8	n/a[d]	n/a[d]	n/a[d]	n/a[d]	n/a[d]	n/a[d]	n/a[d]	n/a[d]	n/a[d]	n/a[d]	n/a[d]	n/a[d]	n/a[d]	n/a[d]	Cal
Mer05-38	n/a[d]	n/a[d]	n/a[d]	n/a[d]	n/a[d]	n/a[d]	n/a[d]	n/a[d]	n/a[d]	n/a[d]	n/a[d]	n/a[d]	n/a[d]	n/a[d]	Prh
Mer05-F4	12.63	4.07	n/a[d]	18.24	0.26	13.04	0.17	0.85	n/a[d]	0.11	35.79	1.43	0.60	87.20	Ab, Chl, Sme, Sulfide?

[a]Aeg=aegirine, Ab=Albite, Anl=analcime, Cal=calcite, Chl=chlorite, Cpx=clinopyroxene (diopside and/or aegirine), Di=diopside, Dol=dolomite, En=enstatite, Gth=goethite Hem=hematite, Ilt=illite, Mnt=montmorillonite, Ms=muscovite, Non=nontronite, Prh=prehnite Qz=quartz, Sme=smectite, Ttn=Titanite, Zeo=zeolite (Whitney and Evans, 2010)
[b]Sample run in triplicate for chemistry analyses
[c]Sample run in duplicate for chemistry analyses
[d]n/a=This element was not analyzed in this particular sample
[e]n.d.=not detected
[f]Greenberger et al. (in review)

FIGURE CAPTIONS

Fig. 1: Field photographs of the outcrop. **a)** Sediments pushed up between pillow basalts and red-orange alteration of sediments and the outcrop. Arrows point to one area of these deformed sediments. **b)** Altered pillow basalts with purple interiors and green rinds stratigraphically higher in the section. **c)** Example of amygdules within pillow basalt. Arrows point to several examples. **d)** Hyaloclastite breccia with calcite and quartz mineralization.

Fig. 2: Laboratory hyperspectral images of baked sedimentary sample Mer05-10. **a-c)** Cross-section of sample. **a)** Color composite image using three bands from the hyperspectral image to approximate true color, red: 0.662 μm, green: 0.531 μm, blue: 0.426 μm. Green arrows point to locations with green crystals. **b)** VNIR spectral parameters, red: red slope, green: green peak, blue: BD660. **c)** SWIR spectral and mineral indicator parameters, red: calcite, green: SWIR positive slope, blue: BD2220. **d-f)** Image of exposed coating of Mer05-10. **d)** Approximate true color image, red: 0.662 μm, green: 0.531 μm, blue: 0.426 μm. **e)** VNIR spectral parameters, red: red slope, green: green peak, blue: BD660. **f)** SWIR spectral and mineral indicator parameters, red: calcite, green: hydrated silica, blue: chlorite. Numbers in a) and d) correspond with spectra in 3a.

Fig. 3: Spectra representative of different units offset for clarity in **a)** Mer05-10 in Fig. 2 (black spectra are from cut interior surface and gray are from exposed coating), **b)** Mer04-13 (black) and Mer04-19 (gray) in Fig. 5, and **c)** Mer05-4 (black) and Mer05-9 (gray) in Fig. 6. All are averages of at least 9 pixels, with most more than 80 pixels. **d)**

Library spectra for comparison with spectra in a-c. Spectra from the USGS spectral library (Clark et al., 2007) are as follows: chlorite (GDS158 Flagstaff), hematite (HS45.3), muscovite (GDS108), montmorillonite (STX-1), opal (TM8896; hyalite), and nontronite (SWa-1.a). The type A pyroxene spectrum is C1PP68 from Cloutis and Gaffey (1991), and the calcite spectrum is CBCB12 from the CRISM spectral library (Murchie et al., 2007).

Fig. 4: Ternary diagrams plotting compositions of samples analyzed (Table 3) with concentrations in moles of Al_2O_3, $Na_2O + K_2O$, and FeO_T (total Fe as FeO) + MgO on the apices. This plot is similar to those used to understand weathering of basalt in Nesbitt and Wilson (1992) but does not include CaO with $Na_2O + K_2O$. CaO here is mostly controlled by calcite. While Nesbitt and Wilson (1992) subtract the CaO in calcite from the total CaO for use in their plots, we cannot easily do that calculation because of the presence of both calcite and dolomite in unknown proportions in some samples. **a)** All samples analyzed and the average composition of unaltered Talcott basalt from Puffer et al. (1981), which is the larger black dot pointed to by the dashed arrow. **b)** Compositions of sediments and coatings on sediments. **c)** Compositions of interiors of pillow basalts (dark red) showing red alteration and rinds (bright red and light pink). **d)** Compositions of interiors of pillow basalts showing green alteration (purple) and their rinds (green). Arrows in b-d show the change in composition between paired interiors and rinds/coatings.

Fig. 5: Laboratory hyperspectral images of two pillow basalts and their rinds characterized by red alteration: Mer04-13 (a-c) and Mer04-19 (d-f). **a, d)** Near true color image, red: 0.662 µm, green: 0.531 µm, blue: 0.426 µm. **b, e)** VNIR spectral parameters, red: red slope, green: green peak, blue: BD660. **c, f)** SWIR spectral and mineral indicator parameters, red: calcite, green: hydrated silica (2.24 µm feature), blue: chlorite. Numbers in a) and d) correspond with spectra in Fig. 3b.

Fig. 6: Laboratory hyperspectral images of two pillow basalts and their green alteration rinds: Mer05-4 **(a-c)** and Mer05-9 **(d-f)**. **a, d)** Near true color image, red: 0.662 µm, green: 0.531 µm, blue: 0.426 µm. **b, e)** VNIR spectral parameters, red: red slope, green: green peak, blue: reflectance at 0.7 µm. **c)** SWIR spectral and mineral indicator parameters for Mer05-4, red: calcite, green: positive SWIR slope 1, blue: chlorite. **f)** SWIR spectral and mineral indicator parameters for Mer05-9, red: calcite, green: positive SWIR slope 1, blue: Fe/Mg-clay. Numbers in a) and d) correspond to spectra in Fig. 3c.

Fig. 7: Laboratory hyperspectral image of a hyaloclastite breccia (Mer05-15) where the clasts have been altered to a green color. **a)** Near true color image, red: 0.662 µm, green: 0.531 µm, blue: 0.426 µm. **b)** VNIR spectral parameters, red: red slope, green: green peak, blue: reflectance at 0.7 µm. **c)** SWIR spectral and mineral indicator parameters, red: calcite, green: positive SWIR slope 1, blue: chlorite.

Fig. 8: Hyperspectral imaging of a wall of the outcrop at the base of the section where Talcott formation pillow basalts and the underlying sediments of the New Haven

formation are exposed. **a)** Near true color composites for three images that have been mosaicked. Red: 0.66 µm, green: 0.53 µm, blue: 0.45 µm. Images have been HSV sharpened in ENVI using the 0.46 µm band. Locations from which samples were collected are labeled by the number of the sample after "Mer" in Table 1. **b)** Spectral parameter image, red: red slope, green: green peak, blue: BD660. Calibration targets, vegetation, and shadows have been masked. The dashed lines indicate the approximate location above which basalt is present. Sediments only are present below that line, and some sedimentary material has been pushed up and is now located above that line.

Fig. 9: Mosaic of hyperspectral images of a portion of the outcrop showing more intense, green alteration of basalt. **a)** Near true color image. Red: 0.66 µm, green: 0.53 µm, blue: 0.45 µm. **b)** Spectral parameter image, red: red slope, green: green peak, blue: reflectance at 0.7 µm. Calibration targets, vegetation, and shadows have all been masked, and stretches on the red and green bands are similar to Fig. 8b.

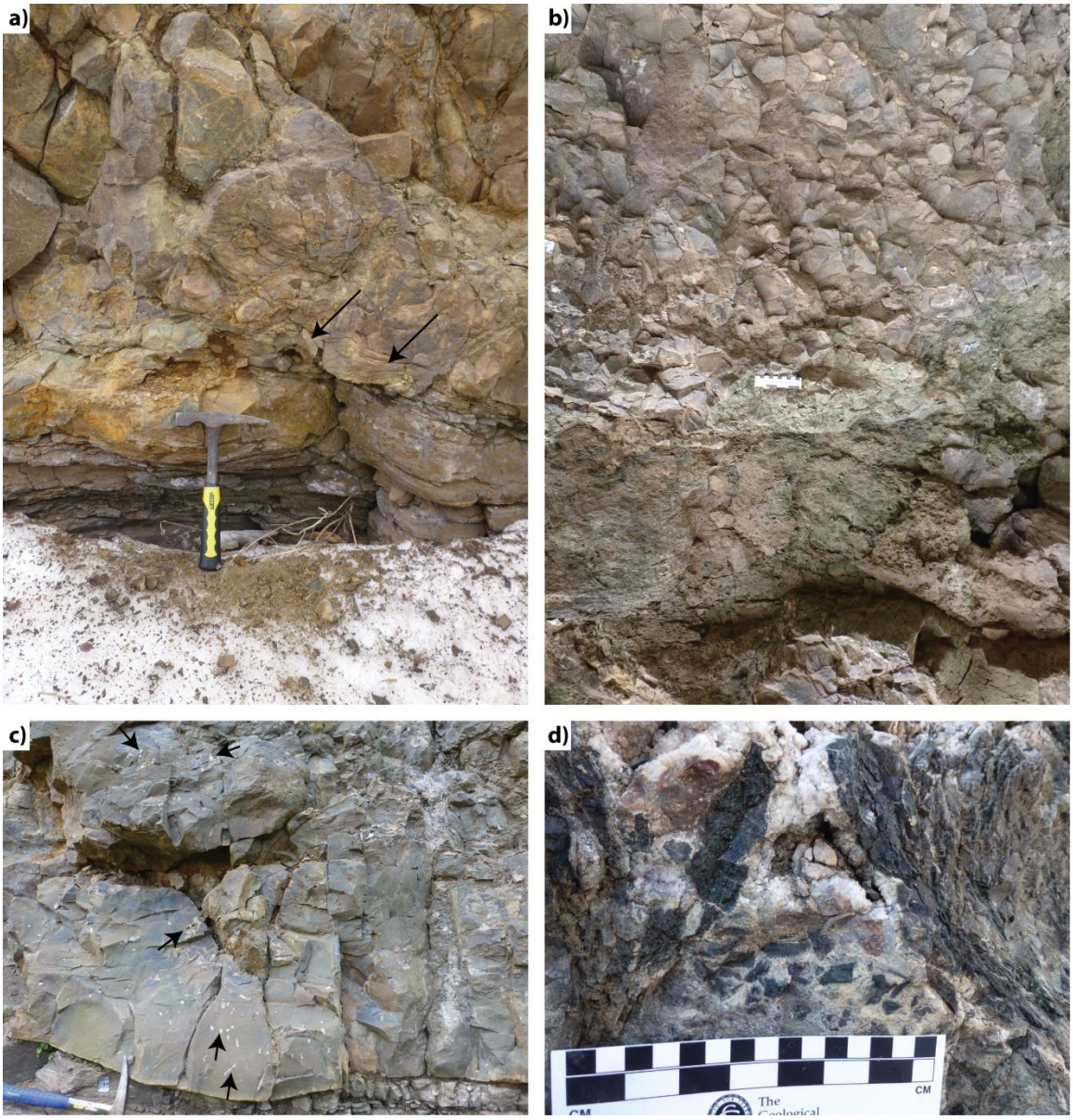

Figure 1.

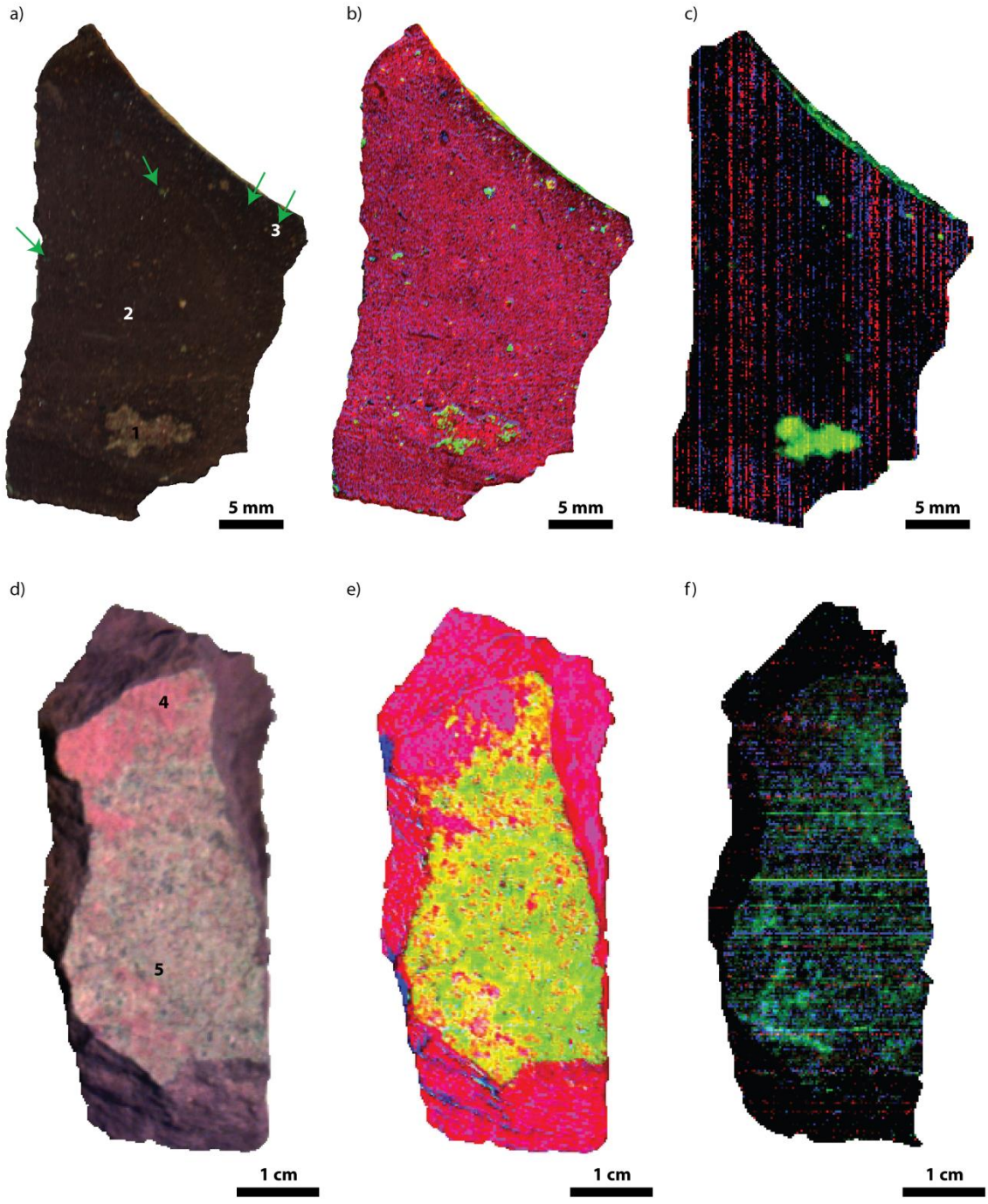

Figure 2.

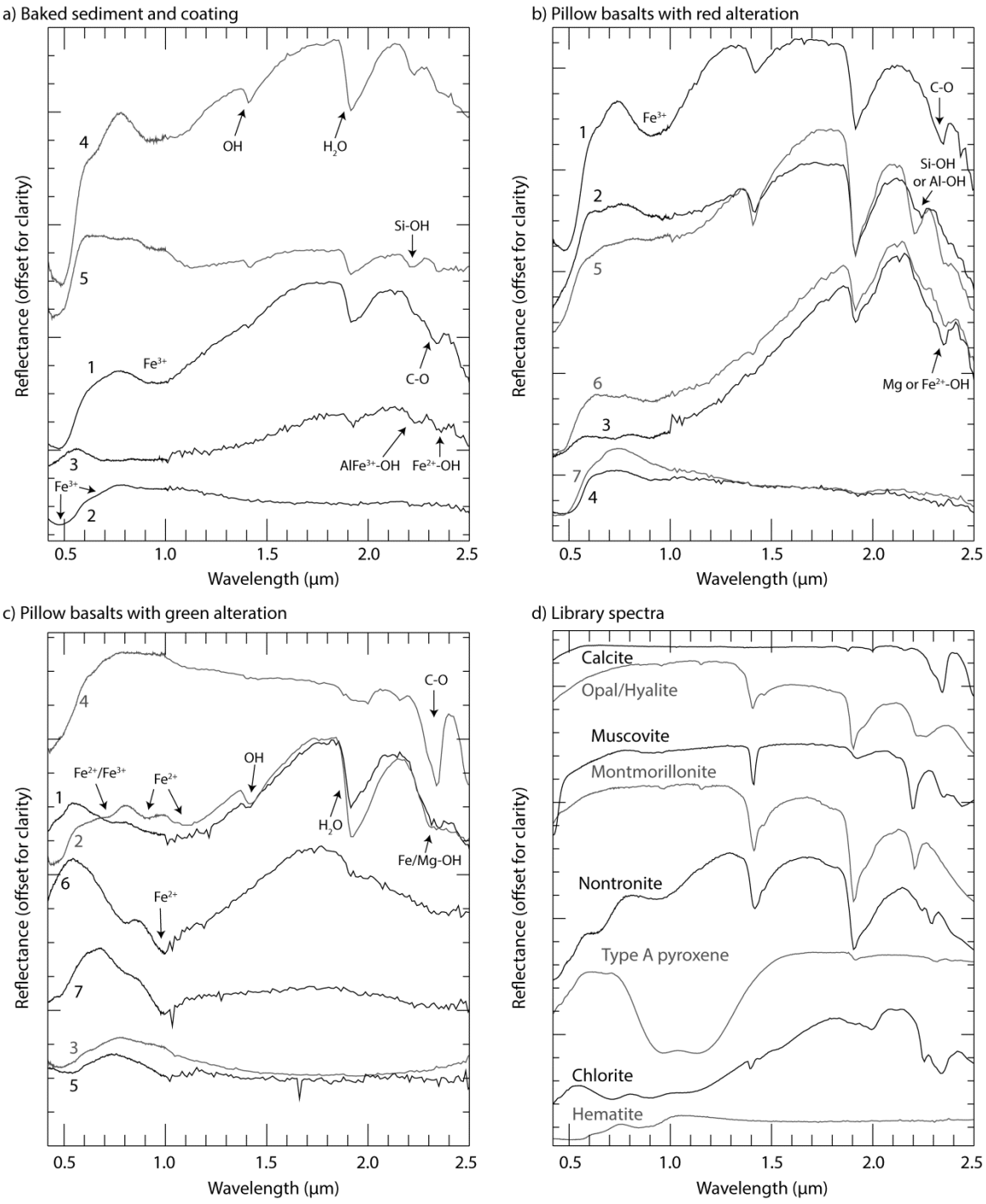
a) Baked sediment and coating
Reflectance (offset for clarity)
Wavelength (μm)
OH
H2O
Si-OH
Fe3+
C-O
AlFe3+-OH
Fe2+-OH
b) Pillow basalts with red alteration
Fe3+
C-O
Si-OH
or Al-OH
Mg or Fe2+-OH
c) Pillow basalts with green alteration
Fe2+/Fe3+
Fe2+
OH
H2O
C-O
Fe/Mg-OH
d) Library spectra
Calcite
Opal/Hyalite
Muscovite
Montmorillonite
Nontronite
Type A pyroxene
Chlorite
Hematite

Figure 3.

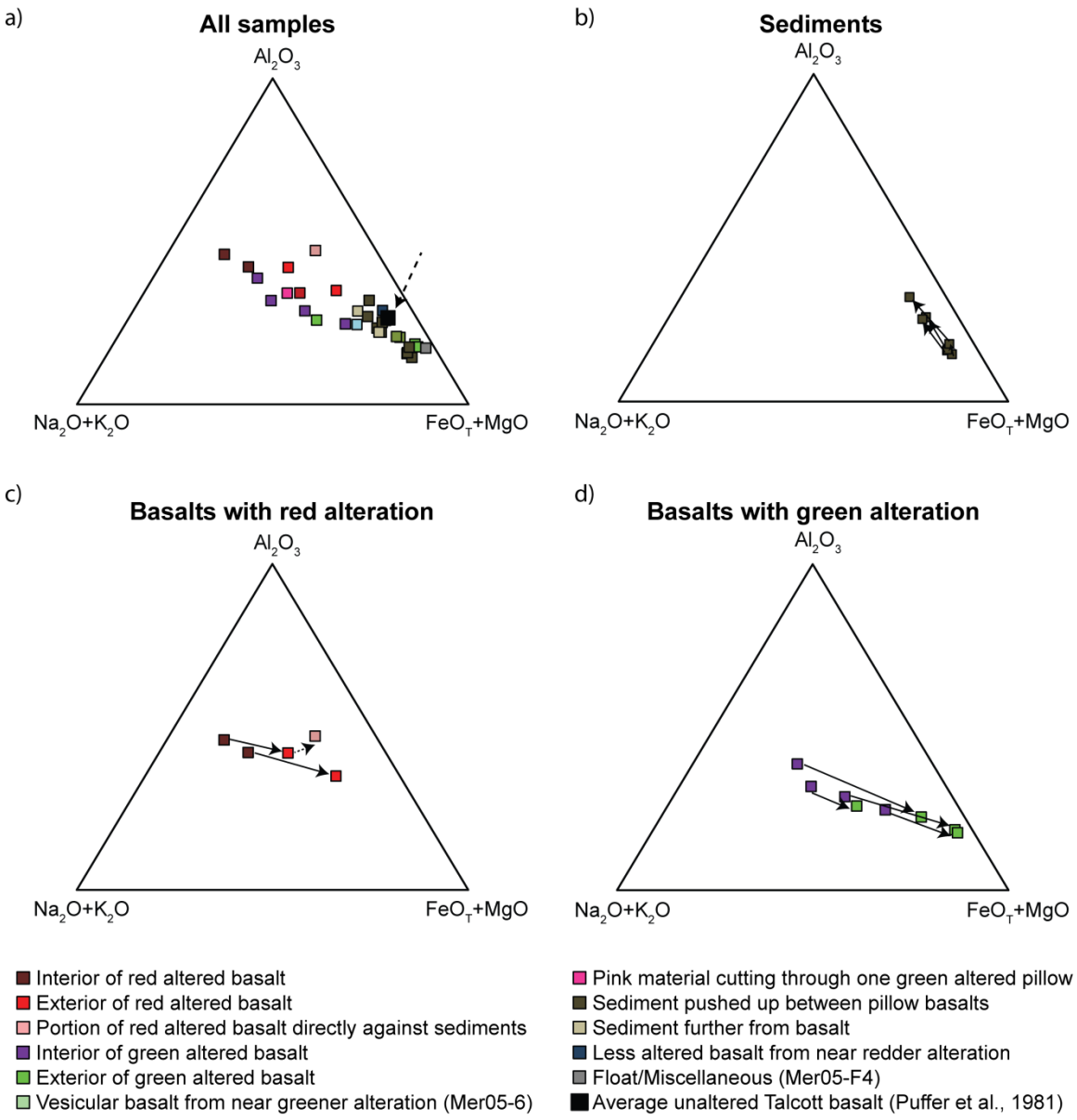
a)
All samples
Al_2O_3
Na_2O+K_2O
FeO_T+MgO
b)
Sediments
Al_2O_3
Na_2O+K_2O
FeO_T+MgO
c)
Basalts with red alteration
Al_2O_3
Na_2O+K_2O
FeO_T+MgO
d)
Basalts with green alteration
Al_2O_3
Na_2O+K_2O
FeO_T+MgO
Interior of red altered basalt
Exterior of red altered basalt
Portion of red altered basalt directly against sediments
Interior of green altered basalt
Exterior of green altered basalt
Vesicular basalt from near greener alteration (Mer05-6)
Pink material cutting through one green altered pillow
Sediment pushed up between pillow basalts
Sediment further from basalt
Less altered basalt from near redder alteration
Float/Miscellaneous (Mer05-F4)
Average unaltered Talcott basalt (Puffer et al., 1981)

Figure 4.

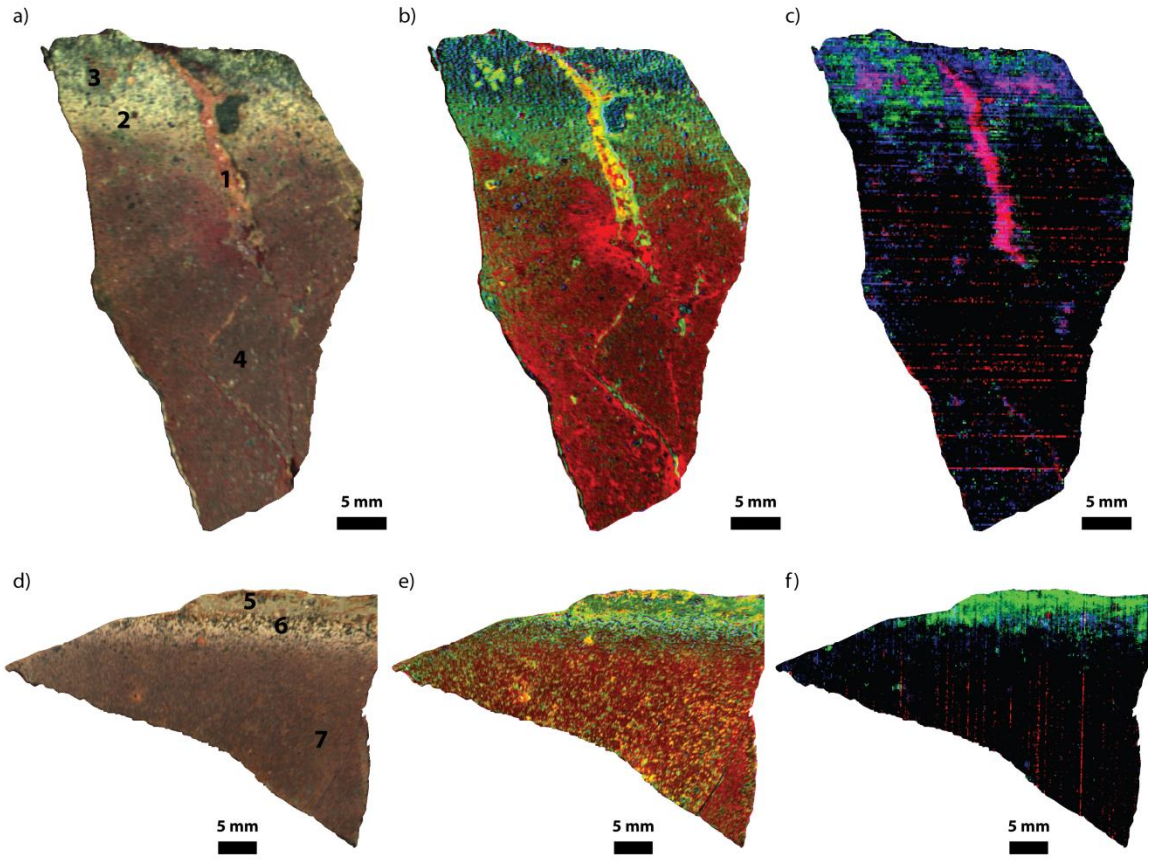

Figure 5.

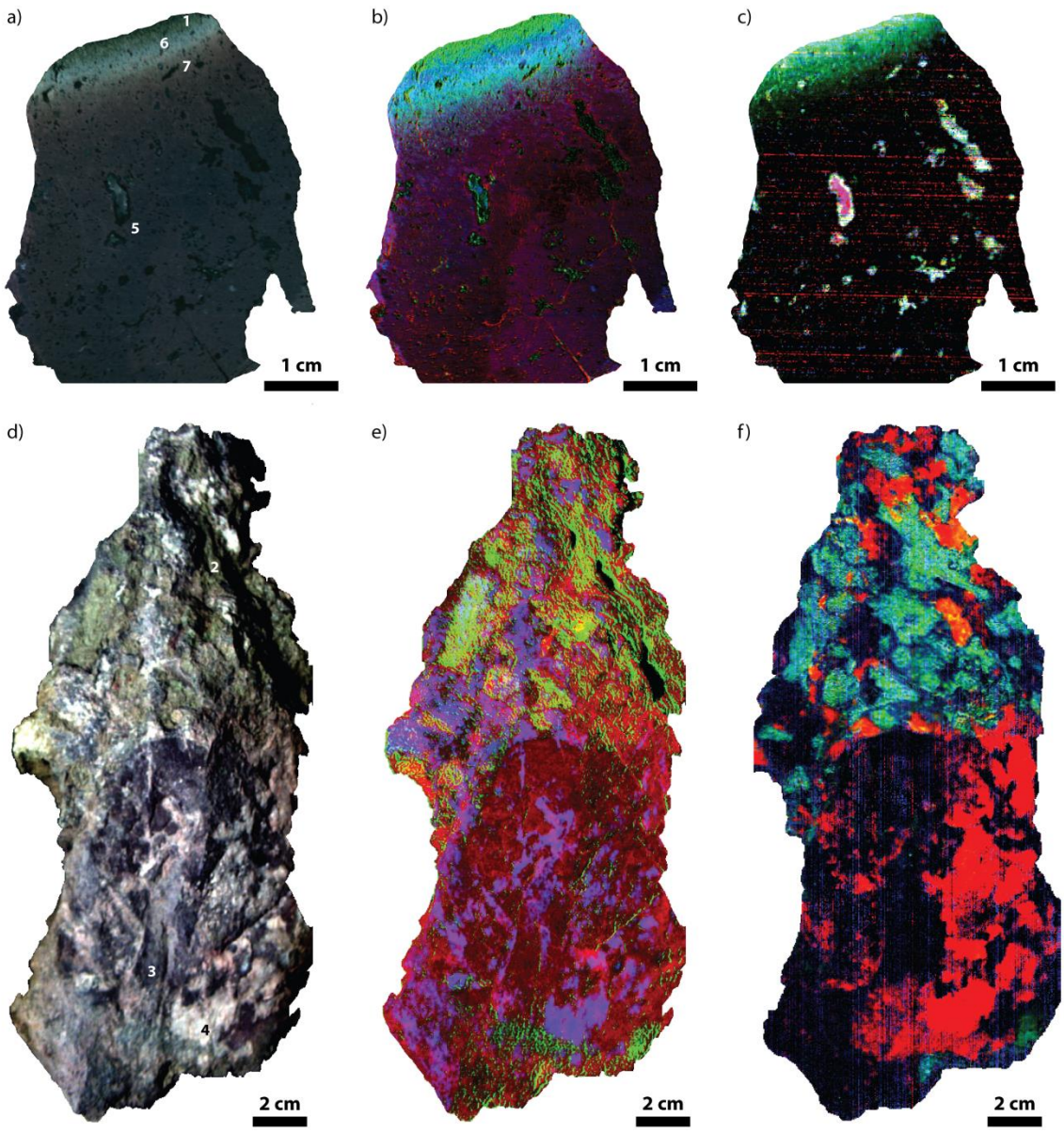

Figure 6.

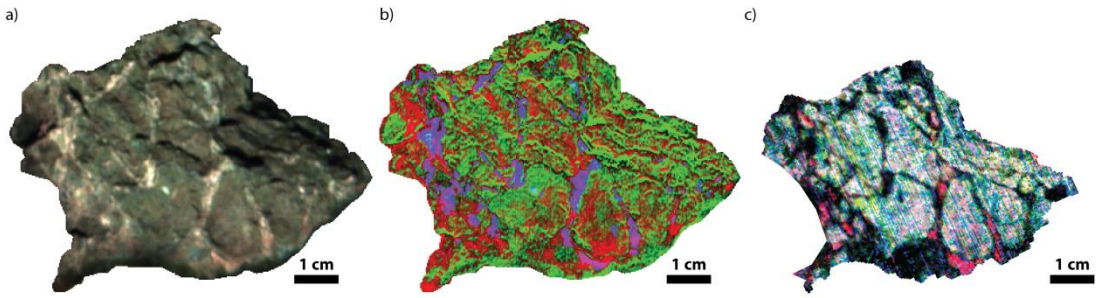

Figure 7.

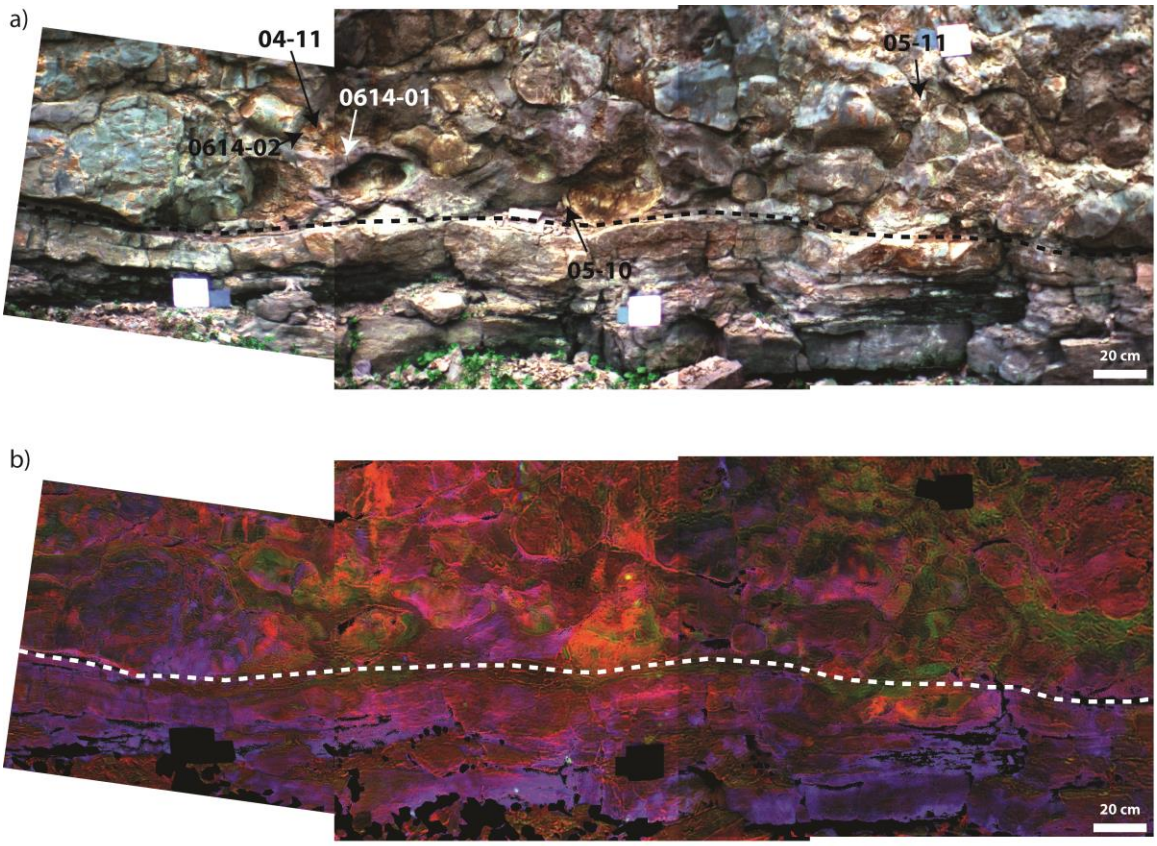

Figure 8.

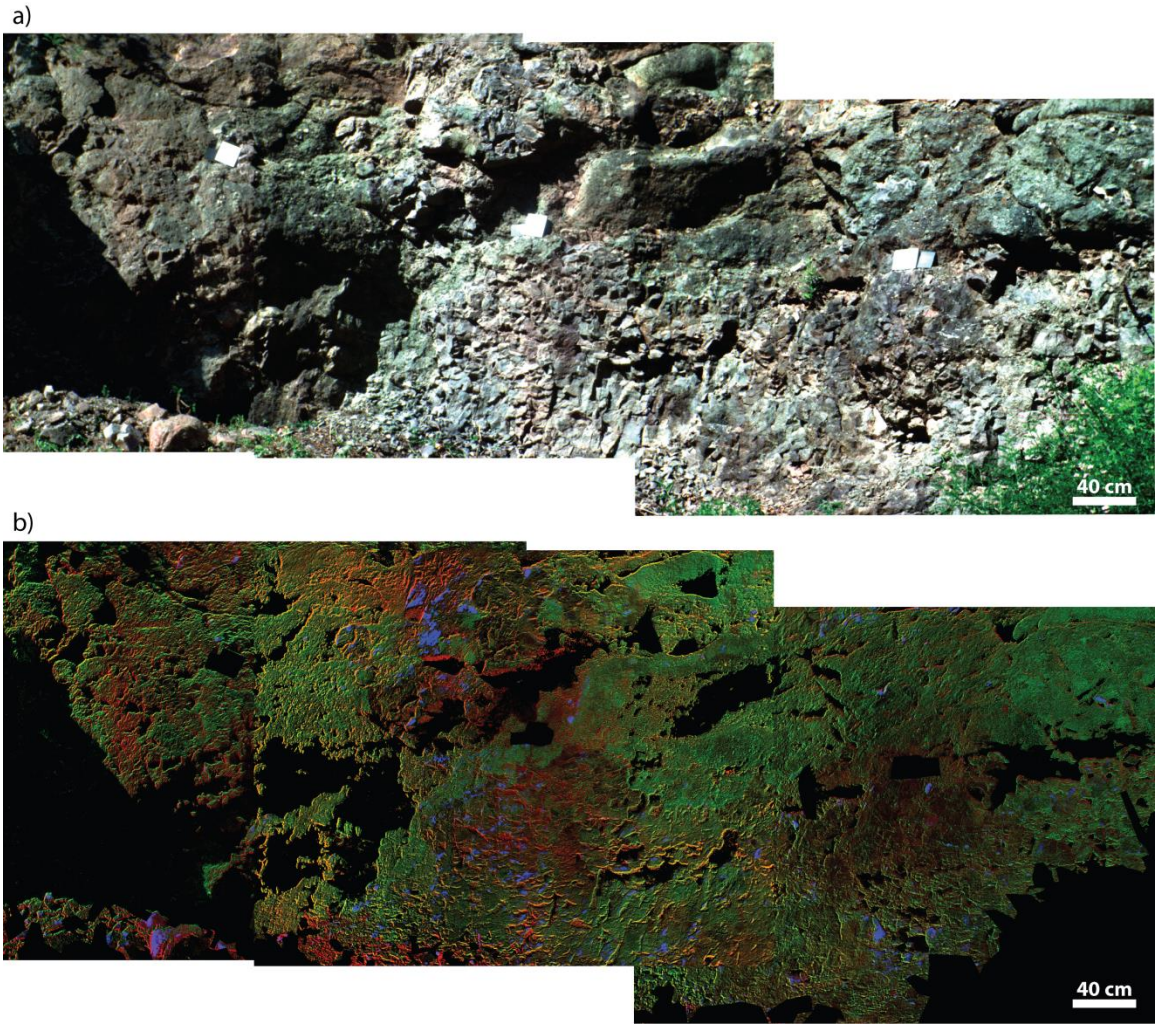

Figure 9.

CHAPTER FOUR

Hyperspectral mapping of alteration assemblages in a hydrothermal vug within the Haughton impact structure

Rebecca N. Greenberger[1], John F. Mustard[1], Gordon R. Osinski[2,3,4], Livio L. Tornabene[2,3,5], Alexandra J. Pontefract[2,3,6], Cassandra L. Marion[2,3], Roberta L. Flemming[2,3], Janette H. Wilson[7], and Edward A. Cloutis[8]

[1]Department of Earth, Environmental, and Planetary Sciences
Brown University, Providence, RI 02906

[2]Centre for Planetary Science and Exploration
University of Western Ontario, London, Ontario, Canada, N6A 5B7

[3]Department of Earth Sciences
University of Western Ontario, London, Ontario, Canada, N6A 5B7

[4]Department of Physics and Astronomy
University of Western Ontario, London, Ontario, Canada, N6A 5B7

[5]SETI Institute
Mountain View, CA, USA 94043

[6]Planetary Science Institute
Tucson, AZ, USA 85719

[7]Headwall Photonics, Inc.
Fitchburg, MA, USA 01420

[8]Department of Geography
University of Winnipeg, Winnipeg, Manitoba, Canada R3B 2E9

In review in its current form in:
Meteoritics and Planetary Science

ABSTRACT

Meteorite impacts on Earth and Mars can generate hydrothermal systems that alter the primary mineralogies of rocks and provide suitable environments for microbial colonization. We investigate a calcite-marcasite-bearing vug at the ~23-km diameter Haughton impact structure, Devon Island, Nunavut, Canada, using hyperspectral imaging of the outcrop in the field (0.65-1.1 μm) and samples in the laboratory (0.4-2.5 μm), point spectroscopy (0.35-2.5 μm), major element chemistry, and X-ray diffraction analyses. The mineral assemblages mapped at the outcrop include marcasite; marcasite with minor gypsum and jarosite; fibroferrite and copiapite/ferricopiapite with minor gypsum, silica, and melanterite; gypsum, Fe^{3+}-oxides, and jarosite; and calcite, gypsum, clay, microcline, and quartz.

Hyperspectral mapping of alteration phases shows spatial patterns that illuminate changes in alteration conditions and formation of specific mineral phases. Marcasite likely formed from the post-impact hydrothermal system under reducing conditions, while weathering oxidized the marcasite at low temperatures and water/rock ratios. The acidic fluids resulting from the oxidation collected on flat-lying portions of the outcrop, precipitating fibroferrite+copiapite. That assemblage then likely dissolved, and the changing chemistry and pH resulting from interaction with the calcite-rich host rock formed gypsum-bearing red coatings. Boundaries between mapped units represent redox gradients that could be energy sources for microbial communities.

INTRODUCTION

Meteorite impacts are an important geological process on Earth and throughout

the solar system; the heat generated from the impact process, including sustained heat provided by impactites and a central uplift consisting of rocks with a geothermal gradient originating from depth, generates hydrothermal systems when water or ice are present in the target rocks (e.g., Newsom, 1980; Naumov, 2005; Osinski et al., 2013). Evidence of these hydrothermal systems is seen at most complex craters on Earth that have been studied in any detail, with hydrothermal mineralization identified in impact melt-bearing units, the central uplift, ejecta, the crater rim, and sediments from lakes filling the craters (Osinski et al., 2013). There is reported post-impact hydrothermal alteration at structures as small as Lonar crater (Hagerty and Newsom, 2003). Although the initial impact can destroy life within and surrounding the resulting impact structure (Kring, 2000; Cockell and Lee, 2002), studies of terrestrial impacts have shown that the impact processes and resulting hydrothermal systems can preserve evidence of life and create and sustain new habitats for microbial communities (Kring, 2000; Parnell et al., 2010; Pontefract et al., 2012, 2014; Sapers et al., 2014; Schultz et al., 2014). A range of secondary minerals have been identified at terrestrial impact structures, including silicates (clays, zeolites, feldspars, quartz), carbonates, sulfides, sulfates, native elements, oxides/hydroxides, and halides (Naumov, 2005; Osinski et al., 2013), and these mineralogies preserve evidence of potentially habitable conditions within post-impact hydrothermal systems.

Studies of terrestrial impact structures can aid our understanding of impact processes on Mars and the implications for the habitability within resulting hydrothermal systems. Impact-driven hydrothermal systems have been proposed to exist on Mars (e.g., Newsom, 1980; Newsom et al., 2001; Osinski et al., 2013; Tornabene et al., 2013). Specific morphologies and special characteristics on Mars have been attributed to such

systems, such as at Toro crater (Marzo et al., 2010) and Holden crater (Tornabene et al., 2009; Osinski et al., 2013). In situ evidence from the Opportunity rover includes Ca-sulfate veins and deposits enriched in Zn that may have formed from impact-driven hydrothermal processes at the ~22 km diameter Endeavour Crater, which is similar in size to the Haughton impact structure studied here (Squyres et al., 2012; Arvidson et al., 2014). Secondary minerals throughout highly-cratered regions of Mars have been suggested to form from a variety of impact-induced alteration pathways, including hydrothermal systems (Tornabene et al., 2013). Models have placed constraints on the mineral assemblages expected (Schwenzer and Kring, 2009, 2013; Schwenzer et al., 2012) and the durations of these systems (e.g., Rathbun and Squyres, 2002; Abramov and Kring, 2005; Barnhart et al., 2010). Estimates of durations of hydrothermal systems on Mars range from 67 Kyr for a 30 km diameter crater to 10 Myr for the ~2000 km diameter Hellas basin (Abramov and Kring, 2005).

It has been suggested that life may have originated in hydrothermal systems on Earth and elsewhere (e.g, Holm, 1992; Shock, 1997; Nisbet and Sleep, 2001; Martin et al., 2008), and impact-driven hydrothermal systems have been suggested to be viable habitats for life on Mars (e.g., Newsom et al., 1996, 2001; Abramov and Kring, 2005; Schulze-Makuch et al., 2007; Osinski et al., 2013). As a result, hydrothermal deposits have been labeled as high priority targets for a future Mars sample return mission (McLennan et al., 2012). Studies of similar deposits on Earth using remote-sensing technologies can help us to better understand such systems and lead to development of exploration criteria for investigating similar deposits on Mars. We have studied a vug lined with hydrothermal calcite and marcasite formed through impact processes at the

Haughton impact structure, Devon Island, Nunavut, Canadian High Arctic, using hyperspectral imaging to map the spatial distributions of the primary mineralization and weathering products. Previous work by Izawa et al. (2011) characterized individual samples at this outcrop and the habitability of the weathering products; their work suggested that the marcasite altered and weathered at low temperatures to sulfates and oxides (Izawa et al., 2011; Osinski et al., 2013). What remains unexamined is an analysis of the spatial patterns of secondary minerals at this site and their spectral signatures, providing new insights into the alteration processes and potential habitability. We report the results of spectral mapping of this deposit and the insights into the evolution of fluids as temperatures, redox states, and chemistries changed.

GEOLOGICAL SETTING

The calcite-marcasite-bearing vug studied here within the Haughton impact structure is located at UTM 16N 0428046 E, 8364683 N (Fig. 1). The Haughton impact structure has a ~23 km apparent diameter (Osinski et al., 2005b) and is dated to 23.5±2.0 Ma (Young et al., 2013). This complex impact structure formed from a meteorite impact into ~1880 m of Lower Paleozoic sedimentary rocks and the underlying Precambrian crystalline basement rocks (Osinski et al., 2005b). The impact melt sheet originally covered an area of approximately 12 km in diameter (125 km^2) and today extends across 9 km of the crater (Osinski et al., 2005b), containing lithic clasts within a matrix of quenched calcite, silicate glass, and anhydrite (Osinski and Spray, 2001, 2003; Osinski et al., 2005b). The geologic units at the impact structure have been mapped on the ground by Osinski et al. (2005b), which are in excellent agreement with spectral mapping from

orbit by Tornabene et al. (2005).

There is evidence for structurally-controlled hydrothermal mineralization throughout the Haughton impact structure, with hydrothermal mineralization identified in the impact melt rocks, central uplift, and faulted crater rim (Osinski et al., 2001, 2005a). Minerals that formed through these hydrothermal systems include, calcite, selenite, marcasite, quartz, celestite, barite, fluorite, and Fe-oxides/hydroxides (Osinski et al., 2005a), and this paper focuses on one such hydrothermal deposit, a calcite-and marcasite-bearing vug within the impact melt rocks (Fig. 1). Osinski et al. (2005a) suggest that the marcasite within this vug formed at temperatures 100-240°C and pH <5 during the main stage of the post-impact hydrothermal system. Homogenization temperatures of fluid inclusions within the late-stage calcite from the same vug give similar formation temperatures of 118-210°C (Osinski et al., 2005a). These minerals formed during the main stages of hydrothermal activity as the system cooled and both liquid and vapor were present (Osinski et al., 2001, 2005a). The sulfides in this deposit weathered to sulfates and oxides/hydroxides, including copiapite, goethite, jarosite, rozenite, fibroferrite, gypsum, melanterite, and szomolnokite (Izawa et al., 2011). The chemical and redox gradients present at this deposit are thought to be good energy sources for microbes (Izawa et al., 2011). In addition, isotopic fractionations between sedimentary gypsum and hydrothermal marcasite and pyrite at Haughton are too high to have formed from abiotic processes but rather are likely the result of microbial activity during the hydrothermal system that was active within 10,000 years of the impact event (Parnell et al., 2010). These microbial signatures are also preserved in the sulfates that formed through weathering of the sulfides (Parnell et al., 2012).

METHODS

Overview

The calcite-marcasite-bearing vug studied here is several meters wide and located within the clast-rich impact melt rocks. This deposit was exposed as the adjacent river systematically eroded into the near-vertical cliff of impact melt rock. The outcrop was imaged in the field with a hyperspectral imager, and samples representative of the different mineral assemblages visibly identified at the site were collected. Sample descriptions are given in Table 1. These samples were analyzed with a point spectrometer in the field and other mineralogical and chemical analyses were completed in the laboratory upon return.

Point spectroscopy

Point spectra were acquired on various coatings and surfaces of each sample with an Analytical Spectral Devices, Inc. (ASD) Fieldspec 3 from 0.35–2.5 μm with spectral resolutions of 3 nm at 0.7 μm and 10 nm at 1.4 and 2.1 μm. This instrument's sampling intervals are 1.4 nm for wavelengths 0.35–1.0 μm and 2 nm for wavelengths 1.0–2.5 μm, and the software automatically resamples spectra to 1 nm spacing for output. Samples collected from the outcrop were stored on ice to minimize changes in mineralogy or hydration state before ASD spectra were obtained in the field. These measurements were done using the ASD contact probe attachment, which has its own internal light source and a viewing geometry of approximately 0° incidence and 30° emission angles. Measurements were made relative to Spectralon® and corrected for the reflectance

properties of Spectralon® by multiplying by spectrum HL-JFM-012 of SRT-99-050 measured in the Reflectance Experiment Laboratory (RELAB, Brown University, Providence, RI, USA) that was resampled to the wavelengths of output ASD spectra.

Hyperspectral imaging in the laboratory

All samples collected at the outcrop except APDI-13-14j were imaged in the laboratory at Headwall Photonics, Inc. (Fitchburg, MA, USA) using their High Efficiency Hyperspec® visible-near infrared (VNIR) E-series imager (338 spectral channels from 0.4 to 1.0 µm, 7 nm spectral resolution defined as the full width at half maximum of the slit image intensity, 1.785 nm sampling interval) and High Efficiency Hyperspec® shortwave infrared (SWIR) X-series imager (138 spectral channels from 1.0 to 2.5 µm, 12 nm spectral resolution, and 12.0656 nm spectral sampling). These are pushbroom imagers with foreoptic lenses, spectrographs, and focal plane arrays, and samples are moved through their fields of view on a motorized scanning table that is part of the Hyperspec® Starter Kit™. The samples were illuminated with a quartz tungsten halogen bulb. The lens on the VNIR imager has in instantaneous field of view (IFOV) of 0.382 mrad, corresponding to spatial resolutions up to ~43.5 µm/pixel, though actual resolutions depend on the distance between the imager and the sample. The lens on the SWIR imager has an IFOV of 1.2 mrad with achievable spatial resolutions up to ~133 µm/pixel. The imagers viewed the sample from nadir. Where possible, SWIR images were warped to VNIR images using manually-selected control points, a first degree polynomial, and nearest neighbor resampling. The VNIR images were then joined at 0.997 µm (VNIR) and 0.998 µm (SWIR) and stacked to create a single image cube, deleting overlapping

bands and removing any offset between the detectors by multiplying the SWIR image by a factor that assumed no change in reflectance between those 0.997 and 0.998 μm. It was not possible to join samples with significant surface topography because the changes in distance from the different lenses of the VNIR and SWIR systems led to spatial offsets that could not be removed with simple polynomials.

Laboratory images were calibrated through a dark current subtraction from a measurement with the lens cap on, ratio to the signal from a Spectralon® panel to correct for spectral and spatial non-uniformities, and corrected for the absolute reflectance properties of Spectralon® from the same RELAB spectrum above resampled to the wavelengths measured by these imagers. The equation used for calibration to reflectance is given below:

$$R = \frac{S_t - S_d}{S_s - S_d} * R_s \ ,$$

where S_t is the signal from the image of the target sample, S_d is the dark current signal, and S_s is the signal from the image of Spectralon®. Analyses of these images were done through use of spectral (e.g., Clark and Roush, 1984; Pelkey et al., 2007; Viviano-Beck et al., 2014) and mineral indicator parameters given in Table 2. The wavelength ranges of these imagers are sensitive to the electronic transitions of Fe in different oxidation states and coordination environments as well as overtones and combination bands of OH, H_2O, and metal-OH bonds within hydrated mineral structures (e.g., Clark et al., 1990; Burns, 1993).

Near infrared (NIR) hyperspectral imaging in the field

The outcrop was imaged in the field during the 2013 field season using a Channel

Systems near infrared (NIR) hyperspectral imager. This imaging system is an acousto-optic tunable filter with 10 nm spectral resolution and sampling that measures from 0.65 to 1.1 μm. An image was taken for use in calibration with the lens cap covering the lens to measure the dark current of the instrument, and this image was subtracted from the image of the outcrop before atmospheric correction. Exposure times at each wavelength were determined using the imager's auto-expose function that maximizes the exposure time at each wavelength without saturating. The exposure times were saved, and the images were normalized to account for the varying exposure times. Tests of the imager showed that dark current was independent of exposure time, and therefore that image was not normalized. Images were calibrated through a dark object subtraction using the minimum measurement of any pixel within the image at each wavelength. This minimum measurement was assumed to be the additive contribution to the signal from atmospheric scattering (Chavez Jr, 1996 and references therein). Then, the image was calibrated to reflectance by dividing by the average spectrum of a Spectralon® panel within an image taken next to the outcrop and multiplied by the same spectrum of Spectralon® used in the ASD calibration but resampled to the wavelengths sampled by this imager. The calibration to reflectance (R) was done using the following equation:

$$R = \frac{\frac{(S_o - S_d) - D_o}{t_o}}{\frac{W_{ds} - D_{ds}}{t_s}} * R_s \ ,$$

where S_o is the signal in the image of the outcrop, S_d is the signal from the dark image, D_o is the dark object spectrum described above for the outcrop image, t_o are the exposure times at each wavelength for the image of the outcrop, W_{ds} is the average signal from the image Spectralon® panel after subtracting the dark current at each pixel, D_{ds} is the dark object spectrum from the image of the Spectralon® panel, t_s are the exposure times at

each wavelength for the image of the Spectralon® panel, and R_s is the reflectance spectrum of Spectralon® measured in RELAB. These methods are similar to calibration of AVIRIS data using the methods of Clark et al. (2002). In total, five images of the outcrop were acquired.

Lithologies were mapped within the hyperspectral images using spectral parameters (e.g., Clark and Roush, 1984; Pelkey et al., 2007; Viviano-Beck et al., 2014) and combinations of spectral parameters (Table 3). In this wavelength range, the spectra show electronic transitions and intervalence charge transfers of transition metal cations, Fe^{2+} and Fe^{3+} at this outcrop (e.g, Burns, 1993). Here, Fe-sulfides, sulfates, and oxides are known to be present (Izawa et al., 2011), and variations in the shape, center wavelength, width, and slope of these features at the wavelengths sampled by the imager are due to the differences in Fe mineralogy. Different units in the map correspond with the samples that were collected and, using the ASD spectra and spectra from the images of the known sampling locations, spectrally-similar materials were mapped across the outcrop. Spectral parameters given in Table 3 calculate depths of absorption features and slopes. Parameters mapping lithologies consistent with the samples collected, also given in Table 3, were determined through an iterative process where combinations of spectral parameters are used to relatively uniquely map spectrally-similar materials.

Major element chemistry analyses

Major element chemistries for samples collected at the outcrop were determined through inductively coupled plasma – atomic emission spectroscopy (ICP-AES) analyses at the Brown University Environmental Chemistry Facilities following a flux fusion

sample preparation for Al, Ca, Cr, Fe, K, Mg, Mn, Na, Ni, P, Si, and Ti using methods modified from Murray et al. (2000). For the flux fusion, 35-45 mg of ground samples were mixed with 155-165 mg lithium metaborate flux and fused for 10 minutes at 1050°C in graphite crucibles. The molten beads were then quenched in 20 ml of 10% nitric acid and agitated for at least 30 minutes. Solutions were filtered through 0.45 micron filters and diluted further by adding 5 mg of solution to 35 ml of 10% nitric acid to achieve ~4000x dilutions. Standard reference materials (NIST2711, MAG-1, DTS-2B, NIST1646a, BIR-1, SGR-1, BHVO-2, NIST2702, BCR-2, G-2, and NIST1c) and blanks were run with the same methods. Diluted solutions were analyzed on a JY2000 Ultrace ICP-AES using intensities for peaks given in Murray et al. (2000), and drift solutions were run initially and periodically throughout the run. Concentration data were determined after correcting for instrument drift and subtracting blanks using linear regression curves from the standard reference materials. One sample was run in duplicate, and three were run in triplicate. These results are reported in oxide weight percentages to be consistent with geochemical convention. However, some Fe is in sulfides and is coordinated by S, not O.

The carbon content of the same samples was measured with elemental analyses on a CE Instruments Model NC2100 Elemental Analyzer. Samples were prepared by weighing 8-10 mg of each into tin capsules, which were then folded and crushed. Two blanks were run, and varying amounts of four standards (acetanilide, cyclohexane, pine - SRM 1575, and Montana soil - SRM 2711) were run to calculate regression curves and to check the quality of the measurements throughout the analyses.

X-ray diffraction (XRD)

Bulk powdered samples were backpacked for powder X-ray diffraction (pXRD) analyses and measured on a Rigaku rotating-anode XRD with Co Kα radiation operated at 45 kV and 160 mA. With this instrument, monochromation is achieved with a curved crystal, diffracted beam, and graphite monochromator, and X-rays were collimated with 1° divergent and scatter slits and a 0.15 mm receiving slit. Samples were scanned from 2 to 82° 2θ with 0.020 steps at a rate of 10° 2θ/minute. Mineralogies of coatings were determined using micro X-ray diffraction (μXRD; Flemming, 2007) with no sample preparation on a Bruker D8 Discover μXRD. A 60 mm Co Gobel Mirror with a 300 μm snout provides a nominal 300 μm beam diameter. This instrument has an area detector, and each sample was scanned in omega (ω) scan mode with two frames. The parameters for the first frame were θ_1=15°, θ_2=20.5°, and ω=10, and this scan ran for 90 minutes. The second frame was acquired over 145 minutes with the following parameters: θ_1=34.5°, θ_2=40°, and ω =19. ω is the degree of rotation of both source and detector in a clockwise direction during analysis. The two frames were converted to two-dimensional XRD patterns and combined to obtain continuous measurements from 14° to 95° 2θ in Diffrac.Suite EVA. Mineralogies from pXRD and μXRD patterns were determined by comparing peak positions of the unknowns with diffraction patterns from the International Centre For Diffraction Data (ICDD) database through an interface in EVA.

RESULTS

Individual sample analyses

Samples were collected from within images of the vug that were representative of

the major mineral assemblages at the site. ASD spectra of sample APDI-13-14a (Table 1, Fig. 2) have electronic transitions of Fe^{3+} at 0.42, 0.55, and 0.82 µm. These bands may be particularly intense due to hydroxo-bridging of Fe^{3+} in a mineral such as copiapite (Cloutis et al., 2006). The wavelength positions of these crystal field transitions are consistent with the Fe^{3+}-bearing sulfate minerals fibroferrite and copiapite/ferricopiapite (Crowley et al., 2003; Cloutis et al., 2006). These minerals are difficult to distinguish at the wavelength range measured here, but the popcorn-texture of the sample is suggestive of copiapite or ferricopiapite while the deep 0.55 µm spectral feature is consistent with fibroferrite (Crowley et al., 2003). Fibroferrite and copiapite/ferricopiapite are both inferred from spectroscopy and confirmed by pXRD data. There are also deep absorption features from OH and H_2O in these spectra. A broad, complex feature is present at ~1.4-1.6 µm composed of overlapping absorptions at ~1.44, 1.49, and 1.55 µm due to the OH stretching overtone of OH and H_2O (Cloutis et al., 2006; Crowley et al., 2003). There also is a broad, weak feature around 1.77 µm consistent with an H_2O-bearing sulfate (Cloutis et al., 2006) and a strong 1.93/1.99 µm H_2O combination band (Hunt et al., 1971; Clark et al., 1990; Cloutis et al., 2006). The spectra are flattened from 2.1 to 2.3 µm possibly due to weak combination bands related to OH and SO_4 in the mineral structures (e.g., Cloutis et al., 2006), but the positions of any features present cannot be determined. These overtones and combination tones of vibrational absorption features are consistent with those previously reported for copiapite/ferricopiapite and fibroferrite (e.g., Crowley et al., 2003; Cloutis et al., 2006) as well as hydrated silica (Aines and Rossman, 1984; Goryniuk et al., 2004). While the ASD measures a larger area, sometimes averaging multiple components within a single spectrum, hyperspectral

imaging allows us to obtain spectra of much smaller areas (100's of μm's) within single pixels. A hyperspectral image of this sample (Fig. 3a) shows small areas of spectrally-distinct gypsum identified by a characteristic triplet at 1.4 μm (e.g., Hunt et al., 1971; Clark et al., 1990). pXRD also identifies melanterite and cristobalite in this sample. The identified cristobalite may actually be opal-C or opal-CT, which have similar diffraction patterns (Smith, 1998), and is present in low abundance (~1% SiO_2 based on the results of chemistry analyses). The sample chemistry is dominated by Fe cations with minor Ca, consistent with the identification of Fe-bearing sulfates (copiapite/ferricopiapite and fibroferrite) with minor gypsum.

ASD spectra of sample APDI-13-14b (Table 1, Fig. 2) have electronic transitions of Fe^{3+} centered at 0.93–0.95 μm and 0.51 μm (e.g., Burns, 1993; Scheinost et al., 1998; Cloutis et al., 2006). These crystal field absorption features could result from a Fe^{3+}-oxide or sulfate, such as goethite or jarosite (e.g., Scheinost et al., 1998; Cloutis et al., 2006), though the spectra lack other SWIR features due to jarosite. Based on μXRD results, this feature is likely due to a combination of both goethite and jarosite, though the jarosite is likely a minor component. In the SWIR, these spectra have a well-expressed triplet at 1.4–1.7 μm from OH stretching overtones consistent with gypsum (e.g., Hunt et al., 1971; Clark et al., 1990). Additional absorption features at 1.75/1.77 μm, 1.94/1.98 μm (H_2O combination band), 2.17-2.18 (S-O overtone or OH/H_2O combination or overtone), 2.22 (S-O overtone or OH/H_2O combination or overtone), 2.27 (S-O overtone or OH/H_2O combination or overtone), 2.43 (S-O overtone), and 2.48 μm (S-O overtone) all confirm the identification of gypsum (e.g., Hunt et al., 1971; Clark et al., 1990; Cloutis et al., 2006). Hyperspectral imaging also shows that this coating is composed of a

fine-grained Fe^{3+}-oxides and sulfates and gypsum, with variations in the relative strengths of absorption features likely due to variations in the relative abundances of the different phases (Fig. 3b). The chemistry of this sample is more complex than APDI-13-14a, with a large component of Ca in addition to Fe being present (Table 4). There is some carbon in this sample that is likely mixed in portions of the calcite rock on which this coating precipitated. pXRD also identifies pyrite, quartz, and marcasite (Table 4). There were sides of this sample with visible marcasite and likely also pyrite, but those were not exposed before sampling and are not the coating mapped in the NIR hyperspectral data. Two µXRD points on the red and orange sample coatings did not target any of the marcasite or pyrite. µXRD identifies gypsum, jarosite, akaganeite, and goethite in the coatings.

The reflectance spectrum of APDI-13-14c (Table 1, Fig. 2) exhibits a crystal field absorption feature centered around 0.83–0.84 µm due to Fe^{2+} and is roughly consistent with reported marcasite reflectance spectra (Hunt et al., 1971; Cloutis and Gaffey, 1994). ASD spectra of other portions of the sample are consistent with the calcite on which the marcasite precipitated and gypsum. The chemistry is consistent with the spectral interpretations, with high Fe contents (Table 4). There is also significant Ca in these samples, likely in the calcite-rich host rock, which could not be completely removed during sample preparation. µXRD data of two points on the surface of the sample identify only marcasite. The ground sample for pXRD incorporated some other phases in the larger rock, including calcite, celestine, pyrite, gypsum, and quartz.

APDI-13-14h spectra (Table 1, Fig. 2) have weak, broad electronic transitions of Fe^{2+} centered at ~0.9 and 1.1 µm, potentially in a Fe^{2+}-bearing clay or a sulfate such as

glauconite or rozenite (Crowley et al., 2003; Cloutis et al., 2006). There also is likely some gypsum identified from a weak triplet from OH stretching overtones near 1.4–1.5 μm and the shape of the 1.9 μm band (e.g., Hunt et al., 1971; Clark et al., 1990). The absorption feature at 2.21 μm could result from an Al-OH combination in a clay such as montmorillonite or illite, from an OH/H_2O combination or S-O overtone in gypsum, or both (e.g., Clark et al., 1990; Cloutis et al., 2006). The feature could also result from minor water in quartz (Aines and Rossman, 1984; Goryniuk et al., 2004). Finally, the deeper 2.34 μm absorption feature is a C-O combination of calcite (Hunt and Salisbury, 1971). From the spectroscopy, this sample is likely a mixture of Fe^{2+}- and Al-bearing clays, calcite, and gypsum with possible silica. While most of the sample is dominated spectrally by calcite, hyperspectral imaging shows small areas with more gypsum (Fig. 3c). Chemistry analyses show high Ca and relatively high Si compared with other samples from this site (Table 4). There is also some Mg and K, and Fe is very low. pXRD analyses identify quartz, microcline, and hematite in addition to phases identified through spectroscopy (Table 4). There are likely both smectite and illite clays present, and a clay such as glauconite is consistent with the pXRD pattern and could explain the Fe^{2+} feature in the spectra.

Spectroscopy of APDI-13-14j (Table 1) shows a peak in reflectance (0.65 μm) at longer wavelengths than APDI-13-14c (0.54 μm) due to the oxidative processes (Fig. 2). There is also a weak Fe^{3+} electronic transition at 0.48 μm in APDI-13-14j (Scheinost et al., 1998) and a stronger crystal field absorption feature centered at 0.87–0.90 μm. The position of the longer wavelength electronic transitions may result from the convolution of a Fe^{3+}-oxide such as goethite, which has a Fe^{3+} electronic transition at 0.95 μm

(Scheinost et al., 1998), a Fe^{3+}-sulfate such as jarosite, and the underlying marcasite. The spectrum has a negative slope into the infrared, which is often seen with fine-grained coatings, where the bright coating dominates the spectrum at the shortest wavelengths but is more transparent at longer wavelengths (Singer and Roush, 1983; Fischer and Pieters, 1993; Johnson and Grundy, 2001). The negative slope may also result from Rayleigh scattering of extremely fine particles (Clark et al., 2008; Brown, 2014). The spectrum also contains an H-O-H combination at 1.9 μm and a very weak, broad feature at ~2.20–2.27 μm from S-O or OH/H_2O overtones or combination bands but is too weak and poorly-defined to assign to a specific mineralogy (e.g., Clark et al., 1990; Cloutis et al., 2006). This sample is similar chemically to APDI-13-14c, though with higher Fe and lower Ca, likely due to a lower proportion of the calcite host rock in the sample (Table 4). μXRD analyses of the surface of this sample identify gypsum and jarosite in addition to marcasite, though low abundances of Ca and K suggest that the gypsum and jarosite are minor.

Outcrop imaging and mapping

The outcrop was imaged in NIR wavelengths, and units that are spectrally-similar to the samples described above were mapped. The spectra from the NIR imager (Fig. 2) are relatively consistent with the ASD spectra of corresponding units, with slight differences in overall slopes probably due to artifacts from the atmospheric correction, differences in viewing geometry between the Spectralon® panel used for calibration and the outcrop, or differences in the spatial area sampled. However, these differences are systematic, and there is remarkable consistency between spectra of the same materials

present across the images. In these data, variations in the positions of Fe^{2+} and Fe^{3+} electronic transitions and slopes result from differences in mineralogy between the units.

Using these differences, spectral parameters (Table 3) were used to map spectrally-similar units, an example of which is shown in Fig. 4. These units were drawn onto a photograph of the outcrop (Fig. 5). Several key relationships between phases are identified. Large areas of marcasite (green) and oxidized marcasite (brown) occur on the roof of the vug. The oxidized marcasite sometimes occurs entirely within the unaltered marcasite and sometimes occurs along the edges of the marcasite. The mixed sulfate phase (yellow) is often found on flat areas below the marcasite, and the red coating (red) generally is present immediately below the mixed sulfates. Only one small patch of the blue-gray phase (blue) is identified.

DISCUSSION

The focus of our investigations is a vug in which there has been significant hydrothermal mineralization within the clast-rich impact melt rocks of the Haughton impact structure. Using imaging spectroscopy of this outcrop, we map the spatial distribution of primary and secondary assemblages to understand the formation pathways and the habitability of the site. The primary hydrothermal mineralogies identified here are calcite and marcasite. Secondary weathering products include a yellow popcorn-textured fibroferrite and copiapite phase with cation chemistry dominated by Fe, a red coating on the calcite host rock consisting of gypsum, akaganeite, goethite, and jarosite with chemistry dominated by Ca and Fe, oxidized marcasite with formation of a thin Fe^{3+}-oxide and sulfate coating, and a blue-gray phase that is a mixture of calcite, gypsum,

clays, microcline, quartz, and hematite. These mineral identifications are similar to those reported for the same site by Izawa et al. (2011) with the exception of jarosite, which was only identified as a minor component in the coatings of APDI-13-14b and APDI-13-14j, likely because locations within the outcrop where jarosite has previously been found as a major component were not sampled. Our work extends the work of Izawa et al. (2011) by measuring the spectroscopic properties of these samples and using hyperspectral imaging in the field to map the distributions of these mineral assemblages in order to gain insight into the alteration processes.

The results of mapping secondary phases using hyperspectral imaging (Fig. 5) show spatial relationships between different assemblages that illuminate some detail regarding the evolving conditions during the post-impact hydrothermal alteration and subsequent low temperature weathering, as summarized in Fig. 6. This marcasite was interpreted by Osinski (2001, 2005a) to form at temperatures of ~100–240°C and pH <5. The sulfur within the marcasite was likely sourced from the gypsum and anhydrite-rich Bay Fiord Formation in the target rocks during post-impact fluid circulation (Osinski et al., 2001). This Formation outcrops nearby and underlies the impact melt-rich breccia here, consistent with field and orbital mapping (Osinski et al., 2005b; Tornabene et al., 2005) The presence of both Fe^{2+} and sulfide cations in the initial fluids from which the marcasite precipitated require reducing conditions. The marcasite that has been preserved and unweathered is mostly located on surfaces such as the ceiling of the outcrop where contact with altering fluids is relatively limited. Nevertheless, regions where there has been enhanced fluid flow are identified, distinct in their mineralogy and spectroscopic signatures, and mapped here in brown as the oxidized marcasite unit (Fig. 5). We

interpret this assemblage as forming *in situ* at low temperatures, under more oxidizing conditions, allowing for the partial oxidation of Fe and S. However, the limited extent of alteration suggests that water/rock ratios were likely low. This unit retains the morphology and hardness of the original marcasite, and marcasite is present close to the exterior of the sample. The location of this oxidized material nearly exclusively on overhanging portions of the outcrop is consistent with the interpreted low water/rock ratios because there is nowhere for water to pool or remain in contact with the marcasite for extended periods of time. In addition, if there were significant water present allowing alteration to continue, the Fe^{3+} in the coating would likely oxidize the S^{-} in the marcasite just below the surface (Jambor et al., 2000).

The efflorescent popcorn-textured mixed sulfate phase (yellow on Fig. 5) has a chemistry dominated by Fe, SO_4, and OH/H_2O. The sulfur in these samples is entirely oxidized, and Fe occurs in both +2 and +3 valence states. The chemical components of this sample likely derive mostly from the marcasite with little to no interaction with the surrounding calcite-rich rock, which would have resulted in incorporation of Ca into the sample mineralogy. There is 2.4 wt% CaO in this sample, and laboratory hyperspectral imaging identifies a minor component of gypsum. However, the dominant mineralogies in this sample are fibroferrite and copiapite, neither of which contain Ca. The oxidation of the primary marcasite produces sulfuric acid (e.g., Jambor et al., 2000), and waters that have been measured elsewhere associated with copiapite have pH values of approximately -1 (Jambor et al., 2000; Jamieson et al., 2005). As a result, this mixed sulfate phase probably formed from extremely low pH fluids that result from oxidation of the marcasite (Fig. 6). These fluids are more oxidizing and contain Fe^{2+}, Fe^{3+}, and SO_4^{2-}

in solution. These sulfates often occur on flatter surfaces below overhanging rock coated with marcasite. We propose that fluids dripped onto these surfaces after interacting with the marcasite and precipitated these mixed sulfates.

Later, we suggest that some of the copiapite and fibroferrite likely dissolved. The reaction between these fluids and the calcite host rock dissolved some of the calcite, adding Ca^{2+} cations to the fluids and neutralizing the acid somewhat. These water-rock interactions resulted in precipitation of gypsum and Fe^{3+}-oxide and sulfate-bearing coatings on the calcite rock directly below the mixed sulfate phases from less acidic fluids with Fe^{3+}, SO_4^{2-}, and Ca^{2+} in solution as well as extremely minor K^+. This process also been shown to occur during neutralization of acid mine waste, where literature has documented the importance of calcite in neutralizing the acidic fluids that result from acid mine drainage and gypsum coatings are often seen on the calcite rock (e.g., Booth et al., 1997; Jamieson et al., 2005; Chou et al., 2013; Lindsay et al., 2015).

The blue-gray material is more difficult to fit into the context of these other units, in part because it is so limited in extent at the outcrop. It may have formed through alteration by sulfate-bearing fluids that resulted from interaction with the mixed sulfates and red coatings with the calcite host rock and silicates within the impact melt rock. The 18.5 wt% SiO_2 in the sample and the identification of clays and microcline suggest a large contribution from the surrounding impact melt rocks, and this lithology may be a weathered clast of the silicate-bearing basement gneiss, which is common in the impact melt rock (e.g., Osinski and Spray, 2001).

The trends in weathering at this site illuminated from the hyperspectral imaging measurements are similar to reactions that have been studied in detail and occur at

gossans and sites of acid mine drainage at much larger scales (e.g., Nordstrom et al., 1999; Bigham and Nordstrom, 2000; Jambor et al., 2000). Zones of sulfate and oxide mineralogies that result from neutralization of acid with distance from the source have been mapped at mine sites with airborne hyperspectral imaging data (Swayze et al., 2000; Roach et al., 2006), though those studies map more mature weathering products (jarosite, goethite, and hematite) than the main units at our site, which are likely less mature due to the low water-rock ratios and low weathering intensity in this polar desert. Where the vug studied here differs from sites of acid mine drainage is in the origin of the deposit. This calcite- and marcasite-bearing vug would not be present if not for the meteorite impact, and the heat source driving the hydrothermal system came directly from the impact processes (Osinski et al., 2001, 2005a).

This site is a good environment for microbial colonization with energy sources from redox and chemical gradients discussed by Izawa et al. (2011) and is relevant to Mars. Indeed, S isotopic fractionations within the marcasite indicate biotic processes during formation of the marcasite (Parnell et al., 2010), and the later low temperature weathering processes may have also had microbial components (Izawa et al., 2011). In acid mine drainage sites with similar mineralogies, microbes are often present and can significantly increase rates of iron and sulfur oxidation (e.g., Nordstrom and Southam, 1997; Al et al., 2000; Schippers et al., 2010). Our map (Fig. 5) shows the locations of redox and chemical gradients discussed by Izawa et al. (2011) where microbes are most likely to be found, and examples of these boundaries are shown in photographs in Fig. 6. For example, boundaries that we have mapped between the marcasite and oxidized marcasite and between the mixed sulfates and red coating would be promising locations

to search for evidence of microbial activity. The imaging spectroscopy technique utilized here allows for remote assessment of the mineralogies present and identification of the ideal sampling locations.

This work has implications for understanding similar mineralogies and aqueous environments in planetary exploration. While the vug itself is covered by clast-rich impact melt rocks and is not clearly visible from orbit, mapping gypsum spectral signatures from orbital datasets shows a strong gypsum signature covering the area of this outcrop, suggesting significant available sulfur for the impact-generated hydrothermal system (Tornabene et al., 2005, 2014). The gypsum signature identified from orbit would make this, and other similar locations, promising sites for further exploration. In addition, the lithologies present at this vug are similar to some minerals detected on Mars. Sulfate-bearing units have been identified on Mars from orbital spectroscopy (e.g., Gendrin et al., 2005; Langevin et al., 2005; Bibring et al., 2006, 2007) and in situ rover measurements (e.g., Squyres et al., 2004a, 2004b, 2009), and there have been limited identifications of carbonates (e.g., Bandfield et al., 2003; Ehlmann et al., 2008; Boynton et al., 2009; Morris et al., 2010). The sulfur present within this vug at the Haughton impact structure was derived from sedimentary sulfates through hydrothermal processes. However, a large portion of the outcrop today is dominated spectrally by sulfates and oxides that formed at ambient temperatures. As a result, the detection of similar low temperature sulfates on Mars does not exclude a hydrothermal origin for the deposit. The results presented here are rather the modern expression of past hydrothermal mineralization that has been weathered at low temperatures in a polar desert environment.

Finally, this study also serves in part as a proof-of-concept for the utility of

hyperspectral imaging in determining mineralogy, past aqueous conditions, and astrobiological potential in planetary exploration. The spectral techniques used here are validated by laboratory measurements and provide new insights into the weathering processes at this vug. These results show the evolution from a reducing hydrothermal system to low temperature fluids that become progressively more oxidizing, evolve from acidic to more neutral, and change from simpler chemistries dominated by Fe and sulfate to more complex solutions incorporating Ca after reacting with the calcite host rock. With a hyperspectral imager extending into the shortwave infrared similar to the SWIR imager used in the laboratory, mineralogies at the outcrop could be mapped directly by the overtones and combination tones of vibrational absorption features, providing additional insights into the mineralogies present, the past aqueous environments, and the habitability at this outcrop or on Mars.

CONCLUSIONS

Hydrothermal systems generated by meteorite impacts are likely to be important in the formation of secondary phases on both Earth and Mars and provide habitats for microbial colonization (e.g., Izawa et al., 2011; Sapers et al., 2014). This work investigated a hydrothermal calcite- and marcasite-bearing vug at the Haughton impact structure that has undergone low temperature weathering using hyperspectral imaging in the field and laboratory as well as supporting spectroscopy, mineralogy, and chemistry measurements. The mineral assemblages identified and mapped at the outcrop are as follows: unaltered marcasite; oxidized marcasite with a coating of gypsum and jarosite; a mixed sulfate phase consisting of fibroferrite, copiapite, and minor gypsum, silica, and

melanterite; a red coating of gypsum, akaganeite, goethite, and jarosite; and a blue-gray phase with calcite, gypsum, clays, microcline, quartz, and hematite.

The aqueous conditions that altered this outcrop have been inferred from the mineral assemblages. The marcasite likely formed at high temperatures during the post-impact hydrothermal system, and the other phases formed at ambient temperatures after the hydrothermal system cooled. The oxidized marcasite probably formed first in a system with low water/rock ratios that partially oxidized the Fe and S. Extremely acidic fluids that had interacted with the marcasite then likely dripped onto flatter surfaces below, resulting in precipitation of the fibroferrite and copiapite/ferricopiapite mixed sulfate phase. We argue that those minerals then underwent some dissolution, and the resulting fluids interacted with the calcite rock below, dissolving some calcite while neutralizing the acidic fluids somewhat, leading to precipitation of gypsum and Fe^{3+}-oxide/sulfate-bearing coatings. The spectral units mapped and the inferred changes in fluid chemistry and oxidation state with progressive alteration can be used to predict the locations of microbial populations, and biosignatures are most likely to be found at the boundaries between various mapped units. This study also shows the utility of hyperspectral imaging in exploring sites that have undergone aqueous alteration, including through impact-driven processes, and in assessing their astrobiological potential on another planet.

ACKNOWLEDGMENTS

We would like to thank Paul Mann for his efforts in maintaining, packing, and shipping the equipment that made this work possible and David Bannon, Kwok Wong,

and Headwall Photonics, Inc. for use of their hyperspectral imagers in the laboratory. We thank Dave Murray and Joe Orchardo for assistance with flux fusion, ICP-AES, and elemental analyses. We are also grateful for help in the field from other members of the field team: Jerome Gattacceca, Jeremy Hansen, Yoann Quesnel, Pierre Rochette, and Scott Simpson. We thank Brown University for supporting this research. The Polar Continental Shelf Program provided field support for this work. Funding from the Natural Sciences and Engineering Research Council (NSERC) Discovery Grant and Northern Supplement program funded GRO, LLT, AP, and CLM. AP and CLM also thank the Northern Scientific Training Program for funding. EAC thanks the University of Winnipeg, the Canadian Space Agency, the Manitoba Research Innovations Funds, and NSERC of Canada for supporting the establishment of the University of Winnipeg's Planetary Spectrophotometer Facility and this study.

REFERENCES

Abramov O., and Kring D. A. 2005. Impact-induced hydrothermal activity on early Mars. *Journal of Geophysical Research* 110:E12S09.

Aines R. D., and Rossman G. R. 1984. Water in minerals? A peak in the infrared. *Journal of Geophysical Research: Solid Earth* 89:4059–4071.

Al T. A., Martin C. J., and Blowes D. W. 2000. Carbonate-mineral/water interactions in sulfide-rich mine tailings. *Geochimica et Cosmochimica Acta* 64:3933–3948.

Arvidson, R.E., Squyres, S.W., Bell, J.F., Catalano, J.G., Clark, B.C., Crumpler, L.S., Souza, P.A. de, Fairén, A.G., Farrand, W.H., Fox, V.K., Gellert, R., Ghosh, A., Golombek, M.P., Grotzinger, J.P., Guinness, E.A., Herkenhoff, K.E., Jolliff, B.L.,

Knoll, A.H., Li, R., McLennan, S.M., Ming, D.W., Mittlefehldt, D.W., Moore, J.M., Morris, R.V., Murchie, S.L., Parker, T.J., Paulsen, G., Rice, J.W., Ruff, S.W., Smith, M.D., and Wolff, M.J. 2014. Ancient aqueous environments at Endeavour Crater, Mars. *Science* 343:1248097.

Bandfield J. L., Glotch T. D., and Christensen P. R. 2003. Spectroscopic identification of carbonate minerals in the Martian dust. *Science* 301:1084–1087.

Barnhart C. J., Nimmo F., and Travis B. J. 2010. Martian post-impact hydrothermal systems incorporating freezing. *Icarus* 208:101–117.

Bibring, J.-P., Arvidson, R.E., Gendrin, A., Gondet, B., Langevin, Y., Mouelic, S.L., Mangold, N., Morris, R.V., Mustard, J.F., Poulet, F., Quantin, C., and Sotin, C. 2007. Coupled ferric oxides and sulfates on the Martian surface. *Science* 317:1206–1210.

Bibring, J.-P., Langevin, Y., Mustard, J.F., Poulet, F., Arvidson, R., Gendrin, A., Gondet, B., Mangold, N., Pinet, P., Forget, F., and the OMEGA team. 2006. Global mineralogical and aqueous Mars history derived from OMEGA/Mars Express data. *Science* 312:400 –404.

Bigham J. M., and Nordstrom D. K. 2000. Iron and aluminum hydroxysulfates from acid sulfate waters. *Reviews in Mineralogy and Geochemistry* 40:351–403.

Bishop J. L., Lane M. D., Dyar M. D., and Brown A. J. 2008. Reflectance and emission spectroscopy study of four groups of phyllosilicates: smectites, kaolinite-serpentines, chlorites and micas. *Clay Minerals* 43:35 –54.

Booth J., Hong Q., Compton R. G., Prout K., and Payne R. M. 1997. Gypsum overgrowths passivate calcite to acid attack. *Journal of Colloid and Interface*

Science 192:207–214.

Boynton, W.V., Ming, D.W., Kounaves, S.P., Young, S.M.M., Arvidson, R.E., Hecht, M.H., Hoffman, J., Niles, P.B., Hamara, D.K., Quinn, R.C., Smith, P.H., Sutter, B., Catling, D.C., and Morris, R.V. 2009. Evidence for calcium carbonate at the Mars Phoenix landing site. *Science* 325:61–64.

Brown A. J. 2014. Spectral bluing induced by small particles under the Mie and Rayleigh regimes. *Icarus* 239:85–95.

Burns R. G. 1993. *Mineralogical applications of crystal field theory*, 2nd ed. Cambridge: Cambridge University Press. 551 p.

Chavez Jr P. S. 1996. Image-based atmospheric corrections-revisited and improved. *Photogrammetric Engineering & Remote Sensing* 62:1025–1036.

Chou I.-M., Seal II R. R., and Wang A. 2013. The stability of sulfate and hydrated sulfate minerals near ambient conditions and their significance in environmental and planetary sciences. *Journal of Asian Earth Sciences* 62:734–758.

Clark R. N. et al. 2008. Compositional mapping of Saturn's satellite Dione with Cassini VIMS and implications of dark material in the Saturn system. *Icarus* 193:372–386.

Clark R. N. et al. 2002. Surface reflectance calibration of terrestrial imaging spectroscopy data: a tutorial using AVIRIS. *Proceedings, 10th Airborne Earth Science Workshop*. pp. 02–1.

Clark R. N., King T. V. V., Klejwa M., Swayze G. A., and Vergo N. 1990. High spectral resolution reflectance spectroscopy of minerals. *Journal of Geophysical Research* 95:12653–12680.

Clark R. N., and Roush T. L. 1984. Reflectance spectroscopy: quantitative analysis techniques for remote sensing applications. *Journal of Geophysical Research* 89:6329–6340.

Clark, R.N., Swayze, G.A., Wise, R., Livo, E., Hoefen, T., Kokaly, R., Sutley, S.J. 2007. USGS digital spectral library splib06a. *U.S. Geological Survey,* Digital Data Series 231.

Cloutis E. A., and Gaffey M. J. 1994. An X-ray diffraction and reflectance spectroscopy study of iron sulphides. Proceedings, 25th Lunar and Planetary Science Conference, p. 273-274.

Cloutis, E. A., Hawthorne, F. C., Mertzman, S. A., Krenn, K., Craig, M. A., Marcino, D., Methot, M., Strong, J., Mustard, J. F., Blaney, D. L., Bell III, J. F., and Vilas, F. 2006. Detection and discrimination of sulfate minerals using reflectance spectroscopy. *Icarus* 184:121–157.

Cockell C. S., and Lee P. 2002. The biology of impact craters — a review. *Biological Reviews* 77:279–310.

Crowley J. K., Williams D. E., Hammarstrom J. M., Piatak N., Chou I.-M., and Mars J. C. 2003. Spectral reflectance properties (0.4–2.5 μm) of secondary Fe-oxide, Fe-hydroxide, and Fe-sulphate-hydrate minerals associated with sulphide-bearing mine wastes. *Geochemistry: Exploration, Environment, Analysis* 3:219–228.

Ehlmann, B. L., Mustard, J. F., Murchie, S. L., Poulet, F., Bishop, J. L., Brown, A. J., Calvin, W. M., Clark, R. N., Marais, D. J. D., Milliken, R. E., Roach, L. H., Roush, T. L., Swayze, G. A., and Wray, J. J. 2008. Orbital identification of carbonate-bearing rocks on Mars. *Science* 322:1828–1832.

Fischer E. M., and Pieters C. M. 1993. The continuum slope of Mars: bidirectional reflectance investigations and applications to Olympus Mons. *Icarus* 102:185–202.

Flemming R. L. 2007. Micro X-ray diffraction (μXRD): a versatile technique for characterization of Earth and planetary materials. *Canadian Journal of Earth Sciences* 44:1333–1346.

Gendrin, A., Mangold, N., Bibring, J.-P., Langevin, Y., Gondet, B., Poulet, F., Bonello, G., Quantin, C., Mustard, J., Arvidson, R., and LeMouélic, S. 2005. Sulfates in Martian layered terrains: the OMEGA/Mars Express view. *Science* 307:1587–1591.

Goryniuk M. C., Rivard B. A., and Jones B. 2004. The reflectance spectra of opal-A (0.5–25 μm) from the Taupo Volcanic Zone: Spectra that may identify hydrothermal systems on planetary surfaces. *Geophysical Research Letters* 31:L24701.

Hagerty J. J., and Newsom H. E. 2003. Hydrothermal alteration at the Lonar Lake impact structure, India: Implications for impact cratering on Mars. *Meteoritics & Planetary Science* 38:365–381.

Holm N. G. 1992. Why are hydrothermal systems proposed as plausible environments for the origin of life?. In *Marine Hydrothermal Systems and the Origin of Life*, edited by Holm D. N. G. Springer Netherlands. pp. 5–14.

Hunt G. R., and Salisbury J. W. 1971. Visible and near infrared spectra of minerals and rocks. II. Carbonates. *Modern Geology* 2:23–30.

Hunt G. R., Salisbury J. W., and Lenhoff C. J. 1971. Visible and near-infrared spectra of

minerals and rocks. IV. Sulphides and sulphates. *Modern Geology* 3:1–14.

Izawa M. R. M., Banerjee N. R., Osinski G. R., Flemming R. L., Parnell J., and Cockell C. S. 2011. Weathering of post-impact hydrothermal deposits from the Haughton impact structure: implications for microbial colonization and biosignature preservation. *Astrobiology* 11:537–550.

Jambor J. L., Nordstrom D. K., and Alpers C. N. 2000. Metal-sulfate salts from sulfide mineral oxidation. *Reviews in Mineralogy and Geochemistry* 40:303–350.

Jamieson H. E., Robinson C., Alpers C. N., McCleskey R. B., Nordstrom D. K., and Peterson R. C. 2005. Major and trace element composition of copiapite-group minerals and coexisting water from the Richmond mine, Iron Mountain, California. *Chemical Geology* 215:387–405.

Johnson J. R., and Grundy W. M. 2001. Visible/near-infrared spectra and two-layer modeling of palagonite-coated basalts. *Geophysical Research Letters* 28:2101–2104.

Kring D. A. 2000. Impact events and their effect on the origin, evolution, and distribution of life. *GSA Today* 10: 1–7.

Langevin Y., Poulet F., Bibring J.-P., and Gondet B. 2005. Sulfates in the north polar region of Mars detected by OMEGA/Mars Express. *Science* 307: 1584–1586.

Lindsay M. B. J., Moncur M. C., Bain J. G., Jambor J. L., Ptacek C. J., and Blowes D. W. 2015. Geochemical and mineralogical aspects of sulfide mine tailings. *Applied Geochemistry* in press.

Martin W., Baross J., Kelley D., and Russell M. J. 2008. Hydrothermal vents and the origin of life. *Nature Reviews Microbiology* 6:805–814.

Marzo G. A. Davila, A. F., Tornabene, L. L., Dohm, J. M., Fairén, A. G., Gross, C., Kneissl, T., Bishop, J. L., Roush, T. L., McKay, C. P. 2010. Evidence for Hesperian impact-induced hydrothermalism on Mars. *Icarus* 208:667–683.

McLennan, S. M., Sephton, M. A., Allen, C., Allwood, A. C., Barbieri, R., Beaty, D. W., Boston, P., Carr, M., Grady, M., Grant, J., Heber, V. S., Herd, C. D. K., Hofman, B., King, P., Mangold, N., Ori, G. G., Rossi, A. P., Raulin, F., Ruff, S. W., Sherwood Lollar, B., Symes, S., and Wilson, M. G. 2012. Planning for Mars Returned Sample Science: Final Report of the MSR End-to-End International Science Analysis Group (E2E-iSAG). *Astrobiology* 12:175–230.

Morris, R. V., Ruff, S. W., Gellert, R., Ming, D. W., Arvidson, R. E., Clark, B. C., Golden, D. C., Siebach, K., Klingelhöfer, G., Schröder, C., Fleischer, I., Yen, A. S., and Squyres, S. W. 2010. Identification of carbonate-rich outcrops on Mars by the Spirit Rover. *Science* 329:421–424.

Murray R., Miller D. J., and Kryc K. 2000. Analysis of major and trace elements in rocks, sediments, and interstitial waters by inductively coupled plasma–atomic emission spectrometry (ICP-AES). *ODP Technical Note* 29:1–27.

Naumov M. V. 2005. Principal features of impact-generated hydrothermal circulation systems: mineralogical and geochemical evidence. *Geofluids* 5:165–184.

Newsom H. E. 1980. Hydrothermal alteration of impact melt sheets with implications for Mars. *Icarus* 44:207–216.

Newsom H. E., Brittelle G. E., Hibbitts C. A., Crossey L. J., and Kudo A. M. 1996. Impact crater lakes on Mars. *Journal of Geophysical Research: Planets* 101:14951–14955.

Newsom H. E., Hagerty J. J., and Thorsos I. E. 2001. Location and sampling of aqueous and hydrothermal deposits in Martian impact craters. *Astrobiology* 1:71–88.

Nisbet E. G., and Sleep N. H. 2001. The habitat and nature of early life. *Nature* 409:1083–1091.

Nordstrom D. K., Alpers C. N., Ptacek C. J., and Blowes D. W.1999. Negative pH and extremely acidic mine waters from Iron Mountain, California. *Environmental Science & Technology* 34:254–258.

Nordstrom D. K., and Southam G. 1997. Geomicrobiology of sulfide mineral oxidation. *Reviews in Mineralogy and Geochemistry* 35:361–390.

Osinski, G. R., Tornabene, L. L., Banerjee, N. R., Cockell, C. S., Flemming, R., Izawa, M. R. M., McCutcheon, J., Parnell, J., Preston, L. J., Pickersgill, A. E., Pontefract, A., Sapers, H. M., and Southam, G. 2013. Impact-generated hydrothermal systems on Earth and Mars. *Icarus* 224:347–363.

Osinski G. R., Lee P., Parnell J., Spray J. G., and Baron M. 2005a. A case study of impact-induced hydrothermal activity: The Haughton impact structure, Devon Island, Canadian High Arctic. *Meteoritics & Planetary Science* 40:1859–1877.

Osinski G. R., Lee P., Spray J. G., Parnell J., Lim D. S. S., Bunch T. E., Cockell C. S., and Glass B. 2005b. Geological overview and cratering model for the Haughton impact structure, Devon Island, Canadian High Arctic. *Meteoritics & Planetary Science* 40:1759–1776.

Osinski G. R., and Spray J. G. 2003. Evidence for the shock melting of sulfates from the Haughton impact structure, Arctic Canada. *Earth and Planetary Science Letters* 215:357–370.

Osinski G. R., and Spray J. G. 2001. Impact-generated carbonate melts: evidence from the Haughton structure, Canada. *Earth and Planetary Science Letters* 194:17–29.

Osinski G. R., Spray J. G., and Lee P. 2001. Impact-induced hydrothermal activity within the Haughton impact structure, arctic Canada: Generation of a transient, warm, wet oasis. *Meteoritics & Planetary Science* 36:731–745.

Parnell J. et al. 2010. Sulfur isotope signatures for rapid colonization of an impact crater by thermophilic microbes. *Geology* 38:271–274.

Parnell J., Boyce A. J., Osinski G. R., Izawa M. R. M., Banerjee N., Flemming R., and Lee P. 2012. Evidence for life in the isotopic analysis of surface sulphates in the Haughton impact structure, and potential application on Mars. *International Journal of Astrobiology* 11:93–101.

Pelkey S. M. et al. 2007. CRISM multispectral summary products: Parameterizing mineral diversity on Mars from reflectance. *Journal of Geophysical Research* 112:E08S14.

Pieters C. M. 1983. Strength of Mineral Absorption Features in the Transmitted Component of Near-Infrared Reflected Light: First Results From RELAB. *Journal of Geophysical Research* 88(B11):9534–9544.

Pontefract A., Osinski G. R., Cockell C. S., Moore C. A., Moores J. E., and Southam G. 2014. Impact-generated endolithic habitat within crystalline rocks of the Haughton impact structure, Devon Island, Canada. *Astrobiology* 14:522–533.

Pontefract A., Osinski G. R., Lindgren P., Parnell J., Cockell C. S., and Southam G. 2012. The effects of meteorite impacts on the availability of bioessential elements for endolithic organisms. *Meteoritics & Planetary Science* 47:1681–1691.

Rathbun J. A., and Squyres S. W. 2002. Hydrothermal systems associated with martian impact craters. *Icarus* 157:362–372.

Roach L. H., Mustard J., Gendrin A., Fernández-Remolar D., Amils R., and Amaral-Zettler L. 2006. Finding mineralogically interesting targets for exploration from spatially coarse visible and near IR spectra. *Earth and Planetary Science Letters* 252:201–214.

Sapers H. M., Osinski G. R., Banerjee N. R., and Preston L. J. 2014. Enigmatic tubular features in impact glass. *Geology* 42:471–474.

Scheinost A. C., Chavernas A., Barron V., and Torrent J. 1998. Use and limitations of second-derivative diffuse reflectance spectroscopy in the visible to near-infrared range to identify and quantify Fe oxide minerals in soils. *Clays and Clay Minerals* 46:528 –536.

Schippers A., Breuker A., Blazejak A., Bosecker K., Kock D., and Wright T. L. 2010. The biogeochemistry and microbiology of sulfidic mine waste and bioleaching dumps and heaps, and novel Fe(II)-oxidizing bacteria. *Hydrometallurgy* 104:342–350.

Schultz P. H., Harris R. S., Clemett S. J., Thomas-Keprta K. L., and Zárate M. 2014. Preserved flora and organics in impact melt breccias. *Geology* 42:515–518.

Schulze-Makuch D., Dohm J. M., Fan C., Fairén A. G., Rodriguez J. A. P., Baker V. R., and Fink W. 2007. Exploration of hydrothermal targets on Mars. *Icarus* 189:308–324.

Schwenzer S. P. Abramov, O., Allen, C. C., Clifford, S. M., Cockell, C. S., Filiberto, J., Kring, D. A., Lasue, J., McGovern, P. J., Newsom, H. E., Treiman, A. H.,

Vaniman, D. T., and Wiens, R. C. 2012. Puncturing Mars: How impact craters interact with the Martian cryosphere. *Earth and Planetary Science Letters* 335–336:9–17.

Schwenzer S. P., and Kring D. A. 2013. Alteration minerals in impact-generated hydrothermal systems – Exploring host rock variability. *Icarus* 226:487–496.

Schwenzer S. P., and Kring D. A. 2009. Impact-generated hydrothermal systems capable of forming phyllosilicates on Noachian Mars. *Geology* 37:1091 –1094.

Sherman D. M., and Waite T. D. 1985. Electronic spectra of Fe (super 3+) oxides and oxide hydroxides in the near IR to near UV. *American Mineralogist* 70:1262–1269.

Shock E. L. 1997. High-temperature life without photosynthesis as a model for Mars. *Journal of Geophysical Research: Planets* 102:23687–23694.

Singer R. B., and Roush T. L. 1983. Spectral reflectance properties of particulate weathered coatings on rocks: Laboratory modeling and applicability to Mars (abstract). *14th Lunar and Planetary Institute Science Conference Abstracts*. pp. 708–709 http://adsabs.harvard.edu/full/1983LPI....14..708S (Accessed September 22, 2013).

Smith D. K. 1998. Opal, cristobalite, and tridymite: Noncrystallinity versus crystallinity, nomenclature of the silica minerals and bibliography. *Powder Diffraction* 13:2–19.

Squyres, S. W., Arvidson, R. E., Bell, J. F., Calef, F., Clark, B. C., Cohen, B. A., Crumpler, L. A., Souza, P. A. de, Farrand, W. H., Gellert, R., Grant, J., Herkenhoff, K. E., Hurowitz, J. A., Johnson, J. R., Jolliff, B. L., Knoll, A. H., Li,

R., McLennan, S. M., Ming, D. W., Mittlefehldt, D. W., Parker, T. J., Paulsen, G., Rice, M. S., Ruff, S. W., Schröder, C., Yen, A. S., and Zacny, K. 2012. Ancient impact and aqueous processes at Endeavour Crater, Mars. *Science* 336:570–576.

Squyres S. W. Knoll, A. H., Arvidson, R. E., Ashley, J. W., Bell, J. F., Calvin, W. M., Christensen, P. R., Clark, B. C., Cohen, B. A., Souza, P. A. de, Edgar, L., Farrand, W. H., Fleischer, I., Gellert, R., Golombek, M. P., Grant, J., Grotzinger, J., Hayes, A., Herkenhoff, K. E., Johnson, J. R., Jolliff, B., Klingelhöfer, G., Knudson, A., Li, R., McCoy, T. J., McLennan, S. M., Ming, D. W., Mittlefehldt, D. W., Morris, R. V., Rice, J. W., Schröder, C., Sullivan, R. J., Yen, A., Yingst, R. A.2009. Exploration of Victoria Crater by the Mars Rover Opportunity. *Science* 324:1058–1061.

Squyres S. W., Grotzinger, J. P., Arvidson, R. E., Bell, J. F., Calvin, W., Christensen, P. R., Clark, B. C., Crisp, J. A., Farrand, W. H., Herkenhoff, K. E., Johnson, J. R., Klingelhöfer, G., Knoll, A. H., McLennan, S. M., McSween, H. Y., Morris, R. V., Rice, J. W., Rieder, R., and Soderblom, L. A.2004b. In Situ evidence for an ancient aqueous environment at Meridiani Planum, Mars. *Science* 306:1709–1714.

Squyres, S. W., Arvidson, R. E., Bell, J. F., Brückner, J., Cabrol, N. A., Calvin, W., Carr, M. H., Christensen, P. R., Clark, B. C., Crumpler, L., Marais, D. J. D., d' Uston, C., Economou, T., Farmer, J., Farrand, W., Folkner, W., Golombek, M., Gorevan, S., Grant, J. A., Greeley, R., Grotzinger, J., Haskin, L., Herkenhoff, K. E., Hviid, S., Johnson, J., Klingelhöfer, G., Knoll, A. H., Landis, G., Lemmon, M., Li, R., Madsen, M. B., Malin, M. C., McLennan, S. M., McSween, H. Y., Ming, D. W.,

Moersch, J., Morris, R. V., Parker, T., Rice, J. W., Richter, L., Rieder, R., Sims, M., Smith, M., Smith, P., Soderblom, L. A., Sullivan, R., Wänke, H., Wdowiak, T., Wolff, M., and Yen, A. 2004a. The Opportunity rover's Athena science investigation at Meridiani Planum, Mars. *Science* 306:1698–1703.

Swayze, G. A., Smith, K. S., Clark, R. N., Sutley, S. J., Pearson, R. M., Vance, J. S., Hageman, P. L., Briggs, P. H., Meier, A. L., Singleton, M. J., Roth, S. 2000. Using imaging spectroscopy to map acidic mine waste. *Environmental Science & Technology* 34:47–54.

Tornabene L. L., Moersch J. E., Osinski G. R., Lee P., and Wright S. P. 2005. Spaceborne visible and thermal infrared lithologic mapping of impact-exposed subsurface lithologies at the Haughton impact structure, Devon Island, Canadian High Arctic: Applications to Mars. *Meteoritics & Planetary Science* 40:1835–1858.

Tornabene L. L., Osinski G. R., Greenberger R. N., Bishop J. L., Cloutis E. A., Marion C. L., Mustard J. F., Pontefract A., and Ramsey M. S. 2014. The Pre-, Syn- and Post-Impact Origin of Hydrated Phases: A Case Study Based on the Remote Sensing and Ground-Truth at the Haughton Impact Structure, Nunavut, Canada (abstract #2710). *45th Lunar and Planetary Science Conference.*

Tornabene L. L., Osinski G. R., and McEwen A. S. 2009. Parautochthonous megabreccias and possible evidence of impact-induced hydrothermal alteration in Holden Crater, Mars (abstract #1766). *40th Lunar and Planetary Science Conference.*

Tornabene L. L., Osinski G. R., McEwen A. S., Wray J. J., Craig M. A., Sapers H. M.,

and Christensen P. R. 2013. An impact origin for hydrated silicates on Mars: A synthesis. *Journal of Geophysical Research: Planets* 118:994–1012.

Viviano-Beck, C. E., Seelos, F. P., Murchie, S. L., Kahn, E. G., Seelos, K. D., Taylor, H. W., Taylor, K., Ehlmann, B. L., Wisemann, S. M., Mustard, J. F., Morgan, M. F. 2014. Revised CRISM spectral parameters and summary products based on the currently detected mineral diversity on Mars. *Journal of Geophysical Research: Planets* 119: 1403–1431.

Whitney D. L., and Evans B. W. 2010. Abbreviations for names of rock-forming minerals. *American Mineralogist* 95:185–187.

Young K. E., van Soest M. C., Hodges K. V., Watson E. B., Adams B. A., and Lee P. 2013. Impact thermochronology and the age of Haughton impact structure, Canada. *Geophysical Research Letters* 40:3836–3840.

Table 1. Sample descriptions.

Sample name	Sample description
APDI-13-14a	Yellow, popcorn-textured mixed sulfate
APDI-13-14b	Dark red coating on calcite host rock
APDI-13-14c	Small green marcasite crystals with minor pyrite on calcite host rock
APDI-13-14h	Friable blue-gray phase
APDI-13-14j	Oxidized, dark red, weathered marcasite with the primary textures and morphologies of the marcasite still visible

Table 2. Equations and interpretations of spectral and mineral indicator parameters for laboratory hyperspectral imaging data.

Spectral parameter	Equation	Interpretation
	Spectral parameters	
BD950	$1-\frac{2.*\sum(R946\ to\ R957)}{(\frac{763}{607.5})*\sum(R722\ to\ R733)+(\frac{3164}{1822.5})*(R1312+R1324+R1336)}$	Fe^{3+} in Fe^{3+}-oxides or sulfates (e.g., Burns, 1993)
BD1410	$1-\frac{2*(R1408+R1420)}{0.72*(R1345+R1360)+1.28*(R1504+R1516)}$	First overtone of OH stretch (e.g., Clark et al., 1990)
R1440/R1490	$R1444/R1493$	OH stretching overtones in sulfates (e.g,. Cloutis et al., 2006); distinguishes copiapite/ fibroferrite from gypsum
BD1450broad	$1-\frac{2*(R1444+R1457)}{(\frac{276}{414})*(R1336+R1348)+(\frac{552}{414})*(R1650+R1662)}$	OH stretching overtone (e.g., Clark et al., 1990); highlights broad bands in minerals such as gypsum
BD1480	$1-\frac{2*(R1468+R1481+R1492)}{0.88*(R1336+R1348+R1360)+1.12*(R1577+R1589+R1601)}$	OH stretching overtone (e.g., Clark et al., 1990)
BD1760	$1-\frac{(\frac{4}{3})*(R1746+R1758+R1770)}{0.92*(R1662+R1673)+1.08*(R1831+R1843)}$	Commonly seen in sulfates (e.g., Crowley et al., 2003; see discussion of possible band assignments in Cloutis et al., 2006)
BD1900	$1-\frac{2*(R1.915+R1.927+R1.939)}{1.34*(R1843+R1854+R1867)+0.66*(R.036+R2047+R2060)}$	H-O-H combination (e.g., Clark et al., 1990)
BD2200	$1-\frac{(\frac{4}{3})*(R2205+R2217+R2229)}{(\frac{58}{108})*(R2132+R2144)+(\frac{158}{108})*(R2241+R2253)}$	S-O combination or OH/H_2O combinations (e.g,. Cloutis et al., 2006)
BD2340	$1-\frac{2*(R2337+R2349)}{0.48*(R2205+R2217)+1.52*(R2386+R.398)}$	Mg_3-OH combination band or third overtone of the C-O asymmetric stretching mode (Bishop et al., 2008; e.g., Hunt and Salisbury, 1971)
D2500	$1-\frac{R2482+R2494}{R2410+R2422}$	C-O combination band in carbonates (Hunt and Salisbury, 1971)
RedSlope SWIR	$\frac{R1794+R1806+R1818}{R1154+R1167+R1179}$	Textural or mineralogical effect
	Mineral indicator parameters	
Copiapite/ fibroferrite	(R1440/R1490) > 1; RedSlopeSWIR < 1; BD1480 > 0; BD2200 < 0.03; Displayed value: BD1480	
Gypsum1	BD1760>0; BD1480>0; Displayed value: BD1760	
Gypsum2	BD1450broad > 0.1; BD2200 > 0; R1440/R1490 < 1; BD1760 > 0; Displayed value: BD1760	
Calcite	BD2340>0 and D2500>0; Displayed value: BD2340	

R# = reflectance at # nm.
Σ(R# to R##) = sum of all bands from R# to R##

Table 3. Equations and interpretations for spectral and lithological indicator parameters for NIR field hyperspectral imaging data.

Spectral parameter	Equation	Interpretation
	Spectral parameters	
BD820	$1-\frac{R810+R820+R830+R840}{13/18*(R670+R680)+23/18*(R1030+R1040)}$	Fe^{3+} in sulfates such as copiapite (e.g., Cloutis et al., 2006)
BD820_2	$1-\frac{R810+R820+R830+R840}{15/11.5*(R670+R680)+8/11.5*(R900+R910)}$	Same as BD820
BD900	$1-\frac{R890+R900+R910+R920}{21/18*(R670+R680)+15/18*(R1030+R1040)}$	Fe^{2+} in marcasite (Hunt et al., 1971; Cloutis and Gaffey, 1994); Fe^{2+} electronic transition in some Fe^{2+} sulfates (e.g., Cloutis et al., 2006); Fe^{3+}-oxides (e.g., Sherman and Waite, 1985; Scheinost et al., 1998)
BD900_2	$1-\frac{R890+R900+R910+R920}{8/10.5*(R820+R830)+13/10.5*(R1030+R1040)}$	Same as BD900
D1000	$1-\frac{R1030+R1040}{(R780+R790)}$	Crystal field transitions of Fe (e.g., Burns, 1993)
BlueSlopeNIR	$\frac{R690+R700+R710}{R1040+R1050+R1060}$	Tied to mineralogy or textural property
RedSlopeNIR	$\frac{R1040+R1050+R1060}{R690+R700+R710}$	Tied to mineralogy or textural property
Slope <750	$\frac{R740+R750}{R650+R660}$	Rise in reflectance due to Fe^{3+} electronic transition at shorter wavelengths
	Lithological indicator parameters for portions of outcrop illuminated by sun	
Mixed sulfate (APDI-13-14a)	BD820_2 > 0.01; BD820 > 0.03; BD900 > 0.03; D1000 < 0; BD820_2 > BD900_2; displayed value: BD820	
Red coating (APDI-13-14b)	BD820 > 0; D1000 > 0.15; (Slope <750) > 0.03; displayed value: D1000	
Marcasite (APDI-13-14c)	R920 < 0.15; BD820_2 > 0.01; BD 820 > 0.03; BD900 > 0.03; D1000 < 0.03; BD820_2 < BD900_2; displayed value: BD900	
Gray-blue material (APDI-13-14h)	BD900_2 > 0; R720 < 0.22; BD820_2 < 0.04; BD900 < 0.09; (Slope <750) < 0.09; BD820 > -0.02; BD900 > 0; D1000 > 0; 1 < BlueSlopeNIR < 1.1; displayed value: BD900	
	Lithological indicator parameters for portions of outcrop in shade	
Mixed sulfate (APDI-13-14a)	R990 > 0.008; BD820 > -0.04; BD900 > 0; BD900_2 < 0.04; 1 < BlueSlopeNIR < 1.5; BD820_2 > 0.1; displayed value: BD820	

Spectral parameter	Equation	Interpretation
Red coating (APDI-13-14b)	BlueSlopeNIR > 1.39; BD820 < 0; D1000 > 0.1; (Slope <750) > 1; displayed value: D1000	
Marcasite (APDI-13-14c)	RedSlopeNIR > 0.92; D1000 < 0.04; BD820 > 0; BD900 > 0.07; (Slope <750) < 1; BD900_2 >0; displayed value: BD900	
Oxidized marcasite (APDI-13-14h)	1.15 < BlueSlopeNIR < 1.5; 0 < BD900 < 0.2; 0 < D1000 < 0.35; -0.1 < BD900_2 < 0.05; displayed value: D1000	

R# = reflectance at # nm.

Table 4. Chemistry (ICP-AES and elemental analyses) in wt% and mineralogy (pXRD and μXRD) for samples discussed in the text.

	APDI-13-14a	APDI-13-14b	APDI-13-14c	APDI-13-14h	APDI-13-14j
Replicates	2	1	3	3	1
Al_2O_3	0.15	0.31	0.14	2.97	0.07
CaO	2.40	18.78	18.60	38.60	3.93
Cr_2O_3	0.001	0.001	n.d.	0.002	0.001
FeO	25.86	28.08	25.97	2.54	38.79
K_2O	0.08	0.14	0.06	1.78	0.03
MgO	0.84	0.47	0.72	2.13	0.13
MnO	0.001	0.005	0.005	0.012	0.002
Na_2O	0.018	n.d.	0.002	0.022	n.d.
NiO	0.001	n.d.	n.d.	0.001	0.002
P_2O_5	0.01	0.01	0.01	0.05	0.01
SiO_2	0.99	2.01	1.15	18.52	0.69
TiO_2	0.005	0.009	0.004	0.128	n.d.
C	0.06	2.99	3.05	8.11	1.77
Mineralogy	pXRD: Fft, Cop, Crs, Gp, Mlt	μXRD (coating): Gp, Jrs, Gth, Akg pXRD: Cal, Gp, Mrc, Py, Qz	μXRD: Mrc pXRD: Mrc, Cal, Py, Clt, Gp, Qz	pXRD: Qz, Cal, Mc, Gp, Hem, Ilt, Mnt	μXRD: Gp, Jrs, Mrc

n.d. = not detected

Mineral abbreviations (from Whitney and Evans, 2010 where possible), endmember chemical formulas, and best matching ICDD card numbers: Akg=akaganeite (Fe^{3+}(O,OH,Cl); 00-042-1315), Cal=calcite ($CaCO_3$; 01-083-1762), Clt=celestine ($SrSO_4$; 00-005-0593), Cop=copiapite ($Fe^{2+}Fe^{3+}_4(SO_4)_6(OH)_2 \cdot 20H_2O$; 00-042-0599), Crs=cristobalite (SiO_2; 00-039-1425), Fft=fibroferrite ($Fe^{3+}(SO_4)(OH) \cdot 5H_2O$; 00-038-0481), Gp=gypsum ($CaSO_4 \cdot 2H_2O$; 00-036-0432), Gth=goethite ($Fe^{3+}OOH$; 00-029-0713); Ilt=illite ($KAl_2(Si_3Al)O_{10}(OH)_2$; 00-010-0490), Jrs=jarosite ($KFe^{3+}_3(SO_4)_2(OH)_6$; 00-002-0602), Mc=microcline ($KAlSi_3O_8$; 00-022-0675) , Mlt=melanterite ($Fe^{2+}SO_4 \cdot 7H_2O$; 00-022-0633), Mnt=montmorillonite ($(Na,Ca)_{0.3}(Al,Mg)_2Si_4O_{10}(OH)_2 \cdot nH_2O$; 00-007-0051), Mrc=marcasite (FeS_2; 00-037=0475), Py=pyrite (FeS_2; 01-073-8127), Qz=quartz (SiO_2; 00-005-0490)

FIGURE CAPTIONS

Fig. 1. Geologic map of the Haughton impact structure modified from Osinski et al. (2005a) with the location of the calcite- and marcasite-bearing vug studied here starred.

Fig. 2. (left) Reflectance spectra of samples measured in the field with an ASD with contact probe attachment. (middle) Reflectance spectra from the NIR images of similar units to those sampled and measured with the ASD. The colors match the corresponding ASD spectra and the units mapped in Fig. 5. (left) Library spectra of some minerals present in the samples analyzed here. Copiapite (GDS21), hematite (GDS27), gypsum (SU2202), montmorillonite (STx-1), and calcite (CO2004) spectra are from the USGS spectral library (Clark et al., 2007). The marcasite spectrum (MAR101) is from the RELAB database (Pieters, 1983) and originally reported by Cloutis and Gaffey (1994). Spectra in all plots are offset and scaled for clarity.

Fig. 3. Hyperspectral images of three samples measured in the laboratory. A-C) Color composite images with bands selected to approximate a true color image for samples (A) APDI-13-14a, (B) APDI-13-14b, and (C) APDI-13-14h. Red: 0.666 μm, green: 0.534 μm, blue: 0.427 μm. D) Mineral indicator map of sample APDI-13-14a. Magenta: fibroferrite + copiapite, green: gypsum2. E) Spectral parameter and mineral indicator map of sample APDI-13-14b. Cyan: gypsum2. Red: BD950 (due to Fe^{3+}). F) Mineral indicator map of sample APDI-13-14h. Magenta: calcite. Green: gypsum1. See Table 2 for descriptions of each parameter. The parameters shown in E) and F) have been median filtered to reduce noise.

Fig. 4. A) Example NIR false color composite image of one portion of the outcrop. Red: 0.99 μm, green: 0.80 μm, blue: 0.71 μm. B) Example lithological indicator parameter image of the outcrop. Red: red coating, green: marcasite, blue: mixed sulfate. Dark/shadowed areas have been masked in both images. See Table 3 for descriptions of each parameter. The location of this image within the outcrop is shown in Fig. 5A.

Fig. 5. Map of different mineral assemblages within this vug. A) Photograph of the vug with locations from which samples were collected labeled. Boxes outline the regions shown in Fig. 4 (light blue), 6B (dark gray), and 6C (light gray. B) Mineral assemblages that are spectrally-similar to the collected samples. Yellow regions are mixed sulfates similar to APDI-13-14a, red regions are red coatings similar to APDI-13-14b, green regions are unaltered marcasite similar to APDI-13-14c, brown regions are oxidized marcasite similar to APDI-13-14j, and blue is the blue-gray phase spectrally similar APDI-13-14h.

Fig. 6. A) Alteration sequence inferred from the results of this paper. Of the minerals represented, only marcasite formed in the post-impact hydrothermal system, but other assemblages would not be present if not for the primary hydrothermal mineralization. B, C) Photographs showing examples of fluid flow pathways over short distances. Sample APDI-13-14b was collected within (B), and sample APDI-13-14a was collected within (C). Locations of these photos within the outcrop are shown in Fig. 5A.

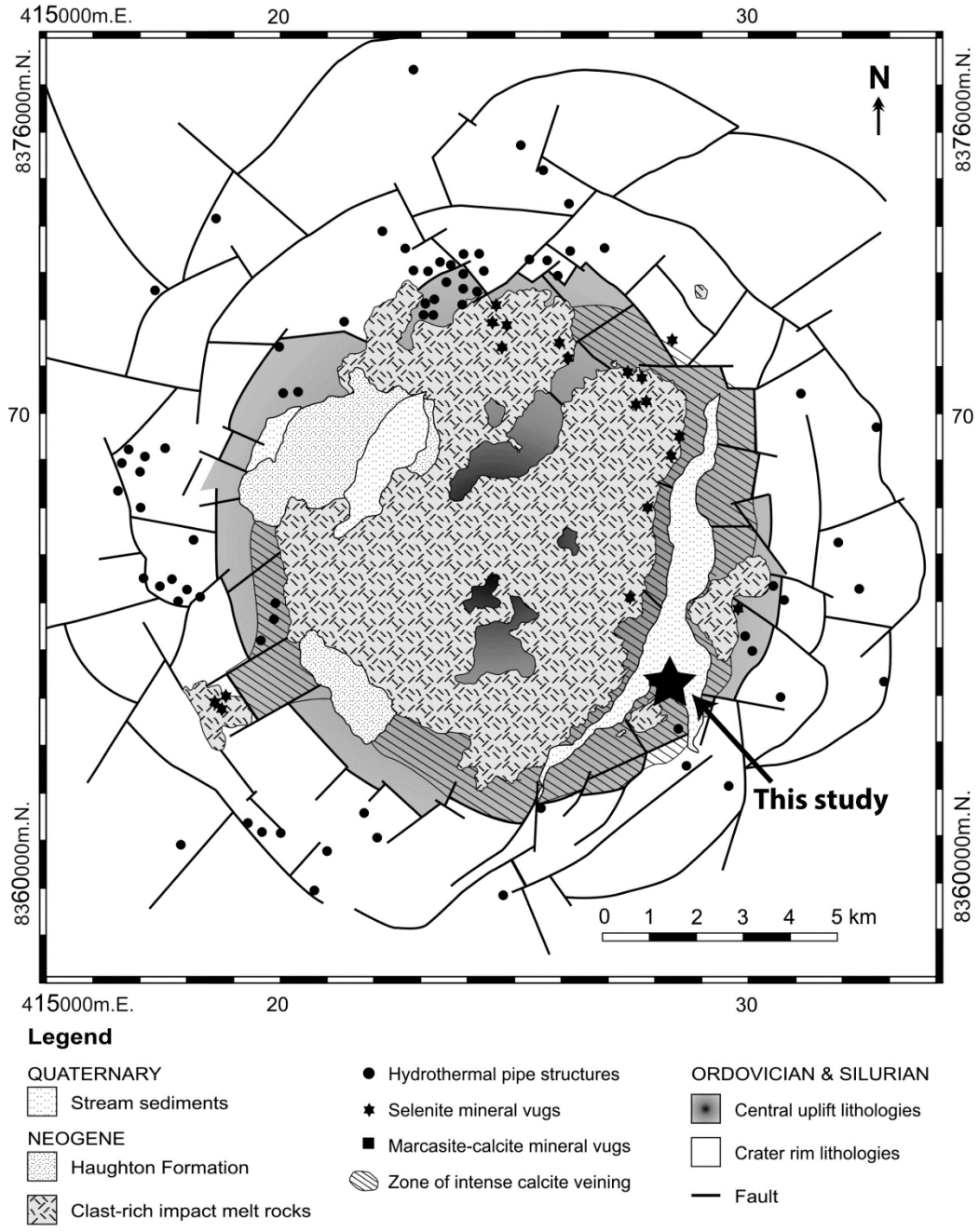
415000m.E.
20
30
8376000m.N.
70
8360000m.N.
N
This study
0 1 2 3 4 5 km
Legend
QUATERNARY
Stream sediments
NEOGENE
Haughton Formation
Clast-rich impact melt rocks
Hydrothermal pipe structures
Selenite mineral vugs
Marcasite-calcite mineral vugs
Zone of intense calcite veining
ORDOVICIAN & SILURIAN
Central uplift lithologies
Crater rim lithologies
Fault

Figure 1.

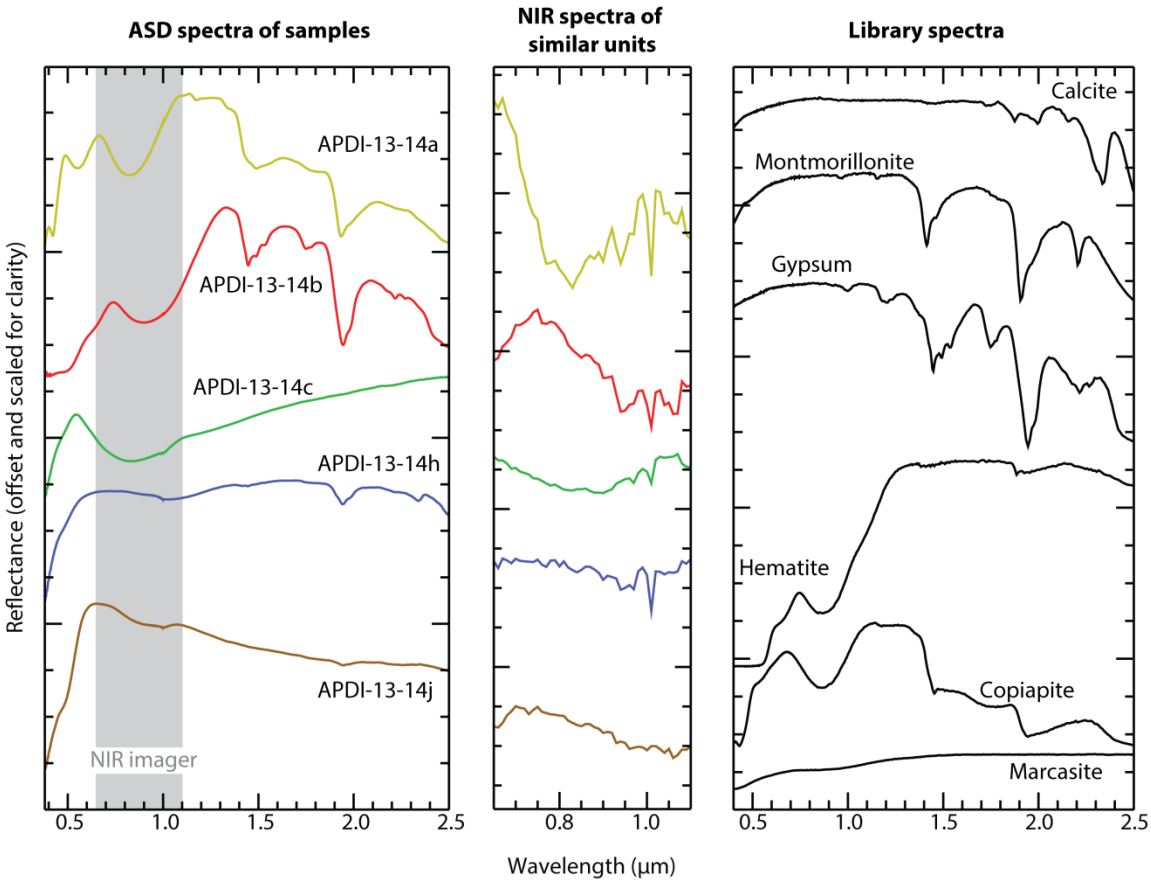
ASD spectra of samples
NIR spectra of similar units
Library spectra
Reflectance (offset and scaled for clarity)
APDI-13-14a
APDI-13-14b
APDI-13-14c
APDI-13-14h
APDI-13-14j
NIR imager
Calcite
Montmorillonite
Gypsum
Hematite
Copiapite
Marcasite
0.5
1.0
1.5
2.0
2.5
0.8
1.0
Wavelength (μm)

Figure 2.

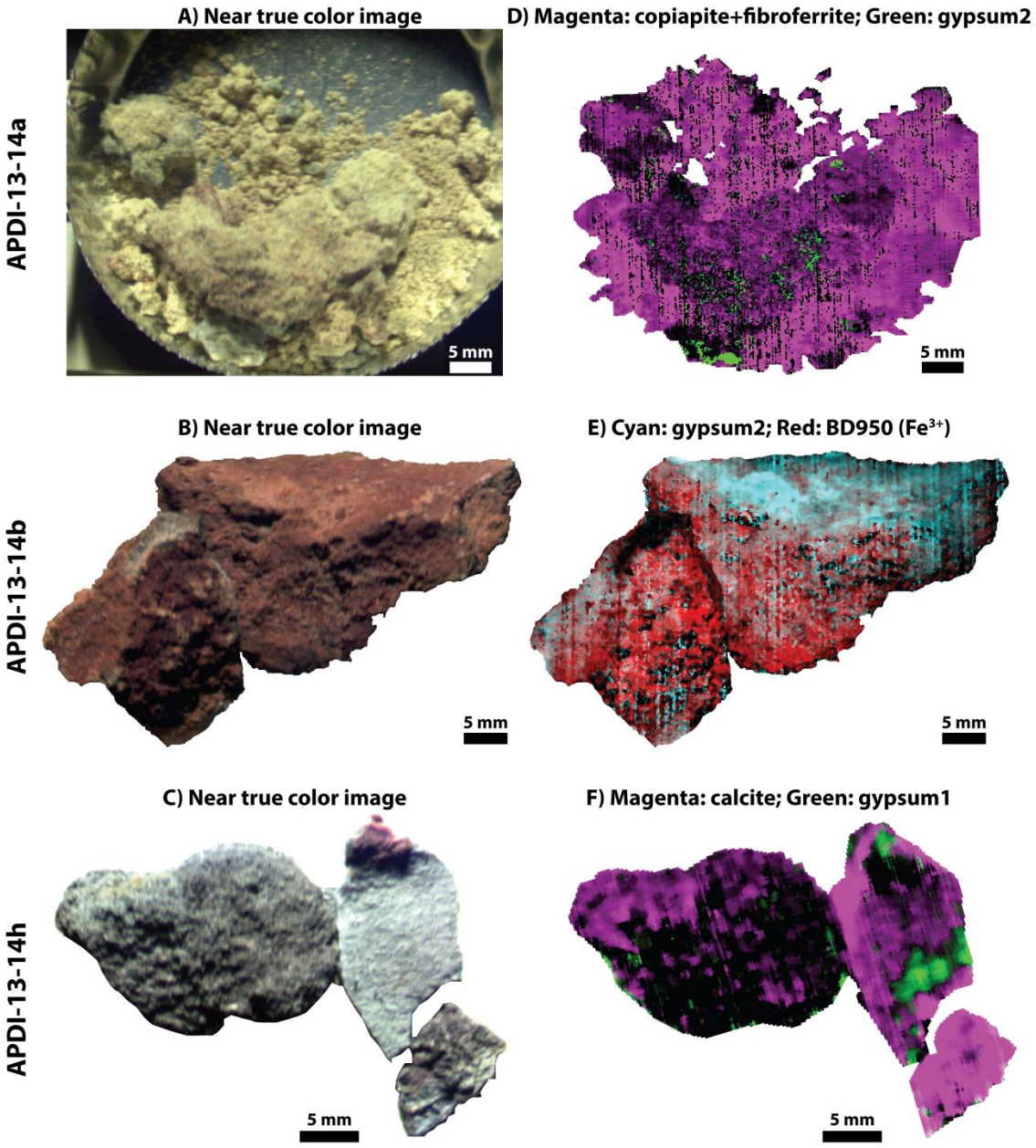
A) Near true color image
D) Magenta: copiapite+fibroferrite; Green: gypsum2
APDI-13-14a
5 mm
5 mm
B) Near true color image
E) Cyan: gypsum2; Red: BD950 (Fe3+)
APDI-13-14b
5 mm
5 mm
C) Near true color image
F) Magenta: calcite; Green: gypsum1
APDI-13-14h
5 mm
5 mm

Figure 3.

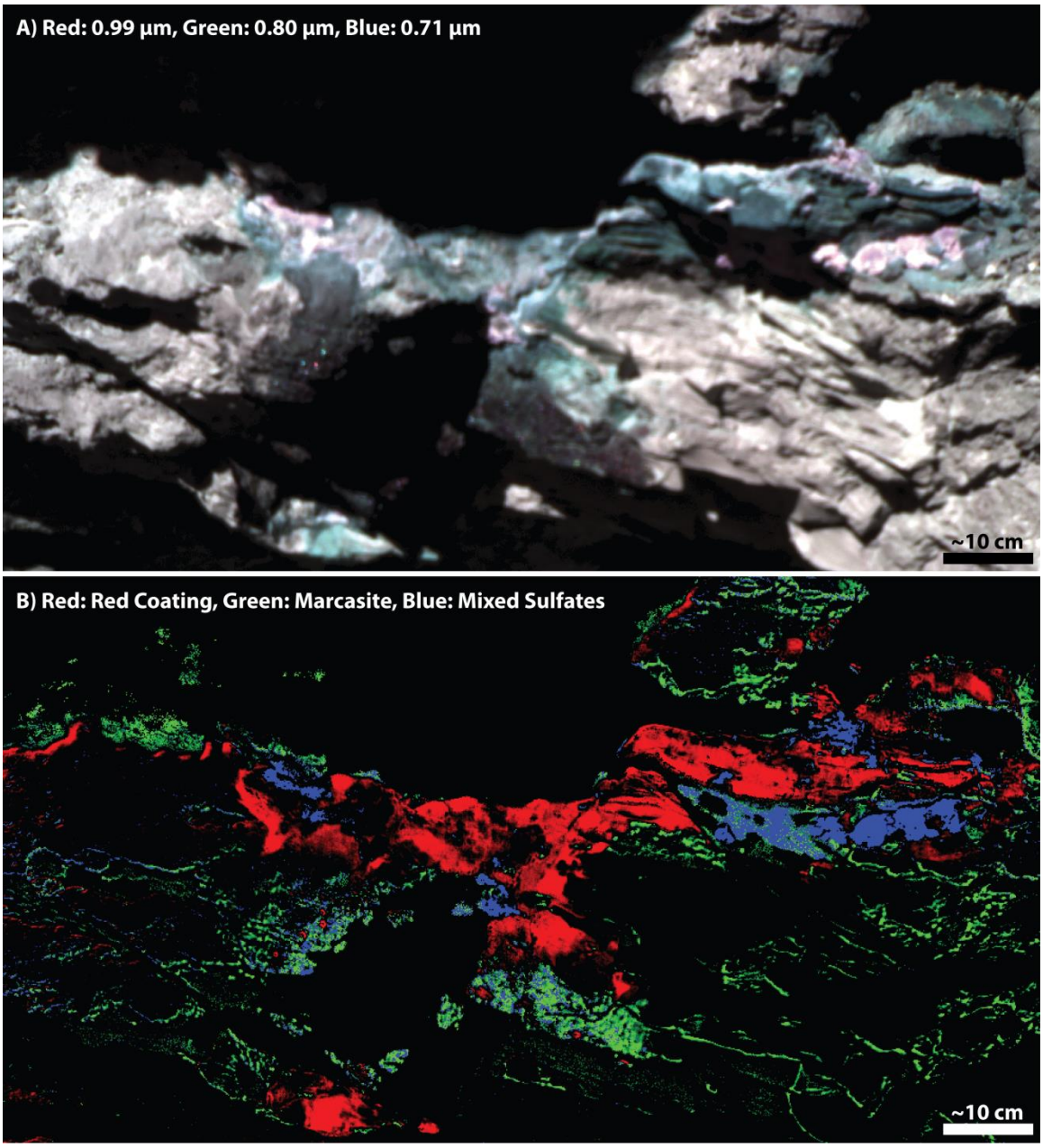
A) Red: 0.99 µm, Green: 0.80 µm, Blue: 0.71 µm
~10 cm
B) Red: Red Coating, Green: Marcasite, Blue: Mixed Sulfates
~10 cm

Figure 4.

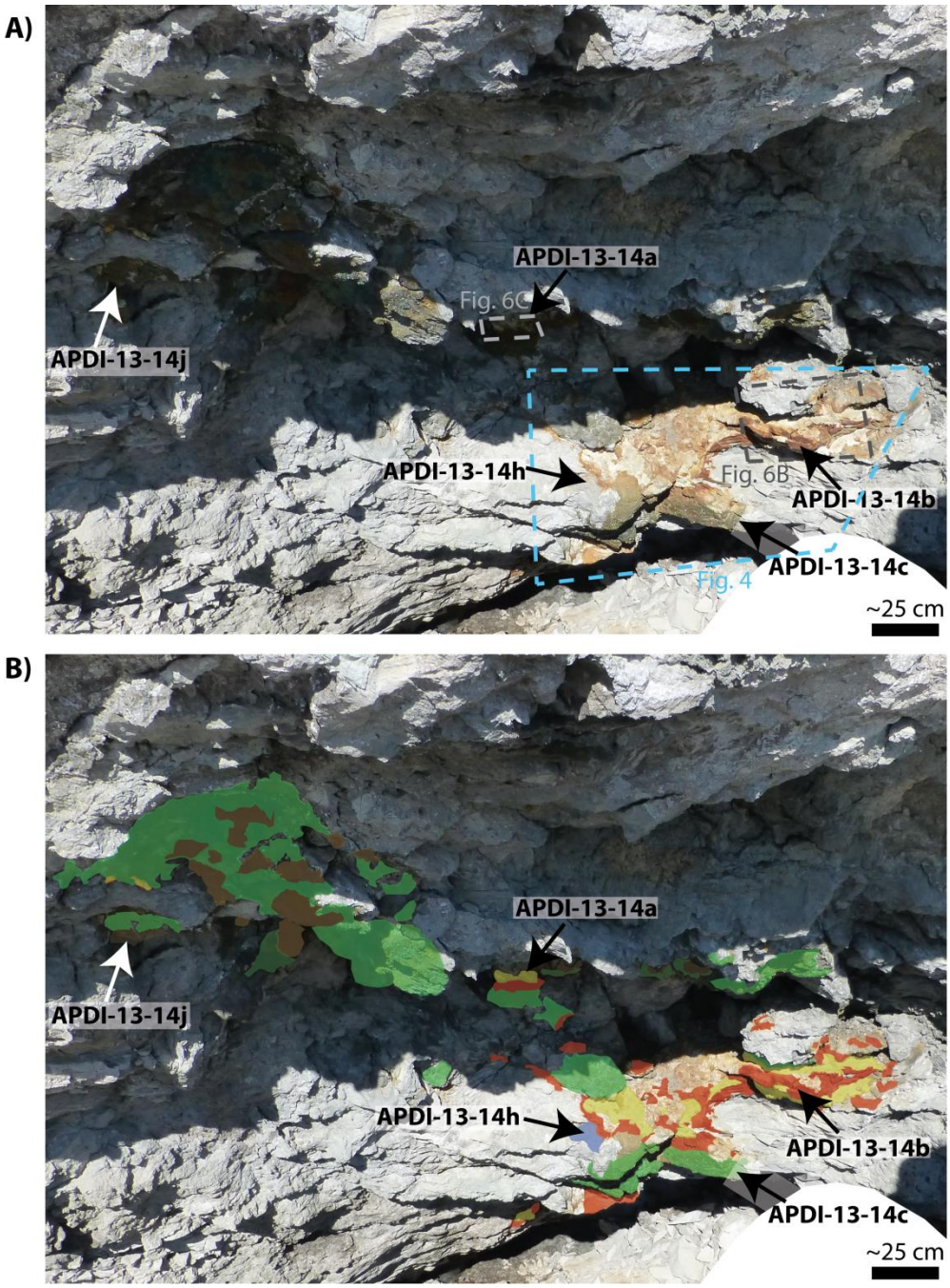
A)
APDI-13-14a
Fig. 6C
APDI-13-14j
APDI-13-14h
Fig. 6B
APDI-13-14b
APDI-13-14c
Fig. 4
~25 cm
B)
APDI-13-14a
APDI-13-14j
APDI-13-14h
APDI-13-14b
APDI-13-14c
~25 cm

Figure 5.

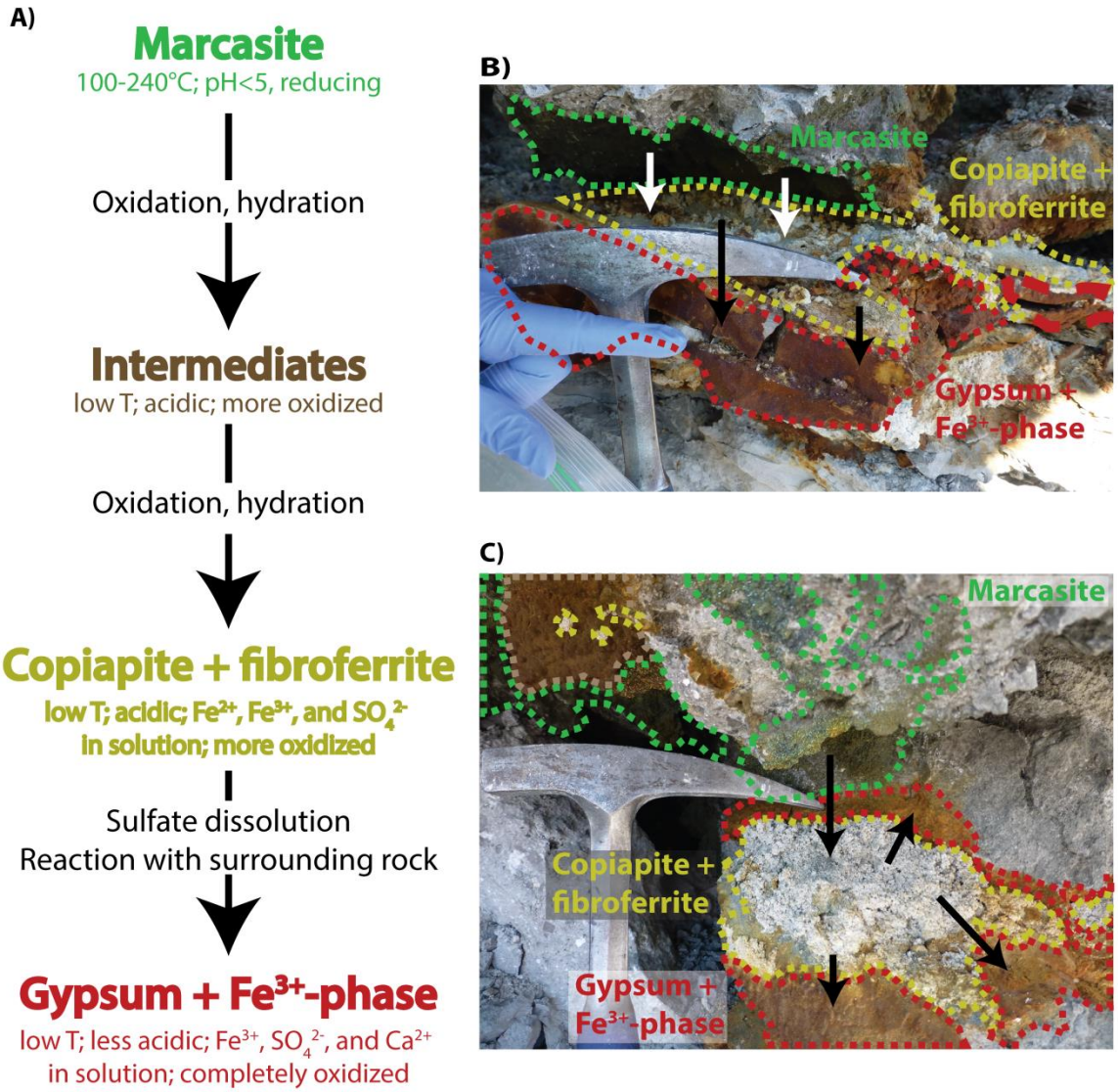
A)
Marcasite
100-240°C; pH<5, reducing
Oxidation, hydration
Intermediates
low T; acidic; more oxidized
Oxidation, hydration
Copiapite + fibroferrite
low T; acidic; Fe2+, Fe3+, and SO4 2- in solution; more oxidized
Sulfate dissolution
Reaction with surrounding rock
Gypsum + Fe3+-phase
low T; less acidic; Fe3+, SO4 2-, and Ca2+ in solution; completely oxidized
B)
Marcasite
Copiapite + fibroferrite
Gypsum + Fe3+-phase
C)
Marcasite
Copiapite + fibroferrite
Gypsum + Fe3+-phase

Figure 6.

CHAPTER FIVE

Imaging spectroscopy of geological samples and outcrops: unexpected insights from microns to meters

Rebecca N. Greenberger[a], John F. Mustard[a], Bethany L. Ehlmann[b,c], Diana L. Blaney[c], Edward A. Cloutis[d], Janette H. Wilson[e], and Robert O. Green[c]

[a]Department of Earth, Environmental, and Planetary Sciences
Brown University, Providence, RI, USA 02912

[b]Division of Geological & Planetary Sciences
California Institute of Technology, Pasadena, California, USA 91125

[c]Jet Propulsion Laboratory
California Institute of Technology, Pasadena, California, USA 91109

[d]Department of Geography
University of Winnipeg, Winnipeg, Manitoba, Canada R3B 2E9

[e]Headwall Photonics, Inc.
Fitchburg, MA, USA 01420

ABSTRACT

Imaging spectroscopy of samples and outcrops is a powerful non-destructive mineralogic and petrologic tool that provides unexpected insights into a variety of geological and planetary processes. This remote sensing technique has been used for decades from orbital or aerial platforms to characterize surface compositions of the Earth and other solar system bodies, and these instruments have now been miniaturized for use in the laboratory and field. Here, we review the technique and present three examples showing the exciting science potential and new insights into geological processes.

INTRODUCTION

Imaging spectroscopy of planetary surfaces has transformed our understanding of surface compositions throughout the solar system. The Compact Reconnaissance Imaging Spectrometer for Mars (CRISM) and the Observatoire pour la Minéralogie, l'Eau, les Glaces et l'Activité (OMEGA) have revealed the presence of clays, sulfates, carbonates, and other minerals that form through interaction with water on Mars, illuminating past environments that may have been habitable (e.g., Bibring et al., 2006; Mustard et al., 2008; Murchie et al., 2009). The Moon Mineralogy Mapper (M^3) provided new insights into the formation, igneous evolution, and composition of the Moon and discovered small amounts of hydroxylated or water-bearing materials in its regolith (Green et al., 2011; Pieters et al., 2009, 2011). The Visible and Infrared (VIR) Mapping Spectrometer has mapped different lithologic units on the surface of Vesta (Sanctis et al., 2012a, 2012b) and is about to arrive at the dwarf planet Ceres. The Visual and Infrared Mapping Spectrometer (VIMS) on the Cassini spacecraft has mapped surface compositions on

satellites of Saturn and discovered a large ethane cloud on Titan (Barnes et al., 2008; Brown et al., 2004, 2006; Griffith et al., 2006). Closer to home, imaging spectrometers flow on aircraft, such as the Airborne Visible/Infrared Imaging Spectrometer (AVIRIS) and HyMap, and in space, such as Hyperion, have mapped mineralogies and monitored dynamic changes in ice, vegetation, and other Earth surface processes over portions of the surface of the Earth (e.g., Vane et al., 1993; Cocks et al., 1998; Green et al., 1998; Swayze et al., 2000; Painter et al., 2003; Pearlman et al., 2003; Asner et al., 2004, 2007).

For geological applications, at the 10's to 100's of meters spatial resolutions of many these imaging spectrometers (Figure 1), regional or global lithologic units can be distinguished, and some components of the mineral assemblages can be identified. At spatial resolutions of meters, the minerals present in individual rock units can be identified. The highest resolution aerial and orbital hyperspectral imaging spectrometers currently achieve spatial resolutions of this magnitude, permitting discrimination of mineralogies at the scale of boulders or larger outcrops. Since these imaging systems view the surface from above, they are viewing the horizontal expression of often vertical stratigraphies and exposures. Surface and laboratory-based imaging at millimeter to centimeter resolutions can distinguish petrologic relationships within rocks (e.g., Figure 1-2).

Recently, visible-shortwave infrared imaging spectrometers have been miniaturized and are now commercially available for use in the field and laboratory (for example, manufactured by Headwall Photonics, Inc. and HySpex) and prototypes have been deployed and demonstrated for use on planetary missions (Blaney et al., 2014; Ehlmann et al., 2014; Van Gorp et al., 2014). While not the focus of this paper, there are

also similar systems being developed to measure thermal infrared emissivity (e.g., Edwards and Christensen, 2013). These instruments are powerful mineralogic and petrologic tools capable of characterizing a variety of geological processes at scales from tens of microns (thick section) to millimeters/centimeters (hand sample) to meters (outcrops) quickly and non-destructively (Figures 1-2). There are a few of examples in the literature of work using imaging spectroscopy of outcrops and samples to answer geologically-relevant questions (Kruse et al., 2012; Kurz et al., 2012; Murphy et al., 2014; Greenberger et al., 2015; Yokoyama et al., 2015). The purpose of this paper is to highlight some of the applications of this emerging technology and the exciting science opportunities.

EXAMPLE 1: CHARACTERIZING HABITABILITY AND SEARCHING FOR BIOSIGNATURES IN SERPENTINE-BEARING ROCK

The serpentinization process liberates molecular hydrogen that can sustain microbial communities (e.g., Kelley et al., 2001, 2005; Schulte et al., 2006; Cardace and Hoehler, 2009; Sleep et al., 2004; McCollom and Seewald, 2013). Hyperspectral imaging can map iron oxidation states and coordination environments within serpentine, which are related to the volumes of hydrogen produced (Marcaillou et al., 2011; Andreani et al., 2013; Greenberger et al., 2015). Work by Greenberger et al. (2015) used imaging spectroscopy (0.42-1.1 μm) to map the depth of an electronic transition of tetrahedrally coordinated Fe^{3+} that occurs at 0.45 μm as a proxy for the degree to which serpentinization proceeded and the hydrogen produced. Here, we extend that work with new imaging at visible through shortwave infrared wavelengths (0.4-2.5 μm) of one

serpentinite sample courtesy of Headwall Photonics, Inc. In Figure 3, we show the spatial associations of this 0.45 μm electronic transition with the two dominant mineralogies in this sample, carbonate and serpentine, using combinations of spectral parameters that are tuned to map narrow absorption features related to hydrated silicates and broader features that result from electronic transitions of Fe within a mineral structure (for more information on the data processing procedures and algorithms, see the supplemental material). It can be seen that the 0.45 μm feature is associated with some but not all of the serpentine. Consistent with the conclusions of Greenberger et al. (2015), different portions of this sample have undergone different degrees of serpentinization, and those areas with tetrahedral Fe^{3+} have undergone advanced serpentinization and are the most promising areas to look for biosignatures or evidence of past serpentinizing conditions. While no biosignatures were found in this investigation, stable isotopes of carbonate on this sample preserve a signature of methane formation during the Early Ordovician serpentinization (Greenberger et al., 2015).

EXAMPLE 2: HYDROTHERMAL ALTERATION AND DIAGENESIS OF LACUSTRINE PILLOW BASALTS

Alteration rinds illuminate conditions of water-rock interactions, and progressive changes from interior to exterior reflect increasing degrees of alteration (e.g., Hausrath et al., 2008). With sub-millimeter spatial resolutions, imaging spectroscopy measurements of alteration rinds resolve fine changes in spectral signatures with alteration. One such example is an Early Jurassic lacustrine pillow lava from the Hartford Basin (Figure 4; Greenberger et al., in review). In this work, coordinated imaging spectroscopy, electron

microprobe, microscopic x-ray diffraction, microscopic thermal emission, and microscopic Raman spectroscopy analyses of a thick section across an alteration rind characterized the spectral, mineralogic, and chemical transformations. Unexpected key identifications with imaging spectroscopy include identification of calcic clinopyroxenes interpreted to have formed through 400+°C hydrothermal alteration (e.g., Bird et al., 1984; Manning and Bird, 1986), pervasive oxidation throughout the sample, signatures of Fe/Mg-clays that increase in strength toward the exterior of the sample, and higher water content in calcites in the rind, either structural or as fluid inclusions (Greenberger et al., in review). In addition, there are very small areas of datolite on this sample resulting from boron-rich hydrothermal fluids. While datolite has been reported throughout the Hartford Basin and is apparent elsewhere in the outcrop from which this sample was collected, we initially did not expect to find datolite in this particular sample. The areas of datolite mineralization are too small to be distinguished visually from the abundant calcite but are spectrally-distinct with the fine spatial resolution of the imaging data. Imaging spectroscopy then scales the results to the hand-sample (the full cross-section of the pillow from which the thick section was made; Figure 4) and the portion of the outcrop characterized by similar green alteration rinds, and the results are consistent at all scales. These results suggest that these pillow lavas were altered initially after emplacement at high temperatures followed by a progressively cooling hydrothermal system. After burial, these rocks were altered through diagenesis, specifically albitization followed by calcite precipitation (Greenberger et al., in review and references therein).

EXAMPLE 3: MAPPING OF SEDIMENTARY ROCKS EXPOSED AT MILLS CREEK

An outcrop of sedimentary rocks exposed along Mills Creek near Mono Lake, California, was imaged with the Ultra Compact Imaging Spectrometer (UCIS; Van Gorp et al., 2014). Using spectral parameters, we map specific mineralogies present at the site including hydrated silica (opal A), clays (Fe-, Mg-, and Al-bearing), calcite, illite/muscovite, and possible epidote (Figure 5). From these results, the lithologic stratigraphy of the outcrop is inferred (middle of Figure 5), showing variations in the hydrated silica (red or orange) and clay (green) contents of the sedimentary layers. The float rocks above the outcrop and along the creekbed at the bottom of the image have diverse compositions. Based on the higher proportions of rocks with significant calcite (cyan) and illite (magenta), we infer calcite- and illite-rich units higher in the stratigraphy that are not exposed at this outcrop. Much of this calcite- and illite-rich talus is located on the left portion of the outcrop near a small fan and likely is sourced from above the layered section, whereas the float rocks to the right are more similar compositionally to the exposed layered outcrop.

CONCLUSIONS

Imaging spectroscopy of samples and outcrops enables new science investigations and yields unexpected mineralogic and petrologic insights into a variety of geological processes. This technique rapidly and non-destructively maps mineralogies with no sample preparation, showing mineral associations that might not otherwise be apparent and guiding further investigations. For example, the prominence of the 0.45 μm

tetrahedral Fe^{3+} electronic transition in the first example became apparent while analyzing the imaging spectroscopy measurements. In another example of the science possible with imaging spectroscopy, the fine-scale changes in mineralogy and chemistry during alteration and diagenesis of a pillow lava have been characterized, with new phases identified, and the results have been scaled up to an outcrop. Others have used imaging spectroscopy at similar scales to find economically-viable deposits of minerals to mine (Kruse et al., 2012), map carbonate lithologies (Kurz et al., 2012), characterize alteration of basaltic samples from an impact structure (Yokoyama et al., 2015), quantify the abundances of iron in a mine wall (Murphy and Monteiro, 2013), map clay layers (Murphy et al., 2014), and study a meteorite (Cannon et al., 2015). These types of studies also aid in preparing for imaging spectrometers on future landed planetary missions. UCIS is being developed by the Jet Propulsion Laboratory for use on future planetary missions (Van Gorp et al., 2014), and the MicrOmega instrument will be on the upcoming ExoMars rover (Pilorget and Bibring, 2013).

ACKNOWLEDGMENTS

We would like to thank Headwall Photonics, especially David Bannon and Kwok Wong, for use of their hyperspectral imagers to acquire the images used in examples 1 and 2. We also thank the JPL team, especially Byron Van Gorp, Zakos Mouroulis, Jose Rodriguez, Mark Helmlinger, and Morgan Cable for UCIS data used in examples 3 and 4.

REFERENCES

Andreani, M., Muñoz, M., Marcaillou, C., and Delacour, A., 2013, μXANES study of iron redox state in serpentine during oceanic serpentinization: Lithos, v. 178, p. 70–83, doi: 10.1016/j.lithos.2013.04.008.

Asner, G.P., Knapp, D.E., Kennedy-Bowdoin, T., Jones, M.O., Martin, R.E., Boardman, J., and Field, C.B., 2007, Carnegie Airborne Observatory: in-flight fusion of hyperspectral imaging and waveform light detection and ranging for three-dimensional studies of ecosystems: Journal of Applied Remote Sensing, v. 1, p. 013536–013536–21, doi: 10.1117/1.2794018.

Asner, G.P., Nepstad, D., Cardinot, G., and Ray, D., 2004, Drought stress and carbon uptake in an Amazon forest measured with spaceborne imaging spectroscopy: Proceedings of the National Academy of Sciences of the United States of America, v. 101, p. 6039–6044, doi: 10.1073/pnas.0400168101.

Barnes, J.W., Brown, R.H., Soderblom, L., Sotin, C., Le Mouèlic, S., Rodriguez, S., Jaumann, R., Beyer, R.A., Buratti, B.J., Pitman, K., Baines, K.H., Clark, R., and Nicholson, P., 2008, Spectroscopy, morphometry, and photoclinometry of Titan's dunefields from Cassini/VIMS: Icarus, v. 195, p. 400–414, doi: 10.1016/j.icarus.2007.12.006.

Bibring, J.-P., Langevin, Y., Mustard, J.F., Poulet, F., Arvidson, R., Gendrin, A., Gondet, B., Mangold, N., Pinet, P., Forget, F., and the OMEGA team, 2006, Global Mineralogical and Aqueous Mars History Derived from OMEGA/Mars Express Data: Science, v. 312, p. 400 –404, doi: 10.1126/science.1122659.

Bird, D.K., Schiffman, P., Elders, W.A., Williams, A.E., and McDowell, S.D., 1984,

Calc-silicate mineralization in active geothermal systems: Economic Geology, v. 79, p. 671–695, doi: 10.2113/gsecongeo.79.4.671.

Blaney, D.L., Murchie, S.L., Green, R.O., Mustard, J., Ehlmann, B., Mouroulis, P., Van Gorp, B., Rodriguez, J., Seelos, F., and Ehlmann, B.L., 2014, Ultra Compact Imaging Spectrometer (UCIS): Technology Maturation and Applications for Mars, the Moon, and Small Bodies, Abstract #1148.

Brown, R., Baines, K., Bellucci, G., Bibring, J.-P., Buratti, B., Capaccioni, F., Cerroni, P., Clark, R., Coradini, A., Cruikshank, D., Drossart, P., Formisano, V., Jaumann, R., Langevin, Y., et al., 2004, The Cassini Visual and Infrared Mapping Spectrometer (VIMS) Investigation, *in* Russell, C. ed., The Cassini-Huygens Mission, Springer Netherlands, p. 111–168.

Brown, R.H., Clark, R.N., Buratti, B.J., Cruikshank, D.P., Barnes, J.W., Mastrapa, R.M.E., Bauer, J., Newman, S., Momary, T., Baines, K.H., Bellucci, G., Capaccioni, F., Cerroni, P., Combes, M., et al., 2006, Composition and Physical Properties of Enceladus' Surface: Science, v. 311, p. 1425–1428, doi: 10.1126/science.1121031.

Cannon, K.M., Mustard, J.F., and Agee, C.B., 2015, Evidence for a widespread basaltic breccia component in the martian low-albedo regions from the reflectance spectrum of Northwest Africa 7034: Icarus, v. 252, p. 150–153, doi: 10.1016/j.icarus.2015.01.016.

Cardace, D., and Hoehler, T.M., 2009, Serpentinizing Fluids Craft Microbial Habitat: Northeastern Naturalist, v. 16, p. 272–284, doi: 10.1656/045.016.0520.

Clark, R.N., King, T.V.V., Klejwa, M., Swayze, G.A., and Vergo, N., 1990, High

Spectral Resolution Reflectance Spectroscopy of Minerals: Journal of Geophysical Research, v. 95, p. 12653–12680, doi: 199010.1029/JB095iB08p12653.

Cocks, T., Jenssen, R., Stewart, A., Wilson, I., and Shields, T., 1998, The HyMapTM airborne hyperspectral sensor: the system, calibration and performance, *in* Proceedings of the 1st EARSeL workshop on Imaging Spectroscopy, Zurich, p. 37–42.

Edwards, C.S., and Christensen, P.R., 2013, Microscopic emission and reflectance thermal infrared spectroscopy: instrumentation for quantitative in situ mineralogy of complex planetary surfaces: Applied Optics, v. 52, p. 2200, doi: 10.1364/AO.52.002200.

Ehlmann, B.L., Mouroulis, P., Van Gorp, B., Green, R., Blaney, D., Rodriguez, J., Mustard, J., Murchie, S., Herd, C., Seelos, F., and Feldman, S., 2014, Microimaging VSWIR Spectroscopy Instruments for Planetary Exploration: Measuring In-Situ Mineralogy, Ices, Organics, and Linking to Remote Observation, Abstract #1046.

Van Gorp, B., Mouroulis, P., Blaney, D., Green, R.O., Ehlmann, B.L., and Rodriguez, J.I., 2014, Ultra-compact imaging spectrometer for remote, in situ, and microscopic planetary mineralogy: Journal of Applied Remote Sensing, v. 8, p. 084988–084988, doi: 10.1117/1.JRS.8.084988.

Green, R.O., Eastwood, M.L., Sarture, C.M., Chrien, T.G., Aronsson, M., Chippendale, B.J., Faust, J.A., Pavri, B.E., Chovit, C.J., Solis, M., Olah, M.R., and Williams, O., 1998, Imaging Spectroscopy and the Airborne Visible/Infrared Imaging

Spectrometer (AVIRIS): Remote Sensing of Environment, v. 65, p. 227–248, doi: 10.1016/S0034-4257(98)00064-9.

Green, R.O., Pieters, C., Mouroulis, P., Eastwood, M., Boardman, J., Glavich, T., Isaacson, P., Annadurai, M., Besse, S., Barr, D., Buratti, B., Cate, D., Chatterjee, A., Clark, R., et al., 2011, The Moon Mineralogy Mapper (M3) imaging spectrometer for lunar science: Instrument description, calibration, on-orbit measurements, science data calibration and on-orbit validation: Journal of Geophysical Research: Planets, v. 116, p. E00G19, doi: 10.1029/2011JE003797.

Greenberger, R.N., Mustard, J.F., Cloutis, E.A., Mann, P., Wilson, J.H., Flemming, R.L., Robertson, K.M., Salvatore, M.R., and Edwards, C.S., Hydrothermal alteration and diagenesis of terrestrial lacustrine pillow basalts: coordination of hyperspectral imaging with laboratory measurements: Geochimica et Cosmochimica Acta, in review.

Greenberger, R.N., Mustard, J.F., Cloutis, E.A., Pratt, L.M., Sauer, P.E., Mann, P., Turner, K., Dyar, M.D., and Bish, D.L., 2015, Serpentinization, iron oxidation, and aqueous conditions in an ophiolite: Implications for hydrogen production and habitability on Mars: Earth and Planetary Science Letters, v. 416, p. 21–34, doi: 10.1016/j.epsl.2015.02.002.

Griffith, C.A., Penteado, P., Rannou, P., Brown, R., Boudon, V., Baines, K.H., Clark, R., Drossart, P., Buratti, B., Nicholson, P., McKay, C.P., Coustenis, A., Negrao, A., and Jaumann, R., 2006, Evidence for a Polar Ethane Cloud on Titan: Science, v. 313, p. 1620–1622, doi: 10.1126/science.1128245.

Hausrath, E.M., Navarre-Sitchler, A.K., Sak, P.B., Steefel, C.I., and Brantley, S.L., 2008,

Basalt weathering rates on Earth and the duration of liquid water on the plains of Gusev Crater, Mars: Geology, v. 36, p. 67–70, doi: 10.1130/G24238A.1.

Kelley, D.S., Karson, J.A., Blackman, D.K., Früh-Green, G.L., Butterfield, D.A., Lilley, M.D., Olson, E.J., Schrenk, M.O., Roe, K.K., Lebon, G.T., Rivizzigno, P., and the AT3-60 Shipboard Party, 2001, An off-axis hydrothermal vent field near the Mid-Atlantic Ridge at 30° N: Nature, v. 412, p. 145–149, doi: 10.1038/35084000.

Kelley, D.S., Karson, J.A., Früh-Green, G.L., Yoerger, D.R., Shank, T.M., Butterfield, D.A., Hayes, J.M., Schrenk, M.O., Olson, E.J., Proskurowski, G., Jakuba, M., Bradley, A., Larson, B., Ludwig, K., et al., 2005, A Serpentinite-Hosted Ecosystem: The Lost City Hydrothermal Field: Science, v. 307, p. 1428–1434, doi: 10.1126/science.1102556.

Kruse, F.A., Bedell, R.L., Taranik, J.V., Peppin, W.A., Weatherbee, O., and Calvin, W.M., 2012, Mapping alteration minerals at prospect, outcrop and drill core scales using imaging spectrometry: International Journal of Remote Sensing, v. 33, p. 1780–1798, doi: 10.1080/01431161.2011.600350.

Kurz, T.H., Dewit, J., Buckley, S.J., Thurmond, J.B., Hunt, D.W., and Swennen, R., 2012, Hyperspectral image analysis of different carbonate lithologies (limestone, karst and hydrothermal dolomites): the Pozalagua Quarry case study (Cantabria, North-west Spain): Sedimentology, v. 59, p. 623–645, doi: 10.1111/j.1365-3091.2011.01269.x.

Manning, C.E., and Bird, D.K., 1986, Hydrothermal clinopyroxenes of the Skaergaard intrusion: Contributions to Mineralogy and Petrology, v. 92, p. 437–447, doi: 10.1007/BF00374426.

Marcaillou, C., Muñoz, M., Vidal, O., Parra, T., and Harfouche, M., 2011, Mineralogical evidence for H2 degassing during serpentinization at 300 °C/300 bar: Earth and Planetary Science Letters, v. 303, p. 281–290, doi: 10.1016/j.epsl.2011.01.006.

McCollom, T.M., and Seewald, J.S., 2013, Serpentinites, Hydrogen, and Life: Elements, v. 9, p. 129–134, doi: 10.2113/gselements.9.2.129.

Murchie, S.L., Mustard, J.F., Ehlmann, B.L., Milliken, R.E., Bishop, J.L., McKeown, N.K., Dobrea, E.Z.N., Seelos, F.P., Buczkowski, D.L., Wiseman, S.M., Arvidson, R.E., Wray, J.J., Swayze, G., Clark, R.N., et al., 2009, A synthesis of Martian aqueous mineralogy after 1 Mars year of observations from the Mars Reconnaissance Orbiter: Journal of Geophysical Research, v. 114, p. 30 PP., doi: 200910.1029/2009JE003342.

Murphy, R.J., and Monteiro, S.T., 2013, Mapping the distribution of ferric iron minerals on a vertical mine face using derivative analysis of hyperspectral imagery (430–970 nm): ISPRS Journal of Photogrammetry and Remote Sensing, v. 75, p. 29–39, doi: 10.1016/j.isprsjprs.2012.09.014.

Murphy, R.J., Schneider, S., and Monteiro, S.T., 2014, Mapping Layers of Clay in a Vertical Geological Surface Using Hyperspectral Imagery: Variability in Parameters of SWIR Absorption Features under Different Conditions of Illumination: Remote Sensing, v. 6, p. 9104–9129, doi: 10.3390/rs6099104.

Mustard, J.F., Murchie, S.L., Pelkey, S.M., Ehlmann, B.L., Milliken, R.E., Grant, J.A., Bibring, J.-P., Poulet, F., Bishop, J., Dobrea, E.N., Roach, L., Seelos, F., Arvidson, R.E., Wiseman, S., et al., 2008, Hydrated silicate minerals on Mars observed by the Mars Reconnaissance Orbiter CRISM instrument: Nature, v. 454,

p. 305–309, doi: 10.1038/nature07097.

Painter, T.H., Dozier, J., Roberts, D.A., Davis, R.E., and Green, R.O., 2003, Retrieval of subpixel snow-covered area and grain size from imaging spectrometer data: Remote Sensing of Environment, v. 85, p. 64–77, doi: 10.1016/S0034-4257(02)00187-6.

Pearlman, J.S., Barry, P.S., Segal, C.C., Shepanski, J., Beiso, D., and Carman, S.L., 2003, Hyperion, a space-based imaging spectrometer: IEEE Transactions on Geoscience and Remote Sensing, v. 41, p. 1160–1173, doi: 10.1109/TGRS.2003.815018.

Pieters, C.M., Besse, S., Boardman, J., Buratti, B., Cheek, L., Clark, R.N., Combe, J.P., Dhingra, D., Goswami, J.N., Green, R.O., Head, J.W., Isaacson, P., Klima, R., Kramer, G., et al., 2011, Mg-spinel lithology: A new rock type on the lunar farside: Journal of Geophysical Research: Planets, v. 116, p. E00G08, doi: 10.1029/2010JE003727.

Pieters, C.M., Goswami, J.N., Clark, R.N., Annadurai, M., Boardman, J., Buratti, B., Combe, J.-P., Dyar, M.D., Green, R., Head, J.W., Hibbitts, C., Hicks, M., Isaacson, P., Klima, R., et al., 2009, Character and Spatial Distribution of OH/H2O on the Surface of the Moon Seen by M3 on Chandrayaan-1: Science, v. 326, p. 568–572, doi: 10.1126/science.1178658.

Pilorget, C., and Bibring, J.-P., 2013, NIR reflectance hyperspectral microscopy for planetary science: Application to the MicrOmega instrument: Planetary and Space Science, v. 76, p. 42–52, doi: 10.1016/j.pss.2012.11.004.

Sanctis, M.C.D., Ammannito, E., Capria, M.T., Tosi, F., Capaccioni, F., Zambon, F., Carraro, F., Fonte, S., Frigeri, A., Jaumann, R., Magni, G., Marchi, S., McCord,

T.B., McFadden, L.A., et al., 2012a, Spectroscopic Characterization of Mineralogy and Its Diversity Across Vesta: Science, v. 336, p. 697–700, doi: 10.1126/science.1219270.

Sanctis, M.C.D., Combe, J.-P., Ammannito, E., Palomba, E., Longobardo, A., McCord, T.B., Marchi, S., Capaccioni, F., Capria, M.T., Mittlefehldt, D.W., Pieters, C.M., Sunshine, J., Tosi, F., Zambon, F., et al., 2012b, Detection of Widespread Hydrated Materials on Vesta by the VIR Imaging Spectrometer on board the Dawn Mission: The Astrophysical Journal Letters, v. 758, p. L36, doi: 10.1088/2041-8205/758/2/L36.

Schulte, M., Blake, D., Hoehler, T., and McCollom, T., 2006, Serpentinization and Its Implications for Life on the Early Earth and Mars: Astrobiology, v. 6, p. 364–376, doi: 10.1089/ast.2006.6.364.

Sleep, N.H., Meibom, A., Fridriksson, T., Coleman, R.G., and Bird, D.K., 2004, H2-rich fluids from serpentinization: Geochemical and biotic implications: Proceedings of the National Academy of Sciences of the United States of America, v. 101, p. 12818–12823, doi: 10.1073/pnas.0405289101.

Swayze, G.A., Smith, K.S., Clark, R.N., Sutley, S.J., Pearson, R.M., Vance, J.S., Hageman, P.L., Briggs, P.H., Meier, A.L., Singleton, M.J., and Roth, S., 2000, Using Imaging Spectroscopy To Map Acidic Mine Waste: Environmental Science & Technology, v. 34, p. 47–54, doi: 10.1021/es990046w.

Vane, G., Green, R.O., Chrien, T.G., Enmark, H.T., Hansen, E.G., and Porter, W.M., 1993, The airborne visible/infrared imaging spectrometer (AVIRIS): Remote Sensing of Environment, v. 44, p. 127–143, doi: 10.1016/0034-4257(93)90012-

M.

Yokoyama, E., Nédélec, A., Baratoux, D., Trindade, R.I.F., Fabre, S., and Berger, G., 2015, Hydrothermal alteration in basalts from Vargeão impact structure, south Brazil, and implications for recognition of impact-induced hydrothermalism on Mars: Icarus, doi: 10.1016/j.icarus.2015.02.001.

FIGURE CAPTIONS

Figure 1: Conceptual plot showing the relative spectral resolutions and samplings versus the spatial scales of observations by various imaging systems and the gap that ground-based imaging spectroscopy fills (dashed box). Blue text indicates imaging systems on Earth, red text is for Mars, gray is for the moon. The number of spectral bands and the spatial resolutions used in this plot are generally those in the visible-shortwave infrared regions. Abbreviations not defined in the text: ASTER=Advanced Spaceborne Thermal Emission and Reflection Radiometer, CAO-AToMS=Carnegie Airborne Observatory-Airborne Taxonomic Mapping System, HiRISE=High Resolution Imaging Spectrometer Experiment, MODIS=Moderate Resolution Imaging Spectrometer, THEMIS VIS=Thermal Emission Imaging System (visible).

Figure 2: Subset of an image cube acquired at Headwall Photonics, Inc. across an alteration rind of a pillow lava shown in more detail in Figure 4. The front of the image cube is a color composite using bands from the hyperspectral image to approximate a true color image. The third dimension is the reflectance as a function of wavelength, where black and purple are low and red is high. Example spectra of the purple oxidized interior (bottom), calcite amygdule (middle), and green rind (top) are shown on the right. Each spectrum is an average of at least 400 pixels and is smoothed with a 3-5 point moving average.

Figure 3: Hyperspectral image acquired at Headwall Photonics, Inc. of a serpentinite sample (Nor4-14 described in Greenberger et al., 2015) from Norbestos, Quebec. The

image on the left is a color composite that approximates true color. The image in the middle uses spectral parameters to map calcite (red), serpentine (green), and a feature at 0.45 μm (BD450) due to tetrahedral Fe^{3+} within serpentine. The plot (right) shows representative spectra of different units within the hyperspectral image. Spectrum 1 is of calcite. Spectrum 2 shows features of both calcite and serpentine. Spectrum 3 is dominated by serpentine but likely has a Fe^{3+}-coating. The 0.45 μm feature is weak to absent. Spectrum 4 is serpentine. Colors correspond to colors in the spectral parameter image. The locations of each spectrum are numbered in both images.

Figure 4: (left) Color composite image from a hyperspectral image acquired at Headwall Photonics, Inc. approximating true color of a cross-section of a pillow lava (top) and mineral indicator and spectral parameter map showing calcite in red, a spectral slope indicative of the rind in green, and Fe/Mg-clay in blue (bottom). The cyan box shows the approximate location of the material directly above from which a thick section was prepared and imaged. (middle) Mineral indicator and spectral parameter image of the thick section using the same parameters as the bottom left image. (right) Spectral transect from interior of the pillow through the alteration rind (purple to green). The position of the transect is shown on the top left image. One anomalous point has been removed from one of the spectra because it is a spike in the data and not the true reflectance value. A spectrum of datolite (red) from the thick section image is also shown. That spectrum has been smoothed with a 3 point moving average and scaled.

Figure 5: (top left) Color composite image approximating true color of an outcrop along

Mills Creek imaged with UCIS. (bottom left) Spectral parameter map. Red is the band depth of a spectral feature at 2.21 μm (BD2210) due to Si-OH and/or Al-OH combination bands. Green is the band depth of a feature at 2.31-2.32 μm (BD2310-20) likely due to Mg-OH combinations. Blue is the band depth of a feature at 2.34-2.35 μm (BD2340-50) due to either a C-O combination in calcite or Fe-OH combinations in a mineral such as chlorite or epidote (Clark et al., 1990). (middle) Stratigraphic section from area outlined in yellow boxes in left image with colors corresponding to the colors in the spectral parameter map. Dark red layers have weak spectral features of hydrated silica and dark green layers have weak Fe/Mg/Al clay features. Other colors correspond with colors of text under the stratigraphic section. Numbers correspond to spectra on the right. (right) Example spectra of different units with colors corresponding to the spectral parameter map. Locations of each spectrum are numbered on both images. Dashed lines are, from left to right, at 2.21, 2.31, and 2.34 μm, corresponding with the positions of spectral features mapped in the bottom left spectral parameter map.

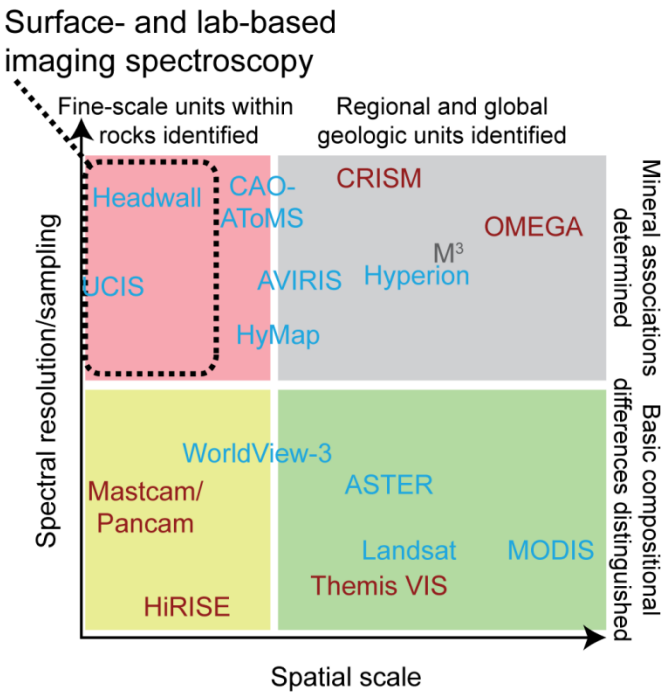
Surface- and lab-based
imaging spectroscopy
Fine-scale units within
rocks identified
Regional and global
geologic units identified
Spectral resolution/sampling
Mineral associations
determined
Basic compositional
differences distinguished
Spatial scale
Headwall
CAO-
AToMS
CRISM
OMEGA
M3
UCIS
AVIRIS
Hyperion
HyMap
WorldView-3
Mastcam/
Pancam
ASTER
Landsat
MODIS
Themis VIS
HiRISE

Figure 1.

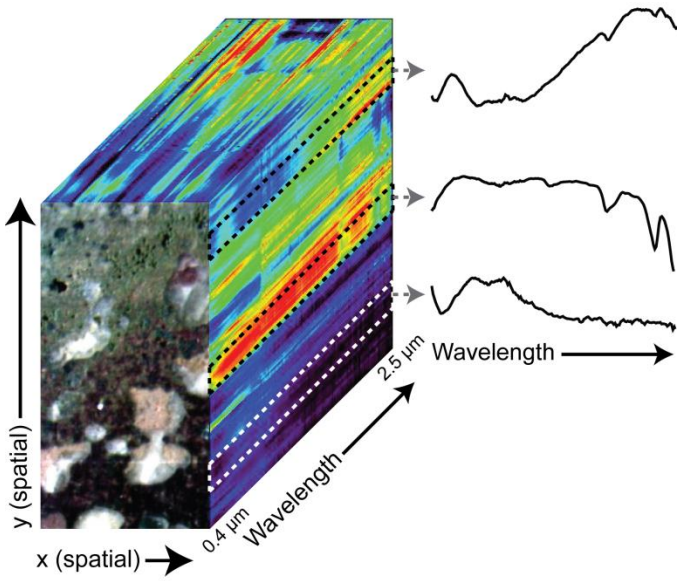

Figure 2.

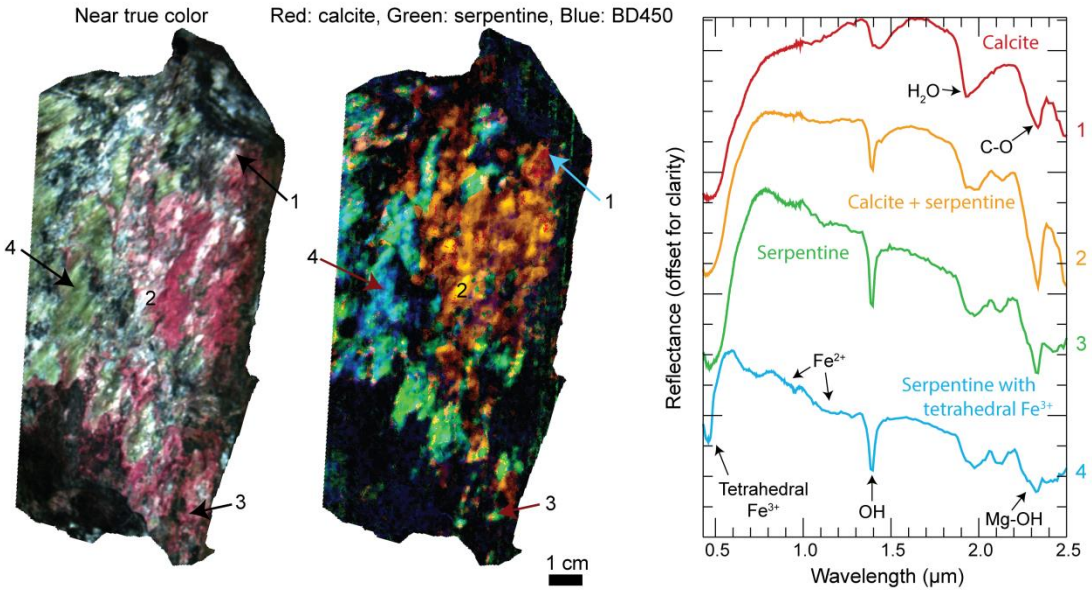
Near true color
Red: calcite, Green: serpentine, Blue: BD450
1
2
3
4
1 cm
Calcite
H2O
C-O
Calcite + serpentine
Serpentine
Fe2+
Serpentine with
tetrahedral Fe3+
Tetrahedral
Fe3+
OH
Mg-OH
Reflectance (offset for clarity)
0.5
1.0
1.5
2.0
2.5
Wavelength (μm)

Figure 3.

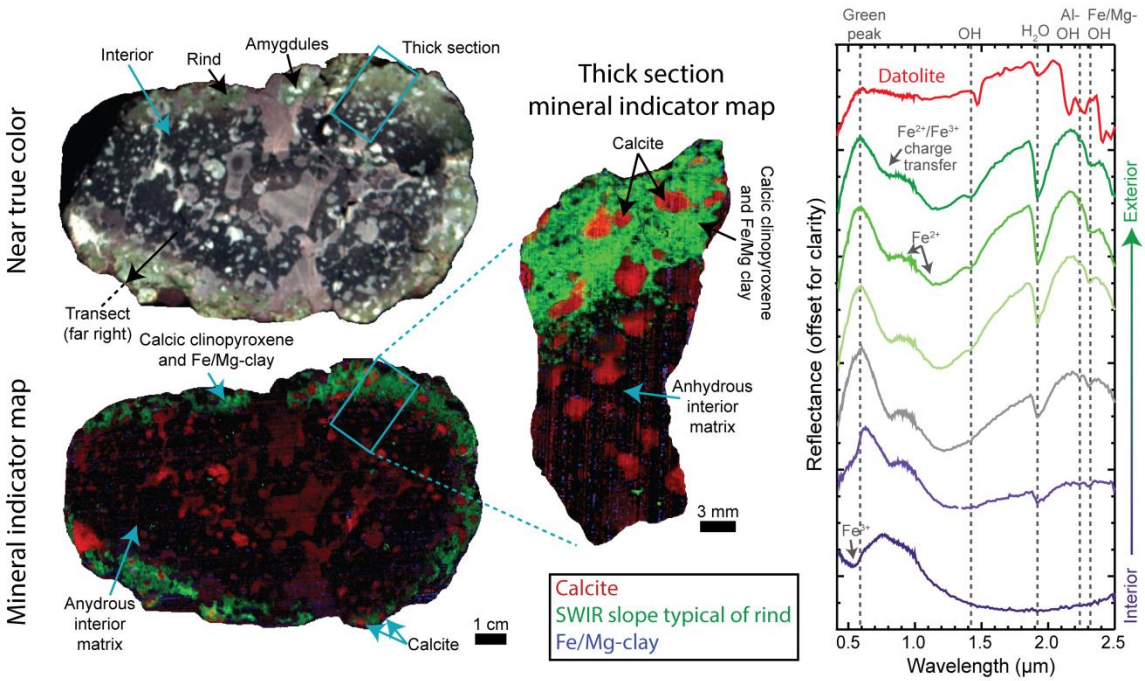
Near true color
Interior
Rind
Amygdules
Thick section
Transect
(far right)
Calcic clinopyroxene
and Fe/Mg-clay
Mineral indicator map
Anydrous
interior
matrix
Calcite
1 cm
Thick section
mineral indicator map
Calcite
Calcic clinopyroxene
and Fe/Mg clay
Anhydrous
interior
matrix
3 mm
Calcite
SWIR slope typical of rind
Fe/Mg-clay
Green
peak
OH
H2O
Al-
OH
Fe/Mg-
OH
Datolite
Fe2+/Fe3+
charge
transfer
Fe2+
Fe2+
Exterior
Interior
Reflectance (offset for clarity)
0.5
1.0
1.5
2.0
2.5
Wavelength (μm)

Figure 4.

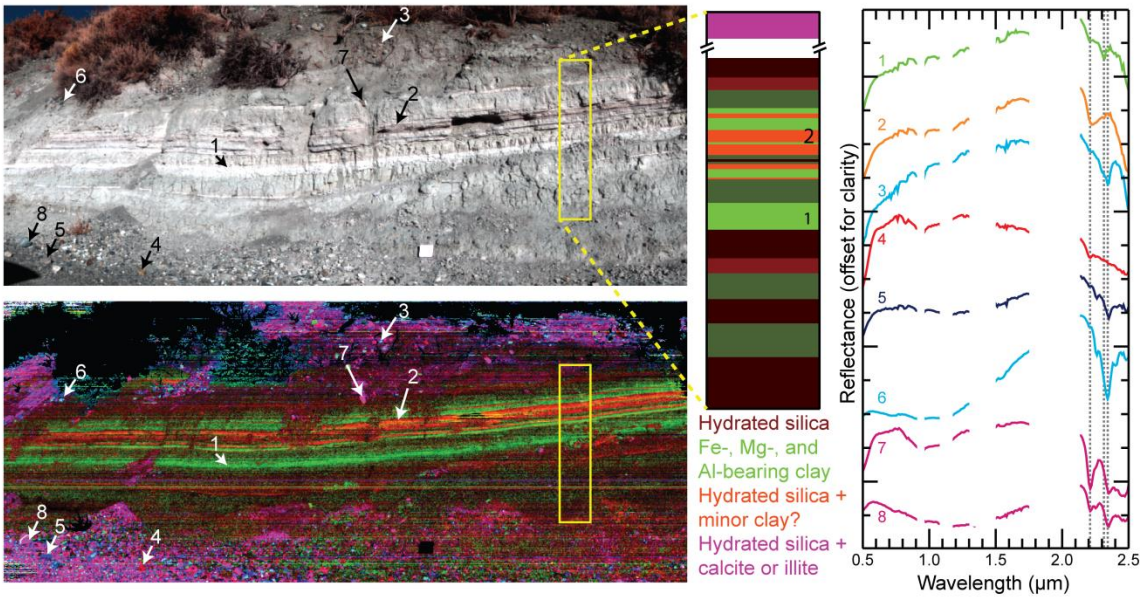
Hydrated silica
Fe-, Mg-, and
Al-bearing clay
Hydrated silica +
minor clay?
Hydrated silica +
calcite or illite
Reflectance (offset for clarity)
Wavelength (μm)
0.5
1.0
1.5
2.0
2.5

Figure 5.

SUPPLEMENTAL MATERIAL

Imaging spectroscopy methods and calibration

Imaging spectroscopy measurements of samples shown in examples 1 and 2 were done at the Headwall Photonics, Inc. (Fitchburg, MA, USA) laboratory using engineering models of their High Efficiency Hyperspec® visible-near infrared (VNIR) E-series and High Efficiency Hyperspec® shortwave infrared (SWIR) X-series pushbroom systems. The VNIR imager covers 0.4 to 1.0 µm with a 1.785 nm sampling interval, 7 nm spectral resolution (the full width at half maximum of the slit intensity image), and 0.382 mrad instantaneous field of view (IFOV). The SWIR imager covers 0.95-2.5 µm with 12.0656 nm sampling, 12 nm spectral resolution, and 1.2 mrad IFOV. Samples were illuminated by a quartz tungsten halogen light source and imaged from nadir while the sample moved below the imager on a computer-controlled motorized scanning table from the Headwall Hyperspec® Starter Kit™. Calibration was done through a dark current subtraction (S_d; image acquired with the lens cap on) and ratio to an image of a Spectralon® panel (S_s), which is a near perfect reflector. Images were then corrected for known reflectance properties of Spectralon® (R_s) using spectrum HL-JFM-012 of the same material measured in the Reflectance Experiment Laboratory (RELAB, Brown University, Providence, RI, USA) and resampled to the wavelengths of the imagers. Calibration to reflectance (R) was done with the following equation:

$$R = \frac{S_t - S_d}{S_s - S_d} * R_s \ .$$

S_t is the image of the sample. VNIR and SWIR images were joined by warping the SWIR image to the VNIR image using manually selected control points, a first degree

polynomial, and nearest neighbor resampling in Exelis Visual Information Systems ENVI®. The images were then merged into a single image cube using VNIR bands covering wavelengths through 0.997 μm and SWIR bands longward of 0.998 μm and deleting overlapping bands. The SWIR bands were scaled to remove any offset between the VNIR and SWIR detectors using a multiplicative factor assuming that the actual reflectance is constant at each pixel at 0.997 and 0.998 μm.

The imaging spectroscopy data shown in example 3 were acquired with the Ultra-Compact Imaging Spectrometer (UCIS) developed by the Jet Propulsion Laboratory (Pasadena, CA, USA) covering wavelengths 0.5-2.5 μm (Van Gorp et al., 2014). Calibration was done following the methods of Van Gorp et al. (2014).

Spectral and mineral indicator parameters

Spectral parameters calculating the depth of absorption features within reflectance spectra are commonly used in remote sensing data to map the likely presence and extent of compositional units (e.g., Clark and Roush, 1984; Pelkey et al., 2007; Viviano-Beck et al., 2014). Here, we calculate traditional spectral parameters mapping single features and then use combinations of those parameters to create mineral indicator parameters. This process allows for more accurate mapping of mineral components. For example, serpentine and calcite both have similar absorption features at 2.33-2.34 μm (e.g., Hunt and Salisbury, 1971; King and Clark, 1989). Calcite, however, also has an absorption feature longward of 2.5 μm (Hunt and Salisbury, 1971) that is expressed in these data as a downturn toward the long wavelength end of the detector at 2.5 μm. Serpentine has a boxy absorption feature at 2.1-2.2 μm (King and Clark, 1989). Calcite is mapped where

the 2.34 μm feature and the downturn toward 2.5 μm are both present, and serpentine is mapped where the 2.1 and 2.33 μm features are present. Formulas for spectral parameters used in this paper are given in Supplemental Table 1, and formulas for mineral indicator parameters are given in Supplemental Table 2.

References

Aines, R.D., and Rossman, G.R., 1984, Water in minerals? A peak in the infrared: Journal of Geophysical Research: Solid Earth, v. 89, p. 4059–4071, doi: 10.1029/JB089iB06p04059.

Bishop, J.L., Lane, M.D., Dyar, M.D., and Brown, A.J., 2008, Reflectance and emission spectroscopy study of four groups of phyllosilicates: smectites, kaolinite-serpentines, chlorites and micas: Clay Minerals, v. 43, p. 35 –54, doi: 10.1180/claymin.2008.043.1.03.

Burns, R.G., 1993, Mineralogical applications of crystal field theory: Cambridge University Press, 578 p.

Clark, R.N., King, T.V.V., Klejwa, M., Swayze, G.A., and Vergo, N., 1990, High Spectral Resolution Reflectance Spectroscopy of Minerals: Journal of Geophysical Research, v. 95, p. 12653–12680, doi: 199010.1029/JB095iB08p12653.

Clark, R.N., and Roush, T.L., 1984, Reflectance Spectroscopy: Quantitative Analysis Techniques for Remote Sensing Applications: Journal of Geophysical Research, v. 89, p. PP. 6329–6340, doi: 198410.1029/JB089iB07p06329.

Cloutis, E.A., Hiroi, T., Gaffey, M.J., Alexander, C.M.O., and Mann, P., 2011, Spectral

reflectance properties of carbonaceous chondrites: 1. CI chondrites: Icarus, v. 212, p. 180–209, doi: 10.1016/j.icarus.2010.12.009.

Dyar, M.D., 2002, Optical and Mössbauer Spectroscopy of Iron in Micas: Reviews in Mineralogy and Geochemistry, v. 46, p. 313–349, doi: 10.2138/rmg.2002.46.06.

Van Gorp, B., Mouroulis, P., Blaney, D., Green, R.O., Ehlmann, B.L., and Rodriguez, J.I., 2014, Ultra-compact imaging spectrometer for remote, in situ, and microscopic planetary mineralogy: Journal of Applied Remote Sensing, v. 8, p. 084988–084988, doi: 10.1117/1.JRS.8.084988.

Goryniuk, M.C., Rivard, B.A., and Jones, B., 2004, The reflectance spectra of opal-A (0.5–25 μm) from the Taupo Volcanic Zone: Spectra that may identify hydrothermal systems on planetary surfaces: Geophysical Research Letters, v. 31, p. L24701, doi: 10.1029/2004GL021481.

Hunt, G.R., and Salisbury, J.W., 1971, Visible and near infrared spectra of minerals and rocks. II. Carbonates: Modern Geology, v. 2, p. 23–30.

King, T.V.V., and Clark, R.N., 1989, Spectral characteristics of chlorites and Mg-serpentines using high-resolution reflectance spectroscopy: Journal of Geophysical Research: Solid Earth, v. 94, p. 13997–14008, doi: 10.1029/JB094iB10p13997.

Pelkey, S.M., Mustard, J.F., Murchie, S., Clancy, R.T., Wolff, M., Smith, M., Milliken, R., Bibring, J.-P., Gendrin, A., Poulet, F., Langevin, Y., and Gondet, B., 2007, CRISM multispectral summary products: Parameterizing mineral diversity on Mars from reflectance: Journal of Geophysical Research, v. 112, p. 18 PP., doi: 200710.1029/2006JE002831.

Viviano-Beck, C.E., Seelos, F.P., Murchie, S.L., Kahn, E.G., Seelos, K.D., Taylor, H.W., Taylor, K., Ehlmann, B.L., Wisemann, S.M., Mustard, J.F., and Morgan, M.F., 2014, Revised CRISM spectral parameters and summary products based on the currently detected mineral diversity on Mars: Journal of Geophysical Research: Planets, v. 119, p. 2014JE004627, doi: 10.1002/2014JE004627.

Supplemental Table 1. Formulas for spectral parameters.

Spectral parameter	Formula	Interpretation
BD450	$1 - \frac{2 * \sum(Refl\ 0.451\ to\ 0.462)}{\sum(Refl\ 0.429\ to\ 0.440\ ) + \sum(Refl\ 0.472\ to\ 0.483)}$	Tetrahedral Fe^{3+} in serpentine[1-3]
Positive SWIR slope	$\frac{R1.794 + R1.806 + R1.818}{R1.154 + R1.167 + R1.179}$	Related to iron oxidation state and mineralogy
BD1390	$1 - \frac{2 * (R1.384 + R1.396)}{1.62 * (R1.345 + R1.360) + 0.38 * (R1.504 + R1.516)}$	Mg_3-OH stretching overtone[4]
BD1410	$1 - \frac{2 * (R1.408 + R1.420)}{0.72 * (R1.345 + R1.360) + 1.28 * (R1.504 + R1.516)}$	Al_2-OH stretching overtone[4]
BD1900	$1 - \frac{2 * (R1.915 + R1.927 + R1.939)}{1.34 * (R1.843 + R1.854 + R1.867) + 0.66 * (R2.036 + R2.047 + R2.060)}$	H-O-H combination[5]
BD2210	$1 - \frac{{}^{4}/_{3} * (R2.20 + R2.21 + R2.22)}{{}^{13}/_{12} * (R2.15 + R2.16) + {}^{11}/_{12} * (R2.27 + R2.28)}$	Al-OH or Si-OH combination[5-7]
BD2300	$1 - \frac{{}^{4}/_{3} * (R2.289 + R2.301 + R2.313)}{R2.205 + R2.217 + R2.386 + R2.398}$	Fe/Mg-OH combination[5]
BD2310-20	$1 - \frac{2 * (R2.31 + R2.32)}{{}^{10}/_{21} * (R2.15 + R2.16) + {}^{32}/_{21} * (R2.36 + R2.37)}$	Fe/Mg-OH combination[5]
BD2340	$1 - \frac{2 * (R2.337 + R2.349)}{0.48 * (R2.205 + R2.217) + 1.52 * (R2.386 + R2.398)}$	Mg_3-OH combination band or C-O overtone[4,8]
BD2340-50	$1 - \frac{2 * (R2.34 + R2.35)}{{}^{12}/_{25} * (R2.15 + R2.16) + {}^{38}/_{25} * (R2.40 + R2.41)}$	Mg_3-OH combination band, Fe^{2+}-OH or C-O overtone[4,8]
D2500	$1 - \frac{R2.482 + R2.494}{R2.410 + R2.422}$	C-O combination band[8]

R# = reflectance at # μm
Σ(Refl # to ##) = sum of reflectance of all bands from # to ## μm
References: [1]Burns (1993); [2]Dyar (2002); [3]Cloutis et al. (2011); [4]Bishop et al. (2008); [5]Clark et al. (1990); [6]Aines and Rossman (1984); [7]Goryniuk et al. (2004); [8]Hunt and Salisbury (1971)

Supplemental Table 2. Formulas for mineral indicator parameters.

Mineral	Formula
Calcite	BD2340>0 and D2500>0; Displayed value: BD2340
Fe/Mg-clay	(BD1390 or BD1410)>0, BD1900>0, BD2300>0, and D2500<0.1; Displayed value: BD2300
Serpentine	BD2120>0 and BD2340>0; Displayed value: BD2340

APPENDIX A

Database of all samples collected

Rebecca Greenberger

Department of Earth, Environmental, and Planetary Sciences
Brown University, Providence, RI, USA 02912

The samples in Tables 1-3 were collected in 2012 from the serpentinite in Norbestos, Quebec, described in Chapter 1 (Table 1), in 2013 from the outcrop of altered lacustrine pillow basalts in Meriden, Connecticut, described in Chapter 2 (Table 2), and in 2013 from the Haughton impact structure (Table 3). The samples in Table 3 are from outcrops not described or analyzed elsewhere in this thesis.

Acknowledgments

I would like to thank those who helped with sample collection at these sites. The Norbestos field work would not have been possible without Ed Cloutis, and Paul Mann and Katie Turner assisted with the sample collection. Ed Cloutis, Paul Mann, Jack Mustard, and Kevin Cannon helped collect samples in Meriden, CT. Gordon Osinski, Livio Tornabene, Alex Pontefract, and Cass Marion were instrumental in collecting the samples from the Haughton impact structure.

Table 1. All samples collected from the Norbestos, Quebec, Canada site described in Chapter 1 (some sample descriptions from Chapter 1)

Sample name	Date	Sample description
Nor3-1	6/19/12	Dark serpentinite with coating of fine white powder; float
Nor3-2	6/19/12	Dark serpentinite with coating of fine white powder; float
Nor3-3	6/19/12	Light green serpentine with likely chrysotile between green serpentine on top and underlying massive serpentinite rock below
Nor3-4	6/19/12	Loose chunks of red, oxidized serpentinite that is still in place on top of large boulder that was imaged
Nor3-5	6/19/12	Thin vein of chrysotile asbestos
Nor3-6	6/19/12	Vein of bendable serpentine and hydromagnesite from shear zone
Nor3-7	6/19/12	Serpentinite with carbonate blebs from shear zone
Nor3-8	6/19/12	Serpentinite from shear zone with carbonate coatings
Nor4-1	6/20/12	Rock with white coating and white veins throughout from shear zone
Nor4-2	6/20/12	Blue-colored serpentinite with carbonate coatings from shear zone
Nor4-3	6/20/12	Serpentinite with carbonate blebs on top and thick white carbonate coating on side from shear zone
Nor4-4	6/20/12	Vein of green serpentine from shear zone with thin carbonate coatings
Nor4-5	6/20/12	Massive serpentinite with patchy carbonate coating from shear zone
Nor4-6	6/20/12	Flat, massive rock with two thick veins of chrysotile asbestos cutting across it; float
Nor4-7	6/20/12	Massive serpentinite rock with green-white coating from shear zone
Nor4-8	6/20/12	Slate rock likely from slate unit stratigraphically above serpentinite and visible at the top of the adjacent cliff
Nor4-9	6/20/12	Green and dark blue serpentinite with rare carbonate coatings from shear zone
Nor4-10	6/20/12	Green serpentine coating on rock with brown oxidation in places and linear white fractures; float boulder from near imaged outcrop 100-200 m south of the shear zone
Nor4-12	6/20/12	Serpentinite rock with red and green coatings from imaged outcrop 100-200 m south of the shear zone
Nor4-13	6/20/12	Brittle light green serpentine from outcrop 100-200 m south of shear zone
Nor4-14	6/20/12	Serpentinite with bright red and green coatings from outcrop 100-200 m south of shear zone
Nor4-15	6/20/12	Massive dark serpentine with green serpentine and some oxidation from outcrop 100-200 meters south of shear zone; between two images

Sample name	Date	Sample description
Nor4-16	6/20/12	Massive serpentinite rock with thin patchy carbonate coatings from outcrop 100-200 m south of shear zone
Nor5-1	6/21/12	Serpentinite with patchy thin films and crystals of carbonate from outcrop 100-200 m south of shear zone
Nor5-2	6/21/12	Serpentinite with patchy thin coatings of carbonate from outcrop 100-200 m south of shear zone
Nor5-3	6/21/12	Serpentinite with green coating
Nor5-4	6/21/12	Dark serpentinite with red oxidation and some green serpentine

Table 2. Descriptions of all samples collected from Meriden, Connecticut, outcrop described in Chapters 2 and 3. Note that some samples described as basalt may actually be baked sediments pushed up into the basalt-dominated section as the origin of the material was not always clear in the field. Some sample descriptions are from Chapter 3.

Sample name	Location	Date	Description
Mer04-1	South wall	6/5/13	Dark basaltic material with white crystals; out of place but resting on outcrop
Mer04-2	South wall	6/5/13	Baked sediment with distinct orange and white coatings
Mer04-3	South wall	6/5/13	Less-altered basalt with a few thin white veins and larger white crystals; red-brown coating on one side
Mer04-4	South wall	6/5/13	Concentric material preserved around pillow interior from altered glassy pillow rim; very altered with white-green color
Mer04-5	South wall	6/5/13	Sediment just below contact with basalt; purple color with thin brown-orange layers
Mer04-6	South wall	6/5/13	Sediments from 12.5+ cm below contact with basalts with a fine-grained, dark red layer on top, coarse-grained lighter red to red-white layer in the middle, and coarser-grained orange layer on bottom
Mer04-10	South wall	6/5/13	Fresh pillow with pocket of alteration
Mer04-11	South wall	6/5/13	Sediment surrounding pillow basalt with orange and green rind
Mer04-12	South wall	6/5/13	Basalt with green coating
Mer04-13	South wall	6/5/13	Pillow basalt with red-pink interior and green and white rind
Mer04-14	South wall	6/5/13	Green altered pillow basalt
Mer04-15	West wall	6/5/13	Pillow with dark green material
Mer04-16	West wall	6/5/13	Dark red sedimentary rock
Mer04-17	West wall	6/5/13	Pillow with dark green patches and white veins
Mer04-18	West wall	6/5/13	Interior of large pillow; contact with dark green material
Mer04-19	West wall	6/5/13	Pillow basalt with redder interior and whiter rind
Mer05-1	West wall	6/6/13	Vein of fibrous crystals in vug
Mer05-2	West wall	6/6/13	Mound of white-gray crystals with some glassy black clasts (hyaloclastite breccia?) in vug

Sample name	Location	Date	Description
Mer05-3	West wall	6/6/13	White crystals in vein surrounded by gray matrix near vug
Mer05-4	North wall	6/6/13	Portion of larger pillow basalt with purple interior, light green-blue inner part of rind, and green outer part of rind; a few pipe vesicles with black rims and filled with white crystals
Mer05-5	North wall	6/6/13	Green crystals (prehnite?) surrounded by rocks with red coating
Mer05-6	North wall	6/6/13	Vesicular basalt with light purple matrix and vesicles filled with white and green crystals; redder rind
Mer05-7	North wall	6/6/13	Rock with purple matrix with green and black coating
Mer05-8	North wall	6/6/13	Transparent orange crystals from a 1-2 cm wide vein within the basalts
Mer05-9	North wall	6/6/13	Portion of pillow basalt with purple matrix with white coatings and more friable green coating
Mer05-10	South wall	6/6/13	Baked sediment directly against pillow basalt with orange-yellow coating
Mer05-11	South wall	6/6/13	Basalt with orange, white, and black coatings
Mer05-12	South wall	6/6/13	Pillow with red, orange, and cream coatings
Mer05-13	West wall	6/6/13	Glassy basalt with blue and orange
Mer05-14	North wall	6/6/13	Basalt with white crystals
Mer05-15	North wall	6/6/13	Breccia with green matrix and calcite veins
Mer05-16	North wall	6/6/13	Purple basalt
Mer05-17	North wall	6/6/13	Gray-green basalt with white crystals
Mer05-18	North wall	6/6/13	Red basalt with gray-green rind
Mer05-19	North wall	6/6/13	Dark gray-green basalt with white patches
Mer05-20	North wall	6/6/13	Basalt with large patch of cream-white crystals
Mer05-21	North wall	6/6/13	Green breccia with white-orange mineralization
Mer05-30	North wall	6/6/13	Altered breccia with green altered clasts and white-orange mineralization; float at base of rock wall but similar to material higher
Mer05-31	North wall (float)	6/6/13	Breccia with light to dark green clasts and light brown matrix
Mer05-32	North wall	6/6/13	Prehnite
Mer05-33	Float	6/6/13	Basalt with white circles
Mer05-34	Float	6/6/13	Basalt with metallic blue mineralization

Sample name	Location	Date	Description
Mer05-35	West wall	6/6/13	Massive lighter gray basalt
Mer05-36	Float	6/6/13	Oxidized, red vesicular basalt with many unfilled vesicles
Mer05-37	Float	6/6/13	Purple interior with white crystals filling veins and green exterior rind, similar to some rinds within images acquired of the north wall
Mer05-38	Float	6/6/13	Large green crystals with some white crystals
MerPillow	Float	6/6/13	Intact altered pillow basalt with oxidized purple interior, green rind, calcite amygdules and veins throughout, and pink material cutting through the pillow; collected at base of north wall outcrop but representative of greener alteration
Mer05-F2	Float	6/6/13	Basalt with brown matrix with thick white vein rimmed with a platy green mineral
Mer05-F4	Float	6/6/13	Breccia with dark blue, almost shiny clasts
MerFloatV	Float	6/6/13	Vesicular basalt with some vesicles filled with calcite and/or prehnite and many remaining unfilled vesicles
Mer06-1	West wall	3/8/14	Dark glassy material with white and pink mineralization cutting through
Mer06-2	West wall	3/8/14	Large white-pink calcite in breccia
Mer06-3	West wall	3/8/14	Hyaloclastite breccia with black glassy clasts surrounded by white mineralization
Mer06-4	West wall	3/8/14	Red altered material filling fracture
Mer0614-01	South wall	6/13/14	Baked sediment between several pillow lavas with red, orange, and green coatings
Mer0614-02	South wall	6/13/14	Smaller piece is the red rind of a pillow against sediment; larger piece is sediment against basalt with red-range hyaloclastite breccia with preserved glass as contact with basalt
Mer0614-03	South wall	6/13/14	Black rock with thick green rind altered zone and calcite between black and green
Mer0614-04	West wall	6/13/14	Extremely friable material from outermost rind of pillow basalt (where Mer04-13 was sampled) against surrounding sedimentary rocks

Table 3. Samples collected from throughout the Haughton impact structure, Nunavut, Canada, that are not described in Chapter 4

Sample name	Location[a]	Date	Description
RG-HMP-13-01	Gully west of camp	7/19/13	Soil in gully, few to no coarse clasts, wet, sample from surface
RG-HMP-13-02	Gully west of camp	7/19/13	Same location as RG-HMP-13-01 but slightly deeper
RG-HMP-13-03	Gully west of camp	7/19/13	Gypsum-rich crust from raised part of gully, fine grained
RG-HMP-13-04	Gully west of camp	7/19/13	Material below sample RG-HMP-13-04
RG-HMP-13-05	Gully west of camp	7/19/13	Large white rock with orange spots along gully traverse, white may be coating, fine-grained
RG-HMP-13-06	Rhinoceros Creek breccia	7/21/13	Piece of polymict impact melt breccia, also carbonate rock from large clast in melt
RG-HMP-13-07	Rhinoceros Creek breccia	7/21/13	Tanner loose clods of regolith in impact melt unit; polygonal cracking, relatively small, sand-sized grains in tan matrix with a few larger clasts
RG-HMP-13-08	Rhinoceros Creek breccia	7/21/13	Dark limestone clast in clast rich impact melt rock ~10 cm long and 7 cm wide, grey fine-grained with near-vertical cracks and some layering
RG-HMP-13-09	Rhinoceros Creek breccia	7/21/13	Sample from large green material near base of melt rock, heterogenous with large clasts
RG-HMP-13-10	Rhinoceros Creek breccia	7/21/13	Vein of green fine-grained material with darker green clasts, may be altered
RG-HMP-13-11	Rhinoceros Creek breccia	7/21/13	Middle of oxidized gneiss clast
RG-HMP-13-13	Rhinoceros Creek breccia	7/21/13	Oxidized, dark red rim around large gneiss clast at base of impact melt rock exposure and just above contact with talus
RG-HMP-13-14	Rhinoceros Creek breccia	7/21/13	Clast-rich impact melt rock with shattercones at the bottom
RG-HMP-13-15	Rhinoceros Creek breccia	7/21/13	Classic clast-rich impact melt rock
RG-HMP-13-16	Rhinoceros Creek breccia	7/21/13	Dark rock with thick white coating

Sample name	Location[a]	Date	Description
RG-HMP-13-17	Rhinoceros Creek breccia	7/21/13	From brown, oval-shaped material within impact melt rocks; polygonally cracked with light gray-brown exterior and darker brown interior
RG-HMP-13-18	Rhinoceros Creek breccia	7/21/13	Green, cracked, less consolidated material; possible lithic breccia
RG-HMP-13-19	Rhinoceros Creek breccia	7/21/13	Talus with angular, loose clasts
RG-HMP-13-20	Rhinoceros Creek breccia	7/21/13	Lithic breccia (monomict) with green/tan matrix and angular clasts; possibly the same unit as RG-HMP-13-18
RG-HMP-13-21	Rhinoceros Creek breccia	7/21/13	Top green rim of lithic breccia in contact with impact melt rock
RG-HMP-13-22	Rhinoceros Creek breccia	7/21/13	Very fine-grained material on talus slope; well cemented with a few larger grains
RG-HMP-13-23	Rhinoceros Creek breccia	7/21/13	Dark, fine-grained rock with white coating
RG-HMP-13-26a	Central uplift	7/22/13	Carbonate rock with white coating
RG-HMP-13-26b	Rhinoceros Creek breccia	7/25/13	Possible monomict, lithic breccia with tan coating and darker interior
RG-HMP-13-27	Rhinoceros Creek breccia	7/25/13	Classic clast-rich impact melt rock
RG-HMP-13-28	Rhinoceros Creek breccia	7/25/13	Monomict breccia with browner color and dark clasts below impact melt rock
RG-HMP-13-29	Rhinoceros Creek breccia	7/25/13	Thick red-brown friable material near base of impact melt rock; almost looks layered
RG-HMP-13-30	Rhinoceros Creek breccia	7/25/13	Shocked gneiss clast with some shocked garnets, large quartz, and thick gray layers within impact melt rock
RG-HMP-13-31	Rhinoceros Creek breccia	7/25/13	Dark clast sticking out of talus below outcrop with brown coating
RG-HMP-13-32	Rhinoceros Creek breccia	7/25/13	Large white rectangular clast at base of outcrop that looks vertical; layers are darker and fine-grained
RG-HMP-13-33	East Rhinoceros Creek outcrop	7/25/13	Gray weathered gypsum from boulder near creek
RG-HMP-13-34	East Rhinoceros Creek outcrop	7/25/13	White sculpted fine-grained gypsum rock (float) on top of boulder (RG-HMP-13-33)

Sample name	Location[a]	Date	Description
RG-HMP-13-35	East Rhinoceros Creek outcrop	7/25/13	Layered brown-black gypsum with white crust
RG-HMP-13-36	East Rhinoceros Creek outcrop	7/25/13	Brown-tan-grey friable talus
RG-HMP-13-37	East Rhinoceros Creek outcrop	7/25/13	Large, fine-grained, light gray limestone clast
RG-HMP-13-38	East Rhinoceros Creek outcrop	7/25/13	Friable, fine-grained, green vein with small angular clasts
RG-HMP-13-39	East Rhinoceros Creek outcrop	7/25/13	Breccia surround RG-HMP-13-37 and RG-HMP-13-38 with small angular clasts and a vein of gypsum
RG-HMP-13-40	East Rhinoceros Creek outcrop	7/25/13	Clear, nearly-horizontal vein of selenite cutting breccia
RG-HMP-13-41	East Rhinoceros Creek outcrop	7/25/13	Fine-grained material with some larger clasts from alluvial fan
RG-HMP-13-42	East Rhinoceros Creek outcrop	7/25/13	Massive brown/black gypsum with possible layering
RG-HMP-13-43	East Rhinoceros Creek outcrop	7/25/13	Large chunk of white and black gypsum falling off wall within breccia matrix
RG-HMP-13-44	East Rhinoceros Creek outcrop	7/25/13	Dark vein of black-gray breccia with fine clasts within larger breccia
RG-HMP-13-45	East Rhinoceros Creek outcrop	7/25/13	Light brown gypsum with massive black gypsum layered
RG-HMP-13-46	East Rhinoceros Creek outcrop	7/25/13	Rectangular, gray-white fine-grained block of limestone
RG-HMP-13-47	East Rhinoceros Creek outcrop	7/25/13	Large, clear selenite crystals lining top of limestone clast
RG-HMP-13-58	Gypsum site 1	7/28/13	Massive white gypsum with some gray coatings
RG-HMP-13-59	Gypsum site 1	7/28/13	Dark and white gypsum coated in brown material from lower portion of outcrop
RG-HMP-13-60	Gypsum site 1	7/28/13	Massive white gypsum with black veins
RG-HMP-13-61	Gypsum site 1	7/28/13	Large, clear selenite crystals forming small vein
RG-HMP-13-62	Gypsum site 1	7/28/13	Vertically-layered dark rock with white veins
RG-HMP-13-63	Gypsum site 1	7/28/13	Friable white layers of probably gypsum next to RG-HMP-13-62

Sample name	Location[a]	Date	Description
RG-HMP-13-64	Gypsum site 1	7/28/13	Thinly layered limestone broken into larger blocks with some dark gray staining
RG-HMP-13-65	Gypsum site 1	7/28/13	White, layered, fine-grained rock, possibly coated in gypsum
RG-HMP-13-66	Gypsum site 1	7/28/13	Loose rock with dark gypsum and white veins
RG-HMP-13-67	Gypsum site 1	7/28/13	Massive white gypsum
RG-HMP-13-68	Gypsum site 1	7/28/13	Brown gypsum crystals with white chunks
RG-HMP-13-69	Gypsum site 1	7/28/13	Selenite crystals

[a]Coordinates of sampling locations are as follows (all are UTM 16N): gully west of camp (0427747 N, 8366445 E), Rhinoceros Creek Breccia (0425959 N, 8371562 E), central uplift (0425062 N, 8369277 E), East Rhinoceros Creek outcrop (0426201 N, 8371224 E), gypsum site 1 (0428622 N, 8369635 E)

APPENDIX B

Database of all hyperspectral images acquired

Rebecca Greenberger

Department of Earth, Environmental, and Planetary Sciences
Brown University, Providence, RI, USA 02912

Most images acquired as part of this thesis are included in the tables below. For laboratory data, nearly all images are calibrated (file names will be followed by '_calib') and have been looked at to validate the calibration, confirm results presented in this thesis, and prioritize the most interesting images. Calibration procedures are described in detail in chapters 1-4. In addition to the images listed in Table 4, nearly all samples from Meriden, CT, were imaged in the laboratory with the visible and near infrared (NIR) Channel Systems imagers.

Acknowledgments:

I would like to thank all of the coauthors on Chapters 1-4 who helped with the imaging and data processing and Headwall Photonics, Inc., especially Janette Wilson, for allowing me to image my samples for free.

Table 1. Hyperspectral imaging in the field at Norbestos, Quebec, site described in Chapter 1. All images were done with the visible (420-720 nm) Channel Systems imager.

Image name	Type	Date	Notes
nor2cliff1_5nm	Outcrop	6/18/12	Rock wall 100-200 m south of shear zone
nor2cliff2_5nm	Outcrop	6/18/12	Rock wall 100-200 m south of shear zone to left of nor2cliff1_5nm
nor2cliff3_5nm	Outcrop	6/18/12	Rock wall 100-200 m south of shear zone to left of nor2cliff2_5nm
nor3float1_5nm	Float	6/19/12	Large boulder (float); mostly green serpentine within image
nor3float2_5nm	Float	6/19/12	Large boulder (float); oxidized, broken material, green serpentine, and vein of asbestos within image; to right of nor3float1_5nm
nor3float3_5nm	Float	6/19/12	Large flat rock with red and brown alteration and a dark coating
nor3float4_5nm	Samples	6/19/12	Images of samples including Nor3-1 and Nor3-2 with friable, fine-grained white coating
rock_nor3_6_5nm	Sample	6/20/12	Sample Nor3-6
rock_nor3_7_5nm	Sample	6/20/12	Sample Nor3-7
rock_nor3_8_5nm	Sample	6/20/12	Sample Nor3-8
rock_nor4_1_5nm	Sample	6/20/12	Sample Nor4-1
rock_nor4_2_5nm	Sample	6/20/12	Sample Nor4-2
rock_nor4_3_5nm	Sample	6/20/12	Sample Nor4-3
rock_nor4_4_5nm	Sample	6/20/12	Sample Nor4-4
rock_nor4_5_5nm	Sample	6/20/12	Sample Nor4-5
rock_nor4_6_5nm	Sample	6/20/12	Sample Nor4-6
rock_nor4_7_5nm	Sample	6/20/12	Sample Nor4-7
rock_nor4_8_5nm	Sample	6/20/12	Sample Nor4-8
rock_nor4_9_5nm	Sample	6/20/12	Sample Nor4-9
rovertarget1left	Mission target	6/21/12	Left portion of Mars Methane Mission rover target 1
rovertarget1left_ref	Mission target	6/21/12	Left portion of Mars Methane Mission rover target 1 with calibration targets
rovertarget1middle	Mission target	6/21/12	Middle portion of Mars Methane Mission rover target 1
rovertarget1middle_ref	Mission target	6/21/12	Middle portion of Mars Methane Mission rover target 1 with calibration targets
rovertarget1right	Mission target	6/21/12	Right portion of Mars Methane Mission rover target 1
rovertarget1right_ref	Mission target	6/21/12	Right portion of Mars Methane Mission rover target 1 with calibration targets
rovertarget2	Mission target	6/21/12	Mars Methane Mission rover target 2

Image name	Type	Date	Notes
rovertarget2_ref	Mission target	6/21/12	Mars Methane Mission rover target 2 with calibration targets
rovertarget3	Mission target	6/21/12	Mars Methane Mission rover target 3
rovertarget3_ref	Mission target	6/21/12	Mars Methane Mission rover target 3 with calibration targets
rovertarget4	Mission target	6/21/12	Mars Methane Mission rover target 4
rovertarget4_ref	Mission target	6/21/12	Mars Methane Mission rover target 4
rovertarget5	Mission target	6/21/12	Mars Methane Mission rover target 5
rovertarget5_ref	Mission target	6/21/12	Mars Methane Mission rover target 5 with calibration targets

Table 2. Laboratory hyperspectral images acquired of samples from Norbestos, Quebec. All images are calibrated

Sample	Image name	Imaging system	Notes
Nor3-1	Nor3_1VISRef3_side1 Nor3_1VISRef3_side2 Nor3_1NIR_650_ref6 Nor3_1NIR_650_ref6_side2	Channel Systems visible/NIR	2 sides imaged
Nor3-2	Nor3_2VISRef1 Nor3_2NIR_650_ref5	Channel Systems visible/NIR	
Nor3-6	Nor3_6VISRef1_1 Nor3_6VISRef1_2 Nor3_6NIR_650_ref5_piece1 Nor3_6NIR_650_ref5_piece2	Channel Systems visible/NIR	2 sides imaged
Nor3-7	Nor3_7VISRef3 Nor3_7NIR_650_ref5_1	Channel Systems visible/NIR	
Nor3-8	Nor3_8VISRef2 Nor3_8NIR_650_ref5	Channel Systems visible/NIR	
Nor4-1	Nor4_1VISRef1 Nor4_1NIR_650_ref4_1	Channel Systems visible/NIR	
Nor4-2	Nor4_2VISRef2 Nor4_2NIR_650_ref4	Channel Systems visible/NIR	
Nor4-3	Nor4_3VISRef1 Nor4_3NIR_650_ref5_1	Channel Systems visible/NIR	
Nor4-3	Nor04_3_2013_10_11_13_29_42 Nor4_3_swir_2013_10_11_14_11_10	Headwall Photonics VNIR+ SWIR	
Nor4-4	Nor4_4VISRef2 Nor4_4VISRef2_back Nor4_4NIR_650_ref4_1 Nor4_4NIR_back_650_ref4_1	Channel Systems visible/NIR	Front and back imaged
Nor4-5	Nor4_5VISRef3 Nor4_5NIR_650_ref5	Channel Systems visible/NIR	
Nor4-7	Nor4_7VISRef3 Nor4_7_NIR_650_ref5	Channel Systems visible/NIR	
Nor4-9	Nor4_9VISRef2 Nor4_9VISRef2_2 Nor4_9VISRef2_3 Nor4_9NIR_650_ref5_rock1 Nor4_9NIR_650_ref5_rock2 Nor4_9NIR_650_ref5_rock2flipped	Channel Systems visible/NIR	3 views of the rocks
Nor4-12	Nor4_12VISRef3 Nor4_12_650_ref6	Channel Systems visible/NIR	

Sample	Image name	Imaging system	Notes
Nor4-13	Nor4_13VISRef1 Nor4_13NIR_650_ref4_1	Channel Systems visible/NIR	
Nor4-14	Nor4_14VISRef3 Nor4_14NIR_650_ref5	Channel Systems visible/NIR	
Nor4-14	Nor4_14_2013_10_11_13_32_44 Nor4_14_swir_2013_10_11_14_08_22	Headwall Photonics VNIR + SWIR	
Nor4-16	Nor4_16VISRef2 Nor4_16NIR_650_ref4_1	Channel Systems visible/NIR	
Nor5-1	Nor5_1VISRef3_1 Nor5_1VISRef3_face2 Nor5_1VISRef3_face3 Nor5_1NIR_650_ref6 Nor5_1NIR_650_ref6_face2 Nor5_1NIR_650_ref6_face3	Channel Systems visible/NIR	3 faces imaged
Nor5-2	Nor5_2VISRef1 Nor5_2NIR_650_ref4_1	Channel Systems visible/NIR	
Nor5-3	Nor5_3VISRef1 Nor5_3NIR_650_ref4_1	Channel Systems visible/NIR	
Nor5-4	Nor5_4VISRef3 Nor5_4NIR_650_ref5	Channel Systems visible/NIR	

Table 3. Hyperspectral imaging data acquired of the Meriden, CT outcrop with the Channel systems visible and near infrared imagers.

Image name[a]	Location imaged	Date	Notes
mer2wall1_dark01_vis mer2wall1_dark01_nir	Southwest corner	6/2/13	Panorama along south wall
mer2wall2_dark01_vis mer2wall2_dark01_nir	South wall	6/2/13	Panorama along south wall
mer2wall3_dark01_vis mer2wall03_dark01_nir	South wall	6/2/13	Panorama along south wall
mer2wall4_dark01_vis mer2wall04_dark01_nir	South wall	6/2/13	Panorama along south wall
mer2wall5_dark01_vis mer2wall05_dark01_nir	South wall	6/2/13	Panorama along south wall
mer2wall6_dark01_vis mer2wall06_dark01_nir	South wall	6/2/13	Panorama along south wall
mer2wall7_dark01_vis mer2wall07_dark01_nir	South wall	6/2/13	Panorama along south wall
mer2wall8_dark01_vis mer2wall08_dark01_nir	South wall	6/2/13	Panorama along south wall
mer2wall9_dark01_vis mer2wall09_dark01_nir	South wall	6/2/13	Panorama along south wall
mer2wall10_dark01_vis mer2wall10_dark01_nir	South wall	6/2/13	Panorama along south wall
mer2wall11_dark01_vis mer2wall11_dark01_nir	South wall	6/2/13	Panorama along south wall
mer3_Wwall_dark01_vis mer3_Wwall_dark01_NIR	West wall	6/4/13	Panorama along west wall
mer3_Wwall02_dark01_vis mer3_Wwall02_dark01_nir	West wall	6/4/13	Panorama along west wall
mer3_Wwall03_dark01_vis mer3_Wwall03_dark01_NIR	West wall	6/4/13	Panorama along west wall
mer3_Nwall01_dark02_vis mer3_Nwall01_dark02_NIR	North wall	6/4/13	Panorama along north wall
mer3_Nwall02_dark02_vis mer3_Nwall02_dark02_nir	North wall	6/4/13	Panorama along north wall
mer3_Nwall03_dark02_vis mer3_Nwall03_dark02_nir	North wall	6/4/13	Panorama along north wall
mer3_Nwall04_dark02_vis mer3_Nwall04_dark02_nir	North wall	6/4/13	Panorama along north wall

[a]Most near infrared (NIR) images are followed by '_650' or '_655.' The intent was to interleave the two images to obtain 5 nm sampling following the procedures described in

Chapter 1. However, during the time that elapsed between the two images, the lighting and shadowing changed enough that this procedure is not possible for laboratory images.

Table 4. Laboratory hyperspectral images acquired at Headwall Photonics, Inc. of select samples from Meriden, CT.

Image name	Sample
Mer_GreenVesicles_2013_10_11_11_24_24 MerGreenVesiscles_SWIR_2013_10_11_14_02_28	Mer_FloatV
Mer_PillowFloat_2013_10_11_11_14_49 Merfloatpillow_swir_2013_10_11_13_54_06	MerPillow
Mer04_3_2013_10_11_13_00_33 Mer04_3_swir_2013_10_11_14_33_53	Mer04-3
Mer04_5_2013_10_11_13_23_51 Mer04_5_swir_2013_10_11_14_28_59	Mer04-5
Mer04_6_2013_10_11_11_45_12 Mer04_6_swir_2013_10_11_13_52_34	Mer04-6
Mer05_4_2013_10_11_13_07_47 Mer05_4_swir_2013_10_11_14_32_05	Mer05-4
Mer05_9_2013_10_11_12_55_45 Mer05_9_SWIR_2013_10_11_14_01_05	Mer05-9
Mer05_10_2013_10_11_13_15_53 Mer05_10_swir_2013_10_11_14_09_47	Mer05-10 (coating)
Mer05_15_2013_10_11_11_58_37 Mer05_15_swir_2013_10_11_14_18_36	Mer05-15
Mer04_6_9p6_VNIR_2014_04_30_15_05_31__bsq Mer04_6_SWIR_2014_04_30_15_33_44	Mer04-6 (cut face)
Mer04_13_9p6_VNIR_2014_04_30_15_05_31__bsq Mer04_13_SWIR_2014_04_30_15_33_44	Mer04-13 (cut face)
Mer04_19_9p6_VNIR_2014_04_30_15_05_31__bsq Mer04_19_SWIR_2014_04_30_15_33_44	Mer04-19 (cut face)
Mer05_4_VNIR_2014_04_30_11_12_03_bsq Mer05_4_SWIR_2014_04_30_15_33_44	Mer05-4 (cut face)
Mer05_6_VNIR_2014_04_30_15_05_31 Mer05_6_SWIR_2014_04_30_15_33_44	Mer05-6 (cut face)
Mer05_10_9p6_VNIR_2014_04_30_15_05_31__bsq Mer05_10_MorethickSections_SWIR_2014_04_30_15_33_44	Mer05-10 (cut face)

Table 5. Hyperspectral images of outcrops at the Haughton impact structure using a Channel Systems near infrared hyperspectral imager.

Image name	Location	Date	Notes
Day2_Wfromcamp_1	Camp	7/17/13	Looking west from campsite
Day2_Wfromcamp_2	Camp	7/17/13	Looking west from campsite
Day2_Wfromcamp_3	Camp	7/17/13	Looking west from campsite
Day2_Wfromcamp_4	Camp	7/17/13	Looking west from campsite
Hau3_ht_far_NIR	Gypsum site 1	7/18/13	Outcrop of altered Bay Fiord Formation
Hau3_ht_far_NIR	Gypsum site 1	7/18/13	Outcrop of altered Bay Fiord Formation
Hau3_ht_close_1_NIR	Gypsum site 1	7/18/13	Outcrop of altered Bay Fiord Formation
Hau3_ht_close_2_NIR	Gypsum site 1	7/18/13	Outcrop of altered Bay Fiord Formation
Hau3_ht_outcrop_1_NIR	Gypsum site 1	7/18/13	Outcrop of altered Bay Fiord Formation
Hau3_ht_outcrop_2_NIR	Gypsum site 1	7/18/13	Outcrop of altered Bay Fiord Formation
Hau3_ht_outcrop_3_NIR	Gypsum site 1	7/18/13	Outcrop of altered Bay Fiord Formation
Hau3_fan_650_NIR	Fan north of gypsum site 1	7/18/13	Fan with many gypsum clasts
Hau3_gypsum1_NIR_650	South of gypsum site 1	7/18/13	Outcrop of altered Bay Fiord Formation
Hau5_Rhino1_far_NIR	East Rhinoceros Creek outcrop	7/20/13	Panorama across gypsum-rich breccia
Hau5_Rhino1_closer_NIR	East Rhinoceros Creek outcrop	7/20/13	Panorama across gypsum-rich breccia
Hau5_Rhino2_closer_NIR	East Rhinoceros Creek outcrop	7/20/13	Panorama across gypsum-rich breccia
Hau5_Rhino2_close_NIR	East Rhinoceros Creek outcrop	7/20/13	Panorama across gypsum-rich breccia
Hau5_Rhino1a_close_NIR	East Rhinoceros Creek outcrop	7/20/13	Panorama across gypsum-rich breccia
Hau5_Rhino1b_close_NIR	East Rhinoceros Creek outcrop	7/20/13	Panorama across gypsum-rich breccia
Hau5_Rhino_Breccia1_NIR	Rhinoceros Creek breccia	7/20/13	Panorama of clast-rich impact melt rock
Hau5_Rhino_Breccia2_NIR	Rhinoceros Creek breccia	7/20/13	Panorama of clast-rich impact melt rock

Image name	Location	Date	Notes
Hau5_Rhino_Breccia3_NIR	Rhinoceros Creek breccia	7/20/13	Panorama of clast-rich impact melt rock
Hau5_Rhino_Breccia4_NIR	Rhinoceros Creek breccia	7/20/13	Panorama of clast-rich impact melt rock
Hau8_Genesis_close1	Calcite-marcasite vug	7/23/13	Close-up views of outcrop
Hau8_Genesis_zoom2	Calcite-marcasite vug	7/23/13	Close-up views of outcrop
Hau8_Genesis_zoom3	Calcite-marcasite vug	7/23/13	Close-up views of outcrop
Hau8_Genesis_close2	Calcite-marcasite vug	7/23/13	Close-up views of outcrop
Hau8_Genesis_far	Calcite-marcasite vug	7/23/13	View of larger outcrop from across river
Hau8_Genesis_mid	Calcite-marcasite vug	7/23/13	View of larger outcrop from across river
Hau8_campW_1	Camp	7/23/13	Panorama of outcrops visible from camp
Hau8_campW_3	Camp	7/23/13	Panorama of outcrops visible from camp
Hau8_campW_2	Camp	7/23/13	Panorama of outcrops visible from camp
Hau8_campW_1_sun	Camp	7/23/13	Panorama of outcrops visible from camp
Hau8_campN_NIR	Camp	7/23/13	Panorama of outcrops visible from camp
Hau8_campW_2_sun	Camp	7/23/13	Panorama of outcrops visible from camp
Hau8_campW_3_sun	Camp	7/23/13	Panorama of outcrops visible from camp
Hau8_CampNandE	Camp	7/23/13	Panorama of outcrops visible from camp
Hau8_CampE_1	Camp	7/23/13	Panorama of outcrops visible from camp
Hau8_CampE_2	Camp	7/23/13	Panorama of outcrops visible from camp
Hau8_CampE_3	Camp	7/23/13	Panorama of outcrops visible from camp
Hau8_CampE_4	Camp	7/23/13	Panorama of outcrops visible from camp
Hau10_RhinoBreccia_Redo_1	Rhinoceros Creek breccia	7/25/13	Panorama of clast-rich impact melt rock
Hau10_RhinoBreccia_Redo_2	Rhinoceros Creek breccia	7/25/13	Panorama of clast-rich impact melt rock

Image name	Location	Date	Notes
Hau10_RhinoBreccia_Redo_3	Rhinoceros Creek breccia	7/25/13	Panorama of clast-rich impact melt rock

Table 6. Hyperspectral images of samples from the Haughton impact structure acquired at visible-near infrared and shortwave infrared wavelengths at Headwall Photonics, Inc.

Image name	Sample
APDI_13_14C_VNIR_2014_04_30_11_38_53 APDI_13_14C_SWIR_2014_04_30_13_34_07	APDI-13-14c (see chapter 3)
RG_HMP_13_06_2013_10_11_13_21_53 RG_HMP_18_06_swir_2013_10_11_14_03_43	RG-HMP-13-06
RG_HMP_13_27_2013_10_11_11_32_48 RG_HMP_13_27_SWIR_2013_10_11_13_58_00	RG-HMP-13-27
RG_HMP_13_30_2013_10_11_13_26_15 RG_HMP_13_30_swir_2013_10_11_14_24_45	RG-HMP-13-30
RG_HMP_13_43_2013_10_11_13_18_24 RG_HMP_13_43_swir_2013_10_11_14_26_46	RG-HMP-13-43
RG_HMP_13_66_2_2013_10_11_13_05_38 RG_HMP_13_66_swir_2013_10_11_14_20_41	RG-HMP-13-66
APDI_13_14a_VNIR_2014_04_30_11_12_03_bsq_calib APDI__13_14a_SWIR_2014_04_30_12_18_40_calib	APDI-13-14a
APDI_13_14b_VNIR_2014_04_30_11_12_03_bsq_calib APDI__13_14b_SWIR_2014_04_30_12_18_40_calib	APDI-13-14b
APDI_13_14d_VNIR_2014_04_30_11_12_03_bsq_calib APDI__13_14d_SWIR_2014_04_30_12_18_40_calib	APDI-13-14d
APDI_13_14e_VNIR_2014_04_30_11_12_03_bsq_calib APDI__13_14e_SWIR_2014_04_30_12_18_40_calib	APDI-13-14e
APDI_13_14g_VNIR_2014_04_30_11_12_03_bsq_calib APDI__13_14g_SWIR_2014_04_30_12_18_40_calib	APDI-13-14g
APDI_13_14h_VNIR_2014_04_30_11_12_03_bsq_calib APDI__13_14h_SWIR_2014_04_30_12_18_40_calib	APDI-13-14h
APDI_13_14i_VNIR_2014_04_30_11_12_03_bsq_calib APDI__13_14i_SWIR_2014_04_30_12_18_40_calib	APDI-13-14i